ASSESSING FRACTURE NETWORKS AND GEOCHEMISTRY OF GEOTHERMAL SYSTEMS IN MAGMA-POOR CONTINENTAL RIFTS: AN EXAMPLE FROM THE MALAWI RIFTED ZONE

By

ESTEFANNY DAVALOS ELIZONDO

Bachelor of Geological Engineer

Autonomous University of Nuevo Leon

Nuevo León, México

2011

Submitted to the Faculty of the
Graduate College of the
Oklahoma State University
in partial fulfillment of
the requirements for
the Degree of
DOCTOR OF PHILOSOPHY
May, 2022

ASSESSING FRACTURE NETWORKS AND GEOCHEMISTRY OF GEOTHERMAL SYSTEMS IN MAGMA-POOR CONTINENTAL RIFTS: AN EXAMPLE FROM THE MALAWI RIFTED ZONE

Dissertation Approved:

Dr. Daniel A. Laó Dávila

Dissertation Adviser

Dr. Mohamed Abdelsalam

Dr. James Knapp

Dr. Jeffrey D. Spitler

ACKNOWLEDGEMENTS

This research has finally been accomplished and this would not be possible without the contributions from different people. I would like to express my deepest appreciation and biggest thanks to my committee chair and Advisor, Dr. Daniel Laó Dávila for his kind gesture, guidance, continuous support, and knowledgeable communication in-depth analysis, which made the successful completion of my doctoral dissertation possible. I thank my co-advisor and committee member, Dr. Mohamed Abdelsalam whose motivation and encouragement was significant in completing the research. In addition, thanks to committee members Dr. James Knapp and Dr. Jeffrey D. Spitler for allowing to be part of this research and for their contributions to refining this work. Furthermore, special thanks to Dr. Eliot and Dr. Estella Atekwana of the University of California, Davis for assisting me with valuable data and insightful contributions to the research. My sincere appreciation also goes to Gift Tsokonombwe, Steven Johnson, Luelseged Emishaw, Jingyao Meng Chase Watkins, Sandra Briceño, and Esteban Gómez for all their general help and shared knowledge that contributed to improving this research. I will always be grateful to the Boone Pickens School of Geology faculty and staff, the Tectonics and Geophysics Investigation Fellows, and the Structural Geology and Tectonics Research Group colleagues for all the support during this research. Many thanks to my colleagues and friends for always staying by my side Sazal Zonaed, Mily Farjana, Conn Wethington, Jamar Bynum, Ruoshi Cao, Wakil Balumi, Oluseun Sanuade, Melina Lazar, Oyewande Ojo, Seyi Scholanke, Alejandra Santiago Torres, Gokce and Andrew Bean, Ines Barrios-Gammon, Xu Liang, Hennessey family, and all my friends and family in general. I would like to sincerely thank my parents Juan De Dios Dávalos and Francisca Elizondo, my sister Ma. Guadalupe Dávalos, my niece Erandi Rodríguez, and my nephew Lander Rodríguez for your love, motivation, and encouragement to pursue higher education. My infinite gratitude to my dear family Alberto, Nora, and Boyd Gallardo for their unconditional love, support, and inspiration, without you this Doctoral Dissertation would not be accomplished, you made my days an adventure and always bring joy and gratitude to my journey.

Name: ESTEFANNY DAVALOS ELIZONDO

Date of Degree: MAY, 2022

Title of Study: ASSESSING FRACTURE NETWORKS AND GEOCHEMISTRY OF GEOTHERMAL SYSTEMS IN MAGMA-POOR CONTINENTAL RIFTS: AN EXAMPLE FROM THE MALAWI RIFTED ZONE

Major Field: GEOLOGY

Abstract: This doctoral dissertation investigates structurally controlled geothermal systems of poor-magma continental rifts in the Western Branch, using as an example the Malawi Rifted Zone (MRZ). The MRZ is at the southern end of the Western Branch of the East African Rift System. It has been affected by repeated stages of deformation, a Paleozoic- Mesozoic rifting event, and the current Cenozoic rifting, which are superimposed on Paleoproterozoic shear zones of mobile belts. Thereby, the propagation and segmentation of the present-day Cenozoic rifting have been controlled by inherited Precambrian suture zones and Mesozoic rift basins structures. The high heat flow and hot springs reported in some segments of the ~N-S Cenozoic rift are the main evidence of the role these structures play in the geothermal systems in this region. The research aims to advance the understanding of structurally controlled geothermal systems to help accelerate the development of low- to medium-temperature geothermal resources in the Western Branch countries. To this end, this research investigates the geochemistry of hot springs and the distribution of estimated reservoir temperatures, the fracture network architecture, and its reactivation potential to identify favorable settings and structures that control the geothermal fluids pathways and storage of geothermal systems. A combination of geochemistry, remote sensing, structural geology, and geophysical methods was implemented to address the objectives of this dissertation. The main results of this research are summarized as follows: (1) the hot springs in the MRZ have their origin in the local meteoric water, infiltrated at depth, and then heated by a high heat flow, where water-rock interaction takes place. Afterward, the parent water ascends through faults to the surface, and processes such as admixture with cold water (>45%) and CO_2 outgassing occur. (2) The northern part of the MRZ shows the hottest area with a maximum reservoir temperature estimated at ~200 °C by geothermometers in the Chiweta zone. (3) Favorable structures control the ascent of geothermal fluids in the northern part of the rift showing high fracture intensity and connectivity proxies a) fault segments coalescing to form hard and soft-linked relays, b) two different oriented fracture segments intersecting each other, and c) on the tips of major normal faults. (4) Aeromagnetic data revealed that possible reactivated foliation planes of Precambrian Shear Zones are important structural controls of geothermal waters at greater depths. (5) A high reactivation potential of ~NW- and ~NNE-striking faults southwest- and northwest dipping respectively, were identified as active fluid pathways in the Chiweta zone. (6) The reactivation potential results allowed defining possible structural boundaries of the Chiweta reservoir and improved its geothermal conceptual model. Detailed information about this doctoral dissertation is presented in the following chapters.

TABLE OF CONTENTS

Chapter Page

LIST OF TABLES

Table Page

Paper 1: Medium to low enthalpy geothermal reservoirs estimated from geothermometry and mixing models of hot springs along the Malawi Rift Zone.

Paper 3: 3D Structural model and slip-dilation tendency analysis of the Chiweta Zone: Geothermal System implications and Fault reactivation potential.

LIST OF FIGURES

Figure Page

Paper 1: Medium to low enthalpy geothermal reservoirs estimated from geothermometry and mixing models of hot springs along the Malawi Rift Zone.

Paper 2: Structural analysis of fracture networks controlling geothermal fluid flow in the northern part of the Malawi Rifted Zone from aeromagnetic and remote sensing data.

Figure Page

Paper 3: 3D Structural model and slip-dilation tendency analysis of the Chiweta Zone: Geothermal System implications and Fault reactivation potential.

Figure Page

CHAPTER I

GENERAL OVERVIEW

1.1 Dissertation Sections

This dissertation has been structured in four sections. The first section gives an overview of the dissertation and introduces the scientific questions investigated in this research. The next sections present three manuscripts resulting from this dissertation that are in various stages of the publication process.

Paper 1: Dávalos-Elizondo, E., Atekwana, E.A., Atekwana, E.A., Tsokonombwe, G. and Laó-Dávila, D.A., 2021. Medium to low enthalpy geothermal reservoirs estimated from geothermometry and mixing models of hot springs along the Malawi Rift Zone. Geothermics, 89, p.101963. https://doi.org/10.1016/j.geothermics.2020.10196

Paper 2: Dávalos-Elizondo, E. and Laó-Dávila, D.A., *under review*, Structural analysis of fracture networks controlling geothermal fluid flow in the northern part of the Malawi Rifted Zone from aeromagnetic and remote sensing data, Journal of Volcanology and Geothermal Research.

Paper 3: Dávalos-Elizondo, E. and Laó-Dávila, D.A., *in preparation*, 3D Structural model and slip-dilation tendency analysis of the Chiweta Zone: Geothermal System implications and Fault reactivation potential, Journal of Structural Geology.

1.2 Research motivation

The East African Rift Systems (EARS) is one of the hottest geothermal regions in the world with more than 20 GW of geothermal resources estimated (Teklemariam, 2018). The highest geothermal potential and installed electricity generation capacity are in the Eastern Branch of the EARS. (Teklemariam, 2018). The tectonic setting of the Eastern Branch is favorable for the presence of high-temperature geothermal resources (>200 °C) due to the high volcanic activity in this region. Currently, the Eastern Branch has about 900 MWe of installed geothermal electricity capacity, led by Kenya with 880 MWe of total geothermal installed capacity (IRENA, 2020).

In contrast, the Western Branch is a magma-poor continental rift segment with volcanic centers limited to few localities at the tips of the rift basins. The low- to medium-temperature geothermal resources (< 200 °C) estimated in the Western Branch have been poorly studied in part because of an absence of economic feasibility analysis. Furthermore, the lack of knowledge, adequate policies, financial support, technical capacity, and appropriate exploration techniques suited to the Western Branch hinder the geothermal development of countries in the region. Therefore, these countries are in their early geothermal exploration stages and do not have installed geothermal capacity (e.g., Dulanya et al., 2010; Kaonga, et al., 2014; Gondwe et al., 2012; and Teklemariam, 2018).

Geothermal systems in the Western Branch are suggested to be primarily structurally controlled (e.g., Hinz et al., 2018), as evidenced by the abundance of hot springs emerging from geological structures along the rift basins. The poorly understood, structurally controlled geothermal resources could be suitable not only for direct uses but also for power generation in countries of the Western Branch (e.g., Hinz et al., 2018; IRENA, 2020). Therefore, geothermal resources can be a good alternative energy source for countries that have an urgent need for electricity generation and at the same time contribute to accelerating the energy transition in this region. For instance, electrical generation in Malawi is 99% based on the Shire River hydropower plant, which experiences recurring shortages problems of more than 50% of its total installed capacity (Gondwe et al., 2012).

In this context, the motivation for pursuing this work is to advance the knowledge of structurally controlled geothermal systems in the Western Branch to help accelerate geothermal energy development in the region, using the Malawi Rifted Zone as an example.

1.3 Current stage of knowledge

The Malawi Rifted Zone (MRZ) is a magma-poor continental rift located at the southern end of the Western Branch. The MRZ has been affected by repeated stages of deformation, a Paleozoic-Mesozoic rifting event, and the current Cenozoic rifting, which are superimposed on Paleoproterozoic shear zones in mobile belts (e.g., Delvaux, 2001). Thereby, the current Cenozoic rifting propagation and segmentation have been controlled by inherited Precambrian suture zones and Mesozoic rift basins structures (e.g., Laó-Dávila et al., 2015).

Geothermal systems in the MRZ are evidenced by (1) the presence of the active Rungwe volcano at the southern tip of the Tanzania border with Malawi, (2) more than 55 hot springs emerging along the border faults of the MRZ (Dávalos-Elizondo et al., 2021), (3) a high heat flow of 60 to 120 mW/m^2 and geothermal gradients of 29 – 32 °C/km (Von Herzen & Vacquier, 1967; Ebinger et al., 1987; Njinju, et al., 2019).

Despite this evidence, Malawi is still in the first stages of exploration due to a dearth of knowledge to quantify and qualify its geothermal resources. The earliest studies on geothermal exploration have focused on the geochemistry and geothermometry estimations of hot springs (e.g., Dulanya et al., 2010; Gondwe et al., 2012; Kaonga et al., 2014; Msika et al., 2014; Tsokonombwe, 2017; Kalebe, 2018; Dávalos-Elizondo et al., 2021). Most of these studies agree that the hottest hot springs are in the northern part of Malawi, particularly the Chiweta hot spring with an estimated reservoir temperatures range of ~130-150 °C from cation and silica geothermometers (Kalebe, 2018; Tsokonombwe, 2017). The Chiweta hot spring is the only place in the entire MRZ where a preliminary conceptual model has been suggested by Tsokonombwe (2017). However, few published studies examine the structural controls and favorable settings of geothermal systems in the MRZ (e.g., Morales-Simfors et al., 2015; Eliyasi, 2016), whereby there are poorly understood.

1.4 Present knowledge gap

Expanding knowledge of structurally controlled geothermal systems and a better understanding of the relationship between geothermal fluids, geochemistry, and structural geology is important for advancing geothermal energy in the Western Branch. Therefore, this dissertation consists of three papers designed to answer some of the following questions related to structurally controlled geothermal systems in magma-poor continental rifts:

Paper 1.- (1) What are the most promising geothermal zones in the MRZ based on their reservoir temperatures and heat flow distribution? (2) What are the different processes that occur during the ascent of geothermal fluids towards the surface?

Paper 2.- (1) What favorable structures control fluid pathways and storage in the geothermal systems in the northern region of the MRZ? (2) What are the spatial arrangement, intensity, and connectivity frequency characterization of fracture networks that can enhance permeability in the northern part of the rift? (3) What role does the spatial arrangement of Precambrian structures (e.g., foliation planes) play in the geothermal systems of this region? (4) What is the structural configuration of geothermal systems in the northern part of the rift?

Paper 3.- (1) What is the fracture network architecture in the Chiweta geothermal zone? (2) What is the geometry of the favorable structures with high reactivation potential able to slip or dilate in the current stress state of the Chiweta zone? (3) What are the possible structural boundaries of the Chiweta geothermal system?

1.5 Research objectives

To answer those questions, we used a combination of remote sensing, geological, structural, geochemical, and geophysical techniques, including cation and silica geothermometers, structural mapping and modeling, structural analysis of fracture networks, and aeromagnetic data analysis. This study achieved the following specific objectives:

Paper 1.- (1) Estimate hot spring reservoir temperatures and estimate relative enthalpies based on chloride mixing models, (2) identify possible origins and processes that could affect hot spring waters during the ascent from their geothermal reservoirs, and (3) analyze reservoir temperatures distribution to identify the most promising areas for geothermal energy generation.

Paper 2.- (1) Identify and characterize fracture networks to better understand the structural controls of geothermal fluids in the northern part of the rift, (2) quantify and identify permeable areas using topological analysis of fracture intensity and connectivity frequency proxies, (3) understand the role that inherited structures play in the geothermal systems of the northern part of the rift through the analysis of aeromagnetic data, and 4) build preliminary geothermal conceptual models of selected geothermal systems.

Paper 3.- (1) construct a three-dimensional structural geometry of the faults identified with remote sensing and aeromagnetic data, (2) perform a slip-dilation tendency analysis to assess the reactivation potential of faults under a stress state condition at depths of reservoir estimation (3) identify, based on the results, which faults are critically stressed and serve as fluid conduits or barriers to the geothermal system, and (4) combine geological, geochemical, and geophysical data with the slip-dilation tendency results to improve the conceptual model of the Chiweta Geothermal System.

1.6 Research findings

The most relevant findings of this research are listed below:

Paper 1.- (1) The stable isotopes results show that hot springs in the MRZ have their origins in the local meteoric water. The hot spring water types were classified as Na-HCO_3, Na-SO_4, or Na-Cl (SO_4) controlled mainly by the mineralogy of the host rocks. (2) Parent geothermal fluids are mixed and diluted with a proportion of more than ~45% of cold water from shallow aquifers. Additionally, other processes such as water-rock interaction, and CO_2 outgassing take place during the ascent of the geothermal fluids to the surface changing the chemistry of the original water. (2) Relative enthalpies of parent geothermal waters estimated from 27 hot springs geothermometer results in the MRZ ranged from 388 kJ/kg to 808 kJ/kg. The highest enthalpy value corresponds to the Chiweta hot spring with an estimated geothermal reservoir temperature from cation geothermometers at 190 °C. (3) Three areas of potential geothermal power generation in the MRZ were identified based on the distribution of estimated reservoir temperature and heat flow. Listed in order of importance are: the Chiweta zone in the northern part of the MRZ, the Nkhokota zone in the north-central part of the rift, and the Shire graben in the south. (4) The conceptual model proposed by this study is that meteoric water from rain recharge infiltrates at high elevations and flows to depth through deep faults (>2.5 km). Then, the meteoric water is heated by a high heat flow to form the parent water (~190°) which flows through permeable zones of the reservoir where water-rock interaction takes place. Afterward, the parent water ascends through faults towards the surface where processes such as admixture with cold water from shallow aquifers (>45%) and CO_2 outgassing take place.

Paper 2.- (1) The fracture networks in the Karonga and Nkhata region comprise a varying degree of complexity along strike. This structural complexity occurs mainly in favorable zones such as a) two fault segments coalescing to form hard and soft-linked relays, b) two different oriented fracture segments intersecting each other, and c) on the tips of major normal faults. The hot springs are located where one or more of these favorable zones occur. (2) The remote sensing analysis shows that Cenozoic normal faults are the primary controlling structures of thermal waters at shallow depths in the Karonga (NW-SE to N-S strike) and Nkhata (N-S strike) regions. (3) The aeromagnetic data revealed that permeable NW-striking foliation planes of the Precambrian Mugesse Shear Zone and WNW to ENE-striking foliation planes of the Mwembeshi Shear Zone are important structural controls of geothermal waters at greater depths in the Karonga and Nkhata region, respectively. (4) The Mwankeja-Mwesia and Chiweta geothermal systems in the Karonga region show favorable structural settings for geothermal fluids related to NNW and NW-striking normal faults segments that coalesce to form hard and soft-linked relay ramps and NW, NNE, and N-striking faults intersecting each other. (5) The Mtondolo geothermal area in the Nkhata region shows that the intersection of N-striking normal faults and ENE-striking foliation planes is the favorable structural setting that controls the emergence of hot springs through the surface. (6) High fracture intensity and connectivity proxies are related to the location of the hot springs at the surface and can be used to determine permeable zones and hidden geothermal fluids. (7) The aeromagnetic data analysis results show that buried faults and possibly reactivated inherited structures (e.g., foliation planes) by brittle deformation are controlling the geothermal fluids at depth. (8) The magnetic basement depth estimation by aeromagnetic data help to interpret that some of the geothermal reservoirs in the northern part of the MRZ have estimated depths from ~500 to ~1000 m.b.g.l.

Paper 3.- (1) ~NW- and ~NNE-striking faults southwest- and northwest dipping, respectively, show segments with the highest dilation values of T_d ~ 0.6 to T_d ~ 0.8 and probably behave as active fluid pathways. This is supported by the Chiweta Fault, a NW-striking and southwest dipping fault that controls the only thermal manifestations in the Chiweta Zone. (2) NW- and NE-striking faults dipping to the northeast and southeast, respectively, show lower dilation values of T_d ~ 0.1 to T_d ~ 0.5 and probably act as fluid barriers. (3) These results allowed us to define, for the first time, possible structural boundaries of the Chiweta geothermal reservoir and to improve its geothermal conceptual model. (4) The recharge of the Chiweta geothermal system comes from northwest and western highlands from an elevation above ~1277 m. (5) Based on observations this study suggests further investigations of uranium deposits near the thermal waters as a possible source of radioactive decay heat for the geothermal system.

1.7 Research Significance

This study sought to advance knowledge of structurally controlled geothermal systems in magma-poor continental rifts to help speed up the exploitation of low to medium-temperature geothermal resources in countries in the Western Branch. The results derived from this study could reduce the risk of drilling unproductive wells in the early phases of exploration, advance the exploration and production of hidden geothermal systems and enhanced geothermal systems (EGS) in this region, as well as in the Eastern Branch. The low-cost methodologies applied in this study could become an exploration strategy for the future development of similar geothermal systems in other countries of the Western Branch of the EARS.

Furthermore, this study may yield important insights into the structure and tectonic evolution of strain localization in early-stage continental rifts and seismic hazards by understanding the fracture reactivation potential favoring fluid pathways and storage. Subsequently, this study emphasized the important role that these geothermal fluids play in increasing pore fluid pressure in favorable segments of faults (or reservoir layers), which is a key factor in triggering earthquakes.

1.8 References

Dávalos-Elizondo, E., Atekwana, E. A., Atekwana, E. A., Tsokonombwe, G., & Laó-Dávila, D. A. (2021). Medium to low enthalpy geothermal reservoirs estimated from geothermometry and mixing models of hot springs along the Malawi Rift Zone. Geothermics, 89, 101963.

Delvaux, D. (2001). Tectonic and palaeostress evolution of the Tanganyika-Rukwa-Malawi rift segment, East African Rift System. Peri-Tethys Memoir, 6, 545-567.

Dulanya, Z., Morales-Simfors, N., & Sivertun, Å. (2010). Comparative study of the silica and cation geothermometry of the Malawi hot springs: Potential alternative energy source. Journal of African Earth Sciences, 57(4), 321-327. doi:10.1016/j.jafrearsci.2009.11.001.

Ebinger, C. J., Rosendahl, B., & Reynolds, D. (1987). Tectonic model of the Malaŵi rift, Africa. Tectonophysics, 141(1-3), 215-235.

Eliyasi, C.N., 2016. Exploration for Geothermal resources using Geological structures with emphasis on faults-A case study of northern Malawi. In Proceedings, 6th African Rift Geothermal Conference Addis Ababa, Ethiopia, 2nd–4th November.

Gondwe, K., Allen, A., Georgsson, L., Loga, U., & Tsokonombwe, G. (2012, November). Geothermal Development in Malawi–a Country Update. In Proceedings 4th African Rift Geothermal Conference, Nairobi, Kenya (pp. 21-23).

Hinz, N. H., Cumming, W. B., & Sussman, D. (2018). Exploration of fault-related deep-circulation geothermal resources in the western branch of the East African Rift System: examples from Uganda and Tanzania. In Proceedings, 7th African Rift Geothermal Conference, Kigali, Rwanda 31st October–2nd November.

IRENA (2020). Geothermal Development in Eastern Africa: Recommendations for power and direct use, International Renewable Energy Agency, Abu Dhabi.

Kalebe, Y. N. (2018). Chemical and isotopic composition of thermal waters in northern part of Malawi. United Nations University, UNU Geothermal Training Programme, Iceland. Report; 2017: 13.

Kaonga, H., Tsokonombwe, G., & Kamanga, T. (2014). Status of Geothermal Exploration in Malawi. In ARGEO-C5 Conf (pp. 29-31).

Laó-Dávila, D.A., Al-Salmi, H.S., Abdelsalam, M.G. and Atekwana, E.A., 2015. Hierarchical segmentation of the Malawi Rift: the influence of inherited lithospheric heterogeneity and kinematics in the evolution of continental rifts. Tectonics 34 (12), 2399–2417. https://doi.org/10.1002/2015tc003953.

Morales-Simfors, N., Dulanya, Z. and Sivertun, Å., 2015. Structural and Stratigraphic Controls of Malawi's Hotsprings: a Review. In World Geothermal Congress 2015 Melbourne, Australia, 19-25 April 2015. International Geothermal Association.

Msika, B. J., Saka, J. D. K., & Dulanya, Z. (2014). Spatial distribution, chemistry and subsurface temperatures of geothermal springs Nkhata bay, Malawi. African Journal of Environmental Science and Technology, 8(8), 464-475.

Njinju, E. A., Kolawole, F., Atekwana, E. A., Stamps, D. S., Atekwana, E. A., Abdelsalam, M. G., and Mickus, K. L., (2019). Terrestrial heat flow in the Malawi Rifted Zone, East Africa: Implications for tectono-thermal inheritance in continental rift basins: Journal of Volcanology and Geothermal Research.

Teklemariam, M. (2018). Geothermal outlook in East Africa and the contribution of UNU-GTP in capacity building.

Tsokonombwe, G. (2017). Hydrogeochemistry modeling of Chiweta geothermal prospect, Northern Malawi (Doctoral dissertation).

Van der Beek, P., Mbede, E., Andriessen, P., & Delvaux, D. (1998). Denudation history of the Malawi and Rukwa Rift flanks (East African Rift System) from apatite fission-track thermochronology. Journal of African Earth Sciences, 26, 363-386.

CHAPTER II

PAPER 1: MEDIUM TO LOW ENTHALPY GEOTHERMAL RESERVOIRS ESTIMATED FROM GEOTHERMOMETRY AND MIXING MODELS OF HOT SPRINGS ALONG THE MALAWI RIFT ZONE.

2.1 Abstract

We investigated the major ion and stable isotope geochemistry and used silica and cation concentrations to assess the geothermometry of hot springs along the Malawi Rift Zone (MRZ). The MRZ is a magma-poor rift, where potential geothermal energy is postulated from elevated heat flow and the occurrence of hot springs. Our objectives were to (1) estimate hot spring reservoir temperatures, (2) identify processes that could affect hot spring water during the ascent from their geothermal reservoirs, and (3) identify the most promising areas for geothermal energy generation. New geochemistry data from 27 hot springs were analyzed and classified as Na-HCO_3, Na-SO_4, or Na-Cl (SO_4) water types controlled mainly by the mineralogy of the host rocks. The hot springs in the MRZ are associated with the local meteoric waters that infiltrate at depth and are heated

by an anomalously high geothermal gradient. Our findings indicate that a parent geothermal fluid is mixed and diluted with a proportion of more than ~45% of cold water from shallow aquifers. Additionally, other processes such as water-rock interaction, and CO_2 outgassing take place during the ascent of the geothermal fluid to the surface. The quartz conductive silica geothermometer indicates reservoir temperatures that range from 60°C to 130°C, with enthalpies ranging from 250 kJ/kg to 537 kJ/kg, respectively. However, the Na-K cation geothermometer indicates reservoir temperatures from 92°C to 190°C with enthalpies from 388 kJ/kg to 808 kJ/kg. Three areas of potential geothermal energy generation were identified: (1) The Chiweta area, (2) the Nkhotakota area, and (3) the Shire graben area. We conclude that the hot springs along the MRZ have geothermal energy capabilities of medium to low enthalpy that can be exploited for electricity generation or other direct uses.

2.2 Introduction

More than 20 GW of geothermal resources is estimated for the East African Rift System (EARS), making it one of the hottest geothermal regions in the world (Teklemariam, 2018). The highest geothermal potential and installed electricity generation capacity are in the Eastern Branch of the EARS (Fig. 1A), where volcanism occurs (Teklemariam, 2018). Currently, Kenya has the greatest geothermal electricity generation in the EARS, with an installed capacity of more than 676 MWe (Teklemariam, 2018). In contrast, low to medium geothermal enthalpy is expected in the Western Branch of the EARS (Fig. 1A; e.g., Hinz et al., 2018), a magma-poor rift segment with volcanic centers limited to a few localities at the tips of the rift basins (Fig. 1A). This has brought into question the source of heat for the geothermal waters along the Western Branch. Countries in the Western Branch of the EARS like Malawi are in their early geothermal exploration stages and have no installed geothermal capacity (e.g., Dulanya et al., 2010; Kaonga, et al., 2014; and Gondwe et al., 2012; Teklemariam, 2018).

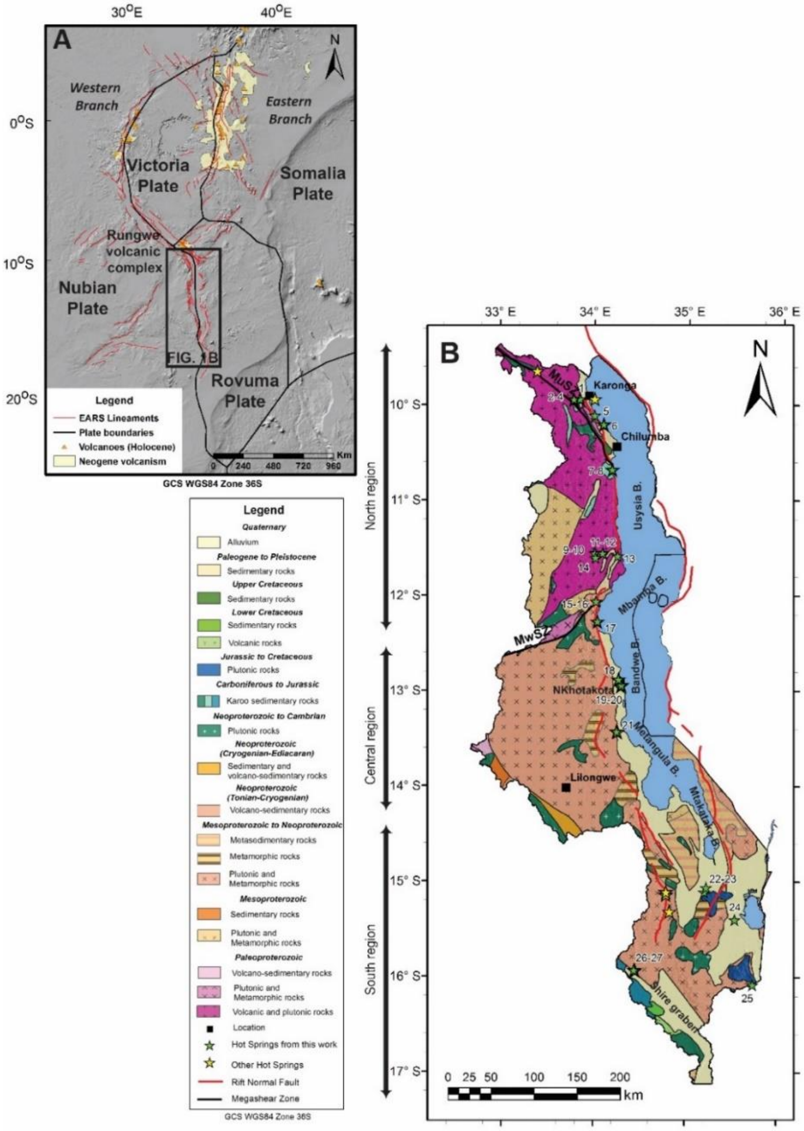

Figure 1. A. Tectonic setting of the East African Rift System showing the Eastern and Western branches, the country boundaries, and the surrounding tectonic plates. B. Geological Map of

Malawi (Modified from Milési et al., 2004) showing main locations of hot springs (as green stars) from this work and other hot springs (as yellow stars) described in previous works (e.g., Dulanya et al., 2010; Kaonga et al., 2014; Msika et al. 2014; Gondwe et al., 2012). From north to south the hot springs studied in this work: 1: Mbande, 2: Mwankenja 2, 3: Mwankenja 1, 4: Mwankenja 3, 5: Chiwondo, 6: Ngala, 7: Chiweta, 8: Mphizi stream, 9: Kajilirwe (DC), 10: Kajilirwe, 11: Chilongozi, 12: Chidha, 13: Kalwe, 14: Kajilirwe 2, 15: Mtondolo 2, 16: Mtondolo, 17: Chiwe, 18: Chombo, 19: Madzimawira, 20: Ling'ona, 21: Chikwizi, 22: Liwonde, 23: Sitima, 24: Mpsupsu, 25: Muloza, 26: July Borehole, and 27: Chipuze. Labels on the left represent the three major segmented regions proposed by Laó-Dávila et al. (2015).

There is a geothermal anomaly beneath certain segments of the MRZ evidenced by a sustained high heat flow of 60 to 120 mW/m^2 (Von Herzen & Vacquier, 1967; Ebinger et al., 1987; Njinju, et al., 2019). Njinju et al. (2019) used aeromagnetic data to argue for high geothermal gradients (29-32°C/km) and a high heat flow (70-82 mW/m^2) within the Karoo basins in the central segment and at the Rungwe Volcanic complex in the north of the MRZ. Besides, the Study of Extension and maGmatism in Malawi aNd Tanzania (SEGMeNT) in the northern part of the MRZ provide seismic evidence of low P-S and Rayleigh waves velocities at depths ~150-200 km beneath the Rungwe Volcanic Complex (Accardo et al., 2017). These low anomalous seismic velocities may result from a mantle superplume (Grijalva et al., 2018) or partial melting of a lithospheric mantle beneath the northern region of the MRZ (Accardo et al., 2017; Borrego et al., 2018). Also, these studies of S-wave velocities infer that the thickness of the lithosphere is between 36 and 38 km beneath most of the MRZ, except for the southern part of the rift where a thicker crust between 38 and 40 km depth is present (e.g., Wang et al., 2019; Borrego et al., 2018).

The geothermal potential of Malawi is estimated at 200 MWe according to the Millennium Challenge Compact's Integrated Resource Plan (MCC, 2011). Despite the evidence of potential geothermal resources in Malawi, there is a lack of development of geothermal energy due to limited technical capacity, lack of investments, financial support, and a dearth of exploration data needed to classify and quantify the resources (Gondwe et al., 2012). Moreover, Malawi has experienced serious electricity generation problems in the Shire River hydropower plant, which is Malawi's major energy source (Gondwe et al., 2012). Because geothermal reservoirs have the potential to be used for electricity generation, they would provide an additional and alternative energy solution to the problem of the electricity generation shortage in Malawi.

Previous studies on geothermal exploration in Malawi have focused on understanding the geochemistry of hot springs. Dixey (1927), Bloomfield (1965), Bloomfield and Garson (1965), Kirkpatrick (1969), Chapusa and Harrison (1975), and Ray (1975) conducted the early studies that identified and geochemically characterized selected hot springs in Malawi. Dulanya (2006) and Dulanya et al. (2010) used the published geochemistry data to estimate geothermometers for 11 hot springs across Malawi and obtained a maximum reservoir temperature of 214 °C. Kaonga et al. (2014) and Gondwe et al. (2012) indicate that over 55 hot springs have been located in Malawi (Table S1, Appendix B), although no chemical data were provided in their publication. Gondwe et al. (2012) showed that most of the hottest hot springs were in the northern part of Malawi between Karonga and the central basin in the Nkhotakota region (Fig. 1B).

Recent studies that provided geochemistry data and geothermometer estimates focused on specific regions and a few hot springs. Msika et al. (2014) reported geothermometer estimates from Na-K for 11 hot springs investigated in 2007 in the central part of the MRZ in the Nkhata Bay area (Fig. 1B). The results of the Msika et al. (2014) study show reservoir temperature ranges of 112 °C – 280 °C, with the highest temperature estimated for the Kanunkha hot spring. Kalebe (2018) estimated reservoir temperatures from silica and cation geothermometers for four hot springs in the northern part of Malawi. The results of the Kalebe (2018) study showed that the Chiweta hot spring contains mature geothermal water with a Cl (SO_4) composition and a reservoir temperature above 100°C. Likewise, Tsokonombwe (2017) reported results for geothermometers in the Chiweta hot spring (Fig. 1B) with reservoir temperatures of about 132°C – 157°C.

Presently, our understanding of the distribution of reservoir temperatures along the MRZ is limited. Even less understood are the sources of anomalous high-temperature geothermal fluids, their dissolved constituents, the geochemical processes taking place in shallow and deep reservoirs, and the interaction between high-temperature hydrothermal fluids and cold-water reservoirs. This study provides more comprehensive geothermometer estimates from new geochemistry data for 27 hot springs along the MRZ collected by Atekwana et al. (2015) in 2013 (Fig. 1B). Additionally, we use geoindicator diagrams and mixing models to determine the reservoir temperatures distribution along the MRZ. We also assess the processes that take place during the ascent of the geothermal waters and provide an estimate of high and low-enthalpy fluids in the geothermal reservoirs to identify the best areas for geothermal energy generation.

The hypothesis that guides this study is that the MRZ has geothermal potential areas of at least medium enthalpy (>100 °C) in the northern part of the country (e.g., Dulanya et al., 2010; Msika et al., 2014; Gondwe et al., 2012; Tsokonombwe, 2017) that could be exploited for electricity generation and direct uses. The geothermal systems are related to meteoric waters infiltrating at depth through faults and are heated by an anomalously high geothermal gradient (e.g., Atekwana et al., 2015; Hinz et al., 2018).

2.3 Regional and Geological Setting

The country of Malawi is bordered by Tanzania to the northeast and north, Zambia to the west and northwest, and Mozambique to the southeast and southwest (Fig. 1A). Malawi is located latitudinally between 9°22' north and 17°7' south and longitudinally between 32°40' west and 35°55' east. The climate in Malawi is extremely variable from subtropical to tropical savanna climate because of the Inter-Tropical Convergence Zone (ITCZ) and the influence of the abrupt topography that consists of plateaus, mountainous areas, escarpments, rift valleys, and Lake Malawi (~19 to 3,000 m.a.s.l). The mean annual temperature is between 22-24°C, whereas during the dry winter season (from May to August) the mean temperature varies between 17-23°C, and from September to October (warm-dry season) the temperatures range between 25-37°C. Rainfall varies from ~725 mm/y to 1700 mm/y with ~95% of the rain falling during the wet season from November to April (http://www.malawi.climatemps.com/).

The MRZ is at the southern end of the Western Branch of EARS and spans ~750 km from the Rungwe volcanic province in Tanzania to the Shire graben in southern Malawi (Fig. 1A; Ebinger, 1989; Ring & Betzler, 1995; Chorowicz, 2005; Laó-Dávila et al., 2015). Lake Malawi extends along the rift axis for ~550 km and varies in width from 75 to 50 km (McCartney & Scholz, 2016; Grijalva et al., 2018). The Rungwe volcanic complex, which is composed of basalt and nephelinite, lies in the northern part of the MRZ and is one of the few volcanoes of the Western Branch, and the only one of the Late-Cenozoic age (Ebinger, 1989; Scholz et al., 2011). Ebinger et al. (1984) suggested that the Malawi Rift developed diachronously from north to south evidenced by different thicknesses in depositional sequences and fault pattern segments. Radiometric dating of rocks in the Rungwe volcanic complex indicates an age of ~18 Ma for the initiation in the northern part (Rasskazov et al., 2003; Mesko et al., 2014; Grijalva et al., 2018). However, fission-track ages for apatite extracted from Precambrian rocks in the north area of Malawi (Van der Beek et al., 1998) and the Rukwa Rift Basin in Tanzania indicate that the Western Branch of the EARS started to extend around 30 Ma in the Oligocene (Roberts et al., 2012; Fagereng, 2013).

The Malawi Rift formed within a high-grade metamorphic Precambrian to Paleozoic age basement (Fig. 1B) composed of feldspathic gneisses, schists, and granulites (Bloomfield, 1968; Flannery & Rosendahl, 1990; Chapola & Kaphwiyo, 1992). The crystalline metamorphic complex is the source of the detrital siliciclastic sediments deposited in the Lake Malawi basin (Scholz et al., 2011). Overlying the crystalline basement is the Permo-Triassic Karoo sandstone, shale, and coal, as well as the red bed terrestrial sedimentary sequence (Fig. 1B) of the Cretaceous age (Chapola & Kaphwiyo, 1992; Scholz et al., 2011). Lacustrine sediments and alluvium along the lakeshore and Shire River basin overlie the Karoo Formation, which is overlain by Neogene and Quaternary age fossiliferous limestones (Chapola & Kaphwiyo, 1992; Scholz et al., 2011). Igneous dikes (Chapola & Kaphwiyo, 1992) intrude the rocks of the Neogene and Quaternary ages (Fig. 1B).

The structure of the MRZ consists of seven asymmetric basins distributed into three major regions (Fig. 1B): the northern, central, and southern regions (Reynolds & Rosendahl, 1984; Ebinger, 1989; Laó-Dávila et al., 2015; Kolawole et al., 2018). The Karonga Basin, Usisya Basin, Mbamba Basin, and the Bandwe Basin constitute the northern portion of the rift. The central region consists of the Metangula Basin, Mtakataka Basin, and the Shire Basin occupies the southern region (e.g., Kolawole et al., 2018). The seven asymmetric basins are linked by accommodation and transfer zones (Fig. 1B; Flannery & Rosendahl, 1990; Ring & Betzler, 1995). Furthermore, the present-day approximate N-S orientation of the MRZ is said to be controlled by pre-rift structures associated with cratons, mobile belts, and basement foliations (Versfelt & Rosendahl, 1989; Ring, 1994; Lyons et al., 2011; Laó-Dávila et al., 2015). The Ubendian, Irumide, and Mozambique mobile belts were formed during three orogenic episodes of the Paleoproterozoic and Neoproterozoic ages (Fritz et al., 2013).

2.4 Data and Methods

2.4.1 Sampling and analytical methods

General descriptions and characteristics of 27 hot springs in the field along the MRZ are summarized in Appendix A. The geochemical data for the 27 geothermal waters (Table 1) were collected along a north to south traverse in July 2013 (Fig. 1B) during the dry season. A total of 17 samples were collected from the North region, four from the Central region, and six from the South region of the rift. The samples from hot springs were collected by the grab technique at the source where the spring discharged to the surface. During collection, the samples were filtered through 0.45 µM nylon filters and stored in 30 mL high-density polyethylene (HDPE) bottles for anion analysis and in pre-acidified (high purity HNO_3) 60 mL HDPE bottles for cation analysis. Water sampled for stable hydrogen (δD) and oxygen ($\delta^{18}O$) isotopes were collected in 20 mL glass scintillation vials with an inverted cone closure. The samples were kept in a 12V portable refrigerated cooler for up to 4 weeks before transportation to Oklahoma State University where they were stored in a 4°C refrigerator until analysis.

At each spring location, the temperature, total dissolved solids (TDS), and pH were measured in situ with a Yellow Spring Instrument (YSI-556® MPS) probe calibrated in accordance with the manufacturer's recommendations. The temperature, pH, and TDS of hot springs with temperatures above 45°C were measured with a Hanna Instruments (HI 9124 Waterproof Portable pH Meter with an HI 1006-3007 Industrial Flat-Tip pH Electrode and an HI 9835 Portable EC/ TDS/ NaCl/°C Meter) calibrated following Hanna Instrument's recommendations. Water with temperatures above 45°C was also collected in a 1L HDPE bottle, allowed to cool, and then SPC, TDS, ORP, and pH were measured with the YSI. Physical parameters measured by the YSI are not temperature-dependent but have to be measured within the 45°C temperature threshold of the instrument.

In the field, alkalinity was determined by a H_2SO_4 titration to an acid equivalent point of 4.2 using a digital titrator (Hach Company, 1992), and dissolved silica was determined using heteropoly blue chemistry® to determine the "molybdate reactive" silica and measured with a CHEMetrics® V-2000 Photometer at 815 nm (CHEMetrics, 2012). Anions (SO_4^-, Cl^-) were determined using ion chromatography (Dionex Chromatography System ICS-3000,) and cations (Ca^{2+}, Mg^{2+}, Na^+, K^+) were determined by inductively coupled plasma-optical emission spectrometer (PerkinElmer OptimaTM 2000 DV). The charge balance between anion and cation, ([ΣAnions – ΣCations] / [ΣAnions + ΣCations]), concentrations in equivalents, were less than 5%, with exception of the Chidha hot spring sample with a charge balance of 8% (Table S2, see Appendix B).

The δD and $\delta^{18}O$ of the water samples were determined by a high-temperature elemental conversion analyzer coupled to a Thermo Finnigan Delta Plus XL IRMS per the Gehre et al. (2004) method. The δ values were determined against the Vienna Standard Mean Ocean Water (VSMOW) for hydrogen and oxygen. Routine determinations of in-house standards and samples have a precision of better than 0.2‰ for $\delta^{18}O$ and 2.0‰ for δD.

2.4.2 Geochemistry analysis

The spreadsheets by Powell and Cumming (2010) were used to generate graphics, ternary diagrams, and cross-plots from water chemistry data using formulas based on equilibrium reactions, and empirical relationships (see Powell & Cumming, 2010 for more information about methods and the use of the spreadsheets). The diagrams display silica and cation geothermometry estimates (e.g., Fournier, 1981; Fournier & Potter, 1982; and Giggenbach, 1991), fluid composition (i.e., Piper diagram), geoindicators (e.g., Giggenbach, 1988; 1991; Giggenbach & Goguel, 1989), and mixing models including the chloride-enthalpy diagram based on quartz and Na-K geothermometers. Additionally, the δD and $\delta^{18}O$ were used to determine the origin of hot springs and to identify secondary processes such as water-rock interaction. Furthermore, supplementary data was added to calculate the mineral saturation index (SI) of hydrothermal minerals and partial pressure of CO_2 (pCO_2) (Table S5, Appendix B) using PHREEQCI software version 3.4 (Parkhurst & Appelo, 1999).

2.4.2.1 Chemical geothermometers

The silica geothermometers are based on the variations of silica phases (mg/kg) solubility equilibrium according to temperature and pressure (e.g., Fournier & Truesdell, 1973; Powell & Cumming, 2010). In general, quartz geothermometers are used for geothermal waters with temperatures ranging from 150 – 225°C, whereas chalcedony, cristobalite, or amorphous silica are used with lower temperatures <180°C (Fournier, 1977). However, groundwater temperatures calculated by silica geothermometers could be affected by different processes that can yield lower or higher temperature estimates, such as dilution with groundwater from shallow aquifers, precipitation of silica due to lower temperatures when water is moved toward the surface, and boiling processes (e.g., Fournier & Truesdell, 1970). Different silica geothermometers were used in this study to estimate reservoir temperatures (e.g., Fournier, 1977; Fournier & Potter, 1982; Arnórsson *et al.,* 1983; & Verma, 2000): α cristobalite, chalcedony conductive, quartz adiabatic, and quartz conductive.

The cation geothermometers are commonly used to estimate the highest temperatures in deeper parts of geothermal systems where waters are in partial or full equilibrium with the rock (Powell & Cumming, 2010). The cation geothermometers are based on Na-K ratios and Na-K-Ca relations in natural waters (e.g., Fournier, 1979; Truesdell, 1976; Fournier, 1981; Arnórsson *et al*., 1983; Giggenbach, 1988). The Na-K-Ca geothermometer (Fournier, 1981; Giggenbach, 1988) and Na/K by Giggenbach (1988) provide more reliable results than other Na/K geothermometers for low temperatures reservoirs (<150˚C). We estimated reservoir temperatures by a Na-K-Ca geothermometer by Fournier (1981), five Na-K geothermometers (Fournier, 1979; Truesdell, 1976; Arnórsson *et al*., 1983; Giggenbach, 1988; and Verma & Santoyo, 1997), and one K/Mg geothermometer (Giggenbach, 1986).

The K-Mg-Na ternary diagram “geoindicator” by Giggenbach (1988) was used to distinguish the geothermal waters at high temperatures that are in equilibrium with the rock and shallow groundwaters in equilibrium at lower temperatures. Likewise, the Giggenbach (1988) diagram was used to identify immature waters for which cation geothermometry estimates should be viewed with caution (Fournier, 1989). Additionally, the Na-K-Mg ternary diagram was used to assess the effects of different processes, such as the mixing of waters (Fournier, 1989). Furthermore, the Na-K/Mg-Ca diagram constructed by Giggenbach and Goguel (1989) is another “geoindicator” that shows how a Na-K geothermometer correlates with the Mg-Ca equilibration system (Powell & Cumming, 2010).

The K-Ca-Mg-CO_2 diagram by Giggenbach (1988) correlates the K-Mg geothermometer with the CO_2 fugacity. This geothermometer assumes the existence of an equilibrium between K-feldspar, calcite, and K-mica versus dissolved Ca and K (Powell & Cumming, 2010). The K-Ca-Mg-CO_2 diagram determines the partial pressure of CO_2 corresponding to the last temperature of the water-rock equilibrium (Powell & Cumming, 2010). Two lines limit the “calcite formation” field: (1) “rock dominated”, and (2) “fluid dominated” (Giggenbach & Corrales-Soto, 1992). The data that plot outside the “calcite formation” field in the K-Ca-Mg-CO_2 diagram should be only interpreted qualitatively (Powell & Cumming, 2010).

2.4.2.2 Mixing models

The chloride-enthalpy diagram was used to calculate enthalpies of high-temperature waters that are mixed with low-temperature waters to give warm springs with “mixed” waters and boiling springs (Fournier, 1979; Fournier and Potter, 1982; Powell & Cumming, 2010). In this study, we constructed the enthalpy-chloride diagrams based on enthalpy estimates from silica (Fournier & Potter, 1982) and Na-K (Giggenbach, 1988) geothermometer temperatures. The assumption made in this study is that a common parent geothermal fluid (juvenile or primary geothermal waters) could exist at depth in the region. The diagram uses a fourth-order polynomial curve that fits the enthalpy of pure water from 50°C to 340°C (Powell & Cumming, 2010). The steam point of 2800 kJ/kg was fixed with a data point in the “enthalpy” axis, typical of steam separated between 200°C and 260°C (Powell & Cumming, 2010).

2.5 Results

2.5.1 Hydrochemistry of geothermal waters

Geothermal fluids in the MRZ are characterized by hot springs controlled by Quaternary rift faults generally aligned ~N-S and ~NW-SE (Fig. 1B). The surface temperatures of the 27 hot springs from which samples were collected along the MRZ ranged from 34.7°C to 79.7°C (Table 1). These waters are classified as thermal waters because they have temperatures higher than 6.5° C above the local mean ambient temperature of ~23°C in Malawi (Leet, 1982). The hottest temperatures of 79.7°C for the Chiweta hot spring and 78.7°C for the Mphizi stream were measured in the northern part of Malawi (Fig. 1B). Kalwe and Chiwondo are the coldest hot springs in northern Malawi (Fig. 1B) with surface temperatures of ~35°C. The pH values of the hot spring waters ranged between 7.3 and 9.6, which correspond to alkaline waters. The TDS concentrations were between 100 and 1300 mg/L and the specific conductance (SpC) ranged from 164 to 2036 µS/cm. The Chiweta hot spring and the Mphizi stream also show the highest TDS and SpC values measured for the hot springs in the North region, along with the July borehole and Chipuze hot springs in the South region (Table 1).

The order of anionic abundance in the hot springs in MRZ is $HCO_3^- > SO_4^{2-} > Cl^- > F^- > CO_3^{2-}$, while the cations are $Na^+ > Ca^{2+} > K^+ > Mg^{2+}$. Three main water facies were identified (Fig. 2) with the Piper diagram: (1) sodium bicarbonate (Na-HCO_3), (2) sodium sulfate (Na-SO_4), and (3) sodium chloride and sulfate (Na-Cl [SO_4]). In all the hot springs, the Na-HCO_3 water type represents 52% of the hot spring waters, while the Na-SO_4 water type represents 33% and the Na-Cl (SO_4) water type represents 15%.

The Chiweta, Mphizi stream, July borehole, and Chipuze hot springs are characterized as Na-Cl (SO_4) waters. These four hot springs have higher chloride concentrations between 120 to 320 mg/L compared to the other hot spring waters. Likewise, the Chiweta, the Mphizi stream, the July borehole, and the Chipuze hot spring waters show higher SiO_2 concentrations of 66 mg/L, 84 mg/L, 68 mg/L, and 61 mg/L, respectively (Table 1).

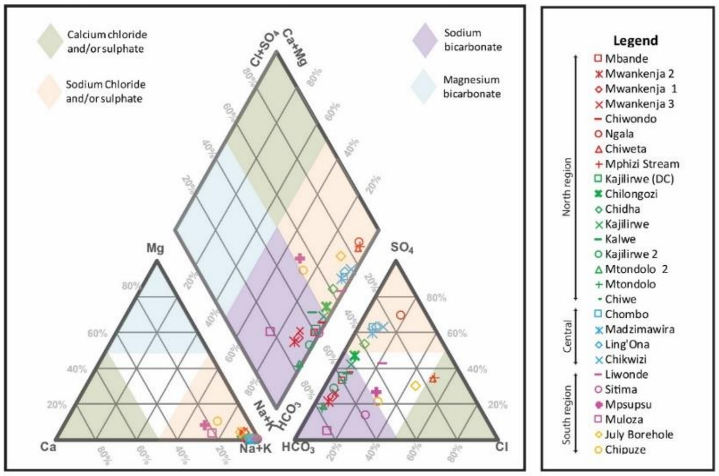

Figure 2. Piper ternary diagram showing major cations and anions (percentage from Eq/L) of Malawi's hot springs and the different water types. The legend shows the hot springs ordered by the three major regions of the rift.

Table 1. Physico-chemical data for 27 hot springs listed from north to south (see Fig. 1B) along the Malawi Rift Zone (Atekwana *et al.*, 2015). The TDS and the major ions are given in units of mg/L and the $\delta^{18}O$ and δD are reported per mil relative to Vienna Standard Mean Ocean Water.

No.	**Hot springs**	**T°C**	**TDS**	**pH**	**EC µS/cm**	**Na^+**	**K^+**	**Ca^{2+}**	**Mg^{2+}**	**SiO_2**	**F^-**	**Cl^-**	**SO_4^{2-}**	**HCO_3^-**	**CO_3^{2-}**	**$\delta^{18}O$**	**δD**
1	Mbande	43.05	451	8.70	694	143.3	2.1	2.4	0.4	37.7	4.4	14.5	92.5	214.7	11.7	-6.5	-34.9
2	Mwankenja 2	48.55	469	7.75	722	152.8	3.3	9.0	3.5	28.0	2.8	15.2	74.3	319.6	0	-6.9	-39.6
3	Mwankenja 1	45.80	474	8.55	729	144.5	2.2	7.5	3.4	28.7	3.5	15.0	77.1	281.1	5.8	-7.0	-38.9
4	Mwankenja 3	36.92	477	8.09	734	152.7	3.4	9.3	3.8	15.9	3.9	17.6	88.8	285.7	2.9	-7.0	-39.4
5	Chiwondo	35.80	568	8.37	873	187.0	2.3	2.5	0.2	8.0	8.4	23.5	139.7	252.3	5.3	-6.7	-40.1
6	Ngala	54.90	851	8.35	1307	238.0	4.4	14.0	0.1	27.2	8.0	65.3	360.5	85.5	1.8	-5.9	-32.8
7	Chiweta	79.70	1301	7.83	2001	389.2	21.3	17.2	0.4	65.8	12.8	315.9	287.3	162.3	0	-5.0	-26.0
8	Mphizi Stream	78.70	1323	8.01	2036	394.5	22.1	17.5	0.4	84.0	13.3	328.5	298.8	154.2	1.5	-4.6	-26.5
9	Kajilirwe (DC)	36.39	215	9.18	331	66.1	0.6	1.8	0.1	18.0	2.5	6.0	48.6	102.5	9.6	-7.1	-40.3
10	Kajilirwe	36.82	216	9.37	333	66.5	0.6	1.7	0.0	18.2	2.7	6.4	51.9	80.7	12.5	-7.3	-39.6
11	Chilongozi	40.39	229	9.15	352	68.8	1.0	2.4	0.0	19.4	3.0	6.1	63.7	81.0	7.5	-6.8	-36.1
12	Chidha	41.84	155	9.06	238	68.8	1.0	3.0	0.4	21.6	3.0	6.6	63.3	58.1	3.8	-6.9	-36.2
13	Kalwe	35.10	278	7.51	428	81.2	2.0	6.2	0.7	50.7	7.2	9.9	63.2	120.8	0	-6.1	-31.8
14	Kajilirwe 2	46.76	209	8.92	321	74.4	1.0	1.1	0.0	53.9	2.7	5.2	40.8	118.6	6.5	-7.2	-40.1
15	Mtondolo 2	72.90	244	9.33	376	83.0	2.0	1.0	0.0	47.4	11.5	4.6	24.0	124.2	19.2	-6.9	-38.1
16	Mtondolo	64.77	265	9.13	407	83.3	2.2	0.9	0.0	44.9	12.3	4.7	24.2	134.2	12.6	-6.9	-38.5
17	Chiwe	74.90	302	9.11	464	101.9	2.4	1.6	0.0	47.8	19.0	9.8	51.6	126.1	11.8	-6.6	-36.7
18	Chombo	66.84	402	8.78	621	120.9	2.6	3.7	0.1	34.5	13.1	13.1	149.1	90.6	2.8	-6.7	-35.5
19	Madzimawira	63.73	408	8.63	627	117.4	2.3	4.8	0.0	39.4	14.0	14.0	135.5	91.7	2.9	-6.6	-36.7
20	Ling'ona	58.08	383	8.68	588	122.7	2.9	5.4	0.0	41.4	13.9	15.1	149.5	84.9	2.6	-	-
21	Chikwizi	52.17	344	9.42	530	110.5	1.6	2.6	0.0	39.1	5.7	19.5	139.2	68.6	11.3	-6.7	-39.9
22	Liwonde	40.32	599	9.21	922	187.2	2.1	1.6	0.1	35.9	8.3	59.3	154.9	164.0	15.4	-6.8	-39.0
23	Sitima	36.43	404	9.66	621	131.6	1.4	0.6	0.0	7.1	9.1	38.9	26.0	139.8	38.5	-7.1	-39.8
24	Mpsupsu	39.88	481	7.38	742	122.8	6.3	35.6	8.0	40.3	6.2	72.9	99.8	219.6	0	-6.2	-35.0
25	Muloza	34.70	110	8.37	164	35.3	1.5	8.9	1.0	24.6	2.7	8.8	4.6	91.9	1.9	-6.2	-29.9
26	July Borehole	51.35	849	7.64	1306	225.0	12.5	16.1	5.6	67.7	8.7	173.3	158.8	172.0	0	-6.7	-38.2
27	Chipuze	42.68	737	7.32	1134	173.8	10.7	32.5	13.1	60.8	6.7	119.1	112.9	324.5	0	-7.3	-42.6

T = temperature; TDS = total dissolved solids; EC = electrical conductivity; $\delta^{18}O$ = stable oxygen isotopes; δD = stable hydrogen isotopes; -= no data

2.5.2 Stable isotopes (δD vs $\delta^{18}O$)

The hot springs samples have δD and $\delta^{18}O$ values that range from -40‰ to -26‰ and -7.3‰ to -4.6‰, respectively (Table 1). Groundwater samples and cold spring waters have δD and $\delta^{18}O$ values that range from -35‰ to -19‰ and -6.2‰ to -3.7‰, respectively (Table S3, see Appendix B). Most of the groundwater, cold spring samples, and hot spring waters plotted along the Global Meteoric Water Line (GMWL) by Gourcy et al. (2005) ($\delta D= 8.14[\pm0.02] * \delta^{18}O + 10.9[\pm0.2]$), which is similar to the GMWL by Craig (1961) ($\delta D= 8 * \delta^{18}O + 10$). The relationship between δD and $\delta^{18}O$ indicates a meteoric origin in general for the hot spring, groundwater, and cold spring samples along the MRZ (Fig. 3). The values of δD and $\delta^{18}O$ for local precipitation are not documented in the study area. However, a least-squares regression line ($\delta D= 7.4*\delta^{18}O + 8.1$; R2= 0.89) was determined from groundwater and cold spring samples (N=37) in the MRZ (Fig. S1 and Table S4, see Appendix B). The slope of this regression line differs from that of the GMWL (Fig. 3), showing a shift of $\delta^{18}O$ and δD, but it is only slightly different from that of the Local Meteoric Water Line (LMWL) from the Ndola station in Zambia ($\delta D = 7.75* \delta^{18}O + 9.68$; IAEA/WMO, 2006). Fig. 3 shows a Local Evaporation Water Line (LEWL) constructed by Missi and Atekwana (2019) from lake samples and stream samples in the South region of Malawi. The LEWL is defined by the equation: $\delta 2H=5.7\delta^{18}O +1.1$, with a regression coefficient (R2) of 0.997. The fact that no hot spring samples plot along the LEWL indicates that evaporation effects are unlikely for the thermal waters along the MRZ. A few groundwater samples show enriched $\delta^{18}O$ and δD values, indicating the effect of meteoric water mixing with an evaporated source. By contrast, approximately ~93% of the hot spring samples plot as a group to the left of the GMWL, showing depleted values of δ^{18}O and δD with respect to the groundwater samples that could be indicative of variability in the isotope composition of a meteoric water source. However, the hot springs along the MRZ do not show a significant increase in their δ^{18}O which can be ascribed to isotope equilibration by water-rock interaction during long residence time in the aquifers. Nevertheless, the Chiweta and Mphizi Na-Cl (SO$_4$) hot spring waters show an increase in δD and δ^{18}O of ~3‰ and ~1‰, respectively, compared to the other hot spring samples (Fig. 3), probably due to an isotope exchange with the host rock during a longer residence time and/or mixing with waters from distinct sources.

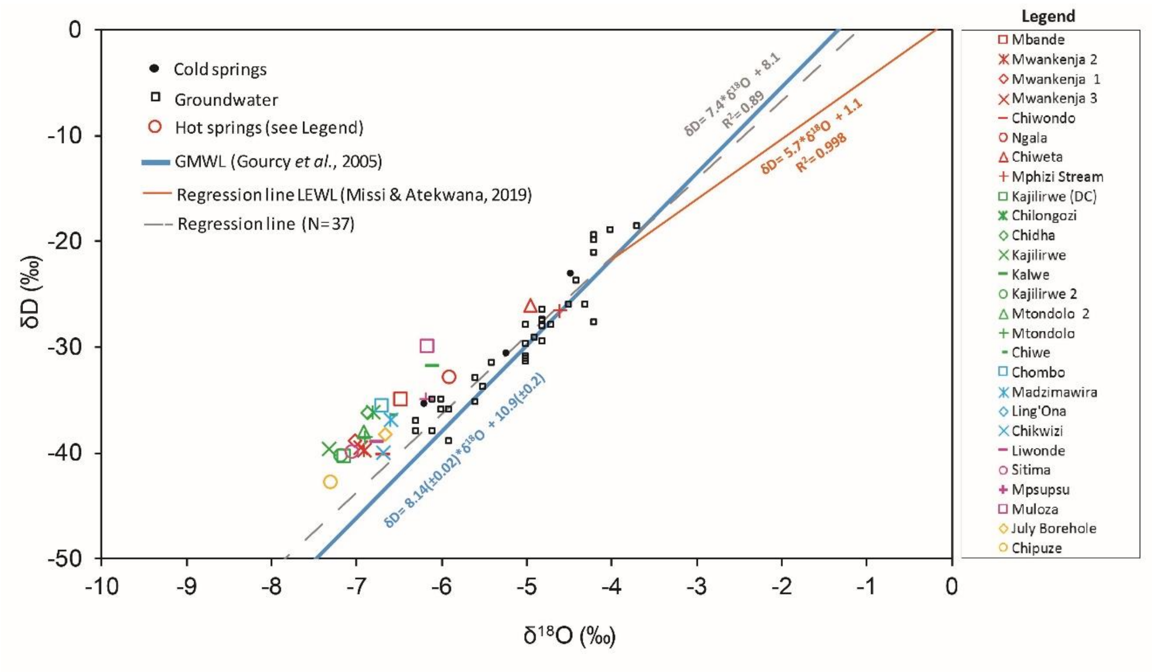

Figure 3. Stable isotopes δ^{18}O vs. δD plot of hot springs in the Malawi Rift Zone (MRZ) and their relationship with a regression line calculated from cold springs and groundwater. The Global Meteoric Water Line of Gourcy et al. (2005) and the Local Evaporation Water Line constructed by Missi and Atekwana (2019) in the South region of the MRZ are shown.

2.5.3 Geothermometry

2.5.3.1 Silica Geothermometry

The results for reservoir temperatures estimated by the different silica geothermometer models are shown in Table 2. The adiabatic and conductive quartz geothermometers give higher temperatures that are above field-measured values and are thus more reliable, except for Chiwondo and Sitima which show lower temperatures than surface temperature values. The quartz conductive geothermometer shows reservoir temperatures ranging from 20°C to 128°C (Table 2). In the North region, the Chiweta hot spring and Mphizi stream are suggested to have the hottest reservoir temperatures of 115°C and 128°C, respectively. The July borehole and Chipuze hot spring waters in the South region show reservoir temperatures of 117°C and 111°C, respectively.

2.5.3.2 Cation Geothermometry

The reservoir temperatures for different cation geothermometers, applied to the 27 hot springs along the MRZ ranged from 21°C to 196°C (Table 3). These cation geothermometry temperatures should be viewed with caution because the estimates depend on the geochemical characteristics and conditions of each hot spring. The Na-K geothermometer by Truesdell (1976) and K-Mg geothermometer by Giggenbach (1986) give the lowest reservoir temperature estimates which ranged from 21°C to 141°C. The Na-K geothermometer by Giggenbach (1988) shows the highest reservoir temperatures from 92°C to 196°C (Table 3). Similar to the silica geothermometry results, the Chiweta hot spring and Mphizi stream in the North region have higher Na-K geothermometer reservoir temperatures of 188°C and 190°C, respectively. The waters from the Chiwe, Mtondolo 1, Mtondolo 2, Chombo, and Ling’ona hot springs come from reservoirs with estimated temperatures between 134°C to 144°C (Table 3). Additionally, the Chipuze and July borehole hot spring waters in the Southern region show Na-K geothermometer reservoir temperatures of 196°C and 189°C, respectively. However, the high concentrations of Mg in the Chipuze, July Borehole, and Mpsupsu hot spring waters (Table 1) can provide incorrect temperature estimates; therefore, they should be viewed with caution.

2.5.3.3 Geoindicators

The results of the K-Mg-Na diagram show that most of the hot spring waters including the Chiweta hot spring and Mphizi stream waters, with the highest temperatures of around 190°C, plot in the region of partial equilibration (Fig. 4). On the other hand, the Chipuze, July borehole, Muloza, Mpsupsu, Mwankenja 1, Mwankenja 2, Mwankenja 3, Chidha, and Kalwe hot spring waters plot in the immature waters zone (Fig. 4). The hot spring waters that plot in the immature waters zone indicate that their Na-K geothermometer results should be taken with caution due to the re-equilibration during ascent to the surface. Moreover, the Chipuze, Mpsupsu, and July borehole hot spring waters have high Mg concentrations (Table 1) that could cause incorrect cation temperature estimates.

The K-Ca-Mg-CO_2 fugacity “geoindicator” shows that 85% of the hot spring waters in MRZ plot above the full equilibrium line (Fig. 5A), which is representative of lower CO_2 concentrations in waters (Giggenbach & Goguel, 1989). Additionally, the CO_2-fugacity calculated by PHREEQCI at the sampling conditions ranged from -4.59 to -1.71 for the 27 hot springs (Table S5, see Appendix B). Likewise, most of the hot spring waters plot in the rock-dominated field, which means that their water composition is controlled by the host rocks. The K-Ca-Mg-CO_2 cross-plot shows four hot spring waters in equilibrium with calcite formation: Chipuze, July Borehole, Chiweta hot spring, and Mphizi stream. This diagram indicates higher temperatures of about 130°C in the Chiweta hot spring and Mphizi stream.

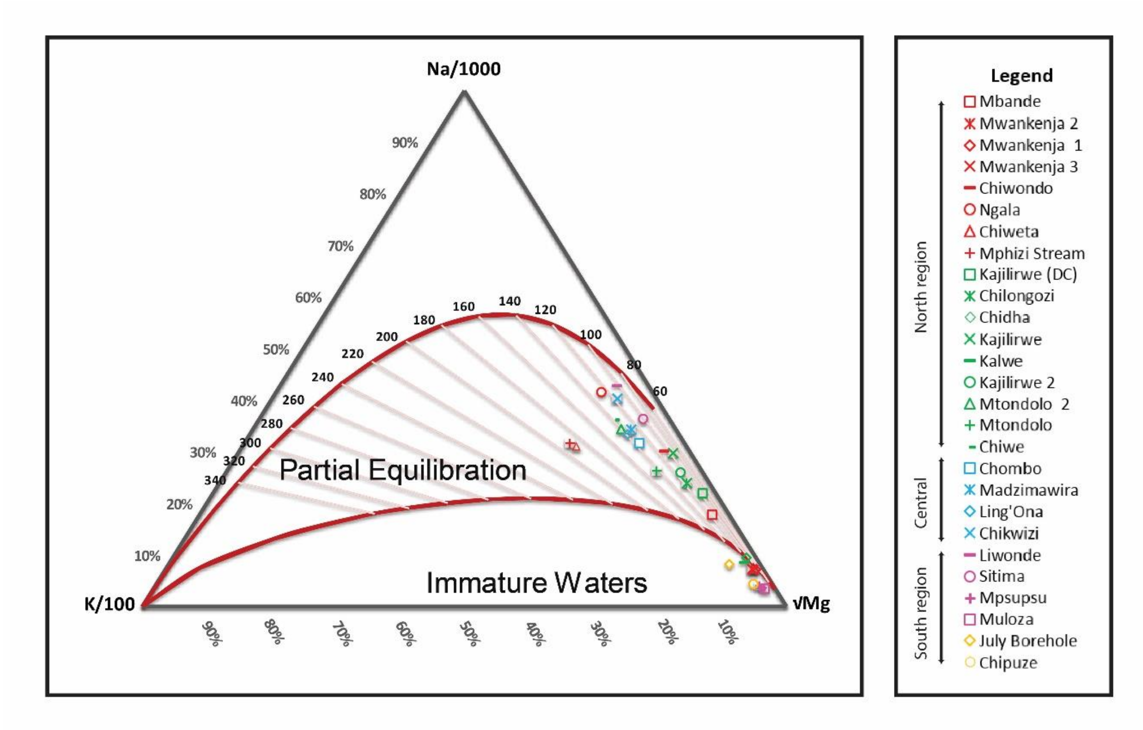

Figure 4. Ternary diagram K-Mg-Na geothermometer by Giggenbach (1988) shows estimated reservoir temperatures and the immature or partial equilibrium water fields. The legend shows the hot springs ordered by the three major regions of the Malawi Rift Zone.

The Na-K/Mg-Ca diagram "geoindicator" shows that 50% of the hot spring waters (e.g., Kajilirwe 2, Mtondolo 2, Sitima, Chiwondo, Chiweta, Mphizi, Chombo) plot close to the "full equilibrium" line (Fig. 5B). The reservoir temperatures shown in the Na-K/Mg-Ca diagram ranged from 100°C to 190°C. The Chiweta hot spring and Mphizi stream waters that have the highest reservoir temperatures plot close to the equilibrium line (Fig. 5B). The Chipuze, July Borehole, Msupsu, Muloza, Kalwe, and Mwankenja 1, 2, and 3 data indicate immature waters with a high Mg concentration.

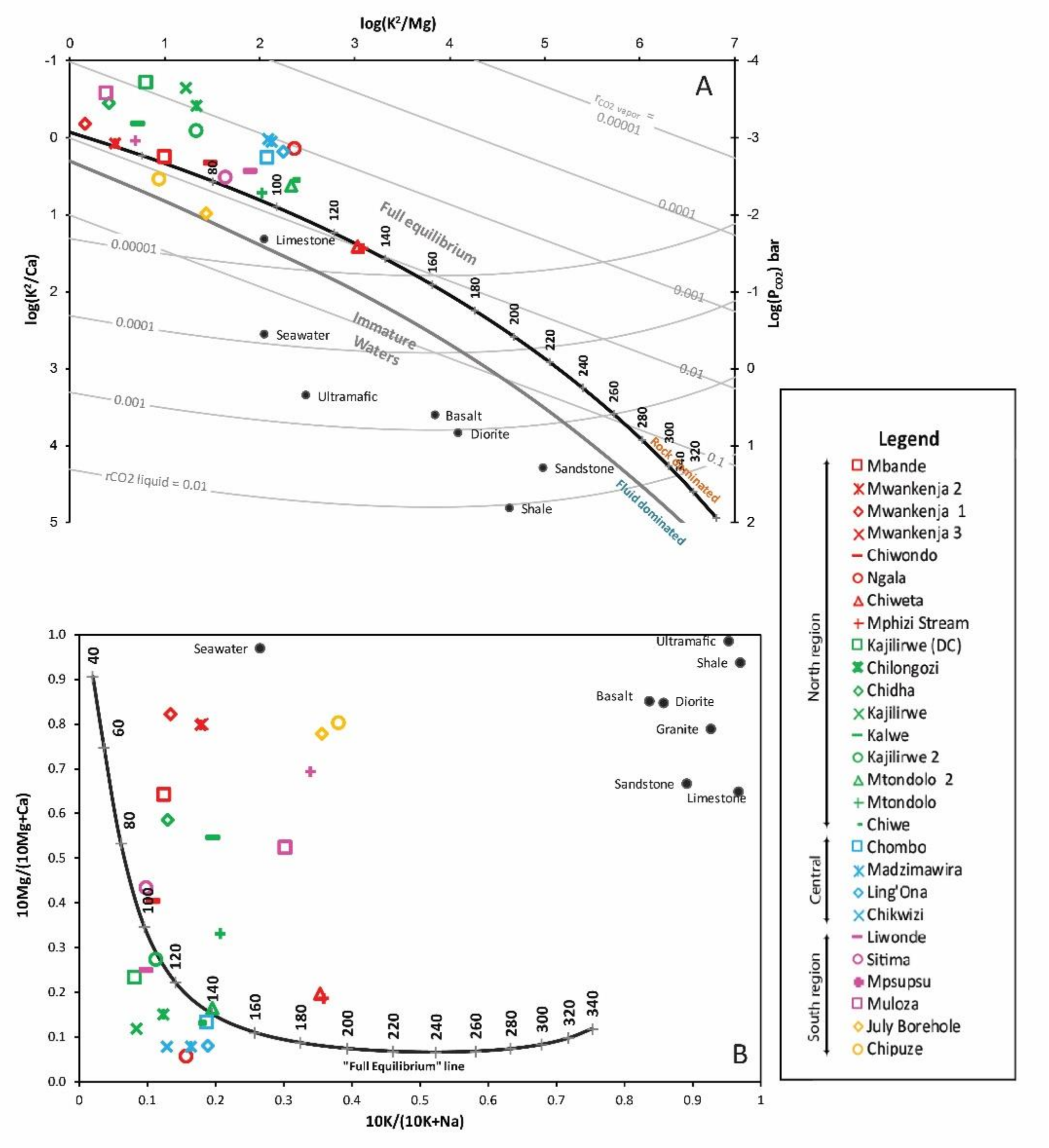

Figure 5. A. The K-Ca-Mg-CO_2 "geoindicator" diagram proposed by Giggenbach (1988) correlates the K-Mg geothermometer with measures of the CO_2 fugacity. B. The Na-K/Mg-Ca "geoindicator" diagram by Giggenbach and Goguel (1989) that the Na-K geothermometer correlated with the

Mg-Ca equilibration system. The legend shows the hot springs ordered by the three major regions of the Malawi Rift Zone.

Table 2. Results for temperatures (°C) from 27 hot springs in Malawi were estimated using different silica geothermometers (Fournier, 1977; Fournier & Potter, 1982; Arnórsson *et al.*, 1983; and Verma, 2000).

No.	Hot Springs	Surface T°C	Alpha Cristobalite (Fournier 1977)	Chalcedony Conductive (Fournier 1977)	Chalcedony (Arnórsson *et al.*, 1983)	Quartz Conductive (Fournier & Potter 1982)	Quartz Conductive (Verma 2000)	Quartz Adiabatic (Fournier 1977)
1	Mbande	43.05	39	58	60	90	83	91
2	Mwankenja 2	48.55	27	45	48	77	69	81
3	Mwankenja 1	45.80	28	46	49	78	70	81
4	Mwankenja 3	36.92	6	23	27	55	46	61
5	Chiwondo	35.80	-15	-1	4	29	22	41
6	Ngala	54.90	26	44	47	76	68	79
7	Chiweta	79.70	64	86	87	115	111	114
8	Mphizi Stream	78.70	77	100	99	128	125	125
9	Kajilirwe (DC)	36.39	11	27	31	60	51	65
10	Kajilirwe	36.82	11	28	32	60	52	66
11	Chilongozi	40.39	13	30	34	62	54	68
12	Chidha	41.84	17	34	38	67	58	71
13	Kalwe	35.10	52	73	74	103	97	103
14	Kajilirwe 2	46.76	55	76	77	106	100	106
15	Mtondolo 2	72.90	49	69	71	100	94	100
16	Mtondolo	64.77	47	67	68	97	91	98
17	Chiwe	74.90	49	70	71	100	94	101
18	Chombo	66.84	35	54	57	86	79	88
19	Madzimawira	63.73	41	60	62	91	85	93
20	Ling'ona	58.08	43	63	65	94	87	95
21	Chikwizi	52.17	41	60	62	91	84	93
22	Liwonde	40.32	37	56	58	87	80	90
23	Sitima	36.43	-19	-4	1	25	19	38
24	Mpsupsu	39.88	42	61	63	92	86	94
25	Muloza	34.70	22	40	43	72	64	76
26	July Borehole	51.35	66	88	88	117	112	115
27	Chipuze	42.68	61	82	83	111	107	111

Table 3. Results for temperatures (°C) from 27 hot springs in Malawi were estimated using different cation geothermometers (Fournier, 1979; Truesdell, 1976; Arnórsson *et al.,* 1983; Giggenbach, 1986; Giggenbach, 1988; and Verma & Santoyo, 1997).

No.	**Hot Spring**	**Surface T°C**	**Na-K-Ca (Fournier, 1981)**	**Na-K-Ca Mg corr**	**Na-K (Fournier, 1979)**	**Na-K (Truesdell, 1976)**	**Na-K (Giggenbach, 1988)**	**Na-K (Arnórsson *et al.,* 1983)**	**Na-K (Verma & Santoyo, 1997)**	**K-Mg (Giggenbach, 1986)**
1	Mbande	43.05	98	95	93	44	114	56	100	67
2	Mwankenja 2	48.55	85	55	114	66	134	78	120	54
3	Mwankenja 1	45.80	75	52	97	48	117	60	103	47
4	Mwankenja 3	36.92	84	54	114	67	135	79	121	54
5	Chiwondo	35.80	103	103	85	36	106	48	92	81
6	Ngala	54.90	90	90	106	58	126	70	112	108
7	Chiweta	79.70	165	165	170	131	188	141	175	131
8	Mphizi Stream	78.70	166	166	172	133	190	143	177	133
9	Kajilirwe (DC)	36.39	55	55	71	21	92	33	78	62
10	Kajilirwe	36.82	58	58	73	23	94	35	80	73
11	Chilongozi	40.39	65	65	92	43	113	55	99	77
12	Chidha	41.84	63	63	95	46	116	58	102	53
13	Kalwe	35.10	69	69	120	74	141	85	127	60
14	Kajilirwe 2	46.76	82	82	87	38	108	50	94	77
15	Mtondolo 2	72.90	126	126	120	73	140	85	126	106
16	Mtondolo	64.77	129	129	124	77	144	89	130	97
17	Chiwe	74.90	109	109	117	70	138	82	124	107
18	Chombo	66.84	94	94	113	66	134	78	120	99
19	Madzimawira	63.73	84	84	109	61	129	73	115	100
20	Ling'ona	58.08	89	89	117	70	138	82	124	104
21	Chikwizi	52.17	85	85	94	45	115	57	101	99
22	Liwonde	40.32	102	102	81	31	102	43	88	93
23	Sitima	36.43	103	103	80	30	101	43	87	85
24	Mpsupsu	39.88	73	73	166	125	184	136	171	60
25	Muloza	34.70	47	47	155	112	173	123	160	52
26	July Borehole	51.35	157	56	171	132	189	142	176	79
27	Chipuze	42.68	97	49	179	141	196	150	183	66

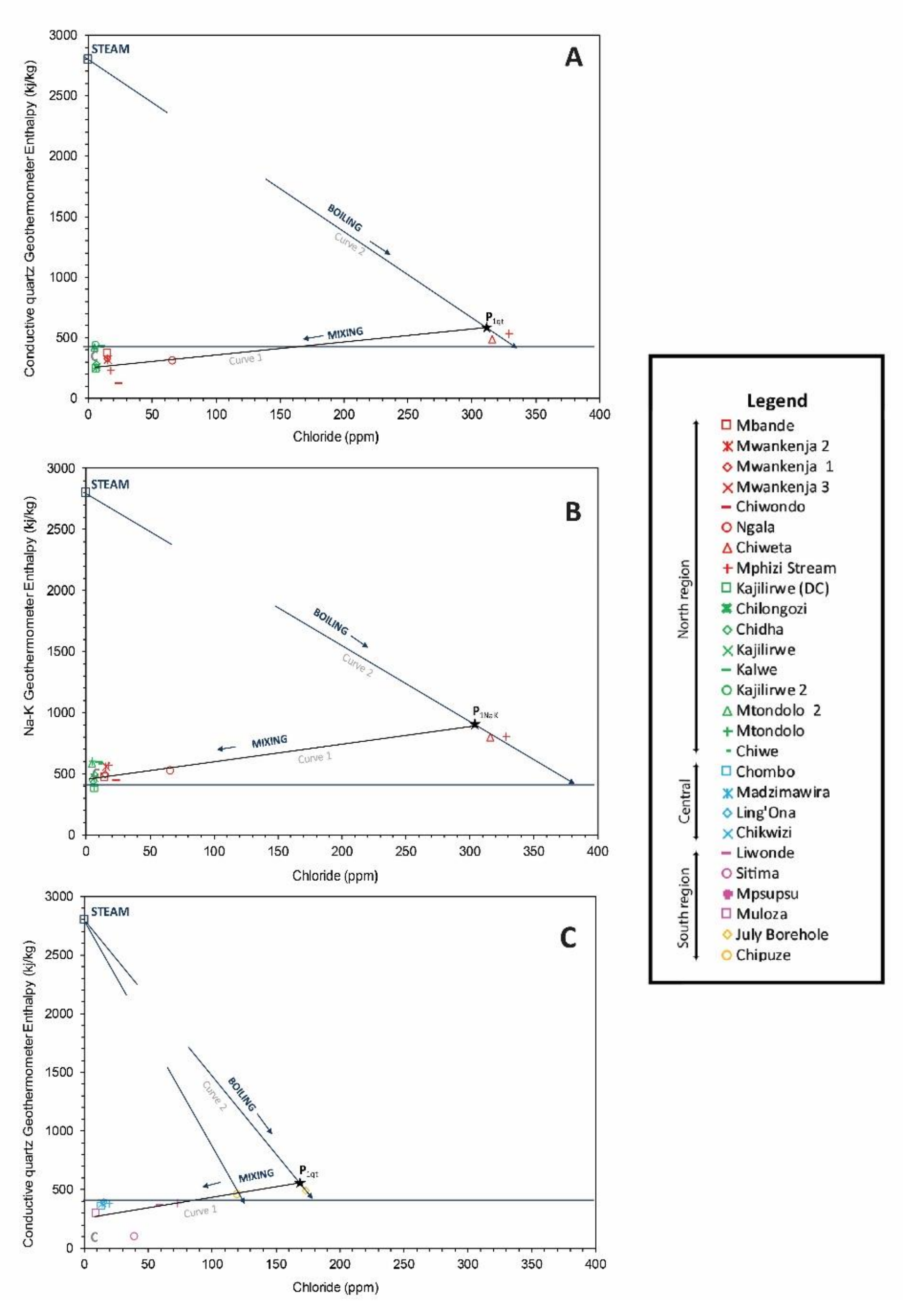

Figure 6. A. Chloride-enthalpy diagram of the North region calculated from the quartz conductive silica geothermometer. B. Chloride-enthalpy diagram of the North region calculated from the Na-K cation geothermometer by Giggenbach (1988). C. Chloride-enthalpy diagram of the South region calculated from quartz conductive silica geothermometer. The horizontal dashed line at 400 kJ/kg shows where boiling springs plot at one bar atmospheric pressure. The diagrams show

Curve 1 is a mixing line drawn radiating from C, which is an assumed low-enthalpy and zero chloride concentration of non-thermal groundwater in the region. Curve 2 is the upper bounding boiling curve. The intersection of these two curves represents the possible parent geothermal liquid (P) underground in the region.

2.5.4 Mixing models and Enthalpy diagrams

An enthalpy-chloride diagram using a temperature estimated from conductive quartz geothermometers for 17 hot spring waters located in the North region is shown in Fig. 6A. The enthalpy-chloride diagram shows enthalpies estimated from 123 kJ/kg to 537 kJ/kg. The highest enthalpy values correspond to the Chiweta hot spring and Mphizi stream waters with 484.1 kJ/kg and 537 kJ/kg, respectively. On the other hand, Figure 6B shows an enthalpy-chloride diagram using temperatures estimated from Na-K geothermometers for 17 hot spring waters located in the North region. The enthalpy estimates range from 388.3 kJ/kg to 808.2 kJ/kg. The highest enthalpy values correspond to the Chiweta hot spring and Mphizi stream waters with 801.1 kJ/kg and 808.2 kJ/kg, respectively.

The parent geothermal fluid estimated from the conductive quartz geothermometer in the North region shows enthalpy values of P_{1qt}, 600 kJ/kg (140°C), and chloride concentrations of 310 mg/L (Fig. 6A). Additionally, the parent geothermal fluids estimated from the Na-K geothermometer in the North region show enthalpy values of P1NaK, 900 kJ/kg (197°C), and chloride concentrations of 305 mg/L (Fig. 6B).

The 10 hot springs from the Central and South region of the MRZ are shown in Fig. 6C. The enthalpy-chloride diagram shows ranges of enthalpy estimates from conductive quartz geothermometers of 106.7 kJ/kg to 490.1kJ/kg. The highest enthalpy values correspond to the July borehole and Chipuze spring waters with 490.7 kJ/kg and 467.9 kJ/kg, respectively. It was not possible to estimate the parent geothermal fluid of the Central region due to the low chloride concentrations of the hot spring waters. However, a possible parent geothermal fluid in the South region shows an enthalpy value of P_{1qt}, 580 kJ/kg (140°C), and a chloride concentration of 170 mg/L (Fig. 6C). An enthalpy-chloride diagram using a temperature estimated from Na-K geothermometers was not made for the South region because most of the hot spring waters show immature waters in the Na-K-Ca diagram.

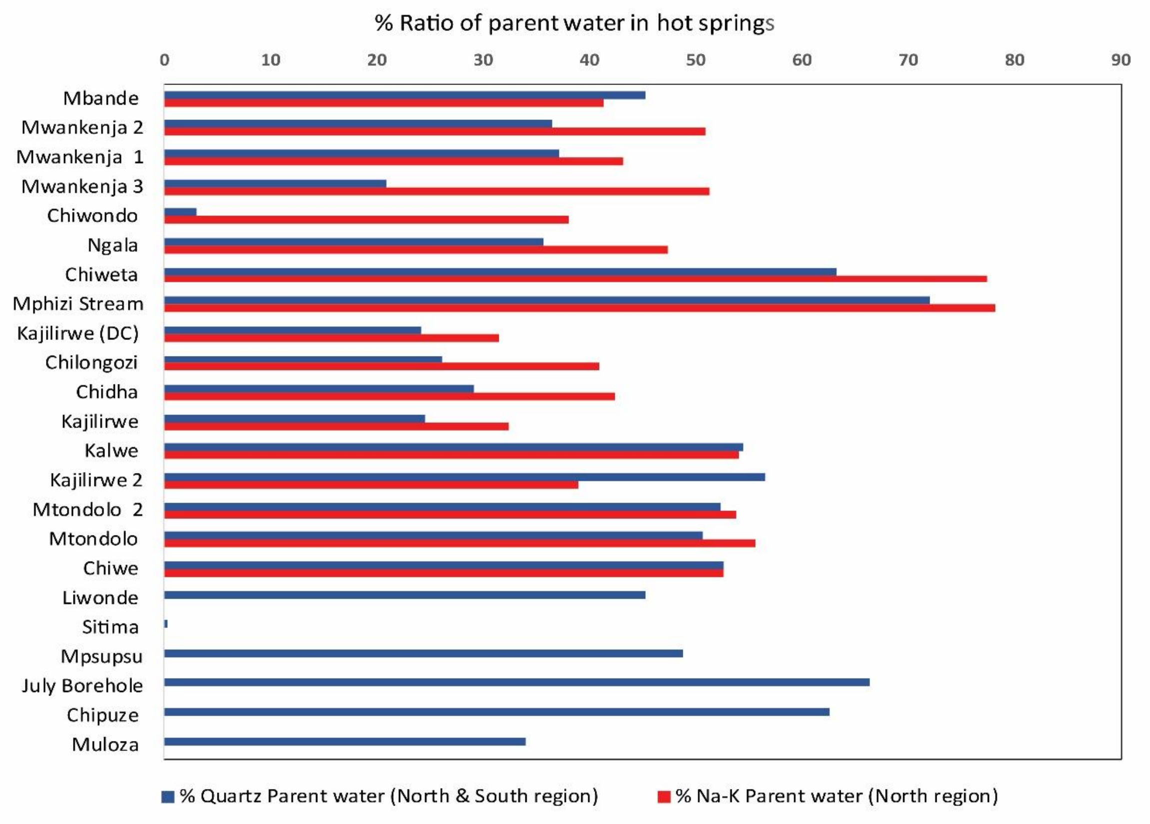

Figure 7. Graph showing the ratio of the concentrations of hot water obtained from the enthalpy-chloride diagram for each hot spring in the North and South region.

Figure 7 summarizes the proportion of hot water obtained from the enthalpy-chloride diagram (Fig. 6A, B, and C) for each hot spring in the North and South regions. We consider that the hot spring waters are mixed waters with different proportions of cold water "C" (105 kJ/kg = 25°C) and a parent geothermal fluid. We used the conductive quartz and Na-K enthalpy of the parent geothermal fluid in the North region (600 and 900 kJ/kg) obtained from the chloride-enthalpy diagrams in Fig. 6A and 6B, respectively. For the South region, the enthalpy of the parent geothermal fluid (580 kJ/kg) was obtained from the enthalpy-chloride diagram in Fig. 6C.

Fig. 7 shows that the Chiweta spring and Mphizi stream have the highest proportion of parent geothermal fluid with ranges of ~60 – 80% in the North region. The rest of the hot springs in the North region have less than 55% of a parent geothermal fluid. Whereas the July borehole and the Chipuze hot spring waters in the South region show the highest percentage of geothermal parent proportion of around 65%.

2.6 Discussion

2.6.1 Hydrochemistry and origin of geothermal waters

The results of this study show that ~85% of the hot springs along the MRZ are Na-HCO_3 and Na-SO_4 water types. Most of the hot springs located in the North region and a few in the South region of the MRZ have predominantly Na-HCO_3 water types. The Central and South region of the MRZ are characterized by a Na-SO_4 water type (Fig. 2). These different ionic proportions of the thermal waters could be related to the differences in rock types and water-rock interactions that affect the chemical composition of the waters along the MRZ (e.g., Missi & Atekwana, 2019). For instance, the North region is dominated by Cenozoic volcanic and plutonic rocks of Paleoproterozoic ages (Fig. 1B), mainly granulites and granites, which are rich in Ca and Na alumino-silicate minerals. Whereas the Central and South part of the MRZ is dominated by a sedimentary sequence of different ages (Quaternary, Pleistocene, and Jurassic ages) and plutonic and metamorphic rocks of Neoproterozoic ages (Fig. 1B).

The high alkalinity of the thermal waters along the MRZ is typical of the EARS and has been discussed by Kebede (2012) in Ethiopia as a product of water-rock interactions at shallow depths with the basement rocks (Na, K - silicates) and CO_2 outgassing from the mantle. Evidence of CO_2 degassing comes from the calculated $\log PCO_2$ values for the hot spring waters where nearly 50% are higher than -3.5 (Table S5, see Appendix B). Additionally, high HCO_3 concentrations in natural groundwater are attributed to carbonate rocks in general (e.g., Quaternary sedimentary rocks and Karoo sedimentary sequence). However, the major components of the basement rocks are not carbonates, but rocks dominated by silicates. Missi and Atekwana (2019) argued that the weathering of feldspars (anorthite) is due to reactions with CO_2 (g) from recharging meteoric waters form clays rich in Ca (Kaolinite). This process is in accordance with the SI results that show oversaturation with respect to calcite and kaolinite in most of the thermal waters (Table S5, see Appendix B) and could be the main source of HCO_3 concentrations along the MRZ (Missi & Atekwana, 2019). Likewise, thermal waters rich in sulfate are also a characteristic of rifting regions and have been associated with the deep circulation of waters through a thick sedimentary sequence (e.g., D'Amore *et al.,* 1998; Awaleh *et al.,* 2015; Awaleh *et al.,* 2017). Nevertheless, the saturation index of the hot spring waters shows undersaturated waters with respect to anhydrite and gypsum within the ranges from -4.52 to -1.59, and from -4.34 to -1.83, respectively in all the thermal waters (Table S5, see Appendix B). The hot spring waters that lie inside Karoo basins, such as Chiweta, Mphizi, July borehole, and Chipuze (Fig. 1B) show a higher SI of anhydrite and gypsum (Table S5) and higher SO_4 concentrations (Table 1) with respect to the others.

The Chiweta hot spring water and Mphizi stream water in the North region, and July borehole and Chipuze in the Southern region of the MRZ are Na-Cl (SO_4) type waters (Fig. 2). The high Cl concentrations in these hot spring waters are unlikely from evaporation according to the $\delta^{18}O$ vs. δD diagram (Fig. 3) which does not show a typical enrichment of the $\delta^{18}O$ and δD in the thermal waters expected for evaporation. Likewise, the TDS vs. $\delta^{18}O$ plot (Fig. S2, see Appendix B) does not show a typical evaporation behavior, TDS values increase while $\delta^{18}O$ remains constant. Then, high Cl concentrations could be attributed to the dissolution of evaporite rocks in sedimentary basins (e.g., Shire graben, Ruhuhu basin, and Maniamba basin). Moreover, high concentrations of Ca are also observed in the Chiweta spring and Mphizi stream waters in the northern part of the MRZ, and the Chipuze, July borehole, and Msupsu springs in the South region (Table 1). These higher Ca concentrations could be attributed to the Karoo sediments where these hot springs are located. In Fig. 5A these five hot spring waters plot are in the area of equilibrium with limestone formation. Otherwise, the high Mg concentrations in the July borehole, Chipuze, and Mpsupsu spring waters in the Southern region of the MRZ could be due to the dissolution of ferromagnesian minerals (biotite [$K (Mg, Fe)_3(AlSi_3) O_{10}$(OH,

$F)_2$] and hornblende [$Ca_2(Mg, Fe, Al)_5(Al, Si)_8O_{22}(OH)_2$]) from the metamorphic basement (e.g., Mapoma *et al*., 2016; Missi, 2018).

The $\delta^{18}O$ vs. δD relationship shows that the hot spring waters plot near the GMWL (Fig. 3) and confirms the assumption of a mainly meteoric water origin (e.g., Atekwana *et al*., 2015; Hinz *et al.* 2018). Different processes such as water-rock interaction, mixing of waters, and CO_2 outgassing affect the isotope and chemical composition of the hot springs (Fig. 3). Additionally, the isotope data and the mixing models suggest that most of the hot springs in the northern region of the MRZ are diluted with more than 45% of meteoric waters (Fig. 7) and are in a partial equilibrium with the rock. For instance, the Ngala hot spring water in the North region of the MRZ plots on the mixing water line in Fig. 6A and 6B. The exception is the Chiweta hot spring and Mphizi stream waters, which are enriched in both δD and $\delta^{18}O$ with respect to the other hot spring waters along the MRZ (Fig. 3). The δD and $\delta^{18}O$ shift for the Chiweta hot spring and Mphizi stream waters may be accounted for by a composition of ~60 to 50 % of a parent geothermal fluid compared to the other hot spring waters mixed with less than ~55% of parent water and more than ~45% of cold water (Fig. 7). The hot spring waters in the South region such as that of the Chipuze and July borehole water with reservoir temperatures of 140°C show a higher parent geothermal fluid proportion of ~65%. The quick ascent of a parent geothermal fluid mixed with meteoric water could be a possible explanation for the immature nature of some of the hot spring waters in the South region (e.g., Chipuze and July borehole waters).

Additionally, the relationship between TDS vs. $\delta^{18}O$ graph shows a wide range in TDS values for the hot spring waters from 110 to 1323 mg/L, and $\delta^{18}O$ variations that are observed over a small range from -7.3‰ to -4.6‰ (Table 1), hence no evaporation effect is observed in comparison with those of Lake Chilwa samples, which show an abrupt and simultaneous increase in TDS and $\delta^{18}O$ (Fig. S2, see Appendix B). Thus, the low $\delta^{18}O$ values in the hot spring waters indicate a short residence time in the aquifers and/or high rates of rain recharge. Whereas high TDS values in some of the hot spring waters indicate extensive reaction with the host rock (water-rock interaction).

2.6.2 Reservoir temperature distribution

We suggest that the conductive quartz geothermometer (Table 2) provides reservoir temperature values for shallow aquifers for the hot spring waters that show high percentages of cold-water admixture (Fig. 7). Thereby, estimates of lower reservoir temperatures for these hot springs are possible due to the dilution of the parent waters from deeper aquifers (e.g., Fournier & Truesdell, 1970). Additionally, the Na-K and Na-K-Ca geothermometers by Giggenbach (1988) provide more reliable results than other Na-K geothermometers for low-temperature reservoirs (Fournier, 1977). Thus, these cation geothermometer temperatures are also reliable reservoir temperature estimates for partial and total equilibrated waters from deep aquifers that have high proportions of a parent geothermal fluid, between 50 and 80% (Fig. 7). Likewise, the Na-Mg-K diagram by Giggenbach (1988) was used to identify immature waters that give misleading temperatures with cation geothermometers. Thus, the hot spring waters displaying immature waters in the K-Mg-Na diagram (Fig. 4) are not reliable for cation geothermometer estimates (e.g., Muloza, Chipuze, Mwankenja 1, 2, and 3, Mpsupsu, July Borehole, Kalwe, and Chidha). Finally, the results show that the hottest surface temperatures (Fig. 8A) and reservoir temperatures (Fig. 8B) occur in the North and Central region of the MRZ. The enthalpy-chloride diagram shows that the enthalpy of a possible parent geothermal fluid in the North region could be in a range between 600 kJ/kg (140°C), similar to the values reported by Tsokonombwe (2017), and 900 kJ/kg (197°C), while in the South region, the parent geothermal fluid could be around 580 kJ/kg (140°C). Some hot spring waters show low to medium enthalpy values from 196.15 kJ/kg (50°C) to 808.5 kJ/kg (190°C).

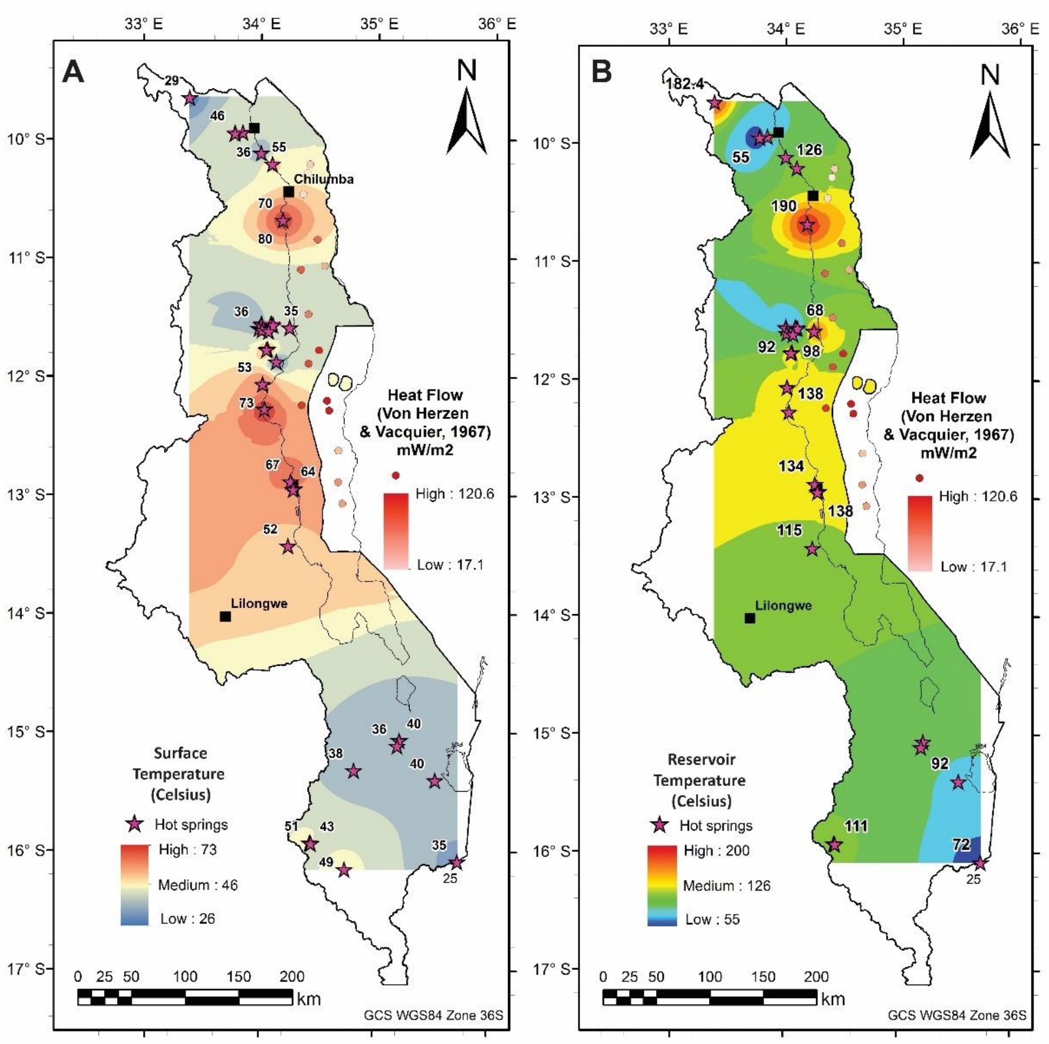

Figure 8. A. Surface temperature interpolation in Malawi of 27 hot springs reported by this study (Atekwana et al., 2015), and 28 reported by previous works (Dulanya, 2006; Dulanya et al., 2010; Kaonga et al., 2014; Msika et al. 2014; and Gondwe et al., 2012). For specific information, refer to Table S1 (Appendix B) in this work. B. Reservoir temperatures interpolation calculated from cation and silica geothermometers in Malawi of 37 hot springs total; 27 reported by this study and 10 reported by previous works (Dulanya et al., 2010; Msika et al., 2014). Heat flow reported by Von Herzen and Vacquier (1967) in sediments of Lake Malawi is shown in filled circles.

2.6.3 Heat flow and reservoir temperatures

The high reservoir temperatures along the MRZ based on the geothermometer results (Fig. 9) are in good agreement with the heat flow values reported by Njinju *et al.* (2019). Njinju *et al.* (2019) reported an elevated heat flow with ranges between 70 - 82 mW/m^2 and a thinner crust within the Karoo rift basins in the Central region and the Rungwe Volcanic Province (RVP) in the North region, and in the Shire graben in the South region of the MRZ.

The evidence that suggests a source for this higher heat flow in the MRZ includes the occurrence of lower Rayleigh and P-S wave velocities interpreted as a mantle superplume and/or mantle upwelling (O'Donnell *et al*., 2013; Grijalva *et al*., 2018; Wang *et al*., 2019). Furthermore, Wanless *et al.* (2016) conducted a study of helium isotopes in hot springs along the Malawi Rift that shows the highest ^{3}He/^{4}He ratios presented in four hot spring waters, two in the north and two in the south. Wanless *et al.* (2016) suggest a mantle contribution of at least 35% and 20% for these hot spring gases. The highest helium ratios in northern Malawi correlate well with areas of thinner continental crust reported by Grijalva *et al*. (2018).

We assessed the relationship between the heat flow estimated by Njinju *et al*. (2019) and the geothermometer reservoir estimates for the 27 hot springs along the MRZ (Fig. 9). The higher heat flow peaks are in the Nkhotakota region at 78 mW/m^2 (Fig. 9), where our results show cation reservoir temperatures of around 140°C in Chiwe, Mtondolo 1, Mtondolo 2, Chombo, and Ling'ona hot springs. While silica reservoir temperatures estimated at around 110°C in the Chipuze and July borehole hot springs in the Shire graben, correlates with high heat flow values of ~76 mW/m^2 (Fig. 9). The Chiweta hot spring and Mphizi stream show the highest cation temperature estimates of 190°C and high heat flow values of ~76 mW/m^2.

The geothermal systems along the MRZ are controlled by circulation in deep faults systems (e.g., Monjerezi *et al*., 2012; Atekwana *et al.,* 2015). Most of the hot spring clusters with the highest reservoir temperatures in the North and Central region of the MRZ spatially overlap with the major segments of rift border faults and Precambrian shear zones (Fig. 9). For instance, the Chiweta geothermal zone lies in a favorable structural setting that enhances permeability and transports the hot fluids directly from depth (Dávalos-Elizondo & Laó-Dávila, 2019). The segmentation between the Livingstone Fault and Usisya Faults controls an accommodation zone where the Chiweta hot springs are located along the rift (Dávalos-Elizondo & Laó-Dávila, 2019). Also, the Chiweta geothermal zone lies at the intersection between the Karonga and Usisya Quaternary faults, the Precambrian Mugesse Shear Zone, and the Mesozoic Karoo sedimentary basin (Dávalos-Elizondo & Laó-Dávila, 2019).

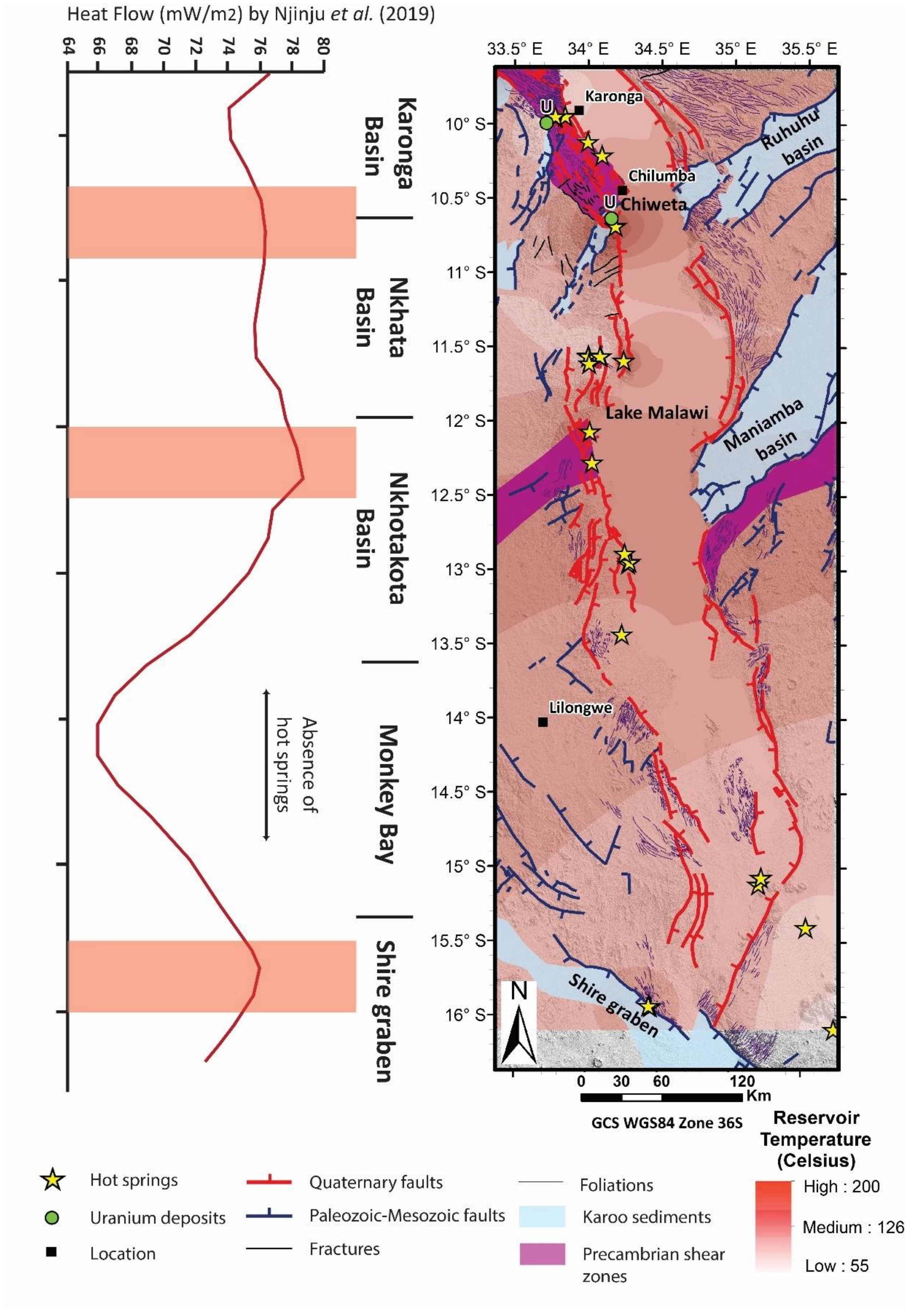

Figure 9. Structural map of the Malawi Rift Zone generated from the Shuttle Radar Topography Mission (SRTM) Digital Elevation Model (DEM) showing the locations of hot springs from

Atekwana et al. (2015), Quaternary faults, Paleozoic-Mesozoic faults, and Precambrian foliations and shear zones (Modified from Laó-Dávila et al., 2015). Reservoir temperatures interpolation of geothermometers estimates showed in Fig. 8B. The heat flow values (mW/m^2) estimated by Njinju et al. 2019 are shown on the left.

The Karoo sediments host uranium deposits that could enhance the highly elevated temperatures in the hot springs in the North region (Fig. 9). Njinju et al. (2019) indicate the importance of these uranium deposits as an additional source of heat flow in the Karoo rifts along the central part of the MRZ (e.g., Ruhuhu and Maniamba troughs). The radioactive decay of the uranium deposits could be a supplementary heat source for the Chiweta hot spring, but further research is needed to estimate the contribution of heat produced by radioactivity.

We use our results to suggest that meteoric waters are infiltrated at depth through high and deep permeable fault zones and heated by a high-temperature gradient followed by secondary processes that change the chemical composition during the ascent of the thermal waters. Fig. 10 shows our general proposed conceptual model of fault-controlled geothermal systems of the MRZ. Meteoric water from rain recharge infiltrates at high elevations and flows to depth through deep faults (>2.5 km). Then, the meteoric water is heated by a high heat flow to form the parent water (~190°) which flows through permeable zones of the reservoir where water-rock interaction takes place. Afterward, the parent water ascends through faults towards the surface where processes such as admixture with cold water from shallow aquifers (>45%) and CO_2 outgassing take place.

The hot springs issue to the surface through favorable structures such as the intersection of faults (Fig. 10).

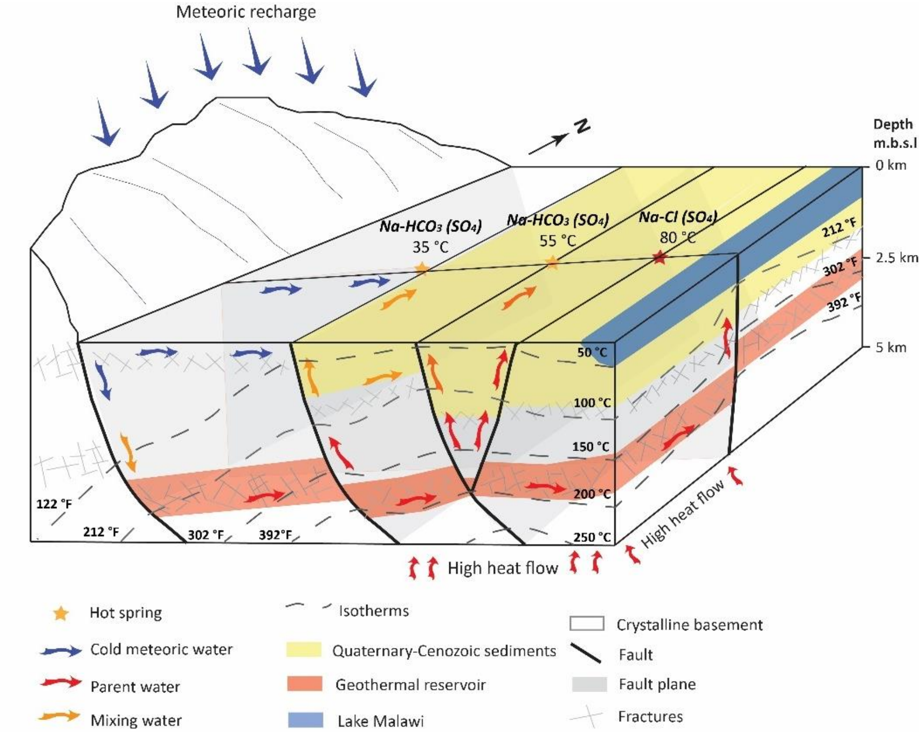

Figure 10. Schematic geothermal conceptual model of the Malawi Rift Zone. The meteoric water (blue arrows) infiltrates at depth through faults and is heated by an elevated geothermal gradient. The parent water (red arrows) ascends again through faults. Processes such as mixing (orange arrows) with shallow aquifers, and CO_2 outgassing occur during the ascent (see more detailed explanation in the text).

2.7 Conclusions

We conducted geothermometer reservoir estimates and mixing models using 27 hot springs to identify the best areas for potential geothermal energy generation in Malawi. We found three potential geothermal zones: (1) The Chiweta geothermal zone located between the Karonga and Nkhata basin in the North region with hot spring reservoir temperatures of ~190°C, (2) The Nkhotakota basin (Chiwe, Mtondolo, Chombo, Ling'ona) with hot spring reservoir temperatures of ~140°C, and (3) The Shire graben (July borehole and Chipuze) in the South region with silica reservoir temperatures of at least 110°C. A possible common parent geothermal fluid enthalpy in the North region is estimated between 600 kJ/kg (140°C) and 900 kJ/kg (197°C), whereas in the South region, a parent geothermal fluid enthalpy is estimated at least 580 kJ/kg (140°C). The reservoir temperature distribution assessed in this study is in good agreement with the elevated heat flow values reported by Njinju *et al.* (2019), except for the temperatures in the Chiweta zone. However, Chiweta lies in a Karoo basin, where uranium deposits have been reported and its radioactive decay can serve as a possible additional source of heat (Njinju *et al*., 2019).

Finally, our results demonstrate that the geothermal systems along the MRZ are controlled mainly by meteoric water circulation through deep permeable fault systems (e.g., accommodation zones, fault intersection, and shear zones). Processes such as equilibration with the host rock, mixing, dilution, and CO_2 outgassing take place during the ascent of the geothermal waters (Fig. 10). A detailed structural geology analysis of these fault-controlled geothermal systems should be conducted mainly in the three geothermal potential zones to better understand the fluid pathways and favorable structures that control the storage of these geothermal waters. The structural analysis and geophysical surveys will give valuable information about the best areas to drill the first exploratory wells.

2.8 Acknowledgments

We are grateful to José Luis Quijano, Steven Johnson, Augusto Rodríguez, Sandra Briceño, Esteban Gómez, and all the anonymous reviewers and editors whose thorough, critical, helpful, constructive comments and general help greatly contributed to improving this manuscript. Chase Watkins is acknowledged for his help in improving English in this paper. The authors are especially grateful to the Boone Pickens School of Geology and the Tectonic Group for all the support during this research. This is Boone Pickens School of Geology contribution 2020-117

2.9 References

Accardo, N. J., Shillington, D. J., Scholz, C. A., McCartney, T., Ebinger, C. J., Gaherty, J. B., Nyblade, A., Eatmon, A., Chindandali, P., & Ferdinand, R. (2016, December). Constraints on the 3D sediment and crustal architecture of the weakly extended Malawi Rift from the onshore/offshore wide-angle refraction experiment. In *AGU Fall Meeting Abstracts*.

Arnorsson, S., Gunnlaugsson, E., & Svavarsson, H. (1983). The chemistry of geothermal waters in Iceland. III. Chemical geothermometry in geothermal investigations. *Geochimica et Cosmochimica Acta, 47*(3), 567-577.

Atekwana, E. A., Tsokonombwe, G. W., Elsenbeck, J., Wanless, V. D., & Atekwana, E. A. (2015). Chemical and isotopic characteristics of hot springs along the Neogene Malawi Rift. In *AGU Fall Meeting Abstracts.*

Awaleh, M. O., Hoch, F. B., Boschetti, T., Soubaneh, Y. D., Egueh, N. M., Elmi, S. A., Jalludin, M. & Khaireh, M. A. (2015). The geothermal resources of the Republic of Djibouti—II: Geochemical study of the Lake Abhe geothermal field. *Journal of Geochemical Exploration, 159*, 129-147.

Awaleh, M. O., Boschetti, T., Soubaneh, Y. D., Baudron, P., Kawalieh, A. D., Dabar, O. A., Ahmed, M. M., Ahmed, S. I., Daoud, M. A., Egueh, N.M., Jalludin, M. & Mohamed, J. (2017). Geochemical study of the Sakalol-Harralol geothermal field (Republic of Djibouti): Evidences of a low enthalpy aquifer between Manda-Inakir and Asal rift settings. *Journal of Volcanology and Geothermal Research, 331*, 26-52.

Bloomfield, K. (1965). The geology of the Zomba area: Government Printer, South Africa.

Bloomfield, K. (1968). The pre-Karoo geology of Malawi. Government Printer, South Africa.

Bloomfield, K., & Garson, M. S. (1965). The Geology of the Kirk Range, Lisungwe Valley Area (No. 17). Government Printer.

Borrego, D., Nyblade, A. A., Accardo, N. J., Gaherty, J. B., Ebinger, C. J., Shillington, D. J., Chindandali, P. R., Mbogoni, G., Ferdinand, R. W., and Mulibo, G., & O'Donnell, J. P. (2018). Crustal structure surrounding the northern Malawi rift and beneath the Rungwe Volcanic Province, East Africa. Geophysical Journal International, 215(2), 1410-1426.

Chapola, L. S., & Kaphwiyo, C. E. (1992). The Malawi rift: geology, tectonics and seismicity. *Tectonophysics, 209*(1-4), 159-164.

Chapusa, F. W. P., & Harrison, D. R. (1975). The Geology of the Nkhotakota-Benga Area. *Bulletin*, (32), 31-32.

Chorowicz, J. (2005). The east African rift system. *Journal of African Earth Sciences, 43*(1-3), 379-410. doi:10.1016/j.jafrearsci.2005.07.019

Craig, H. (1961). Isotopic variations in meteoric waters. *Science, 133*(3465), 1702-1703.

D'Amore, F., Giusti, D., & Abdallah, A. (1998). Geochemistry of the high-salinity geothermal field of Asal, Republic of Djibouti, Africa. Geothermics, 27(2), 197-210.

Dávalos-Elizondo, E. & Laó-Dávila, D.A. (2019). Structural controls and slip tendency in the Chiweta geothermal zone: Northern part of the Malawi Rift, Africa: A progress report: *Geothermal Resources Council Transactions, 43,* 178-199.

Dixey, F. (1927). The tertiary and post-tertiary lacustrine sediments of the Nyasan Rift-valley. *Quarterly Journal of the Geological Society, 83*(1-5), 432-442.

Dulanya, Z. (2006). Geothermal resources of Malawi-An overview. In *Thirty-First Workshop on Geothermal Reservoir Engineering* (p. 5).

Dulanya, Z., Morales-Simfors, N., & Sivertun, Å. (2010). Comparative study of the silica and cation geothermometry of the Malawi hot springs: Potential alternative energy source. *Journal of African Earth Sciences, 57*(4), 321-327. doi:10.1016/j.jafrearsci.2009.11.001.

Ebinger, C. J. (1989). Tectonic development of the western branch of the East African rift system. *Geological Society of America Bulletin, 101*(7), 885-903.

Ebinger, C. J., Crow, M. J., Rosendahl, B. R., Livingstone, D. A., & LeFournier, J. (1984). Structural evolution of Lake Malaŵi, Africa. Nature, 308(5960), 627.

Ebinger, C. J., Rosendahl, B. R., & Reynolds, D. J. (1987). Tectonic model of the Malaŵi rift, Africa. *Tectonophysics, 141*(1-3), 215-235.

Fagereng, Å. (2013). Fault segmentation, deep rift earthquakes and crustal rheology: Insights from the 2009 Karonga sequence and seismicity in the Rukwa–Malawi rift zone. *Tectonophysics, 601*, 216-225. doi:10.1016/j.tecto.2013.05.012.

Flannery, J. W., & Rosendahl, B. R. (1990). The seismic stratigraphy of Lake Malawi, Africa: implications for interpreting geological processes in lacustrine rifts. *Journal of African Earth Sciences (and the Middle East), 10*(3), 519-548.

Fournier, R. O. (1977). Chemical geothermometers and mixing models for geothermal systems. *Geothermics, 5*(1-4), 41-50.

Fournier, R. O. (1979). A revised equation for the Na-K geothermometer. *Transactions Geothermal Resources Council, 3*, 221-224.

Fournier, R. O. (1981). Application of water geochemistry to geothermal exploration and reservoir engineering. *Geothermal System: Principles and Case Histories*, 109-143.

Fournier, R. O. (1989). Lectures on geochemical interpretation of hydrothermal waters (No. 10). UNU Geothermal Training Programme.

Fournier, R. O., & Potter, R. W. (1982). Revised and expanded silica (quartz) geothermometer. *Bull., Geotherm. Resour. Counc. (Davis, Calif.); (United States), 11*(10).

Fournier, R. O., & Truesdell, A. H. (1970). Chemical indicators of subsurface temperature applied to hot spring waters of Yellowstone National Park, Wyoming, USA. *Geothermics, 2*, 529-535.

Fournier, R. O., & Truesdell, A. H. (1973). An empirical Na-K-Ca geothermometer for natural waters. *Geochimica et Cosmochimica Acta, 37*(5), 1255-1275.

Fritz, H., Abdelsalam, M., Ali, K. A., Bingen, B., Collins, A. S., Fowler, A. R., Ghebreab, W., Hauzenberger, C., Johnson, P. R, Kusky, T. M., Macey, P., Muhongo, S., Stern, R. J., & Viola, G. (2013). Orogen styles in the East African Orogen: a review of the Neoproterozoic to Cambrian tectonic evolution. *Journal of African Earth Sciences, 86*, 65-106.

Gehre, M., Geilmann, H., Richter, J., Werner, R. A., & Brand, W. A. (2004). Continuous flow $^{2}H/^{1}H$ and $^{18}O/^{16}O$ analysis of water samples with dual inlet precision. *Rapid Communications in Mass Spectrometry, 18*(22), 2650-2660.

Giggenbach, W. F. (1986, November). Graphical techniques for the evaluation of water/rock equilibration conditions by use of Na, K, Mg and Ca contents of discharge waters. In *Proc. 8th New Zealand Geothermal Workshop* (pp. 37-44).

Giggenbach, W. F. (1988). Geothermal solute equilibria. Derivation of Na-K-Mg-Ca geoindicators. *Geochimica et cosmochimica acta, 52*(12), 2749-2765.

Giggenbach, W. F. (1991). Chemical techniques in geothermal exploration. *Application of geochemistry in geothermal reservoir development*, 119-144.

Giggenbach, W. F., & Corrales-Soto, R. (1992). Isotopic and chemical composition of water and steam discharges from volcanic-magmatic-hydrothermal systems of the Guanacaste Geothermal Province, Costa Rica. *Applied Geochemistry, 7*(4), 309-332.

Giggenbach, W. F., & Goguel, R. L. (1989). Collection and analysis of geothermal and volcanic water and gas discharges. Report No. CD 2401. *Chemistry Division, DSIR, Petone, New Zealand.*

Gondwe, K., Allen, A., Georgsson, L., Loga, U., & Tsokonombwe, G. (2012, November). Geothermal Development in Malawi–a Country Update. In *Proceedings 4th African Rift Geothermal Conference, Nairobi, Kenya* (pp. 21-23).

Gourcy, L. L., Groening, M., & Aggarwal, P. K. (2005). Stable oxygen and hydrogen isotopes in precipitation. In *Isotopes in the Water Cycle* (pp. 39-51). Springer, Dordrecht.

Grijalva, A., Nyblade, A. A., Homman, K., Accardo, N. J., Gaherty, J. B., Ebinger, C. J., Ferdinand, R. W., & Mulibo, G. (2018). Seismic Evidence for Plume-and Craton-Influenced Upper Mantle Structure Beneath the Northern Malawi Rift and the Rungwe Volcanic Province, East Africa. *Geochemistry, Geophysics, Geosystems, 19*(10), 3980-3994.

Hinz, N. H., Cumming, W. B., & Sussman, D. (2018). Exploration of fault-related deep-circulation geothermal resources in the western branch of the East African Rift System: examples from Uganda and Tanzania. In *Proceedings, 7th African Rift Geothermal Conference, Kigali, Rwanda 31st October–2nd November*.

Kalebe, Y. N. (2018). Chemical and isotopic composition of thermal waters in northern part of Malawi. *UNU Geothermal Training Programme, Iceland.* Report: 13.

Kaonga, H., Tsokonombwe, G., & Kamanga, T. (2014). Status of Geothermal Exploration in Malawi. In *ARGEO-C5 Conf.* (pp. 29-31).

Kebede, S. (2012). *Groundwater in Ethiopia - Features, Numbers and Opportunities*. Springer Science & Business Media.

Kirkpatrick, I.M. (1969). The Thermal Springs of Malawi. *Rept. XXIII Int. Geol Congr. 19B*, 111-120

Kolawole, F., Atekwana, E. A., Laó-Dávila, D. A., Abdelsalam, M. G., Chindandali, P. R., Salima, J., & Kalindekafe, L. (2018). Active deformation of Malawi rift's north basin Hinge zone modulated by reactivation of preexisting Precambrian Shear zone fabric. *Tectonics, 37*(3), 683-704.

Laó-Dávila, D. A., Al-Salmi, H. S., Abdelsalam, M. G., & Atekwana, E. A. (2015). Hierarchical segmentation of the Malawi Rift: The influence of inherited lithospheric heterogeneity and kinematics in the evolution of continental rifts. *Tectonics, 34*(12), 2399-2417. doi:10.1002/2015tc003953.

Leet, D.L. (1982). Physical Geology (6th ed.). Englewood Cliffs, NJ: Prentice-Hall. ISBN 978-0-13-669706-0

Lyons, R. P., Scholz, C. A., Buoniconti, M. R., & Martin, M. R. (2011). Late Quaternary stratigraphic analysis of the Lake Malawi Rift, East Africa: An integration of drill-core and seismic-reflection data. *Palaeogeography, Palaeoclimatology, Palaeoecology, 303*(1-4), 20-37.

Mapoma, H. W. T., Xie, X., Zhang, L., Nyirenda, M. T., Maliro, A., & Chimutu, D. (2016). Hydrochemical characteristics of rural community groundwater supply in Blantyre, southern Malawi. *Journal of African Earth Sciences, 114*, 192-202.

McCartney, T., & Scholz, C. A. (2016). A 1.3 million year record of synchronous faulting in the hangingwall and border fault of a half-graben in the Malawi (Nyasa) Rift. *Journal of Structural Geology, 91*, 114-129. doi:10.1016/j.jsg.2016.08.012.

Mesko, G. T., Class, C., Maqway, M. D., Boniface, N., Manya, S., & Hemming, S. R. (2014, December). The timing of early magmatism and extension in the southern East African rift: Tracking geochemical source variability with 40Ar/39Ar geochronology at the Rungwe Volcanic Province, SW Tanzania. In *AGU Fall Meeting Abstracts, 1*, 4730.

Milési, J.P., Feybesse, J.L., Pinna, P., Deschamps, Y., Kampunzu, H., Muhongo, S., Lescuyer, J.L., Le Goff, E., Delor, C., Billa, M., Ralay, F., & Heinry, C., (2004, June). Geological map of Africa 1:10,000,000, SIGAfrique project. In *20th Conference of African Geology, BRGM, Orléans, France* (pp. 2-7).

Millennium Challenge Compact (2011, August). Malawi Power System Project Studies – Phase II. *Integrated Resource Plan (IRP) for Malawi, 1.*

Missi, C. (2018). Physical, chemical and isotopic characteristics of groundwater and surface water in the Lake Chilwa Basin, Malawi: *Unpublished Master's Thesis, Oklahoma State University, Stillwater, OK.*

Missi, C., & Atekwana, E. A. (2019). Physical, chemical and isotopic characteristics of groundwater and surface water in the Lake Chilwa Basin, Malawi. *Journal of African Earth Sciences, 162,* 103737.

Monjerezi, M., Vogt, R. D., Aagaard, P., & Saka, J. D. (2012). The hydro-geochemistry of groundwater resources in an area with prevailing saline groundwater, lower Shire Valley, Malawi. *Journal of African Earth Sciences, 68,* 67-81.

Msika, B. J., Saka, J. D. K., & Dulanya, Z. (2014). Spatial distribution, chemistry and subsurface temperatures of geothermal springs Nkhata bay, Malawi. *African Journal of Environmental Science and Technology, 8*(8), 464-475.

Njinju, E. A., Kolawole, F., Atekwana, E. A., Stamps, D. S., Atekwana, E. A., Abdelsalam, M. G., & Mickus, K. L. (2019). Terrestrial heat flow in the Malawi Rifted Zone, East Africa: Implications for tectono-thermal inheritance in continental rift basins. *Journal of Volcanology and Geothermal Research, 387*, 106656.

O’Donnell, J. P., Adams, A., Nyblade, A. A., Mulibo, G. D., & Tugume, F. (2013). The uppermost mantle shear wave velocity structure of eastern Africa from Rayleigh wave tomography: Constraints on rift evolution. *Geophysical Journal International, 194*(2), 961-978.

Parkhurst, D. L., & Appelo, C. A. J. (1999). User's guide to PHREEQC (Version 2): A computer program for speciation, batch-reaction, one-dimensional transport, and inverse geochemical calculations. *Water-resources investigations report, 99*(4259), 312.

Powell, T., & Cumming, W. (2010, February). Spreadsheets for geothermal water and gas geochemistry. In *Proceedings,* 35th Workshop on Geothermal Reservoir Eng., SGP-TR-188, Stanford University (pp. 1-3).

Rasskazov, S. V., Logachev, N. A., Ivanov, A. V., Boven, A. A., Maslovskaya, M. N., Saranina, E. V., Brandt, I. S. & Brandt, S. B. (2003). A magmatic episode in the Western Rift of East Africa (19-17 Ma). *Geologiya i Geofizika, 44*(4), 317-324.

Ray, G. E. (1975). The geology of the Chitipa-Karonga area. Government Printer, South Africa. *Geol. Surv, Malawi, 42*, 101.

Reynolds, D., & Rosendahl, B. (1984). Tectonic expressions of continental rifting. *EOS, Trans. Am. Geophys. Union*, *65*, 1055.

Ring, U. (1994). The influence of preexisting structure on the evolution of the Cenozoic Malawi rift (East African rift system). *Tectonics, 13*(2), 313-326.

Ring, U., & Betzler, C. (1995). Geology of the Malawi Rift: kinematic and tectono-sedimentary background to the Chiwondo Beds, northern Malawi. *Journal of Human Evolution, 28*(1), 7-21.

Roberts, E. M., Stevens, N. J., O'Connor, P. M., Dirks, P. H. G. M., Gottfried, M. D., Clyde, W. C., Armstrong, R. A., Kemp, A. I. S., & Hemming, S. (2012). Initiation of the western branch of the East African Rift coeval with the eastern branch. *Nature Geoscience, 5*(4), 289. doi:10.1038/ngeo1432.

Scholz, C. A., Cohen, A. S., Johnson, T. C., King, J., Talbot, M. R., & Brown, E. T. (2011). Scientific drilling in the Great Rift Valley: the 2005 Lake Malawi Scientific Drilling Project—an overview of the past 145,000 years of climate variability in Southern Hemisphere East Africa. *Palaeogeography, Palaeoclimatology, Palaeoecology, 303*(1-4), 3-19.

Teklemariam, M. (2018). Geothermal outlook in East African and contribution of UNI-GTP in capacity building: In *Proceedings of the 40th Anniversary Workshop of UNU-GTP*, Reykjavik, Iceland.

Truesdell, C. (1976). Correction of two errors in the kinetic theory of gases which have been used to cast unfounded doubt upon the principle of material frame-indifference*. Meccanica, 11*(4), 196-199.

Tsokonombwe, G. (2017). Hydrogeochemistry modelling of Chiweta geothermal prospect, Northern Malawi. Master's Thesis, *University of Iceland, Reykjavik*.

Van der Beek, P., Mbede, E., Andriessen, P., & Delvaux, D. (1998). Denudation history of the Malawi and Rukwa Rift flanks (East African Rift System) from apatite fission track thermochronology. *Journal of African Earth Sciences, 26*(3), 363-385.

Verma, M. P. (2000, May). Revised quartz solubility temperature dependence equation along the water–vapor saturation curve. In *World Geothermal Congress, Kyushu-Tohoku, Japan* (pp. 1927-1932).

Verma, S. P., & Santoyo, E. (1997). New improved equations for NaK, NaLi and SiO2 geothermometers by outlier detection and rejection. *Journal of Volcanology and Geothermal Research, 79*(1-2), 9-23.

Versfelt, J., & Rosendahl, B. R. (1989). Relationships between pre-rift structure and rift architecture in Lakes Tanganyika and Malawi, East Africa. *Nature, 337(*6205), 354.

Von Herzen, R. P., & Vacquier, V. (1967). Terrestrial heat flow in lake Malawi, Africa. *Journal of Geophysical Research, 72*(16), 4221-4226.

Wang, T., Feng, J., Liu, K. H., & Gao, S. S. (2019). Crustal structure beneath the Malawi and Luangwa Rift Zones and adjacent areas from ambient noise tomography. *Gondwana Research, 67*, 187-198.

Wanless, V. D., Kurz, M. D., Elsenbeck, J., Curtice, J., Shaw, A. M., & Atekwana, E. A. (2016, December). Helium isotopes in hot spring gases as magmatic tracers during incipient rifting in Malawi and Zambia. In *AGU Fall Meeting Abstracts*.

APPENDICES

Appendix A.

Supplementary material about field descriptions, characteristics, and photographs of 27 hot springs along the MRZ collected by this research and complemented with published information.

North Region

1. Mbande

Type of sample:

Hot spring

Physical parameters:

pH=8.70 T°C= 43.05

Location UTM WGS84 (Zone 36 South):

8900635.24 S - 592359.64 E

Elevation (m.a.s.l.):

519 m

Description:

- About 10 km east of Karonga just north of the public highway M26 and in the North Rukuru river.
- This spring was very difficult to measure because it issues at the bottom of a small depression and was full of women and children washing clothes and bathing.
- The locals have created different pools with rocks to wash and add cold water from the cold spring that issues out of the hill with the hot spring water.

Characteristics:

- The spring has a strong sulfurous smell with some white sulfur powder in the surroundings (Dulanya, 2006).

Photograph:

Photo 1. Sample collection at the source.

2. Mwankenja 2

Type of sample:

Hot spring

Physical parameters:

pH=7.75 T°C= 48.55

Location UTM WGS84 (Zone 36 South):

8900470.53 S - 585090.01 E

Elevation (m.a.s.l.):

550 m

Description:

- About 17 km east of Karonga on the M26 taking the dirt road before the bridge about 0.1 km northwest of Mwanknja Hot Spring #1.
- Localize it on the hill under a tree along a fault with strike N-S and dip about 72-75° W.
- The rocks are banded biotite gneisses and mylonites with slickensides marks present.

Characteristics:

- This spring was the hottest of the 3 in this area.
- Sulfurous smell can be perceived (Dulanya, 2006).

Photograph:

Photo 2. Sample collection at the source.

3. Mwankenja 1

Type of sample:

Hot spring

Physical parameters:

pH=8.55 T°C= 45.80

Location UTM WGS84 (Zone 36 South):

8900370.00 S - 585049.22 E

Elevation (m.a.s.l.):

550 m

Description:

- About 17 km east of Karonga on the public highway M26 taking the dirt road before the bridge.
- The rocks are banded biotite gneisses.

Characteristics:

- A green algal film is present on the surrounding rocks.
- The spring bubbled most of the time.
- Mica flakes that bubbling out of the source.

Photograph:

Photo 3. Sample collection and parameters measured at the source.

4. Mwankenja 3

Type of sample:

Hot spring

Physical parameters:

pH=8.09 T°C= 36.92

Location UTM WGS84 (Zone 36 South):

8899644.86 S - 584957.63 E

Elevation (m.a.s.l.):

559 m

Description:

- About 17 km east of Karonga on the M26 taking the dirt road before the bridge and 0.7 km southwest from Mwanknja Hot Spring #2.
- This spring issues out of fractures and flows into a stream.
- The hot spring is used for washing clothes and bathing; detergent is presented in the water.

Characteristics:

- This spring was the coolest of the 3 in this area.

- The springs flow slowly and flows again in a cycle.
- Mica flakes deposits and green algae surrounding.

Photograph:

Photo 4. Sample collection and parameters measured at the source.

5. Chiwondo

Type of sample:

Hot spring

Physical parameters:

pH=8.37 T°C= 35.80

Location UTM WGS84 (Zone 36 South):

8881453.34 S - 609321.27 E

Elevation (m.a.s.l.):

483 m

Description:

- About 25 km south of Karonga on the M1.
- This spring issues in the middle of a field of tall green lush grass.
- The spring is used for bathing and it is polluted by human and animal usage.

Characteristics:

- No bubbling is presented.

- Some sulfur smell (Dulanya, 2006)

Photograph:

Photo 5. Sample collection and parameters measured at the source.

6. Ngala

Type of sample:

Hot spring

Physical parameters:

pH=8.35 T°C= 54.90

Location UTM WGS84 (Zone 36 South):

8871144.06 S - 619840.74 E

Elevation (m.a.s.l.):

484 m

Description:

- About 3 km north of Ngala on the public highway M1.
- The spring issues out of a gneiss outcrop that is continuous to the lakeshore 100 m from Lake Malawi.

Characteristics:

- The spring is very hot and we had to be creative to collect enough water to sample.
- This spring continually bubbles.

- Sulfur smell and yellowish sulfur deposits are present in the spring (Dulanya, 2006).

Photograph:

Photo 6. Sample collection and parameters measured at the source.

7. Chiweta

Type of sample:

Hot spring

Physical parameters:

pH=7.83 T°C= 79.70

Location UTM WGS84 (Zone 36 South):

8818602.22 S - 629672.50 E

Elevation (m.a.s.l.):

495 m

Description:

- About 0.7 km north of Chiweta, north of the bridge along with the M1.
- The spring issues at a few spots along the bank of the stream where a E-W fault intersects a N-S fault.

Characteristics:

- The spring is probably the hottest in the country.
- There is an amount of green, yellow, and long stringy algae.

- The spring is bubbled.
- There is a strong sulfur smell in steaming waters.

8. Mphizi Stream

Type of sample:

Stream

Physical parameters:

pH=8.01 T°C= 70.30

Location UTM WGS84 (Zone 36 South):

8818602.22 S - 629672.50 E

Elevation (m.a.s.l.):

495 m

Description:

- About 0.7 km north of Chiweta, north of the bridge along with the M1.
- Chiweta Hot Spring flows into this stream.
- On the bank some potatoes were growing in the hot water, 37°C and pH 9.15

Characteristics:

- There is a strong sulfur smell in steaming waters.

Photograph:

Photo 7. Sample collection and parameters measured at the source.

9. Kajilirwe (DC)

Type of sample:

Hot spring

Physical parameters:

pH=9.18 T°C= 36.39

Location UTM WGS84 (Zone 36 South):

8722286.66 S - 609585.24 E

Elevation (m.a.s.l.):

828 m

Description:

- About 1 km north of Kajilirwe Hot Spring in the valley.
- This spring issued out of the gneiss outcrop on the side of the valley.

Characteristics:

- There is algae growth on the outcrop.

Photograph:

Photo 8. Sample collection at the source.

10. Kajilirwe

Type of sample:

Hot spring

Physical parameters:

pH=9.37 T°C= 36.82

Location UTM WGS84 (Zone 36 South):

8721435.78 S - 609392.51 E

Elevation (m.a.s.l.):

816 m

Description:

- About 12 km south of Mzuzu and 3 km southeast of Luwafa. It took over an hour to get to the top of the valley and then a 30-minute hike down into the valley.
- The spring issued out of the gneiss outcrop in an area that was very overgrown.

Characteristics:

- There are no algae present

- Mica flakes that bubble out of the source.

Photograph:

Photo 9. Sample collection at the source.

11. Chilongozi

Type of sample:

Hot spring

Physical parameters:

pH=9.15 T°C= 40.39

Location UTM WGS84 (Zone 36 South):

8721675.52 S - 618822.90 E

Elevation (m.a.s.l.):

727 m

Description:

- About 6 km southeast of Tunduma.
- The spring is used for bathing and washing clothes.

Characteristics:

- This spring had a sand boil and exhibited lots of bubbling with upwelling of sand mica.

Photograph:

Photo 10. Spring with upwelling of sand.

12. Chidha

Type of sample:

Hot spring

Physical parameters:

pH=9.06 T°C= 41.84

Location UTM WGS84 (Zone 36 South):

8721420.88 S - 618313.75 E

Elevation (m.a.s.l.):

713 m

Description:

- About 8 km northwest of Chinyakula.
- The source was up the hill above the main pool where people bathe. We climbed up the waterfall to try to find the source and think that we collected at the source or as close as we were able to get.

Characteristics:

- There are algae present

Photograph:

Photo 11. Close to the source

13. Kalwe

Type of sample:

Hot spring

Physical parameters:

pH=7.51 T°C= 35.10

Location UTM WGS84 (Zone 36 South):

8718255.76 S - 635870.67 E

Elevation (m.a.s.l.):

539 m

Description:

- Off the M5 about 2 km before the fork with T318 towards Nkhata Bay.
- The spring is very swampy and stagnant-looking.
- The source was not figured out due to the muddy water.

Photograph:

Photo 12. Close to the source.

14. Kajilirwe 2

Type of sample:

Hot spring

Physical parameters:

pH=8.92 T°C= 46.76

Location UTM WGS84 (Zone 36 South):

8716254.11 S - 610142.94 E

Elevation (m.a.s.l.):

731 m

Description:

- About 5 km south of Kahilirwe Hot Spring #2. Have to climb out of the valley because this spring was not in the same valley as the other Kajilirwe springs. We had to drive over a very sketchy wooden bridge to get to this site.
- The hot spring is used for washing clothes.

Characteristics:

- Mica flakes in the rocks around the spring.

Photograph:

Photo 13. Sample collection at the source.

15. Mtondolo 2

Type of sample:

Hot spring

Physical parameters:

pH=9.33 T°C= 74.70

Location UTM WGS84 (Zone 36 South):

8665612.61 S - 610563.80E

Elevation (m.a.s.l.):

549 m

Description:

- About 5 km northwest of Mtawali at a school in the middle of nowhere.
- The spring issued as a seep in a vegetated area.

Characteristics:

- This spring was very hot and both the YSI and Hanna meters were not working properly at this point.
- There are algae present at the site.

Photograph:

Photo 14. The photo shows the issuing site of the spring in a very vegetated area.

16. Mtondolo

Type of sample:

Hot spring

Physical parameters:

pH=9.13 T°C= 52.77

Location UTM WGS84 (Zone 36 South):

8665528.78 S - 610502.54 E

Elevation (m.a.s.l.):

544 m

Description:

- About 5 km northwest of Mtawali at a school in the middle of nowhere.
- This spring issued from a circular seep about 1 meter in diameter at the edge of the river.

Characteristics:

- The spring is bubbled.
- Mica deposits surrounding.

Photograph:

Photo 15. Sample collection and parameters measured at the source.

17. Chiwe

Type of sample:

Hot spring

Physical parameters:

pH=9.11 T°C= 73.10

Location UTM WGS84 (Zone 36 South):

8642423.11 S - 612186.85 E

Elevation (m.a.s.l.):

476 m

Description:

- About 5 km southeast of Kamphambale on the beach of Lake Malawi.
- The spring is used as a washing site.

Characteristics:

- This spring bubbles out of a small pool in the sand.
- Sulfur compounds (Dulanya, 2006).

Photograph:

Photo 16. Sample collection at the source.

Central Region

18. Chombo

Type of sample:

Hot spring

Physical parameters:

pH=8.78 T°C= 66.84

Location UTM WGS84 (Zone 36 South):

8574748.45 S - 636521.83 E

Elevation (m.a.s.l.):

487 m

Description:

- About 6 km northwest of Nkhotakota.

- The spring is issued in a marshy swamp area that is used to cultivate rice patties.
- Casava is planted next to the spring.

Characteristics:

- This spring has a sulfur smell (Dulanya, 2006).

Photograph:

Photo 17. Sample collection at the source.

19. Madzimawira

Type of sample:

Hot spring

Physical parameters:

pH=8.63 T°C= 63.73

Location UTM WGS84 (Zone 36 South):

8568352.67 S - 640105.35 E

Elevation (m.a.s.l.):

490 m

Description:

- About 2 km southwest of Nkhotakota.

- This spring issues in a valley out of a gneiss outcrop.
- There are 3 springs, one is free-flowing, one altered for bathing, and one for women only (don't know if it is altered).

Characteristics:

- There are algae present.
- This spring has sulfur smell and steaming waters (Dulanya, 2006).

Photograph:

Photo 18. Sample collection at the source.

20. Ling'ona

Type of sample:

Hot spring

Physical parameters:

pH=8.68 T°C= 58.08

Location UTM WGS84 (Zone 36 South):

8567141.07 S - 639081.62 E

Elevation (m.a.s.l.):

500 m

Description:

- About 3.5 km southwest of Nkhotakota.
- This spring issued in the middle of weeds in the middle of farm fields.
- There are gneiss outcrops on the way down the valley

Characteristics:

- It bubbled more vigorously periodically, about every 3-5 seconds.
- There was a slight sulfur smell.
- There are some green algae upstream on the side

Photograph:

Photo 19. Sample collection at the source.

21. Chikwizi

Type of sample:

Hot spring

Physical parameters:

pH=9.42 T°C= 52.17

Location UTM WGS84 (Zone 36 South):

8514563.52 S - 634256.69 E

Elevation (m.a.s.l.):

524 m

Description:

- About 9 km southwest of Benga on the M5.
- Micaceous rock is surrounding the site.
- People were bathing downstream

Characteristics:

- This spring has significant bubbling with a mud boil in the center.
- The spring water steams and has a sulfur smell (Dulanya, 2006).

Photograph:

Photo 20. The hot spring is bubbled.

South Region

22. Liwonde

Type of sample:

Hot spring

Physical parameters:

pH=9.21 T°C= 40.32

Location UTM WGS84 (Zone 36 South):

8332984.80 S - 737990.47 E

Elevation (m.a.s.l.):

472 m

Description:

- About 2 km from Liwonde city center close to the Shire River.
- This spring has a structure built around the issuing site to create a pool for bathing.
- The spring was not measured directly at the source.

Characteristics:

- There are green algae where the waterfalls into the pool.

Photograph:

Photo 21. Hot spring.

23. Sitima

Type of sample:

Hot spring

Physical parameters:

pH=9.66 T°C= 36.43

Location UTM WGS84 (Zone 36 South):

8327888.99 S - 735976.75 E

Elevation (m.a.s.l.):

478 m

Description:

- About 6 km southwest of Liwonde.
- The hot spring issued in the middle of a large pool
- The area was kind of marshy and the water was very silty.
- The spring is used for bathing.

Photograph:

Photo 22. Hot spring and parameters measured at the source.

24. Mpsupsu

Type of sample:

Hot spring

Physical parameters:

pH=7.38 T°C= 39.88

Location UTM WGS84 (Zone 36 South):

8295702.66 S - 771154.70 E

Elevation (m.a.s.l.):

645 m

Description:

- About 7 km southwest of Mchenga.
- The spring is used for bathing and the water was very dirty.
- Reeds were growing around the pool.

Photograph:

Photo 23. Children bathing in the hot spring.

25. Muloza

Type of sample:

Hot spring

Physical parameters:

pH=8.37 T°C= 34.70

Location UTM WGS84 (Zone 36 South):

8219890.78 S - 791833.53 E

Elevation (m.a.s.l.):

642 m

Description:

- The spring is surrounded by alluvial sands and green algae.

Characteristics:

- The spring has mud boiling.
- The spring is flowing approx. 400 L/min.

Photograph:

Photo 24. Mud boiling spring.

26. July Borehole

Type of sample:

Hot spring

Physical parameters:

pH=7.64 T°C= 51.35

Location UTM WGS84 (Zone 36 South):

8237661.92 S - 654120.32 E

Elevation (m.a.s.l.):

232 m

Description:

- About 7 northwest of Mikolongo in the village of July.
- This borehole is 32 m deep. It is located in the valley.
- The borehole was drilled on 07/24/09 by Saifro

Photograph:

Photo 25. The village helped to pump water for collecting samples.

27. Chipuze

Type of sample:

Hot spring

Physical parameters:

pH=7.32 T°C= 42.68

Location UTM WGS84 (Zone 36 South):

8236999.75 S - 655308.36 E

Elevation (m.a.s.l.):

236 m

Description:

- About 6 km northwest of Mikolongo inside the Majete Game Reserve.

Characteristics:

- There were a few bubbles and the spring was flowing.
- The spring is flowing approx. 400 L/min.

Photograph:

Photo 26. Hot spring and parameters measured at the source.

APPENDIX B.

Table S1. Locations in UTM WGS84 (Zone 36 South) and surface temperatures of 55 hot springs in the Malawi Rift Zone (from north to south) were reported by Dulanya (2006), Msika *et al.* (2014), Kaonga *et al.* (2014), and this study.

No.	Hot Spring	Latitude	Longitude	Temperature (°C)
1	Chinuka	8933182.49	542605.93	29.00
2	Mbande	8900635.24	592359.64	43.05
3	Mwankenja 2	8900470.53	585090.01	48.55
4	Mwankenja 1	8900370.00	585049.22	45.80
5	Mankenja 3	8899644.86	584957.63	36.92
6	Chiwondo	8881453.34	609321.27	35.80
7	Ngala 2	8871198.12	619804.64	-
8	Ngala	8871144.06	619840.74	54.90
9	Chiweta	8818602.22	629672.50	79.70
10	Mphizi Stream	8818602.22	629672.50	70.30
11	Chiwisi	8761965.00	630933.00	-
12	Sanga	8757501.00	632384.00	-
13	Kajilirwe	8722286.66	609585.24	36.82
14	Movya	8721976.00	618818.00	41.20
15	Chilyalya	8721782.00	618291.00	46.00
16	Chilongozi	8721675.52	618822.90	40.39
17	Kavuzi	8721622.00	618187.00	50.30
18	Kajilirwe (DC)	8721435.78	609392.51	36.39
19	Chiyagha	8721422.00	618316.00	49.00
20	Chidha	8721420.88	618313.75	41.84
21	Nalunguwa	8720782.00	620479.00	39.50
22	Kanunkha	8718574.00	635870.00	53.20
23	Kalwe	8718255.76	635870.67	35.10
24	Saka 1	8717700.00	607229.00	36.00
25	Kauziru	8716788.00	609554.00	-
26	Kajilirwe 2	8716254.11	610142.94	46.76
27	Chiling'ombe	8715216.00	616070.00	40.40
28	Chadonga 2	8714990.00	616096.00	39.60
29	Chadonga 1	8714909.00	616078.00	42.00
30	Kasanama 3	8698416.00	615297.00	65.00
31	Kasanama 1	8697772.00	614246.00	61.50
32	Kasanama 2	8697752.00	614163.00	-
33	Ndunduzi	8694896.00	609352.00	-
34	Chimaliro	8686536.00	623411.00	26.00
35	Mtondolo 2	8665612.61	610563.80	74.70
36	Mtondolo	8665528.78	610502.54	52.77
37	Chiwe	8642423.11	612186.85	73.10
38	Chombo	8574748.45	636521.83	66.84
39	Mawira 3	8568538.71	640076.49	-
40	Mawira2	8568352.71	640105.49	-
41	Madzimawira	8568352.67	640105.35	63.73
42	Ling'ona	8567141.07	639081.62	58.08
43	Chikwizi	8514563.52	634256.69	52.17
44	Liwonde	8332984.80	737990.47	40.32
45	Buche 2	8328051.64	691423.33	-
46	Sitima	8327888.99	735976.75	36.43
47	Buche 1	8324969.64	691242.33	-
48	Manondo	8305225.65	695398.32	38.00
49	Mpsupsu	8295702.66	771154.70	39.88
50	Chipuze 2	8237767.71	654567.30	-
51	July Borehole	8237661.92	654120.32	51.35
52	Chipuze	8236999.75	655308.36	42.68
53	Chipuze 3	8236989.71	655307.29	-
54	Muloza	8219890.78	791833.53	34.70
55	Tisola	8212845.00	686533.00	48.50

\- = no data

Table S2. Charge balance calculation between anions and cations, concentrations in mg/L.

Sample Name	sum cations	sum anions	Charge Balance
Mbande	6.44	6.48	0%
Mwankenja 2	7.47	7.36	1%
Mwankenja 1	7.00	7.01	0%
Mwankenja 3	7.50	7.33	1%
Chiwondo	8.33	8.32	0%
Ngala	11.17	11.23	0%
Chiweta	18.42	18.23	1%
Mphizi Stream	18.68	18.77	0%
Kajilirwe (DC)	2.98	3.31	-5%
Chilongozi	3.14	3.23	-1%
Chidha	3.20	2.74	8%
Kajilirwe	3.00	3.14	-2%
Kalwe	3.95	3.95	0%
Kajilirwe 2	3.32	3.30	0%
Mtondolo 2	3.71	3.91	-3%
Mtondolo	3.73	3.90	-2%
Chiwe	4.57	4.81	-3%
Chombo	5.51	5.74	-2%
Madzimawira	5.41	5.55	-1%
Ling'Ona	5.68	5.75	-1%
Chikwizi	4.98	5.25	-3%
Liwonde	8.28	8.54	-2%
Sitima	5.80	5.69	1%
Mpsupsu	7.94	8.06	-1%
July Borehole	11.40	11.47	0%
Chipuze	10.56	11.38	-4%
Muloza	2.10	2.05	1%

Table S3. Stable isotopic (δD and $\delta^{18}O$*)* data in per mil with respect to VSMOW of cold springs samples reported by this study, and groundwater sample reported by Missi & Atekwana (2019) and Mapoma *et al.* (2016). See Figure 3.

No.	Name	Type	δ^{18}O	δD
1	Nbade spring	Cold spring	-6.2	-35
2	N Rumphi spring	Cold spring	-5.2	-31
3	Mphizi stream	Cold spring	-4.5	-23
4	Dzinja	Borehole (cold water)	-6.3	-38
5	Namthiya	Borehole (cold water)	-6.3	-37
6	Thumbulu	Borehole (cold water)	-6.1	-35
7	Nambwale	Borehole (cold water)	-6.0	-35
8	Namuli	Borehole (cold water)	-6.0	-36
9	Chambeni	Borehole (cold water)	-6.1	-38
10	Nanthenga	Borehole (cold water)	-5.9	-36
11	Govala	Borehole (cold water)	-5.6	-33
12	Kachoka	Borehole (cold water)	-4.7	-28
13	Pirimiti	Borehole (cold water)	-5.0	-31
14	Jali	Borehole (cold water)	-5.9	-39
15	N Rukuru KA-01	Borehole (cold water)	-5.6	-35
16	N Rukuru KA-02	Borehole (cold water)	-4.9	-30
17	N Rukuru KA-03	Borehole (cold water)	-5.4	-31
18	N Rukuru KA-04	Borehole (cold water)	-4.8	-29
19	N Rukuru KA-05	Borehole (cold water)	-5.5	-34
20	N Rukuru KA-06	Borehole (cold water)	-5.0	-30
21	N Rukuru KA-07	Borehole (cold water)	-5.0	-31
22	N Rukuru KA-08	Borehole (cold water)	-5.0	-31
23	N Rukuru KA-10	Borehole (cold water)	-4.2	-27
24	Songwe KA-11	Borehole (cold water)	-4.0	-19
25	Songwe KA-12	Borehole (cold water)	-4.2	-20
26	Songwe KA-13	Borehole (cold water)	-4.2	-21
27	Songwe KA-14	Borehole (cold water)	-3.7	-19
28	Songwe KA-15	Borehole (cold water)	-4.2	-19
29	Lufira KA-16	Borehole (cold water)	-4.4	-24
30	Lufira KA-17	Borehole (cold water)	-4.3	-26
31	Lufira KA-18	Borehole (cold water)	-5.0	-28
32	Lufira KA-19	Borehole (cold water)	-4.8	-27
33	Lufira KA-21	Borehole (cold water)	-4.8	-28
34	Lufira KA-22	Borehole (cold water)	-4.8	-26
35	Lufira KA-23	Borehole (cold water)	-4.8	-28
36	Karonga KA-24	Borehole (cold water)	-4.5	-26
37	Karonga KA-25	Borehole (cold water)	-4.9	-29

Table S4. Statistical information of the “Regression Line” calculated from 11 cold surface samples in the Malawi Rift Zone.

Summary OUTPUT

Regression Statistics	
Multiple R	0.94452204
R Square	0.89212188
Adjusted R Square	0.88903965
Standard Error	1.89377771
Observations	37

ANOVA

	df	*SS*	*MS*	*F*	*Significance F*
Regression	1	1038.04664	1038.04664	289.440212	1.6847E-18
Residual	35	125.523791	3.58639402		
Total	36	1163.57044			

	Coefficients	*Standard Error*	*T Stat*	*P-value*	*Lower 95%*	*Upper 95%*	*Lower 95.0%*	*Upper 95.0%*
Interception	8.12570017	2.24051971	3.62670328	0.00090519	3.57720335	12.674197	3.57720335	12.674197
X Variable 1	7.43608306	0.43708389	17.0129425	1.6847E-18	6.54875559	8.32341053	6.54875559	8.32341053

Table S5. The mineral saturation index of the MRZ hot springs waters was calculated at the sampling conditions and equilibrated with K-feldspar.

No.	Hot Spring	Temp	Albite	Anhydrite	Anorthite	Aragonite	Ca-Montmorill	Calcite	Chalcedony	CO2(g)	Dolomite	Fluorite	Gypsum	Halite	Illite	Kaolinite	Quartz	SiO2(a)	Talc
1	Mbande	43.05	-0.33	-3.15	-2.4	-0.58	1.4	-0.45	0.15	-2.59	-1.2	-1.39	-3.04	-7.26	0.86	2.53	0.52	-0.63	1.03
2	Mwankenja 2	48.55	-0.47	-2.63	-1.29	-0.12	2.11	0	-0.01	-2.1	0.1	-1.26	-2.58	-7.22	1.64	3.29	0.35	-0.77	2.09
3	Mwankenja 1	45.8	-0.38	-2.77	-1.32	0.44	0.83	0.57	0	-2.98	1.31	-1.17	-2.68	-7.25	0.9	2	0.37	-0.78	6.4
4	Mwankenja 3	36.92	-0.6	-2.68	-1.61	0.02	1.87	0.16	-0.12	-2.56	0.38	-0.86	-2.5	-7.15	1.62	3.21	0.27	-0.92	2.12
5	Chiwondo	35.8	-0.47	-3.1	-1.64	-0.37	1.81	-0.23	-0.26	-2.89	-1.13	-0.79	-2.91	-6.94	1.53	3.34	0.14	-1.06	-0.93
6	Ngala	54.9	-0.36	-1.83	-0.79	0.01	0.85	0.14	-0.07	-3.24	-1.45	-0.33	-1.83	-6.43	0.52	2.08	0.27	-0.82	0.95
7	Chiweta	79.7	-0.52	-1.59	-0.98	0.16	-0.07	0.27	0.06	-2.27	-0.81	-0.01	-1.83	-5.57	-0.2	1.17	0.34	-0.63	3.15
8	MphiziStream	70.3	-0.61	-1.69	-2.17	0.21	-0.96	0.32	0.22	-2.55	-0.62	0.07	-1.84	-5.54	-0.99	0.19	0.53	-0.49	3.87
9	Kajilirwe (DC)	36.39	-0.57	-3.58	-1.57	-0.09	0.53	0.05	-0.13	-4.1	-0.69	-1.91	-3.4	-7.95	0.63	1.87	0.27	-0.93	3.78
10	Kajilirwe	36.82	-0.62	-3.58	-1.52	-0.06	0.17	0.08	-0.16	-4.39	-1.25	-1.88	-3.4	-7.92	0.29	1.56	0.23	-0.97	2.76
11	Chilongozi	40.39	-0.64	-3.29	-1.37	-0.06	0.35	0.08	-0.14	-4.15	-1.11	-1.66	-3.15	-7.93	0.4	1.68	0.25	-0.93	2.97
12	Chidha	41.84	-0.61	-3.15	-1.25	-0.17	0.47	-0.04	-0.1	-4.21	-0.48	-1.55	-3.02	-7.9	0.67	1.75	0.28	-0.89	5.71
13	Kalwe	35.1	-0.62	-2.91	-3.26	-1.05	2.02	-0.92	0.36	-2.36	-2.35	-0.4	-2.71	-7.65	0.95	2.98	0.76	-0.44	-1.71
14	Kajilirwe 2	46.76	-0.34	-3.74	-2.17	-0.35	0.05	-0.22	0.18	-3.75	-1.36	-2.14	-3.67	-7.97	-0.12	1.12	0.55	-0.59	3.93
15	Mtondolo 2	74.7	-0.77	-3.82	-0.75	-0.04	-1.3	0.08	-0.16	-4	-1.1	-1.26	-4.02	-8.01	-0.68	0.16	0.13	-0.86	6.54
16	Mtondolo	52.77	-0.59	-4.06	-1.91	-0.2	-0.62	-0.08	0	-3.87	-0.91	-1.03	-4.04	-7.98	-0.34	0.68	0.35	-0.75	5.16
17	Chiwe	73.1	-0.62	-3.29	-0.68	0.06	-0.89	0.17	-0.1	-3.75	-1.02	-0.58	-3.47	-7.6	-0.5	0.46	0.2	-0.8	5.8
18	Chombo	66.84	-0.52	-2.51	-0.53	0	-0.02	0.11	-0.09	-3.57	-0.92	-0.47	-2.63	-7.4	0.12	1.25	0.23	-0.8	4.98
19	Madzimawira	63.73	-0.45	-2.46	-0.62	0.01	0.31	0.13	-0.02	-3.42	-1.39	-0.26	-2.55	-7.38	0.14	1.49	0.3	-0.75	2.98
20	Ling'ona	58.08	-0.47	-2.44	-1.01	0.01	0.14	0.14	0.01	-3.57	-1.34	-0.18	-2.48	-7.32	-0.01	1.3	0.35	-0.73	3
21	Chikwizi	52.17	-0.5	-2.88	-1.08	0.04	-0.73	0.17	-0.11	-4.59	-1.26	-1.26	-2.86	-7.25	-0.4	0.58	0.24	-0.87	4.98
22	Liwonde	40.32	-0.28	-3.28	-2.43	-0.01	-0.54	0.12	0.02	-3.98	-0.47	-1.12	-3.14	-6.55	-0.28	0.76	0.41	-0.77	4.88
23	Sitima	36.43	-0.67	-4.52	-1.93	-0.16	-0.51	-0.03	-0.39	-4.44	-0.64	-1.44	-4.34	-6.86	0.21	1.24	0.01	-1.19	4.16
24	Mpsupsu	39.88	-0.88	-2.04	-2.59	-0.17	1.74	-0.04	0.21	-1.96	-0.27	0.09	-1.9	-6.63	1.04	2.81	0.6	-0.58	0.61
25	Muloza	34.7	-0.91	-3.81	-1.71	-0.11	1.53	0.03	0.05	-3.33	-0.44	-1.02	-3.61	-8.04	1.15	2.65	0.45	-0.76	2.79
26	July Borehole	51.35	-0.79	-2.1	-3.2	-0.26	0.09	-0.14	0.32	-2.25	-0.26	-0.11	-2.07	-6.02	-0.17	1.16	0.67	-0.44	3.51
27	Chipuze	42.68	-0.93	-2.05	-3.51	-0.1	0.82	0.03	0.36	-1.71	0.14	0.04	-1.94	-6.28	0.28	1.85	0.74	-0.42	1.8

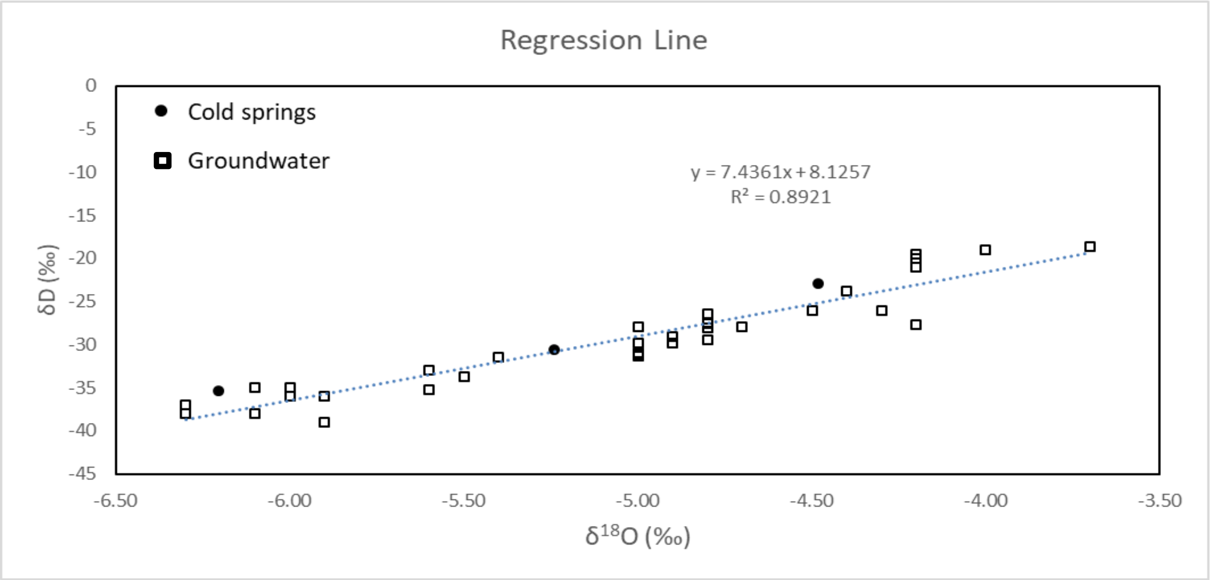

Fig. S1. Graph showing the regression line calculated from 37 cold springs and groundwater samples along the Malawi Rift.

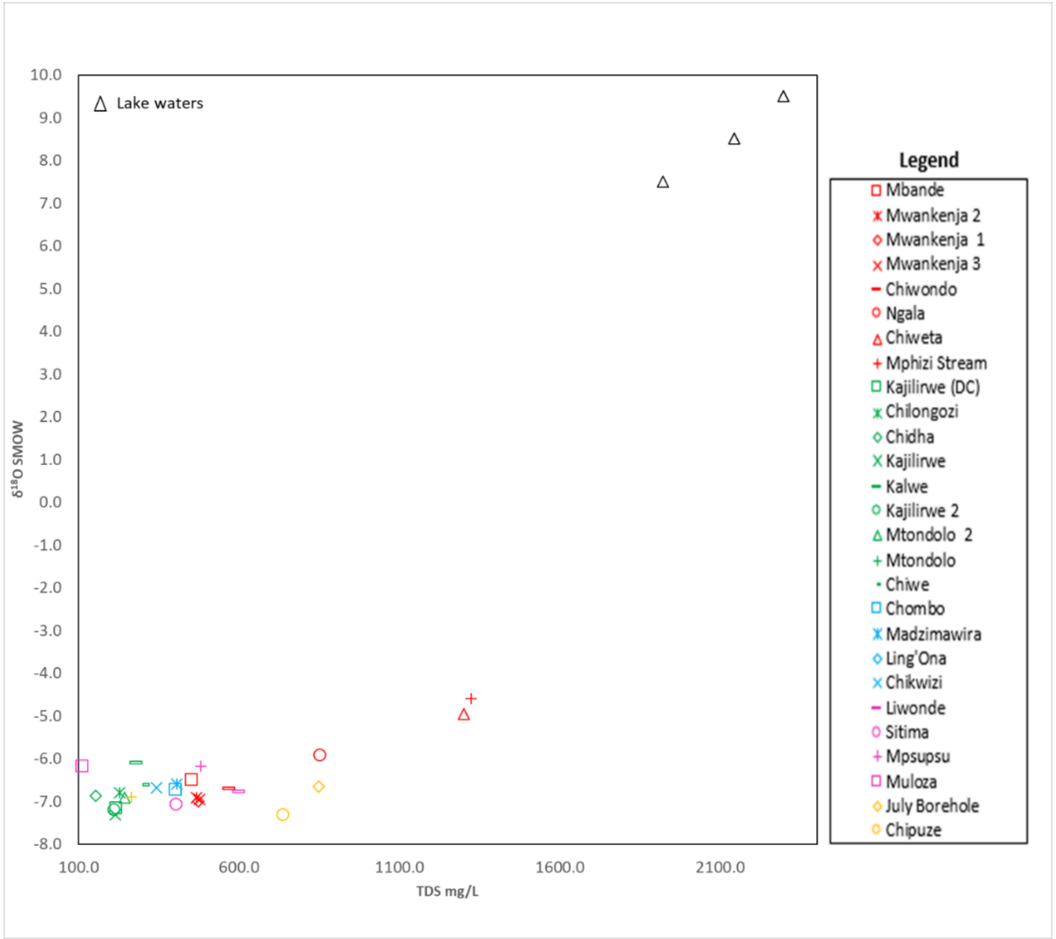

Fig. S2. TDS vs $\delta^{18}O$ graph for the thermal waters along the MRZ compared to the Lake Chilwa waters (Missi & Atekwana, 2019)

CHAPTER III

PAPER 2: STRUCTURAL ANALYSIS OF FRACTURE NETWORKS CONTROLLING GEOTHERMAL FLUID FLOW IN THE NORTHERN PART OF THE MALAWI RIFTED ZONE FROM AEROMAGNETIC AND REMOTE SENSING DATA

3.1 Abstract

We investigated the relationship between the geothermal fluids and fracture networks that control the storage and fluid pathways of geothermal systems in the northern part of the Malawi Rifted Zone (MRZ). It is suggested that low to medium enthalpy geothermal systems in the MRZ are mainly non-magmatic and structurally controlled. However, structural controls and favorable settings of geothermal fluids are poorly understood in this region. We used remote sensing and aeromagnetic data analysis to 1) identify and characterize fracture networks to better understand the structural controls of geothermal fluids in the northern part of the rift, 2) quantify and identify permeable areas using topological analysis of fracture intensity and connectivity frequency proxies, 3) understand the role that inherited structures play in the geothermal

systems of the northern part of the rift, and 4) build preliminary geothermal conceptual models of selected geothermal systems. Our findings show that fracture networks in the Karonga and Nkhata region comprise a varying degree of complexity along strike. This structural complexity occurs mainly in favorable zones such as 1) two fault segments coalescing to form hard and soft-linked relays, 2) two different oriented fracture segments intersecting each other, and 3) on the tips of major normal faults. The hot springs are located where one or more of these favorable zones occur. The remote sensing analysis shows that Cenozoic normal faults are the primary controlling structures of thermal waters at shallow depths in the Karonga (NW-SE to N-S strike) and Nkhata (N-S strike) regions. The aeromagnetic data revealed that permeable NW-striking foliation planes of the Precambrian Mugesse Shear Zone and WNW to ENE-striking foliation planes of the Mwembeshi Shear Zone are important structural controls of geothermal waters at greater depths in the Karonga and Nkhata region, respectively. The Mwankeja-Mwesia and Chiweta geothermal systems in the Karonga region show favorable structural settings for geothermal fluids related to NNW and NW-striking normal faults segments that coalesce to form hard and soft-linked relay ramps and NW, NNE, and N-striking faults intersecting each other. The Mtondolo geothermal area in the Nkhata region shows that the intersection of N-striking normal faults and ENE-striking foliation planes is the favorable structural setting that controls the emergence of hot springs through the surface. We conclude that high fracture intensity and connectivity are related to the location of the hot springs at the surface and can be used to determine permeable zones and hidden geothermal fluids together with other methodologies. Additionally, the aeromagnetic data analysis results concluded that buried faults and possibly reactivated inherited structures (e.g., foliation planes) by brittle deformation are controlling the geothermal fluids at depth. Our aeromagnetic analysis also shows that some of the geothermal reservoirs in the northern part of the MRZ have estimated depths from ~500 to ~1000 m.b.g.l. The low-cost methodology applied in this study can reduce the risk of drilling non-productive wells in the early exploration phases and become an exploration strategy for similar geothermal systems in countries of the Western Branch of the East African Rift System.

3.2 Introduction

The Western Branch is a magma-poor early-stage segment of the East African Rift System (EARS; Fig. 1a). Extension in the Western Branch is dominated by strain localization accommodated by rupture along border faults (McCartney & Scholz, 2016). Active volcanic centers in this region are limited to a few locations of favorable settings with deep magmatic sources (Hinz et al., 2018). In this tectonic context, the geothermal systems in the Western Branch are characterized by low to medium geothermal enthalpy resources (e.g., Hinz et al. 2018; Dávalos-Elizondo et al., 2021) heated mainly by the deep circulation of water associated with permeable structures. It has been suggested that the structural geothermal systems in this region have similarities with the geothermal resources developed in the Basin and Range region, U.S.A, where more than 98% are non-magmatic resources (Hinz et al., 2018). This has brought into question the heat source and structural controls that act as conduits for geothermal waters along the Western Branch.

This study focuses on the northern part of the Malawi Rifted Zone (MRZ) located in the southern end of the Western Branch, which has been affected by repeated rifting events, before the current Cenozoic Rifting (e.g., Delvaux, 2001). Geothermal systems in the MRZ are evidence of the presence of the active Rungwe volcano at the southern tip of the Tanzania border with Malawi, as well as hot springs emerging along the border faults of the MRZ (Dávalos-Elizondo et al., 2021), and a high heat flow of 60 to 120 mW/m^2 (Von Herzen & Vacquier, 1967; Ebinger et al., 1987; Njinju, et al., 2019). Despite this evidence, few studies have focused on understanding geothermal systems in the MRZ and most of them have focused on the geochemistry and geothermometry of hot springs (e.g., Dulanya et al., 2010; Gondwe et al., 2012; Kaonga et al., 2014; Msika et al., 2014; Tsokonombwe, 2017; Kalebe, 2018; Dávalos-Elizondo et al., 2021). Most of these studies agree that the hottest geothermal systems are found in the northern part of the MRZ with reservoir temperatures ranging from 100 °C to 200 °C and are mainly controlled by fracture networks. However, structural controls and favorable settings of geothermal systems in the MRZ have not yet been studied in sufficient detail (e.g., Morales-Simfors et al., 2015; Eliyasi, 2016; Dávalos-Elizondo & Laó-Dávila, 2019). As a result, there is limited knowledge about this type of geothermal system not only in the MRZ but also throughout the Western Branch.

On the other hand, studies focused on the relationship between fluid flow and the characterization of fracture networks have used high fracture intensity and connectivity proxies to identify permeable areas that favor the fluid flow of hydrocarbon leakages (e.g., Caine & Forster, 1999; Eichhubl et al., 2000; Gosh & Mitra, 2009; Dockrill & Shipton, 2010; Dimmen et al., 2017). These studies along with those conducted for structurally controlled geothermal systems in the Basin and Range, U.S.A. (e.g., Faulds et al., 2006; 2011; 2013; Siler et al., 2016) can be applied to characterize and quantify the relationship between geothermal fluids, fracture networks, and permeable zones in geothermal systems of the Western Branch.

Therefore, the purpose of this research is to quantify and characterize the geometry, topology, intensity, and connectivity frequency of complex fracture networks and to understand their relationship with geothermal fluids and permeability in the northern part of the MRZ, specifically in the Karonga and Nkhata regions. Here the terms “complex” or “complexity” are referring to fracture networks that show a wider range of orientations and higher intensity than other areas. The specific questions addressed in this study are: (1) What are the favorable structures that control fluid pathways and storage in geothermal systems in the northern region of the MRZ? (2) What are the spatial arrangement, intensity, and connectivity frequency characterization of fracture networks that can enhance permeability in the Karonga and Nkhata regions? (3) What role does the spatial arrangement of Precambrian structures (e.g., foliation planes) play in the geothermal systems of these regions? (4) What is the configuration of geothermal systems in the northern part of the rift?

The hypotheses that follow these questions are: (1) the active rifting in the region is creating favorable settings for geothermal fluids storage and/or pathways such as the intersection between faults, normal fault terminations, transfer zones, accommodation zones, and others (e.g., Faulds et al., 2006; 2011; Faulds & Hinz, 2015). (2) Complex fracture networks formed by a combination of interconnected faults, inherited reactivated structures (e.g., foliation planes), and regional joints improve the permeability and control the movement of geothermal fluids in the northern part of the MRZ. (3) The reactivation of inherited Precambrian structures has been suggested as a significant factor that influences the strike and height of the Quaternary border faults of the active rifting (e.g., Versfelt & Rosendahl, 1989; Delvaux, 1991; Ring, 1994; Ring et al., 2002; Laó-Dávila et al., 2015) and thus may control geothermal fluids pathways at depth. (4) Geothermal fluids are heated by deep-circulation along structures (e.g., Hinz et al., 2018; Dávalos-Elizondo et al., 2021), ascend through faults, and are hosted in shallow sedimentary and/or fractured metamorphic rocks reservoirs.

The low-cost methodology applied to test these hypotheses is a combination of remote sensing using Digital Elevation Model images of 12.5 and 2.5 m spatial resolution, high-resolution aeromagnetic data, and ArcGIS and QGIS statistical tools to characterize, analyze, and quantify fracture networks of the surface and subsurface. In addition, the Source Parameter Imaging method has been useful in estimating sedimentary thickness and reservoir depths in different geothermal zones.

The results of this research provide a better understanding of structurally controlled geothermal systems in the MRZ and contribute to the knowledge of the geothermal energy development in this region. The ability to quantify, characterize, and understand fracture networks and their relationship with geothermal fluids is relevant for identifying permeable areas, which will reduce the risk of drilling non-productive wells in the early exploration phases. These results provide a better understanding of the favorable settings, structural controls, and permeable zones of the geothermal systems in the MRZ. Additionally, we created preliminary conceptual models of selected geothermal systems in the northern part of the MRZ.

3.3 Tectonics and geothermal background

The Malawi Rift is a magma-poor Cenozoic rift located at the southern end of the Western Branch of the East African Rift System (EARS). It extends for ~750 km from the south of Tanzania to the southern border of Malawi (Fig. 1a; Chorowicz, 2005; Láo-Dávila et al., 2015). The Rungwe volcano is the only active volcano in the entire MRZ located at the northern tip of the rift in southern Tanzania (Scholz et al., 2011). Despite the lack of recent volcanism, more than 55 hot springs have been reported in the MRZ (e.g., Gondwe et al., 2012; Dávalos-Elizondo et al., 2021).

The heat source for the geothermal waters is still uncertain. However, a regional anomalous geothermal gradient responsible for the extension of the continental lithosphere between the Nubia and Rovuma plates occurs below certain segments of the MRZ (Von Herzen & Vacquier, 1967; Ebinger et al., 1987; Njinju et al., 2019). Njinju et al. (2019) have estimated from aeromagnetic data high heat flow around 70 – 82 mW/m^2 and high geothermal gradients between 29 – 32 °C/km within Permian-Triassic basins in the north-central segment, and in the northern end of the MRZ, where active volcanism is concentrated. Furthermore, it is suggested that the seismic data of anomalous low velocities of P-S waves in the northern part of the MRZ are due to a superplume and/or partial melting of the lithospheric mantle (e.g., Accardo et al., 2018; Grijalva et al., 2018; Borrego et al., 2018). Also, estimates of the thickness of the lithosphere derived from S-wave velocities have an average of between 36 and 38 km for the northern and central part of the rift, while the crust is 38 – 40 km thick in the southern part of the rift (e.g., Wang et al., 2019; Borrego et al., 2018).

This information agrees with the higher extensional rate in the northern region (2.2 mm/yr) than in the south (0.8 mm/yr) estimated from a GPS-derived model in the MRZ by Saria et al. (2014). Additionally, the highest reported surface temperature (80 °C) of hot springs is found in the northern part of the MRZ (e.g., Dulanya et al., 2010; Gondwe, 2012; Dávalos-Elizondo et al., 2021).

3.3.1 Geology and structural controls in the MRZ

The Malawi Cenozoic rift is divided into three first-order segments comprising the northern, central, and southern regions (Fig. 1a; Reynolds & Rosendahl, 1984; Láo-Dávila et al., 2015; Dawson et al., 2018). Second-order segmentation is recognized only in the northern section, where this study is focused, and consists of several asymmetric grabens, half-grabens, and full grabens (Laó-Dávila et al., 2015) with alternate polarities linked through accommodation zones (e.g., Ebinger et al., 1987; Rosendahl, 1987; Ring, 1994). Four basins comprise the second-order segmentation in the northern region: the Karonga Basin (Fig. 1b), the Usisya Basin, Mbamba Basin (both also called Nkhata basin; Fig. 1c), and the Bandwe Basin (e.g., Láo-Dávila et al., 2015).

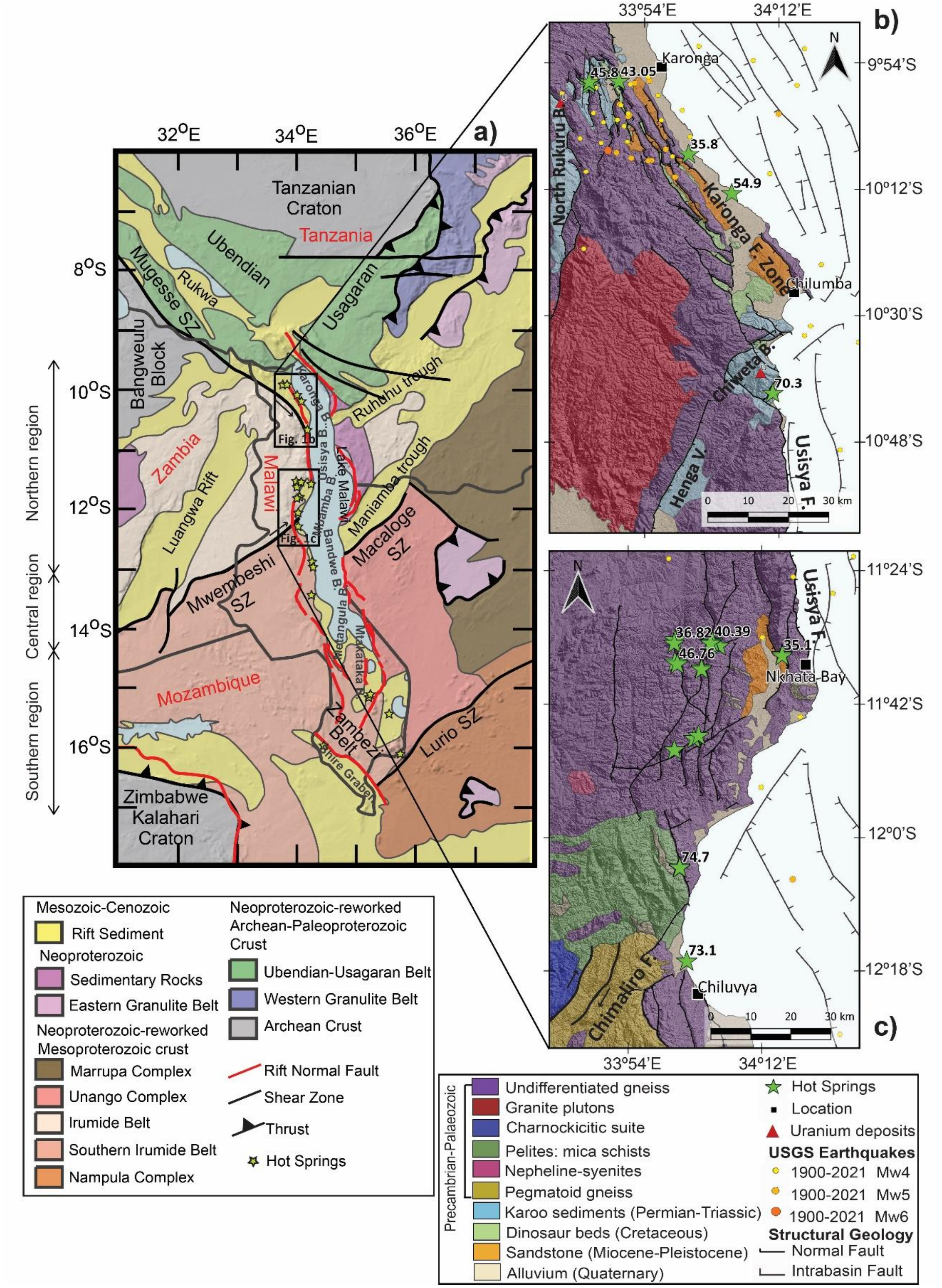

Figure 1. a) Tectonic and geological settings of Precambrian complex, orogenic belts, Paleozoic-Mesozoic basins, Cenozoic Malawi Rift border faults, and hot springs around the MRZ. Modified

after Fritz et al. (2013), Láo-Dávila et al. (2015), and Dávalos-Elizondo et al. (2021). b) Geological and structural settings of the Karonga region. Modified after Bloomfield (1968) and Biggs et al. (2010). c) Geological and structural settings of the Nkhata region. Modified after Bloomfield (1968). The surface temperatures of hot springs are Celsius from a previous study by Dávalos-Elizondo et al. (2021).

Several studies have discussed the strain localization as a mechanism of the Cenozoic rifting in the MRZ and the important role that inherited structures play during the segmentation and extension of the rift (e.g., McConnell, 1972; Van Wijk, 2005; Corti et al., 2007; Katumwehe et al., 2015; Láo-Dávila et al., 2015; Leseane et al., 2015; Kolawole et al., 2018). However, other studies suggested that strain localization cannot be the only driver in the early stages of extension in the MRZ (e.g., Njinju et al., 2019; Hooper et al., 2020). For instance, Njinju et al. (2019) proposed that the lithosphere weakening mechanism is driven by a decoupled extension beneath some segments of the rift and assisted by a concentration of fluids due to deeper asthenospheric melting in the subsurface. Likewise, Hopper et al. (2020) suggested that elevated temperature and partial melting conserved in areas such as Precambrian sutures (e.g., Ubendian Belt) provided an early source of melt that allowed the alteration and/or removal that caused the thinning of the lithospheric mantle based on results of seismic data.

Therefore, several studies have highlighted the important role of inherited structures in the Cenozoic rifting process (e.g., Versfelt & Rosendahl, 1989; Ring, 1994; Láo-Dávila et al., 2015; Kolawole et al., 2018) but not many have recognized the contribution of fluids and geothermal activity (e.g., Njinju et al., 2019; Hopper et al., 2020). However, previous studies that focused on geothermal systems in the MRZ suggested that they are associated with the circulation of meteoric waters through deep structures (e.g., Dávalos-Elizondo et al., 2021) and most of the thermal waters are aligned with the current Cenozoic border faults. Thus, structural controls and geothermal activity are interrelated and play an important role in the mechanism of the Cenozoic rifting that needs to be studied further. Furthermore, the role that inherited structures play in geothermal systems must also be understood.

The tectonic history of inherited structures in MRZ includes important orogenic events during the Precambrian and previous rifting events during the Paleozoic-Mesozoic that are summarized as follows. During the Precambrian orogenic events, three orogenic belts were formed during collision episodes: the Archean-Paleoproterozoic Ubendian-Usagaran belt (~2000 – 1090 Ma), the Mesoproterozoic Irumide belt (~1350 – 950 Ma), and the Pan-African Mozambique belt (~900 – 450 Ma; Ring, 1993; 1994; Ring et al., 1992). A reworked Proterozoic basement is found at the junction of these orogenic belts in the northern region of the MRZ (Fritz et al., 2013). The Ubendian belt is in the Karonga region and is made up of syn- to post-tectonic granitoids, gneisses, volcano-sedimentary rocks, and migmatites (e.g., Ring, 1993; Ring et al., 2002). The accretion boundary between the northwestern Ubendian orogenic belt and the Irumide orogenic belt is the transcurrent Mugesse Shear Zone (MuSZ; Fritz et al., 2013) crosses the Karonga region from NW to SE (Fig. 1a). The MuSZ contains steeply dipping foliation planes that potentially serve as inherited structures where different reactivation events have occurred (e.g., Ring 1994; Fritz et al., 2013; Dawson et al., 2018). For instance, Ring et al.

(2002) mentioned a strike-slip movement of the MuSZ during the Pan African orogeny. Furthermore, Dawson et al. (2018) suggested reactivation of the MuSZ foliation planes by the Quaternary Karonga Fault Zone with a general foliation strike of N301°W and a dip of 79° towards the NE.

The Irumide mobile belt is a NE-striking thrust-fold belt that extends from eastern Zambia to southern Tanzania through northern Malawi (Fig. 1a; Ring, 1993; De Waele et al., 2006; Fritz et al., 2013). The lithological units of the Irumide belt recognized in the MRZ are reworked Neoproterozoic Ubendian basement, sedimentary sequences (Muva Supergroup: Mafingi Group), Mesoproterozoic syn- to post-kinematic emplaced granitoid, and high-low grade metamorphic rocks (e.g., Ring, 1993; De Waele et al., 2006; Fritz et al., 2013). The Mwembeshi Shear Zone (MwSZ) represents the border between the Irumide Orogenic Belt and the Southern Irumide Belt (Fig. 1a; Fritz et al., 2013). Ring et al. (2002) suggested a continuous dextral strike-slip motion combined with SE transport along the MwSZ during the Pan African orogenic event (Ring et al., 2002; Fritz et al., 2013). It is suggested that the ENE-striking Chimaliro fault zone with a dextral strike-slip motion (Fig. 1c) is a reactivation of the MwSZ in the MRZ (Ring, 1993; Bjerkgard et al., 2009), and is present in the Nkhata region (Fig. 1a, 1c).

During the Paleozoic and Mesozoic eras NE to N-striking (Late Carboniferous to Early Triassic), and NW-striking (Late Carboniferous-Permian) rift basins, known as Karoo basins, were formed during the break-up of Gondwana (Ring & Betzler, 2015; Delvaux, 2001). Delvaux (2001) suggested that the NW-striking Karoo basins were formed due to transpressional reactivation of the Ubendian foliation planes in northern Malawi.

Likewise, Dawson et al. (2018) mentioned that the major faults in the Karoo basins may have served as inherited structures that may have slipped during the Cenozoic Rifting in the MRZ. The most important Karoo basins in the MRZ are (Fig. 1a): Luangwa Rift, Ruhuhu trough, Maniamba trough, and Shire graben, while patches of these Karoo basins lie onshore along the Karonga region (Kolawole et al., 2018). These minor remnants of Karoo basins on the western side of the Karonga region are (Fig. 1b): Mwankenja-Mwesia basin, North Rukuru basin, Henga Valley, and Chiweta basin. The sedimentary cover of the Karoo basins has been estimated to be more than 2 – 4 km in some areas (Ring & Betzler, 1995; Accardo et al., 2018). The lower Karoo sedimentary succession that overlaps the metamorphic basement comprises basal conglomerates, followed by laminated shale interbedded with thin layers and lenses of sandstone (Ring, 1995). The upper Karoo beds consist of siltstones and calcareous shale, where a significant unconformity separated the shale unit from the coal layers (Ring, 1995). Subsequently, dolerite and basalt dikes were intruded in the early Jurassic (Ring & Betzler, 1995). Then, a red bed terrestrial sedimentary sequence (Dinosaur beds) overlaps the Karoo succession during the Cretaceous (Scholz et al., 2011).

3.3.2 Geothermal energy in the MRZ

Most of the published literature on geothermal exploration in Malawi focuses on the chemistry and geothermometry of hot springs (Dixey, 1927; Bloomfield, 1965; Bloomfield & Garson, 1965; Kirkpatrick, 1969; Chapusa & Harrison, 1975; Ray, 1975; Dulanya, 2006; Dulanya et al., 2010; Msika et al., 2014; Tsokonombwe, 2017; Kalebe, 2018; Dávalos-Elizondo et al., 2021). The hottest geothermal reservoirs reported by these geothermometry studies are between ~100 – 250 °C and are in the northern part of the MRZ (e.g., Dulanya et al., 2010; Msika et al., 2014; Tsokonombwe, 2017; Kalebe, 2018; Dávalos-Elizondo et al., 2021). Dávalos-Elizondo et al. (2021) suggested that local meteoric waters infiltrate deeply, are heated by anomalous heat flow, then hot water rises to the surface through permeable zones. In this way, it is suggested that most of the geothermal systems in the MRZ are structurally controlled (e.g., Gondwe et al., 2012; Dávalos-Elizondo et al., 2021).

Despite the importance of understanding the favorable structural settings and the fracture networks that act as pathways and/or storage for geothermal fluids in the MRZ, there are few studies focused on this issue (e.g., Morales-Simfors et al., 2015; Eliyasi, 2016; Dávalos-Elizondo & Láo-Dávila, 2019). For instance, Morales-Simfors et al. (2015) reviewed the structural and stratigraphic controls of hot springs in Malawi. These authors emphasized the need to understand the fracture networks and permeable rocks that control geothermal fluids. Furthermore, Eliyasi (2016) studied the general relationship between faults and the occurrence of hot springs in the northern part of Malawi. This author argued that the occurrence of hot springs is associated with high fracture intensity and hot springs with higher temperatures are associated with major border faults. Dávalos-Elizondo and Láo-Dávila (2019) studied structural controls and slip tendency in the Chiweta geothermal prospect. Their results show that the intersection of structures NW, NE, and N-striking are present in the Chiweta zone, and the NW-striking faults show a greater slip tendency compared to the NE-striking faults.

3.3.3 Hot springs in the Northern part of the MRZ

The Karonga region has five geothermal potential zones (Fig. 1b): Mwankenja, Mbande, Chiwondo, Ngala, and Chiweta (Dávalos-Elizondo et al., 2021). Most of the hot springs in the Karonga region are classified as Na-HCO3 waters, except for the Chiweta hot springs which have Na-Cl (SO4) waters (Dávalos-Elizondo et al., 2021). The hot spring of Mwankeja, Mbande, Chiwondo, Ngala, and Chiweta have surface temperatures of approximately 48 °C, 43 °C, 35 °C, 55 °C, 80 °C, respectively (Dávalos-Elizondo et al., 2021). The maximum geothermal reservoir temperatures estimated from cation geothermometry by Dávalos-Elizondo et al. (2021) in the same hot springs are 114 °C, 135 °C, 106 °C, 126 °C, and 190 °C, respectively. However, other studies have reported lower reservoir temperatures between 100 °C and 157 °C in the Chiweta hot springs using silica geothermometry (e.g., Kalebe, 2018; Tsokonombwe, 2017).

The Nkhata region has at least five geothermal potential zones (Fig. 1c): Kajilirwe, Chidha or Kanunkha, Kasanama, Mtondolo or Kawira, and Chiwe (e.g., Msika et al., 2014; Dávalos-Elizondo et al., 2021). The geothermal waters of the Nkhata region are classified as Na-HCO3 and Na-SO_4 (Dávalos-Elizondo et al., 2021). The maximum surface temperatures reported by Dávalos-Elizondo et al. (2021) in the hot springs of Kajilirwe, Chidha, Mtondolo, and Chiwe are 47 °C, 41 °C, 73 °C, and 75 °C, respectively. Msika et al. (2014) reported maximum surface temperatures of Kasanama hot springs of 65 °C. The maximum estimate of geothermal reservoirs from cation geothermometry in the Kajilirwe, Chidha, Mtondolo, and Chiwe geothermal zones are 108 °C, 116 °C, 144 °C, and 138 °C, respectively. Meanwhile, Msika et al. (2014) estimated reservoir temperatures from cation geothermometry of 283 °C in the Kanunkha/Chidha hot spring, 159 °C in the Kasanama hot spring, and 156 °C in the Mtondolo/Kawira hot spring.

3.4 Data and Methods

3.4.1 Remote sensing analysis

A morphostructural analysis of surficial fault scarps and other structures (e.g., joints, foliation planes) of brittle and ductile deformation in the Karonga (76 x 134 km^2) and Nkhata (75 x 124 km^2) regions was performed using satellite data and hillshade relief images processed from Digital Elevation Models (DEMs). An initial analysis was performed to identify shallow expressions of lineaments and fault scarps presented in the Karonga and Nkhata regions at scales of ~1:500,000 was done using the freely available Advanced Land Observing Satellite (ALOS) PALSAR Mission data of 12.5 m spatial resolution. Most of the normal faults digitized were modified from previous studies (e.g., Bloomfield, 1968; and Biggs et al., 2010) and others were identified in this study through geomorphology and topographic profiles (Fig. 2a).

Afterward, three areas of interest were selected using the preliminary results in this study and the geothermal reservoir temperatures calculated by Dávalos-Elizondo et al. (2021). We acquired high-resolution Digital Surface Model (DSM) data AW3D WORLD 3D of 2.5m spatial resolution by the Japan Aerospace Exploration Agency (JAXA). The high-resolution topographic data were used to perform the morphostructural analysis at scales of ~1:50,000 in the Mwankenja-Mwesia, Chiweta, and Mtondolo geothermal prospect areas. The three zones show different scenarios to have a better understanding of the structural controls of the geothermal fluids in the northern part of Malawi.

The hillshade relief images were processed with the GlobalMapper® software, using different sun azimuth angles (e.g., 45°, 60°, 165°, 315°), sun elevations (30° and 45°), and Z-factors (1 and 3) to highlight the major structural features of the study areas. Different directional filter angles and synthetic color images were obtained with the ENVI® software to reduce bias when mapping the structures. Fault scarps and lineaments were mapped with QGIS software. Additionally, the QGIS was used for the analysis of available spatial information such as geology, structural geology, geochemistry, and geophysics (e.g., Bloomfield, 1968; Fritz et al., 2013; Biggs et al., 2010; Shillington et al., 2020; Scholz et al., 2020), which assisted in the verification of the identified structures in our analysis.

Spatial and statistical information such as trace azimuth, length, slope angle (minimum dip value), fracture intensity (a structural proxy for network complexity), connectivity node frequency (a topological proxy for network connectivity), and cross-cutting relationship were extracted from the remote structural analysis. A linear directional mean expression applied with the QGIS software was used to calculate trace azimuths of the lineaments. Then, rose diagrams were plotted using the Stereonet software by R. W. Allmendinger © 2020 to better visualize the main orientations and frequency of the structural data. Likewise, topographic profiles built perpendicular to the main structures were generated to identify the geometry of fault scarps, joints, and foliations. Additionally, cross-sections across the selected three geothermal areas were used to create preliminary geothermal conceptual models.

3.4.1.1 Topological analysis

The 12.5 and 2.5 m spatial resolution hillshade relief images were used to digitize the topological features using the Network GT plugin QGIS (Nyberg et al., 2018) as used by Dimmen et al. (2017). The topological characterization consisted of describing the geometrical relationships of fractures (e.g., Sanderson & Nixon, 2015; Dimmen et al., 2017) and can be applied to characterize the spatial distribution, determine connectivity, fracture intensity, and identify potential permeable zones. The methodology is used to quantify the characteristics mentioned above in two dimensions, using nodes (ends or intersection points of structures) and branches (segments of a fracture with a node at each end) of fracture networks (Dimmen et al., 2017). Three types of nodes, depending on their connectivity and geometry characteristics were identified following the criteria by Sanderson and Nixon (2015): I-nodes (isolated tips of fractures), Y-nodes (intersection of fractures abutments that connect three branches), X-nodes (intersections of crossing fractures that connect four branches). Likewise, branches were classified into three types depending on the type of node at each end (Sanderson and Nixon, 2015): isolated I-I branches (the two tips are I-nodes), singly connected I-C branches (one tip is an X or Y-node), or doubly connected C-C branches (the two tips are X or Y-nodes).

Density maps were also built-in QGIS to evaluate and visualize better the permeable zones distribution from fracture intensity, connectivity frequency proxies, and their relationship with the hot springs. All nodes and branches were considered as a complete fracture network to create the density maps of (1) fracture intensity, which is equal to the total branch length per square kilometer (km/km^2), and (2) connectivity frequency, which corresponds to the number of connections (Nc) per square meter (NC/m^2):

$$NC = NX + NY \tag{1}$$

where NY, and NX correspond to the different node types Y-node, and X-node, respectively. See Sanderson and Nixon (2015) for full equation derivations and Dimmen et al. (2017) for more information about this topological method.

3.4.2 Aeromagnetic data analysis

High-resolution aeromagnetic data was used to identify subsurface structures, such as foliations and buried faults. The aeromagnetic data was used to understand the spatial distribution of foliations, buried structures, and their relationship with geothermal fluids at depths. The foliated fabric produces a conspicuous magnetic signal that can be used for mapping the subsurface structures in the MRZ (e.g., Dawson et al., 2018; Kolawole et al., 2018; Laó-Dávila et al., 2015). The geophysical data was acquired by the Government of Malawi in 2013 with a flight elevation of ~60 m, spacing lines of 250 m NE-SW oriented, and control lines-oriented NW-SE with 5 km spacing.

Reduce to the Pole (RTP) and edge-detection filters were applied to the aeromagnetic data using the Geosoft Oasis Montaj software. The RTP process corrects the spatial location of the magnetic anomalies directly over the magnetized body and eliminates the distortion of the normal magnetic field (Baranov, 1957). The first-order horizontal-Y derivative (Dy) filter was selected to better map the orientation of foliation planes from the aeromagnetic data in both the Karonga and Nkhata regions. Dy estimates the rate of change of total magnetic intensity in the N-S direction, which enhanced structures subparallel to the E-W (Miller & Singh, 1994; Salem et al., 2007; Kolawole et al., 2018) such as the ~E-W trend of the foliation planes in the Nkhata region or the foliations mainly oriented ~NW-SE in the Karonga zone. Afterward, we digitized the foliation planes from the horizontal-Y derivative image in QGIS. The corresponding azimuthal strikes of these structures were extracted and plotted on rose diagrams to better visualize their orientations.

Tilt-angle derivative maps were used to delineate the strike orientation of shallow subsurface crustal structures. The tilt-angle derivative represents the ratio of the vertical derivative and the total horizontal derivative of the total field magnetic data in all directions (e.g., Katumwehe et al., 2015; Dawson et al., 2018). The tilt-angle derivative is an effective edge detection filter to identify surficial faults with continuity at depth and buried faults. The dip direction of the structures could be determined by the tilt angle grid, where the angle values with the "+" sign represent the variation of the tilt through the magnetic anomaly and the "-" sign represents the variation of the tilt opposite from the magnetic anomaly (see Salem et al., 2007; and Katumwehe et al., 2015). We used the 0° tilt-angle derivative contour (e.g., Salem et al., 2007) to delineate the edges of basement faults in specific geothermal prospects selected in this study. We also draped the surficial lineaments obtained from the hillshade topographic image analysis on the tilt-angle derivative map to better identify faults that have a surficial expression and others that are buried structures at depth.

Additionally, the Source Parameter Imaging (SPITM) method (Thurston & Smith, 1997; Smith & Salem, 2005) was used as a proxy for estimating the magnetic basement depth (i.e., magnetic source). In the MRZ "the magnetic basement" can be interpreted as the rock basement (metamorphic complex) due to its high-magnetic susceptibility compared with other types of rock. The methodology applied in this work subtracted the flight altitude from the SPI results to obtain values of meters below ground level (m.b.g.l) instead of below the sensor. Also, a cutoff of 5 km was used in both Karonga and Nkhata regions. We used depth control points from seismic data from Accardo et al. (2020) and Shillington et al. (2020) to compare the SPI results on the Karonga region coastline and to validate the tested accuracy of ± 20% on real data sets with drill hole control (e.g., Gay, 2009; Salako, 2014) for the SPI method. Finally, the SPI method was used to estimate the thickness of the sedimentary sequences and the depths of the magnetic basement to create the preliminary geothermal conceptual models of three geothermal prospects.

3.5 Results

3.5.1 ALOS PALSAR DEM analysis

3.5.1.1 Karonga region

Remote sensing analysis of the ALOS PALSAR DEM image with 12.5 m spatial resolution in the Karonga region (~76 x 134 km^2) shows that the most prominent morphostructures are: (1) the normal fault scarps located near the coastline that form part of the Karonga Fault Zone (KFZ), and (2) the Nyika Plateau, a granite pluton located SW of the study area (Fig. 1b). The maximum inland elevation point of 2,607 m in the study area corresponds to the Nyika Plateau, while the minimum inland elevation point of 477 m corresponds to the Quaternary basin on the shoreline of Lake Malawi.

Surface structural DEM analysis helped identify a total of 601 lineaments, representing mainly normal faults and regional joints in the Karonga region. (1) Of the 601 lineaments, 132 of them were identified as normal faults (Fig. 2a). The 132 normal fault lineaments show a more frequent azimuthal strike of ~NW-trending (n=63) within a mean vector of 329.3° ± 05.4° (Fig. 2a, 3a), followed by ~N (n=20) and ~NE (n=49) striking faults. Of these 132 normal faults, 50 lineaments show an azimuthal strike range of 300 – 339° (NW-SE; Fig. 3a). (2) The remaining 469 lineaments were identified as regional joints with a general azimuthal orientation ~NE-SW, a mean vector of 058.1° ± 01.6° (Fig. 2a). Of the 469 lineaments identified as regional joints, the most common strike direction was in the range of 050° – 069° (NE-SW strike) with 278 lineaments (Fig. 3c). Additionally, intrabasin normal faults (n=23) from previous studies were digitized (e.g., Shillington et al., 2020 and

Scholz et al., 2020). These normal faults have a general ~N-S strike and a mean azimuthal vector of 346.7° ± 09.4° (Fig. 2a).

Within the different lithologies analyzed, three main surface structures with a NW, N, and NE trends were recognized. The Precambrian basement and the Cretaceous to Quaternary sediments contacts are mainly bounded by NW-striking normal faults (Fig. 2a). The contacts between the Karoo sediments and the Precambrian basement are mainly bounded by N to NE-striking normal faults. While the NE-striking regional joints intersect mainly the metamorphic rocks but not the sedimentary rocks (Fig. 2a).

The regional-scale analysis allowed us to calculate the length of the normal faults (n=132) which vary from 534 m to 48,709 m and with an average length of 9,087 m (Fig. 2a, 3b). The frequency length distribution of normal faults is in the ranges of 2.0 – 2.9 km and 4.0 – 4.9 km comprising a total of 39 out of 132 lineaments (Fig. 3b). The most frequent azimuthal orientation by number and by cumulated length is NW-SE. The length of the Karonga regional joints (n= 469) ranges from 544 m to 16,352 m with an average length of 3,144 m (Fig. 2b, 3d). The frequency length distribution of the regional joints is in the range of 1.0 – 2.9 km with a total of 264 out of 469 lineaments (Fig. 3d).

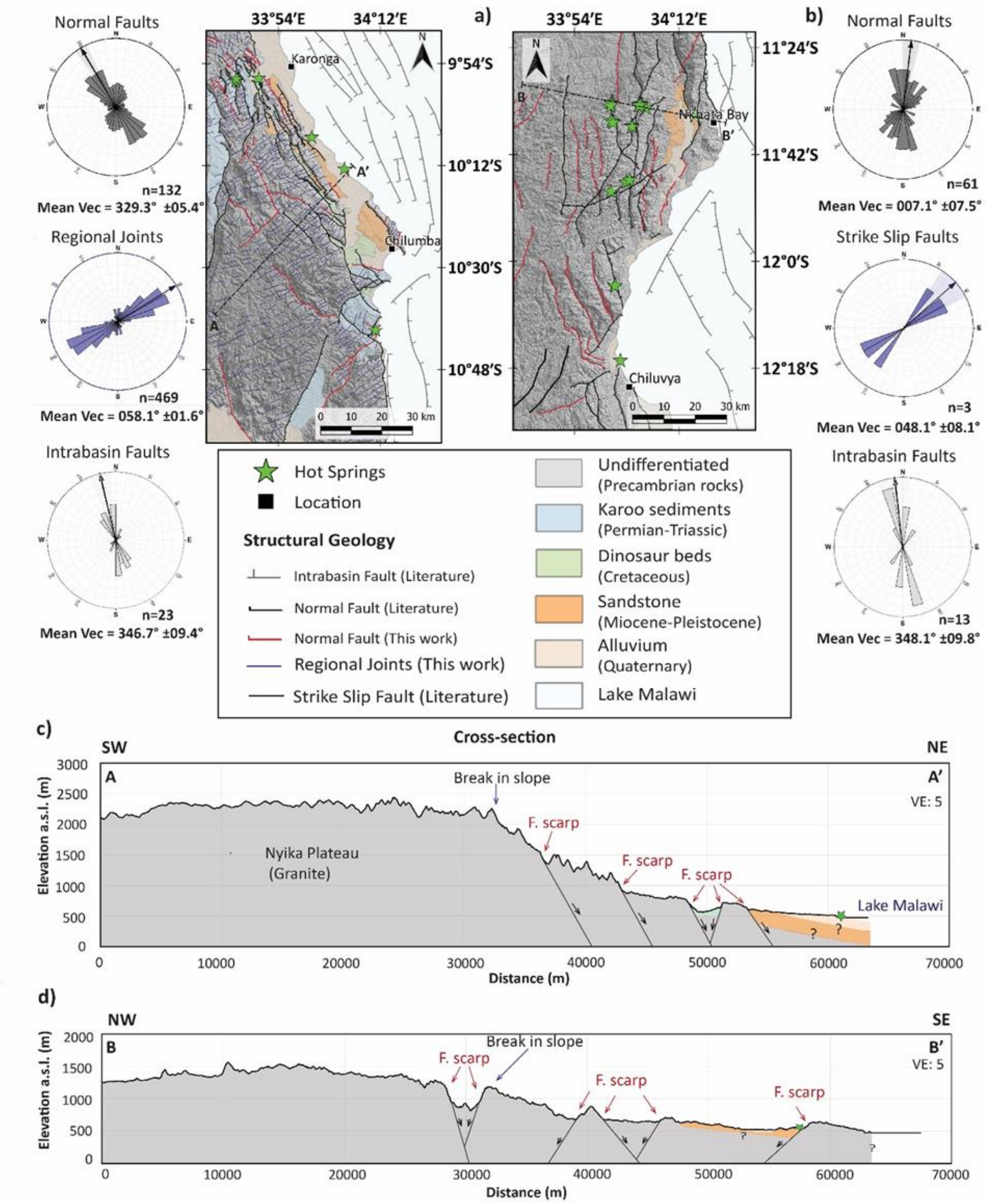

Figure 2. a) Structural geology map from the ALOS PALSAR DEM image of 12.5 m spatial resolution of the Karonga region. b) Structural geology map from the ALOS PALSAR DEM image of 12.5 m spatial resolution of the Nkhata region. Modified after Bloomfield (1968) and Biggs et al. (2010) and this study. Rose diagrams of all normal faults, regional joints, strike-slip faults, and intrabasin faults. Mean Vec= Mean Vector. Dashed black lines in the structural maps are showing the location of cross-sections shown in c) and d). c) Cross-sections A – A' and d) cross-section B – B' show the most prominent morphostructures such as fault scarps.

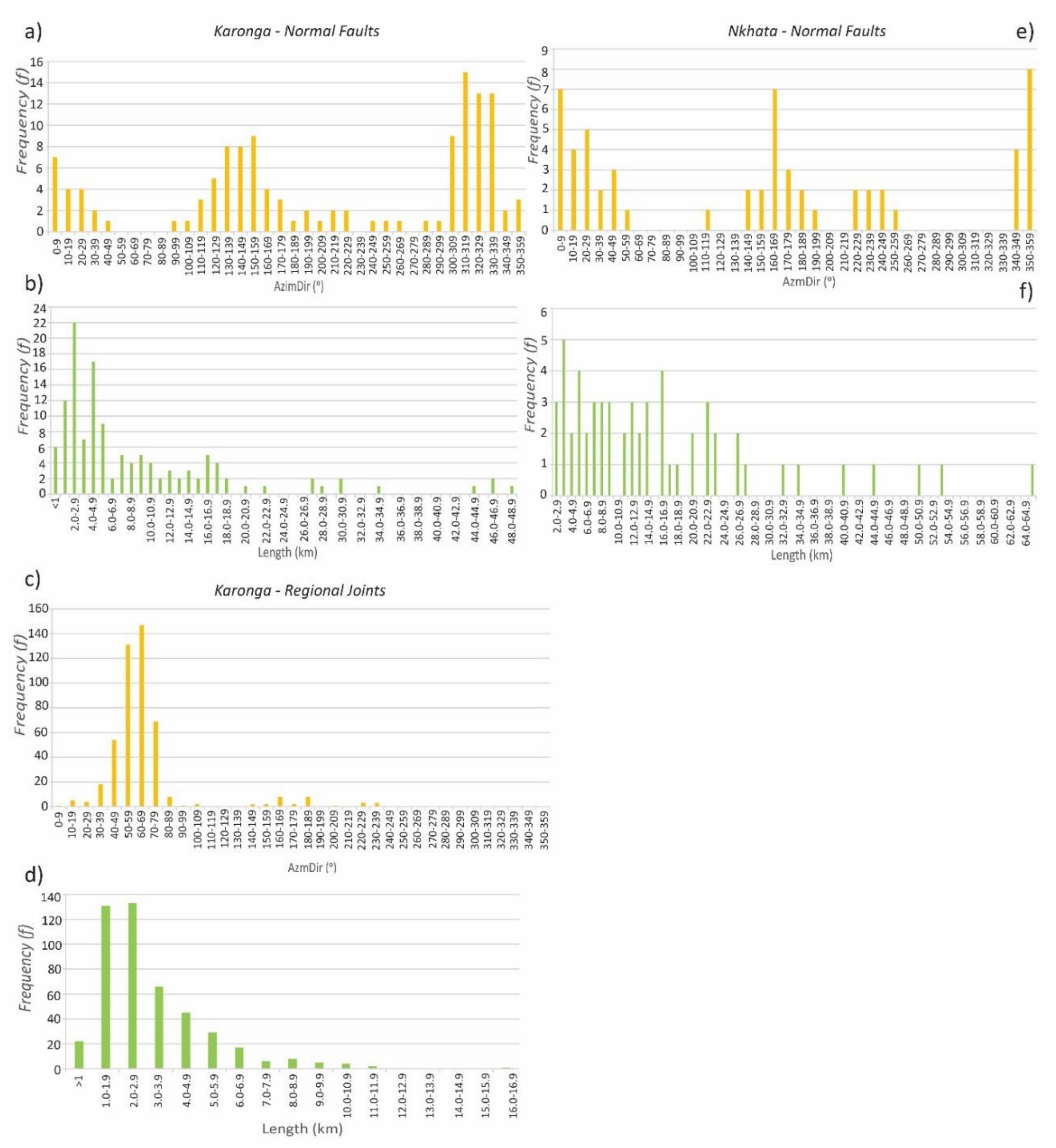

Figure 3. a) Lineament direction frequency detected by the ALOS PALSAR DEM analysis for all normal faults in Fig. 2a, the direction in azimuth (°). b) Lineament length and frequency detected for all normal faults in Fig. 2a. c) Lineament direction frequency detected by the ALOS PALSAR DEM analysis for all regional joints in Fig. 2a, the direction in azimuth (°). d) Lineament length and frequency detected for all regional joints in Fig. 2a. e) Lineament direction frequency detected by

the ALOS PALSAR DEM analysis for all normal faults in Fig. 2b, the direction in azimuth (°). f) Lineament length and frequency detected for all normal faults in Fig. 2b.

3.5.1.2 Nkhata region

Analysis of the ALOS PALSAR DEM image in the Nkhata region (75 x 124 km^2) shows that the most prominent morphostructures are: (1) the normal fault scarps that are part of the Cenozoic Rifting, and (2) the Chimaliro strike-slip fault in the southwestern part of the study area (Fig. 1c). The maximum elevation of 1,950 m corresponds to the Precambrian basement in the northwest and the minimum elevation of 475 m is found in the southeastern part of the Lake Malawi shoreline.

A total of 64 lineaments corresponding to faults (Fig. 2b) were identified by the ALOS PALSAR DEM analysis. (1) Normal faults were identified as 61 of the 64 lineaments with a mean azimuthal vector of 007.1° ± 07.5° with most of them striking ~N-S to ~NNW-SSE (n=43) and a minority of them trending ~NE-SW (n=18). The frequency azimuth distribution shows that the most common azimuth direction (n=22 of 61 total) ranges from 350 – 360°, 000 – 009°, 160 – 169° (~N-S; Fig. 3e). (2) The remaining three lineaments were identified as strike-slip faults corresponding to the Chimaliro Fault with a mean azimuthal vector of 0.48.1° ± 08.1°. Like the Karonga region, 13 intrabasin normal faults lineaments were digitized from previous studies (e.g., Shillington et al., 2020 and Scholz et al., 2020) with a general ~N-S strike and a mean azimuthal vector of 348.1° ± 09.8°. The Precambrian basement is mostly intersected by ~N-striking normal faults, while the NE-trending strike-slip faults cross the Charnockitic dome and the Pegmatoid gneisses (Fig. 1c, 2b). Regional joints were not identified due to the difficulty of distinguishing them from other reactivated structures that follow the foliation planes (~WNW-ESE) in this region.

Regional-scale analysis in the Nkhata region indicates the normal faults (n=61) have lengths from 2,211 m to 65,753 m and an average length of 16,424 m (Fig. 2b and 3d). The normal fault frequency length distribution in this region is in the range of 3.0 – 3.9 km with a total of 5 out of 61 lineaments (see Fig. 3d). The Chimaliro fault zone has a length from 24,548 m to 52,502 m.

3.5.2 Aeromagnetic data analysis

3.5.2.1 Edge-detection filter analysis

The first-order horizontal-Y derivative images show in detail the crystalline basement fabric related to the suture zones of the MuSZ in the Karonga region and the MwSZ in the Nkhata region (white arrows in Fig. 4a and 4b). The foliation planes are shown as lineaments of high and low magnetic gradients within the high frequency and short wavelength in both regions, which are related to Precambrian metamorphic rocks. On the other hand, lower frequency, and longer wavelength magnetic anomalies with a general ~NNW-SSE trend appear to be associated with Cenozoic and Paleo-Mesozoic sedimentary basins and major faults near the coast of the Karonga region (Fig. 4a). While in the Nkhata region, the low-frequency and long-wavelength anomalies have ~N-striking faults associated with Quaternary sediments in the coastline and ~ENE-striking fractures associated with pelitic schists in the central part of the study area (Fig. 4b).

The first-order horizontal-Y derivative map helped identify a total of 495 foliation planes that strike ~NW-SE (290° – 320°) with a mean azimuthal vector of 124.0° ± 00.9° in the Karonga region (Fig. 4a). A total of 1,422 foliation planes were digitized from the horizontal-Y derivative map with a general strike of ~WNW-ESE to ~W-E (280° – 300°; Fig. 4b) in the Nkhata region. The mean vector of 107.3° ± 00.7° (WNW-ESE strike) was obtained from the rose diagram analysis of the 1,422 foliation planes identified in this region.

The tilt-angle derivative map was used to show the edge geometry (0° tilt-angle degree contour) of the surface and buried faults. Our results show a good correlation between the surficial lineaments obtained from the ALOS PALSAR DEM image analysis and the magnetic anomalies of the tilt-angle derivative map in both regions (Fig. 4c and 4d). We also identified buried faults and undifferentiated fractures in both regions from the tilt-angle derivative map after a comparison with the ALOS PALSAR DEM image and observed the absence of surficial expressions of these buried structures (Fig. 4c and 4d). The tilt-angle derivative maps show the buried structures as low-amplitude, high frequency, and short-wavelength magnetic lineaments in both areas (black arrows in Fig. 4c and 4d). While the first-order horizontal-Y derivative maps show a lower frequency and longer wavelength magnetic signal related to buried fault lineaments found in areas filled with sedimentary rocks.

A total of 32 buried fault lineaments were identified in the Karonga region from the tilt-angle derivative map (Fig. 4c). Most of these buried faults are hidden beneath the sediments deposited in the coastal plain and most of them were first identified by Kolawole et al. (2018) using aeromagnetic data (e.g., SMF, KPF, and MF, see Fig. 4c). The rose diagram shows a main ~NW-SE trend for buried faults (330° – 339°) and a mean azimuthal vector of 329.2° ± 09.5° (Fig. 4c). The NW-striking buried faults are parallel to the surface expression of normal faults that correspond to the KFZ and foliation planes of the MuSZ (Fig. 4c). Most of the hot springs in the Karonga region are aligned with these normal faults and foliation planes of the MuSZ (white arrows in Fig. 4c). We also identified for the first time ~NE and NW-striking buried structures (black arrows in Fig. 4c) in the southeast coastal plain of the study area that follows the same trends as the Karoo basins and the NW-striking surface expressions of normal faults, respectively. Additionally, seven undifferentiated buried fractures in the Karonga region were revealed from the tilt-angle derivative map and are in the Nyika Plateau (black dashed lines in Fig. 4c). The general orientation of these fractures is ~NNE-SSW strike with a mean azimuthal vector of 025.2° ± 25.8° (Fig. 4c).

The tilt-angle derivative map helped identify a total of 21 buried faults located near the coast and inland in the Nkhata region (black arrows in Fig. 4d). Most of the buried faults identified have a ~ENE-WSW trend with a mean azimuthal vector of 081.7° ± 25.1° (Fig. 4d). Likewise, we identified 31 undifferentiated buried fractures (black dashed lines in Fig. 4d) from the aeromagnetic tilt-angle derivative map with ~WNW-ESE and ~ENE-WSW trends (280° – 060°) with a similar orientation as the foliation planes and buried faults. Analysis of the rose diagram indicates a mean azimuthal vector of 082.8° ± 07.2° for these undifferentiated buried fractures in the Nkhata region (Fig. 4d). The buried faults and undifferentiated buried fractures are hidden by Quaternary sediments and by pelitic schists, respectively (black arrows in Fig. 4d).

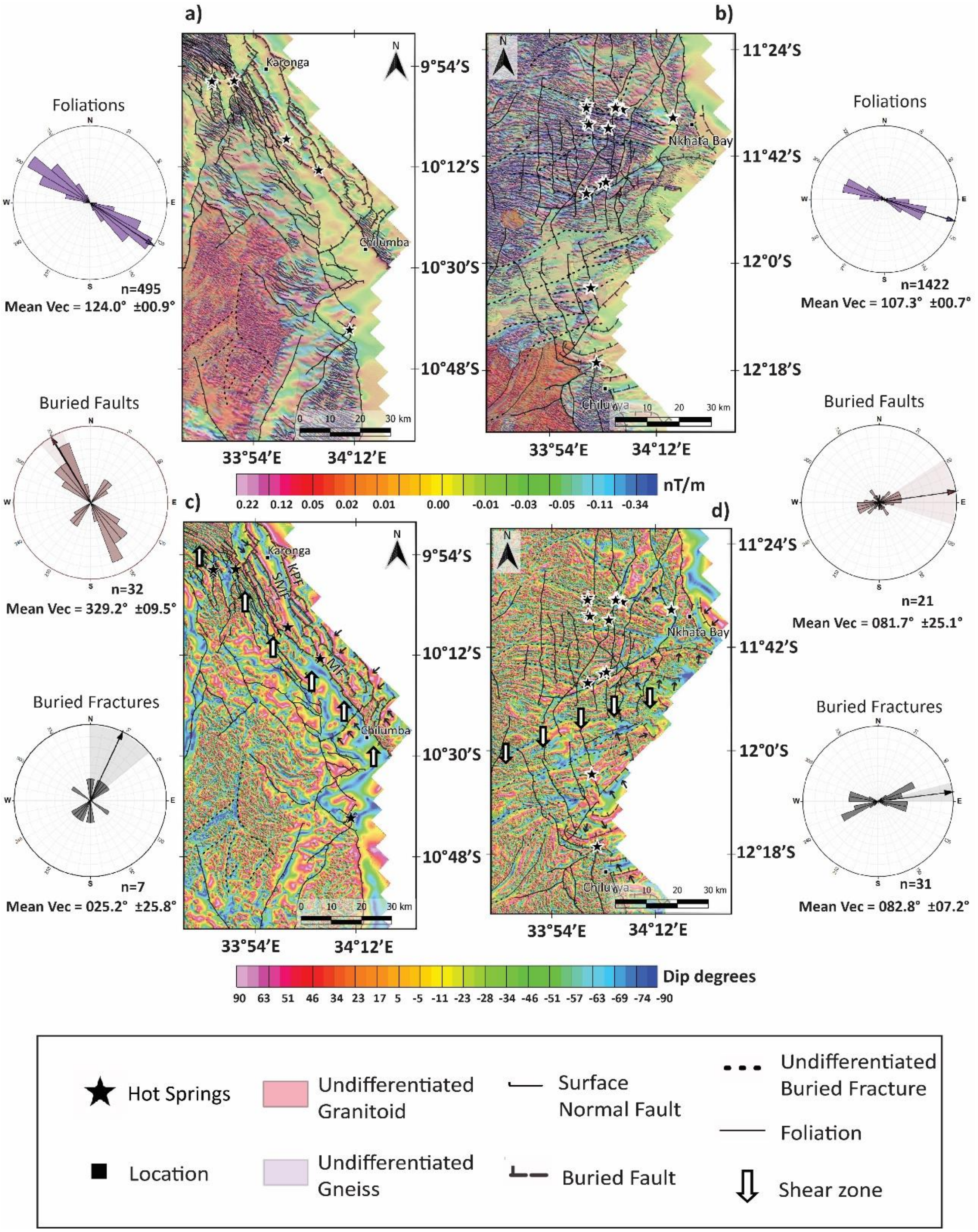

Figure 4. a) and b) Horizontal-Y derivative map of the 2013 aeromagnetic data in the Karonga and Nkhata regions used to identify the magnetic fabric of metamorphic Precambrian rocks,

respectively. c) and d) Tilt-angle derivative map of the Karonga and Nkhata region used to identify buried fractures (Kolawole et al., 2018 and this study) with surface normal faults from the ALOS PALSAR DEM image draped over it, respectively (Fig. 2a and b). Black arrows are showing buried faults. SMF= St. Mary Fault, KPF= Kaporo Fault, and MF= Mbiri Fault. Rose diagrams of the different structures identified from the aeromagnetic data. Mean Vec= Mean Vector.

3.5.2.2 Magnetic basement depths

Figure 5a shows the depth of magnetic sources which range from 0 to 4,937.3 m.b.g.l. in the Karonga region. The greatest depths are mainly found in three different areas in the Karonga region (Fig. 5a): (1) an asymmetric graben located on the east coast with a ~NW-SE trend filled with Cretaceous, Miocene-Pleistocene, and Quaternary sediments which follow the MuSZ and the KFZ (Fig.4c and 5a), (2) the east shoreline of Lake Malawi bounded by the Usisya normal fault with a ~N-S strike and E-dip filled mainly by Quaternary sediments, and (3) ~NE and ~N-striking inland full-grabens and half-grabens filled mainly by Karoo sediments and deposited during the Permian and Triassic (Fig. 1b and 5a). The shallower magnetic sources (Fig. 1b and 5a) are consistent with the metamorphic basement outcrops (Fig. 1b), and the syenite-granite of the Nyika Plateau in the southwestern part of the study area.

Previous studies indicate a standard accuracy of ±20% for the SPI method when compared with data sets from boreholes (e.g., Gay, 2009; Salako, 2014). Our results of the magnetic basement depths estimated from the SPI aeromagnetic method are generally consistent with the seismic basement depths estimated from seismic profiles by Accardo et al. (2018) and Shillington et al. (2020). The control point values used in this study to compare seismic and magnetic data show a similar accuracy of ±20% in 11 control points in the Karonga region (Fig. 5b).

The magnetic basement depth in the Nkhata region ranges from 0 to 4,918.3 m.b.g.l. (Fig. 5c). The highest magnetic source depths are found in three areas: (1) the eastern coastline of the Lake Malawi bounded by the southern continuation of the Usisya normal fault with a ~N-S strike and E-dip that is filled primarily by Quaternary sediments, (2) an ~ENE-trending region found in the central part of the study area that follows the MwSZ (Fig. 4d and 5c), where pelitic schists are deposited (Fig.1b), and (3) the ~NNE-SSW and ~NNW-SSE trends found in the southeastern part of the coastline of the study area (Fig. 5c), which correspond to the E-dipping Bandwe half-graben and filled mainly by Quaternary sediments. The shallower magnetic basement depths are consistent with three rock types in the region (Fig. 1c and 5c): (1) the metamorphic gneiss outcrops, (2) the Charnockitic dome, and (3) the Pegmatoid gneiss. Hot springs in the Nkhata region are found in areas between deep and shallow magnetic basement (Fig. 5c) associated with structures in this region (Fig. 4d and 5c).

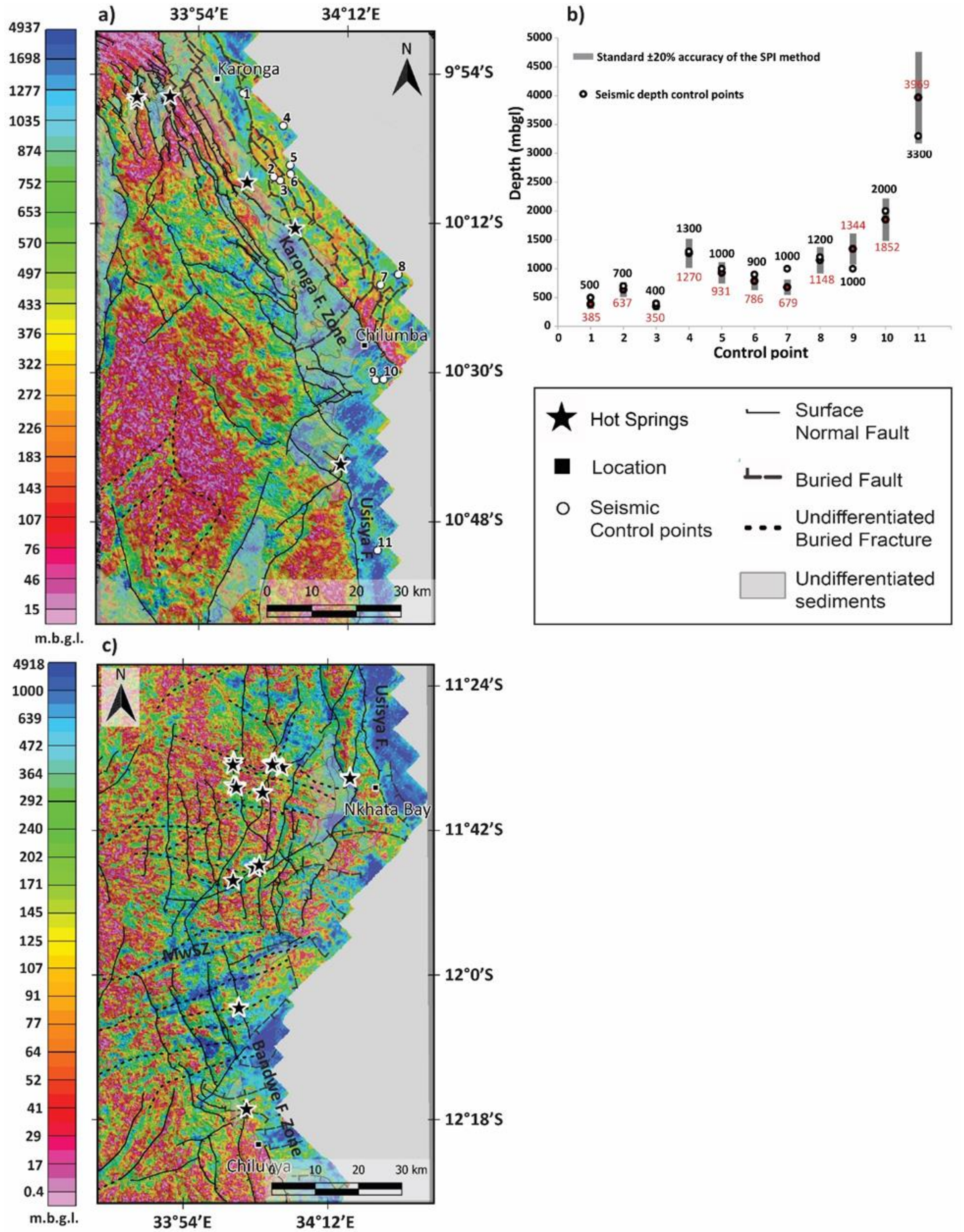

Figure 5. a) and c) Source Parameter Imaging (SPI) method indicating the depth of the magnetic basement in the Karonga and Nkhata region, respectively. b) Chart displays 11 seismic depth control points in Fig. 5a from seismic data by Accardo et al. (2018) and Shillington et al. (2020).

The 11 red points are magnetic basement depths from the SPI method. Gray bars represent the standard ±20% accuracy of the SPI reported by other studies (e.g., Gay, 2009; Salako, 2014).

3.5.3 Fracture network analysis

To investigate the spatial and causal relationship between fractures and hot springs in the Karonga and Nkhata regions, we carried out a geometric, topological, and quantitative analysis of fracture networks. The fracture networks were identified using the ALOS PALSAR DEM image of 12.5 m spatial resolution and high-resolution aeromagnetic data (see sections 4.1 and 4.2). A complex fracture network identified in both areas consists of normal faults, buried faults, undifferentiated buried fractures, regional joints, and reactivated inherited structures, such as foliation planes of Precambrian shear zones. Our results show that the fracture networks in the Karonga and Nkhata region comprise a varying degree of complexity along strike. This structural complexity occurs in favorable zones such as (1) two fault segments coalescing to form hard-linked relays, (2) two different oriented fracture segments intersecting (splays or abuts) against each other, and 3) on the tips of major normal faults. The hot springs are located where one or more of these favorable zones occur.

We created several density maps of fracture intensity proxies to better understand the relationship between these complex zones and the hot springs. These density maps comprise the following: a) surface faults and buried faults (Fig. 6a and 7a), b) surface and buried faults (all faults) and regional joints (Fig. 6b) or all faults and undifferentiated buried fractures (Fig. 7b), and c) all faults and foliation planes (Fig. 6c and 7c). Additionally, Figures 6d and 7d are showing the connectivity node frequency (NC= NX + NY) using all faults and/or undifferentiated buried fractures.

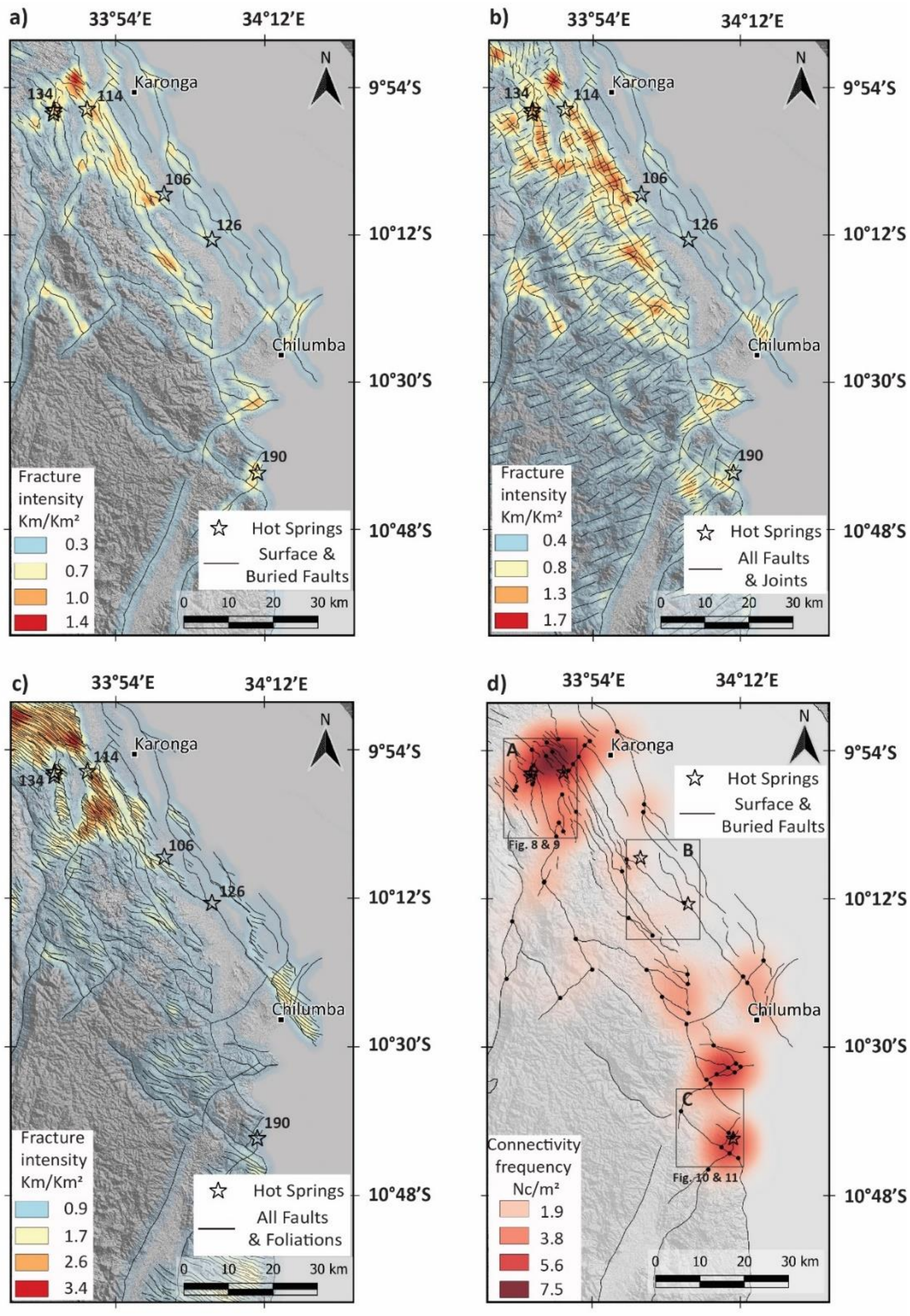

Figure 6. a) Fracture intensity analysis in the Karonga region using surface and buried faults, b) all faults and regional joints, and c) all faults and foliations. Hot springs show reservoir temperatures

(° C) estimated from Na-K geothermometry by Dávalos-Elizondo et al. (2021). d) Fracture connectivity node frequency map in the Karonga region using surface and buried faults. Black rectangles A-C show the areas where hot springs are located, rectangles A and C are used in Fig. 8 – 11.

The fracture intensity proxy density maps in the Karonga region show a range from 0.3 to 3.4 km/km^2. The connectivity node frequency proxy has a range from 1.9 to 7.5 Nc/m^2. We divided the hot springs into three zones to better explain our results, marked as A, B, and C (Fig. 6d). Zone A shows the highest values of fracture intensity and connectivity node frequency, followed by zone C, while zone B shows the lowest values of these proxies. Zone A is dominated by hard-linked relays of normal faults with a general NNW-SSE trend. Our results show that zone B is dominated by isolated and bifurcated NW-striking major normal faults and is in an area of thicker sedimentary cover, which may obscure the results of this analysis. Meanwhile, zone C is dominated by the intersection of three different oriented arrays of normal faults striking NE, NW, and N (Fig. 6d). Zone A and C show the highest number of hot springs, while zone B has fewer hot springs in the area may be due to the thicker sedimentary cover.

The density maps of fracture intensity proxies in the Nkhata region show a range from 0.3 to 2.6 km/km^2 (Fig. 7a-c). The connectivity node frequency proxy shows a range from 2.3 to 9.3 Nc/m^2 (Fig. 7d). Similar to what we did for the Karonga region, we also divided the hot springs in the Nkhata region into four zones, marked as A, B, C, and D (Fig. 7d). Zone B shows the highest values of fracture intensity and connectivity node frequency followed by zone A, while zone C and D show the lowest values of these proxies. Zones A, B, and C are dominated by the intersection of the N-striking normal faults and undifferentiated buried fractures striking ENE-WSW and WNW-ESE. While zone D is dominated by the intersection of a N-striking normal fault and an ENE-striking normal fault (Fig. 7a-d). Zone A and B show the highest number of hot springs, while zone C and D have fewer hot springs (Fig. 7d).

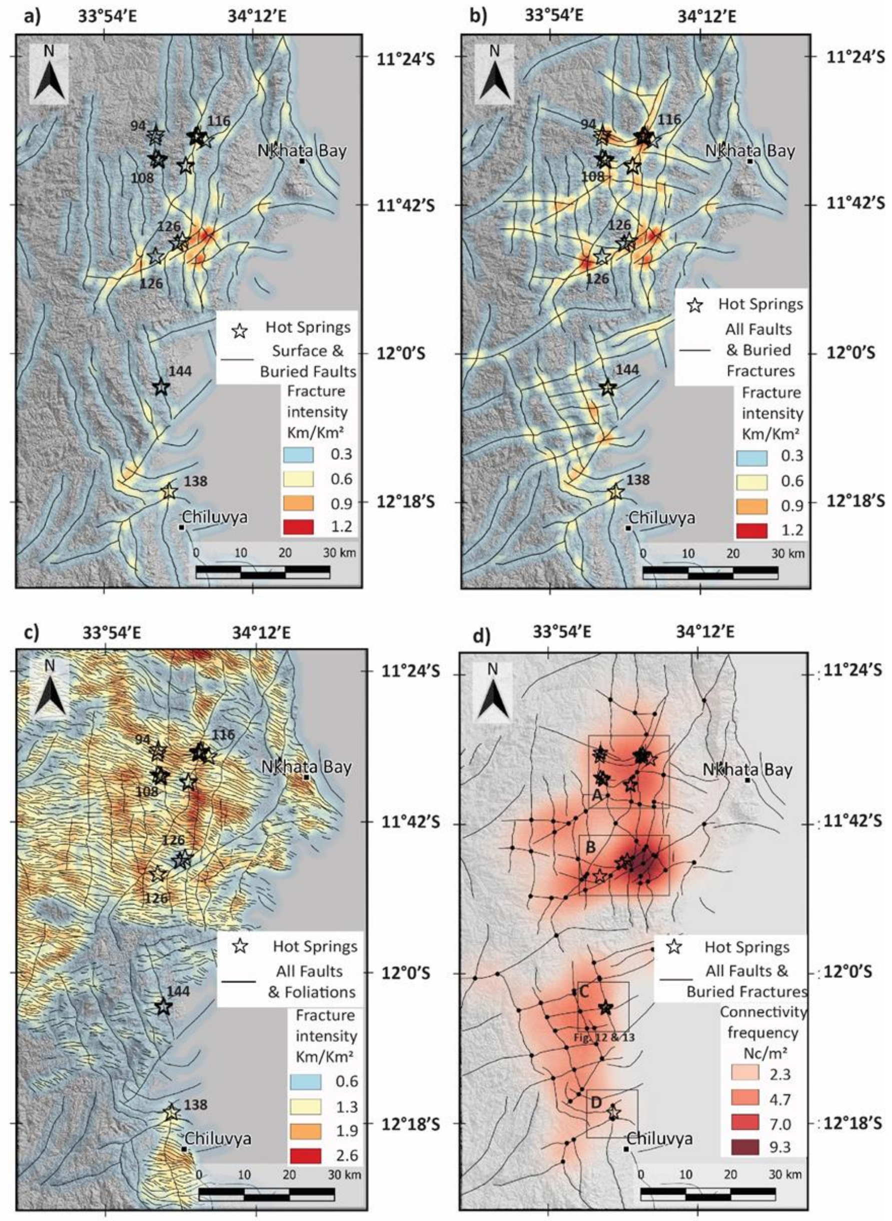

Figure 7. a) Fracture intensity analysis in the Nkhata region using surface and buried faults, b) all faults and buried undifferentiated fractures, and c) all faults and foliations. Hot springs show

reservoir temperatures (° C) estimated from Na-K geothermometry by Dávalos-Elizondo et al. (2021). d) Fracture connectivity node frequency map in the Nkhata region using all faults and buried undifferentiated fractures. Black rectangles A – D show the areas where hot springs are located, rectangles C are used in Fig. 12 and 13.

3.5.4 Geothermal zones analysis

Three areas of interest were selected for further detailed structural analysis based on the results from the ALOS PALSAR DEM images analysis of 12.5 m spatial resolution, the aeromagnetic data analysis (see section 4.1-4.5), and geothermal reservoir temperatures estimated from hot springs in these regions using cation geothermometry (Dávalos-Elizondo et al., 2021). In the Karonga region, we selected zones A and C (Fig. 6d) and named in this study the Mwankenja-Mwesia and the Chiweta geothermal zone, respectively. Likewise, zone C was selected in the Nkhata region (Fig. 7d) and named in this study as the Mtondolo geothermal zone.

3.5.4.1 The Mwankenja-Mwesia geothermal zone

The AW3D DSM image analysis of 2.5 m spatial resolution shows that the Mwankenja and Mbande hot springs lie within major faults that bound the eastern side of ~N-striking narrow basins (Fig. 8a). The remote sensing analysis from the AW3D DEM image shows that sedimentary layers in the Karoo basins are dipping mainly to the east and that the slope angles agree with the published dip angles of around 25° (Fig. 8a and 8b).

The Mwankenja hot springs lie between two subparallel N-striking normal faults hard-linked segments with azimuths of 350° and 360°, respectively (Fig. 8). While the Mbande hot springs are located near the intersection of two subparallel NW-striking normal fault hard-linked segments with azimuths of 323° and 327°, respectively, and a NE-striking normal fault with an azimuth of 044°. The slope degree calculation of the Mwankenja and Mwesia major faults has a minimum dip angle between ~30° – 50° and dipping to the west (Fig. 8b and 8e). The fracture intensity and connectivity node frequency density maps show values from 1.0 to 3.9 km/km^2 and from 1.1 to 3.4 Nc/m^2, respectively (Fig. 8c and 8d).

Figure 8e displays different data extracted from profile C - C’ that crosses from W to E through the hot springs of Mwankenja-3 and Mbande: 1) topographic profile, 2) slope degree calculation, 3) fracture intensity proxy, and 4) fracture connectivity frequency. The topographic profile C - C’ shows the highest elevations between ~800 to 750 m.a.s.l. in the west and central part of the profile, which corresponds to the Mwapu and Mwankenja horst, respectively. The lowest elevation of profile C - C’ ranges from ~510 to 550 m.a.s.l. and it is related to the Mwankenja and Mwesia grabens, where the geothermal waters are located. The topographic profile shows an approximate elevation of 559 m.a.s.l. in the Mwankenja-3 hot spring, while the Mbande hot spring is located at about 519 m.a.s.l. (Fig.8e). The highest values of fracture intensity in profile C - C’ are 3.1 km/km^2 located in the Mwankenja major fault and 2.2 km/km^2 in the Mwesia major fault, both related to the geothermal waters zone. Similarly, the highest connectivity node frequency ranges from 3.0 to 2.59 Nc/m2 and corresponds to the area where geothermal fluids emerge through the Mwankenja and Mwesia major faults, respectively (Fig. 8e). The Mwankenja and Mwesia major faults show a minimum dip of ~37° and ~30° estimated from the slope calculation in profile C – C’ (Fig. 8e).

The Mwankenja-Mwesia geothermal zone was analyzed using the high-resolution aeromagnetic data of the tilt-angle derivative and the SPI method maps. Figure 9a shows the following information: 1) the tilt-angle derivative map, 2) surface faults identified from the AW3D DSM image analysis, 3) foliation planes digitized from the first-order horizontal-Y derivative map (see Fig. 4a), and 4) buried faults identified in our preliminary aeromagnetic analysis from the tilt-angle derivative map (see Fig. 4c).

The tilt-angle derivative map shows negative (-) dip degrees extended with a ~N-S trend related to depressions that correspond to structural grabens (Mwapu, Mwankenja, and Mwesia; see Fig. 8a). In general, the positive (+) dip angles areas correspond to metamorphic rocks (see Fig. 8a). Likewise, the tilt-derivative map shows ~NW-striking magnetic lineaments corresponding to foliation planes that alternate between (+) to (-) dip angles. This magnetic fabric forms part of the NW-trending MuSZ (see Fig. 4c). The Mwankeja hot springs lie in the intersection between N-striking normal faults segments identified from the AW3D DEM image, and NW-striking foliation planes with an azimuth of 306° identified from the aeromagnetic data. Likewise, the Mbande hot springs lie in the intersection between NW-striking normal faults segments, NE-striking normal fault identified from the AW3D DEM image, and NW-striking foliation planes with an azimuth of 314° identified from the aeromagnetic edge-enhancement directional filter maps.

Figure 9b displays the results of the SPI method corresponding to the magnetic basement depth calculation and normal faults identified from the AW3D DSM image analysis. Our results show that the magnetic basement depth in the Mwankenja-Mwesia geothermal zone varies mainly from ~0 to 2500 m.b.g.l. with an average value of 441.8 m.b.g.l. and a median value of 323.2 m.b.g.l. The hot springs are found in areas where the magnetic basement depth is changing from shallow (red color in Fig. 9b) to deeper depths (blue color in Fig. 9b). The deepest magnetic basement depth corresponds to the Mwesia graben, followed by the Mwapu and Mwankenja grabens (see Fig. 9b)

Additionally, we extracted the following information along profile C - C’ that passes through the hot springs in Fig. 9: 1) topography, 2) tilt-angle, and 3) SPI depth. The tilt-angle derivative data along profile C – C’ shows the 0° tilt angle contour corresponds approximately to the edge of the major faults in the topographic profile (see Fig. 9c and 9d). The lower elevations (Mwankenja and Mwesia grabens) in the topographic profile are consistent with (-) tilt-angles and deeper magnetic basement depths (Fig. 9c-e). The Mwankenja-3 hot spring shows an approximate tilt-angle value of -45° and SPI depths of ~670 m.b.g.l. The Mwande hot spring has a tilt-angle of approx. -11° and ~130 m.b.g.l. of the magnetic basement depth (Fig. 9d and 9e). Additionally, profile C - C’ shows a maximum magnetic basement depth of ~1050 m.b.g.l. in the Mwapu basin, ~955 m.b.g.l. in the Mwankenja basin, and ~2400 m.b.g.l. in the Mwesia basin.

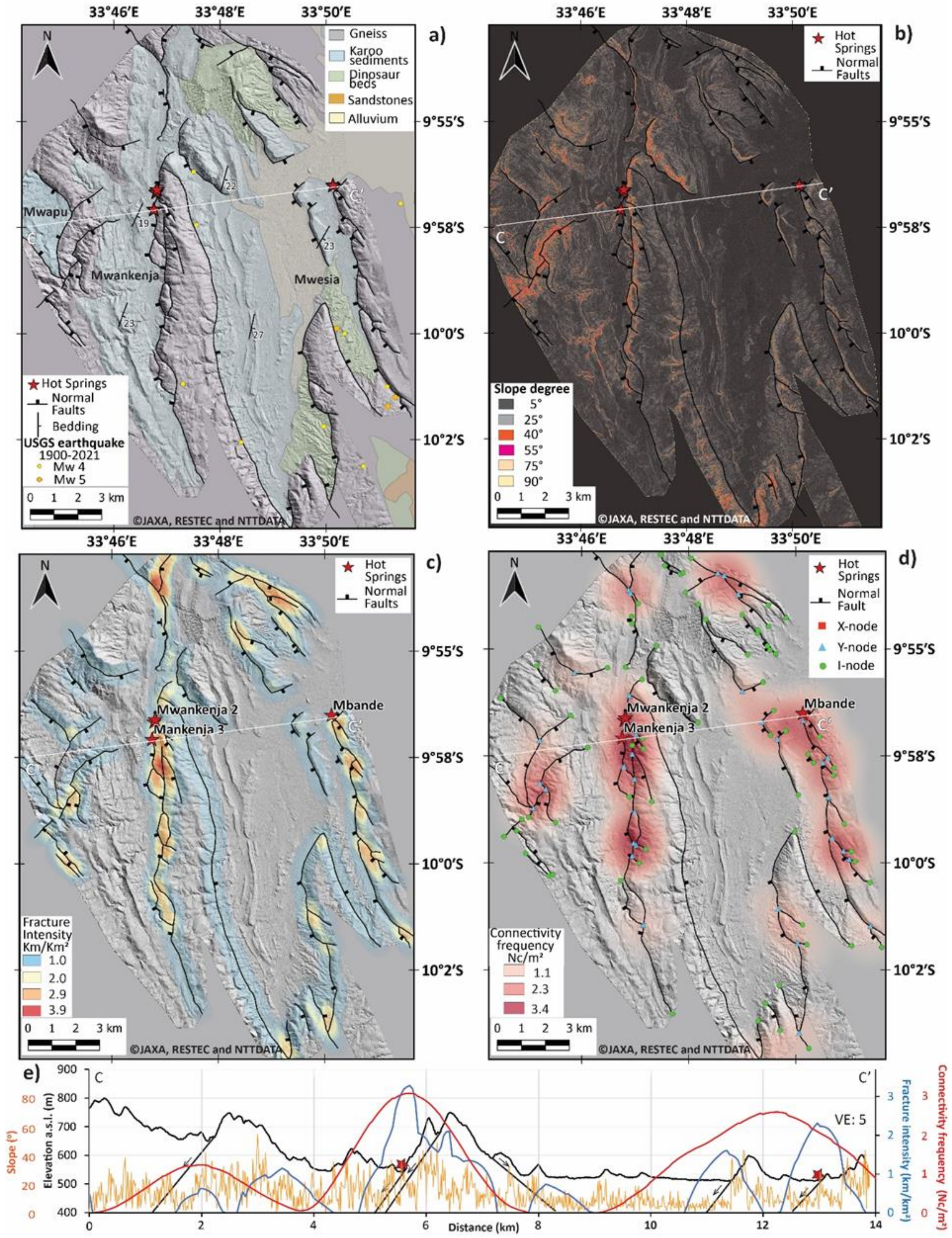

Figure 8. a) Mwankenja-Mwesia geothermal zone geological map (modified after Bloomfield, 1968, Biggs et al., 2010, and this study) and normal faults digitized and updated from the AW3D DSM image 2.5 m spatial resolution. b) Slope angle calculation (Az°) and normal faults. c) Fracture

intensity analysis using the surface faults from the AW3D DSM image. d) Connectivity node frequency map using the surface normal faults and showing the different types of nodes (I-, Y-, and X- nodes). e) Profile C – C’ showing the topography and normal faults, slope angle (Az°), fracture intensity proxy, and fracture connectivity proxy.

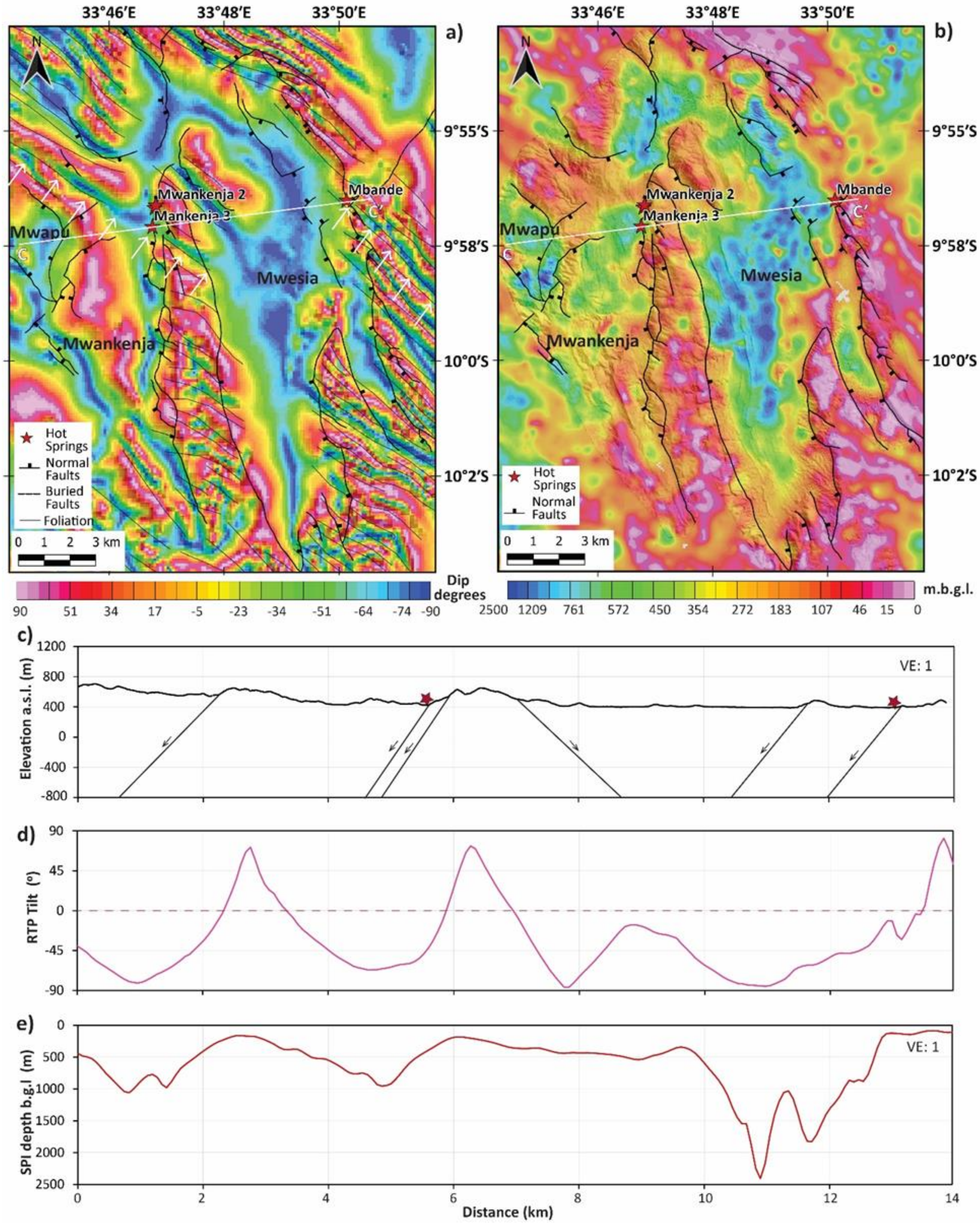

Figure 9. a) Tilt-angle derivative map of the Mwankenja-Mwesia geothermal zone showing the

foliation planes identified from the horizontal-Y derivative map (Fig. 4a), normal faults from the AW3D DSM image, and buried fractures from the Tilt-angle derivative map. b) SPI magnetic basement depth map and normal faults from the AW3D DSM image. c) Profile C – C' showing the topography in meters above sea level (m.a.s.l.) and normal faults, d) the tilt-angle derivative and the 0° contour, e) the SPI magnetic basement depth in meters below ground level (m.b.g.l.).

3.5.4.2 The Chiweta geothermal zone

Remote sensing analysis using AW3D DSM image of 2.5 m spatial resolution shows that the Chiweta geothermal zone is within an ~NNE-striking half-graben formed during Karoo rifting (Fig. 1b) intersected by ~NW-striking normal faults of the Cenozoic rifting (Fig. 10a). The Chiweta geothermal zone shows a complex array of fracture networks with different strikes. The remote sensing analysis from the AW3D DEM image shows that sedimentary layers in the Karoo basin are dipping east and west and that the slope angles agree with the published dip angles between 5 ° to 40 ° (Fig. 10a and 10b).

The result of the high-resolution remote sensing analysis revealed that the Chiweta hot springs lie in the intersection between a NW-striking normal fault with an azimuth of 309° and NNE-striking normal faults with azimuths of ~ 018° - 042° (Fig. 10a). The slope degree calculation shows that most normal faults have a minimum dip angle range from ~40 to 75° (Fig. 10b and 10e). Fracture intensity and connectivity frequency values range from 1.1 to 4.2 km/km^2 and from 1.4 to 4.1 Nc/m^2, respectively (Fig. 10c and 10d).

Figure 10e displays data extracted from profile D - D′, which passes through the Chiweta hot springs from SW to NE: 1) topography profile, 2) slope angles, 3) fracture intensity proxy, and 4) fracture connectivity proxy. The topography values along profile D - D′ show the highest elevation in the western and central part with an elevation range of ~1097 to 831 m.a.s.l. The lowest elevations are found in the eastern part of the profile and range from ~478 to 573 m.a.s.l. (Fig. 10e). The Chiweta hot springs are emerging from an elevation of ~495 m.a.s.l. The highest fracture intensity in profile D – D′ ranges from ~1.5 to 3.0 km/km^2 and the area where the hot springs emerge has an approximate value of 2.0 km/km^2 (Fig. 10e). The highest fracture intensity values in profile D – D′ are consistent with the fault scarps across profile D – D′ (Fig. 10e). Likewise, the highest connectivity node frequency ranges roughly from ~3.7 to 3.5 Nc/m^2 and agrees with the location of the hot springs (Fig.10e). The NW-striking major fault from where the hot springs emerge has an estimated minimum dip angle of ~54° (Fig.10e).

The tilt-angle derivative map in Fig. 11a shows the faults identified from the AW3D DSM image analysis. In addition, the tilt-angle map in Figure 11a shows foliations planes digitized from the first-order horizontal-Y derivative map in our previous analysis (Fig.4a). The tilt-angle derivative map reveals an extended area with negative (-) dip degrees along with a ~NNW-SSE trend (white arrows in Fig. 11a) that follows the same orientations of the foliation planes and NW-striking major faults that intersect ~NE-striking major faults (white arrow in Fig. 11a). Likewise, the aeromagnetic edge-enhancement filter analysis shows a buried N-striking major normal fault with an azimuth of 353° (gray dashed line in Fig. 11a) intersecting the previously mentioned NW and NE-striking normal faults.

Figure 11b displays the results of the SPI method showing the magnetic basement depth and normal faults and buried faults from the previous remote sensing and aeromagnetic analysis. The magnetic basement depth mainly ranges from ~0 to 3,000 m.b.g.l. with an average value of 974.7m.b.g.l. and a median value of 803.4 m.b.g.l. in the Chiweta geothermal zone. The SPI depth map shows that the hot springs are found in a zone between two regions with NW-SE and N-S trends that display deeper magnetic basement depths (blue color in Fig. 11b).

Profile D – D’ crosses the Chiweta hot springs area from southwest to northeast (Fig. 11 c-e) and displays a topographic profile, the tilt-angle derivative, and the magnetic basement depth. The tilt-angle derivative data along the profile shows the 0° tilt angle contour corresponds approximately to the edge of the major faults in the topographic profile (Fig. 11d and 11c). Negative (-) dip angles coincide with deeper magnetic basements depths (Fig. 11d and 11e). The results of the SPI data extracted from profile D – D’ show three depressions where the magnetic basement depth is deeper than 600 m.b.g.l. (Fig. 11e). The Chiweta hot spring lies in an area with a tilt angle value of approximately -30° and SPI depths of ~700 m.b.g.l. (Fig. 11e). The deepest magnetic basement area along profile D – D’ has a depth of ~2,460 m.b.g.l. and it is located on the west side of Lake Malawi and the hot springs area (Fig. 11c-e). The Chiweta hot springs are found in an area where the magnetic basement depth is changing from shallow (green colors in Fig. 11b) to deeper depths (blue color in Fig. 11b).

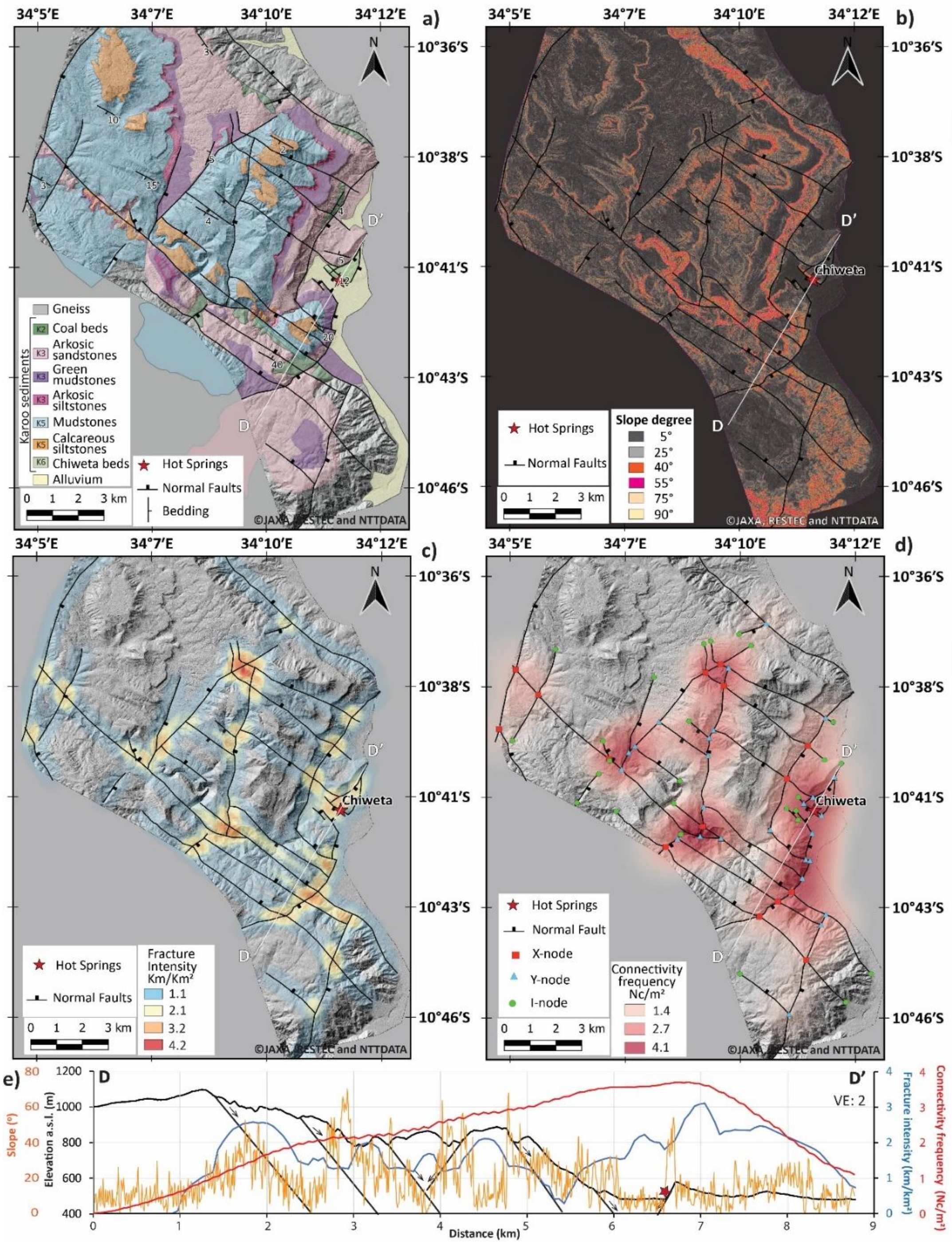

Figure 10. a) Chiweta geothermal zone geological map (modified after Kemp, 1975, and this study) and normal faults digitized and updated from the AW3D DSM image 2.5 m spatial resolution. b) Slope angle calculation (Az°) and normal faults. c) Fracture intensity analysis using the surface faults from the AW3D DSM image. d) Connectivity node frequency map using the surface normal faults and showing the different types of nodes (I-, Y-, and X- nodes). e) Profile D – D′ showing the

topography and normal faults, slope angle (Az°), fracture intensity proxy, and fracture connectivity proxy

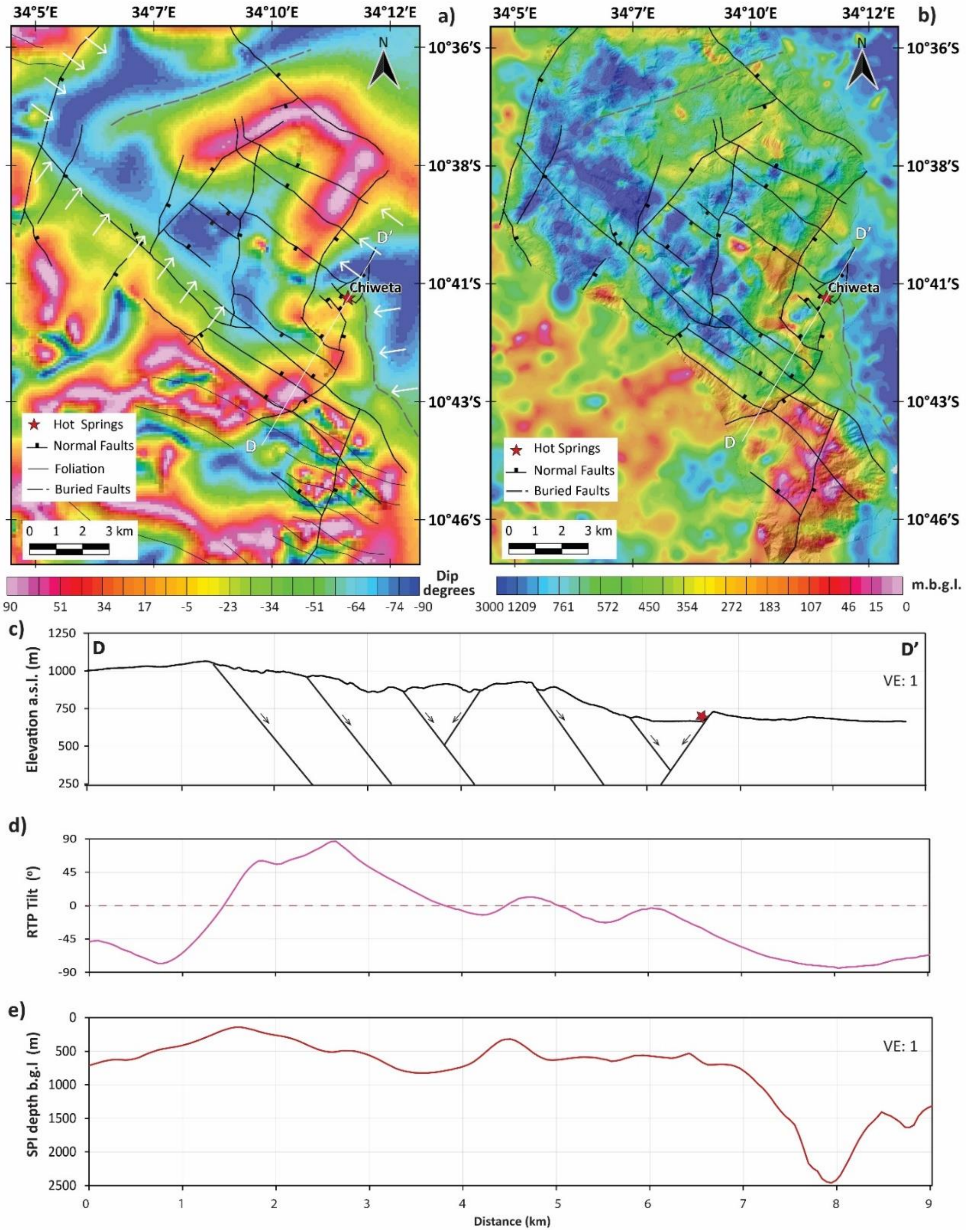

Figure 11. a) Tilt-angle derivative map of the Chiweta geothermal zone showing the foliation planes identified from the horizontal-Y derivative map (Fig. 4a), normal faults from the AW3D

DSM image, and buried fractures from the Tilt-angle derivative map. b) SPI magnetic basement depth map and normal faults from the AW3D DSM image. c) Profile D – D’ showing the topography in meters above sea level (m.a.s.l.) and normal faults, d) the tilt-angle derivative and the 0° contour, e) the SPI magnetic basement depth in meters below ground level (m.b.g.l.).

3.5.4.3 The Mtondolo geothermal zone

The AW3D DSM image analysis of 2.5 m spatial resolution shows that the Mtondolo hot springs are found at the intersection between an NNW-striking and E-dipping major fault with an azimuth of 345°, a WNW-striking and S-dipping minor fault with an azimuth of 296°, and an E-striking and N-dipping minor fault with an azimuth of 082° (Fig. 12a).

The slope angle estimate from the AW3D DSM image shows fault scarps with minimum dip angles ranging from 30° to 55° (Fig. 12b). The values of fracture intensity and connectivity frequency range from ~0.8 to 3.4 km/km^2 and from ~2.6 to 7.8 Nc/m^2, respectively (Fig. 12c and 12d). Profile E – E’ crosses the Mtondolo hot springs area from southwest to northeast and displays data on the topographic profile, slope angles, fracture intensity, and fracture connectivity (Fig. 12e). The topography profile shows the highest elevation in the western part with values ranging from ~1,176 to 956 m.a.s.l. (Fig. 12e). The lowest elevations along profile E -E’ range from ~520 to 589 m.a.s.l. The Mtondolo hot springs are emerging from approximately ~549 m.a.s.l. The highest fracture intensity values along profile E – E’ range from ~3.35 to 1.27 km/km^2, while the highest connectivity node frequency ranges between ~3.67 and 1.67 Nc/m^2 (Fig. 12e). The

Mtondolo hot springs area has a fracture intensity of ~2.6 km/km^2 and a connectivity frequency of ~3.43 Nc/m^2 (Fig. 12e). The NNW-striking major fault from where the Mtondolo hot springs emerge has an estimated minimum dip angle of ~32° (Fig. 12e).

Figure 13a displays the 1) tilt-angle derivative map, 2) normal faults identified from the AW3D DSM image, 3) foliation planes digitized from the horizontal-Y derivative map, and 4) undifferentiated buried fractures identified from the tilt-angle derivative map (Fig. 4d). The tilt-angle derivative map shows highly restricted areas with negative (-) dip degrees that correspond to magnetic foliation lineaments (Fig. 8a, 11a & 13a). The Mtondolo hot spring is found within a (-) dip degree E-striking magnetic lineament with an azimuth of 077° (white arrow in Fig. 13a). This buried E-striking magnetic lineament is intersected by a major N-striking and E-dipping fault (345°), and two WNW and E-striking minor faults (296° and 082°, respectively) identified from the AW3D DSM image analysis (Fig. 13a).

Figure 13b displays the results of the SPI magnetic basement depth estimations and the normal faults from the AW3D DSM image. The magnetic basement depth in the Mtondolo geothermal zone mainly ranges from ~0 to 3,000 m.b.g.l. with an average value of 522 m.b.g.l. and a median value of 330.5 m.b.g.l. The deepest magnetic basement depths are found in the northern and southern parts of the study area (Fig. 13 b). The Mtondolo hot springs, similar to the Mwankenja and Chiweta hot springs, are located in an area where the magnetic basement depth is changing from shallow (red and green colors in Fig. 13b) to deeper depths (blue colors in Fig. 13b).

Profile E – E’ was used to compare the information of the topography, the tilt-angle derivative, and the SPI method where it crosses the Mtondolo hot springs (Fig. 13 c-e). The tilt-angle derivative along profile E – E’ shows the 0° tilt angle contour, which corresponds to the edges of the N-striking major faults (Fig. 13d). The magnetic (-) sign shown in the tilt-angle profile matches with areas where the magnetic basement becomes deeper (see Fig. 13d and 13e). The Mtondolo hot springs are found where the magnetic basement has an approximate depth of ~378.1 m.b.g.l. (Fig. 13e). Three areas of a deeper magnetic basement are revealed in profile E - E’ with depths of 561, 483, and 600 m.b.g.l. (from left to right Fig. 13e).

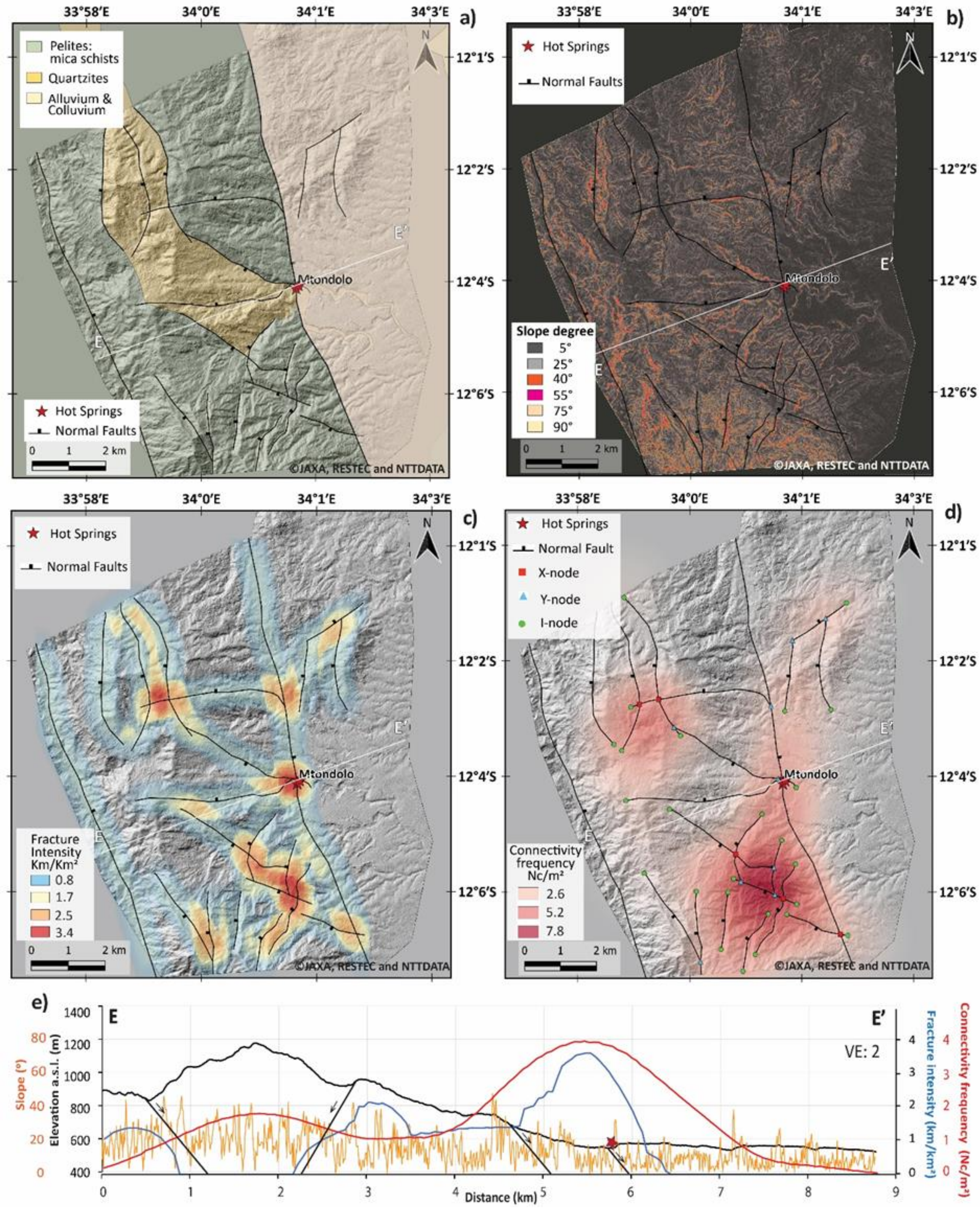

Figure 12. a) Mtondolo geothermal zone geological map (modified after Bloomfield, 1968, and this study) and normal faults digitized and updated from the AW3D DSM image 2.5 m spatial resolution. b) Slope angle calculation (Az°) and normal faults. c) Fracture intensity analysis using the surface faults from the AW3D DSM image. d) Connectivity node frequency map using the surface normal faults and showing the different types of nodes (I-, Y-, and X- nodes). e) Profile E

– E' showing the topography and normal faults, slope angle (Az°), fracture intensity proxy, and fracture connectivity proxy.

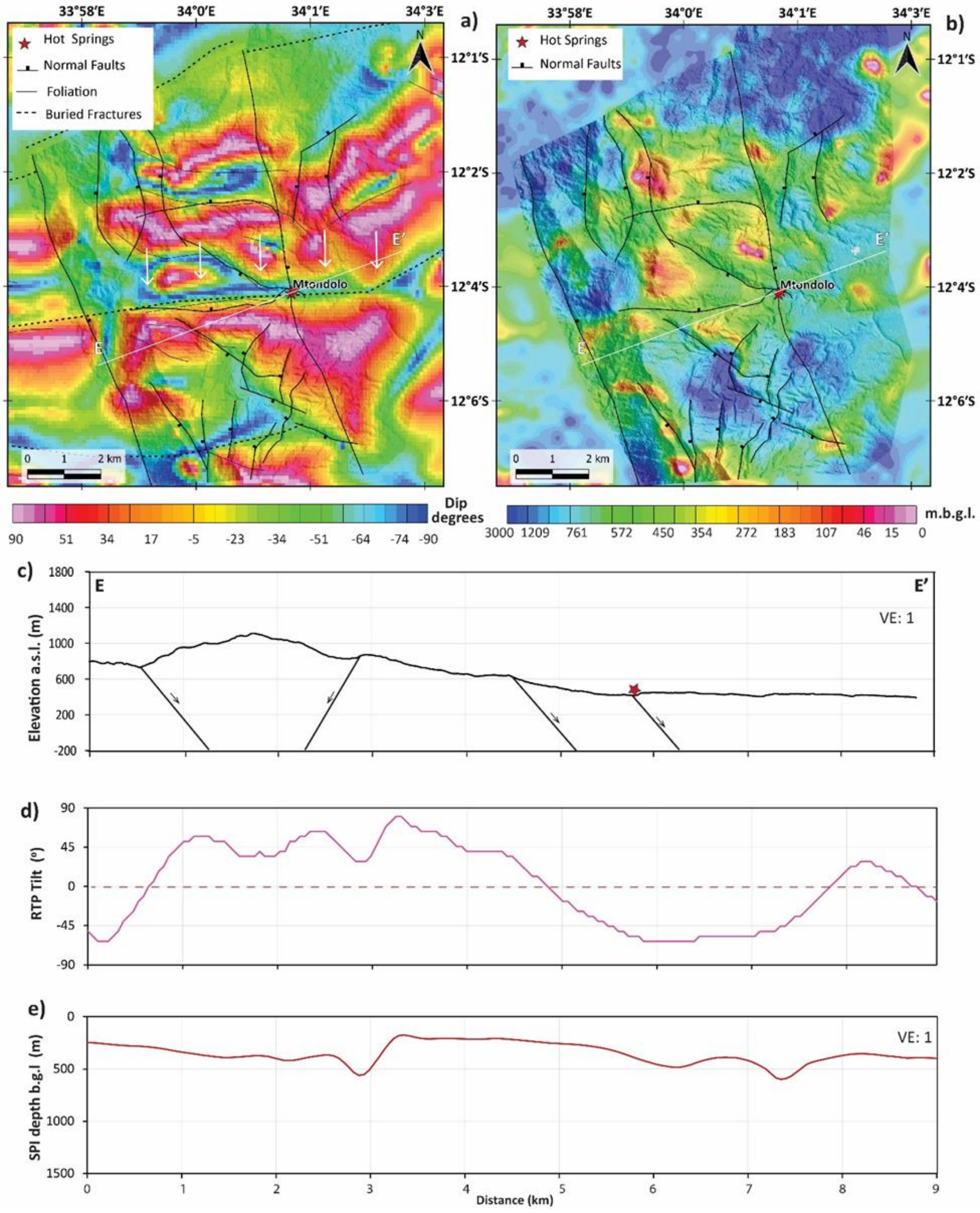

Figure 13. a) Tilt-angle derivative map of the Chiweta geothermal zone showing the foliation planes identified from the horizontal-Y derivative map (Fig. 4b), normal faults from the AW3D

DSM image, and buried undifferentiated fractures from the Tilt-angle derivative map. b) SPI magnetic basement depth map and normal faults from the AW3D DSM image. c) Profile E – E’ showing the topography in meters above sea level (m.a.s.l.) and normal faults, d) the tilt-angle derivative and the 0° contour, e) the SPI magnetic basement depth in meters below ground level (m.b.g.l.).

3.6 Discussions

3.6.1 Favorable settings and Spatial arrangement

The active regional tectonism of the Cenozoic rifting event appears to be the primary driving force for geothermal activity in the MRZ, as evidenced by the active normal faults and the distribution of hot springs aligned to these structures along the rift (Fig. 1a). Our findings show that the hot springs are clustered at the surface into specific zones where the major normal faults of the active Cenozoic rifting intersect the Precambrian Shear Zones (MuSZ: NW-SE strike and MwSZ: ENE-WSW strike) and/or Paleozoic structures of different orientations in the Karonga and Nkhata region (Fig. 1).

The MRZ was divided into first order and second order segments into previous studies (e.g., Ebinger et al., 1987; Laó-Dávila et al., 2015). The northern portion of the rift is the only section that presents second-order segmentation, and this study focuses on this part of the rift. The second-order segmentation is divided into four half-grabens/asymmetrical grabens (Laó-Dávila et al., 2015) and the Karonga and Nkhata regions form part of two of these favorable structures that alternate polarities (Fig. 1a).

Some of the hot springs in the MRZ appear to be in these favorable areas of changing polarity within overlap zones associated with alternating border fault segments (Fig. 1a).

3.6.1.1 Favorable settings of the Karonga region

The Karonga geothermal region in the MRZ is within the hinge zone of a half-graben, bound on the east by the Livingstone border fault, which strikes N060°W and dips to the southwest (e.g., Kolawole et al., 2018). The hinge zone presents active brittle deformation evidenced by the occurrence of earthquake swarms, which most recently occurred in 2009 and 2014 (e.g., Biggs et al., 2010; Zheng et al., 2020; Fig. 1b and 8a). This seismic region with active Quaternary faults is suitable for geothermal fluid flow evidenced by several hot springs aligned to these structures.

Our regional assessments of structural controls using ALOS PALSAR images with 12.5 m spatial resolution (Fig. 2a) show that N to NW-striking normal faults related to the Karonga Fault Zone (KFZ) are important structural controls at shallow depths for geothermal fluids in the Karonga region. These Quaternary active NW-striking structures are formed by overlap zones of hard and soft-linked segments (Fig. 2a). Likewise, the aeromagnetic high-resolution data analysis shows that overlap zones of NNW-striking buried faults are located near the shoreline (Fig. 4a and 4c; e.g., Kolawole et al., 2018).

Additionally, our remote sensing and aeromagnetic data analysis suggest that NW-striking Precambrian Mugesse shear zone (MuSZ) and Paleozoic N to NE-striking normal faults (Karoo basins) have been inherited structures reactivated by brittle deformation during the Cenozoic rifting and are permeable structural controls of geothermal fluids at high depths (Fig. 2a and 4c).

3.6.1.2 Favorable setting of the Nkhata region

The Nkhata region is located within an accommodation zone between the Usisya and Bandwe asymmetrical grabens (e.g., Láo Dávila et al., 2015). Our findings demonstrate that N to NNW-striking normal faults formed during the Cenozoic rifting are important structural controls for geothermal fluids at shallow depths.

Also, we suggest based on the results of the aeromagnetic data analysis that reactivated ENE and WNW-striking fractures that follow the foliation planes of the MwSZ (Fig. 4b) and WNW and ENE-striking undifferentiated buried fractures are important structural controls for geothermal fluids at great depths. Therefore, most of the hot springs in the Nkhata region emerge from the intersection of the N-striking normal faults formed by the Cenozoic rifting and WNW-striking reactivated structures (e.g., foliation planes) and/or ENE-striking undifferentiated fractures related to the MwSZ (Fig. 4b and 4d).

3.6.2 The role of inherited structures in the geothermal systems

Even if the Cenozoic rifting is considered the primary driver of active geothermal systems in the MRZ, inherited structures also play an important role in the geothermal systems in the MRZ. As we already mentioned in the last section, our findings show that possible reactivated inherited structures that follow foliation planes of the Precambrian shear zones and Paleozoic-Mesozoic faults formed during previous rifting events are controlling the geothermal fluid flow and storage at depth (Fig. 4). We interpreted that foliations of ductile shear zones are planes of weakness that have been reactivated by brittle deformation during different tectonic events and continue actively during the present rifting. These inherited reactivated structures following the foliation planes are enhancing permeability and help store and circulate the geothermal fluids at depth.

Previous studies have suggested that reactivation of the Precambrian foliation planes and Paleo-Mesozoic faults control the strike and height of the Quaternary border faults in the MRZ (e.g., Versfelt & Rosendahl, 1989; Delvaux, 1991; Ring, 1994; Ring et al., 2002; Laó-Dávila et al., 2015; Dawson et al., 2018; Kolawole et al., 2018). Other studies reported the presence of ore mineral deposits in the Precambrian shear zones, such as the one reported by Bjerkgard et al. (2009) in the Niassa Gold Belt in Mozambique with an age of 483 ± 72 Ma from gold-bearing quartz veins. The study by Bjerkgard et al. (2009) evidence the presence of fossil geothermal systems controlled by these shear zones. Likewise, Hopper et al. (2020) mentioned the possibility of partial melting present in these Precambrian sutures.

Our aeromagnetic data results show a strong correlation between the location of hot springs and the Precambrian shear zones (Fig. 4). For instance, the hot springs in the Mwankenja-Mwesia geothermal zone are in major border normal faults of Paleozoic-Cenozoic sedimentary basins at the surface, while the tilt-derivative angle image shows that hot springs are also correlated with high-magnetic foliation lineaments (Fig. 9a).

Therefore, our results support the claim that inherited structures are important planes of weakness that have been reactivated and increase permeability for geothermal fluids at depth in the MRZ. However, more studies need to be conducted in terms of estimation of the local stress field, and slip/dilation tendency analysis to determine the reactivation potential of these inherited structures. Additionally, more studies are needed to understand the role of geothermal fluids as drivers of slip tendency due to the increment of pore fluid pressure in the rocks.

3.6.3 Structural complexity and potential permeable zones

The fracture networks analysis performed in this study demonstrates the presence of structural complexity in the Karonga and Nkhata regions (Fig. 1 and 4). Most of the hot springs in the MRZ are within structural complexity favorable zones such as (1) two faults segments that coalesce to form hard and soft-linked relays, (2) two different oriented fracture segments that intersect (splays or abuts) against each other, and 3) on the tips of major normal faults.

Also, geothermal systems around the world most commonly occur in these extensional favorable settings of fault tips, overlapping and/or intersecting faults, such as the Great Basin in the U.S.A. (e.g., Faulds et al., 2006; Faulds & Hinz, 2015) and the Taupo volcanic zone in New Zealand (e.g., Rowland & Simmons, 2012). Likewise, other studies have mentioned the importance of secondary structures near fault tips, and other structural complex zones such as relay ramps and fault intersections as fluid flow conduits along active faults (e.g., Martel, 1990; Kattenhorn et al., 2000; Tamagawa & Pollard, 2008).

Our results also demonstrate that higher fracture intensity and connectivity are proxies of permeable zones that could be associated with geothermal fluids. This claim is supported by the fact that most of the hot springs in the Karonga and Nkhata region are in high fracture intensity and connectivity frequency zones related to major Quaternary faults that traverse Precambrian and Paleozoic-Mesozoic structures of different orientations (Fig. 6 and 7). Likewise, other studies such as Gartrell et al. (2004) and Dimmen et al. (2017) suggested that structurally complex areas of high fracture intensity and connectivity tend to act as fluid flow conduits.

Additionally, our finding shows that high intensity and connectivity, as well as other parameters such as low-high magnetic basement depth transition zones, low-high tilt-derivative angle transition zones, and high slope angles (Fig. 8, 9, 10, and 11), could be used as indicators to identify other permeable zones. The detection of other permeable zones may help find hidden geothermal systems in the MRZ. Our methods can be combined with other techniques such as the ones described by Addison et al. (2021) who used chemical proxies and groundwater data to identify hidden hot springs as a source of groundwater fluoride in the southern part of Malawi. Finally, as the geothermal exploration advances and geothermal wells are drilled, additional information about the permeable zones at the subsurface will be acquired for advancing the knowledge of these structural geothermal systems.

3.6.4 Geothermal conceptual models of selected areas

Our results support the argument that geothermal systems in the Western Branch, specifically in the MRZ are heated by deep-circulation along structures that penetrate to depths of several km into Precambrian crystalline basement rocks (e.g., Omenda et al., 2016; Hinz et al.,2018; Dávalos-Elizondo et al., 2021). High-temperature geothermal fluids are hosted in fractured upflows at depth and mix with cool-water aquifers mainly in sedimentary basins to produce low-temperature fluid outflows (e.g., Hinz et al., 2018; Dávalos-Elizondo et al., 2021).

Our study suggests that the Mwankenja-Mwesia, Chiweta, and Mtondolo geothermal zones are structurally controlled geothermal systems mostly in sedimentary basins, but there are also other geothermal systems stored in aquifers of fractured Precambrian rocks (Fig. 1). Furthermore, previous studies suggested that geothermal systems in the MRZ are non-magmatic (e.g., Hinz et al., 2018). However, the specific heat sources of geothermal systems in Malawi are still uncertain and further studies are needed to determine them.

Njinju et al. (2019) demonstrated the presence of high heat flow (70 – 82 mW/m^2) and high geothermal gradients (29 – 32 °C/km) in certain segments of the rift that could be a possible explanation for a regional heat source. Likewise, it is suggested that the isotopic decay of uranium deposits from Paleozoic-Mesozoic sediments deposited within the Karoo basins can be a possible explanation for the high heat flow presented in some segments of the MRZ (Njinju, 2016). Additionally, seismic studies suggested the presence of a superplume or partial melting of the lithospheric mantle in the northern part of the MRZ (e.g., Accardo et al., 2018; Grijalva et al., 2018; Borrego et al., 2018).

3.6.4.1 Mwankenja-Mwesia geothermal zone

The structural settings of the Mwankenja-Mwesia geothermal zone consist of the Mwapu half-graben, Mwankenja N-striking half-graben, and the Mwesia NW-striking full-graben. These basins have been documented to have been formed during the Karoo rifting and reactivated during the Cenozoic rifting (e.g., Ring, 1995; Dawson et al., 2018). The Permian-Triassic grabens are filled mainly by Karoo sediments that are tilted towards the east (e.g., Ring, 1995). The Mwesia basin has Cretaceous Dinosaur beds overlapping the Karoo sediments in the northern and southern parts of the graben (Fig. 8a).

The hot springs reported in the Mwankenja-Mwesia geothermal zone are the Mwankenja 1-3 and Mbande hot springs (Fig. 8). Dávalos-Elizondo et al. (2021) estimated the geothermal reservoir temperatures of these hot springs from Na-K geothermometry at 117 °C, 134 °C, 135 °C, and 114°C (Mwankenja 1, 2, 3, and Mbande, respectively). Njinju et al. (2019) reported a heat flow of approximately 74 mW/m^2 for this zone.

Our results show that the N-striking Mwankenja (350°) and NW-striking Mwesia (323°) major normal faults are important structural controls of the geothermal fluids evidenced by the presence of the hot springs at the surface. The favorable settings at shallow depths that control the thermal waters of Mwankenja and Mbande are hard and soft-linked fault segments of the Mwankenja and Mwesia normal faults (Fig. 8). Additionally, Mbande hot springs emerge at the intersection of the NW-striking Mwesia major faults and a NE-striking normal fault. The geothermal fluids at greater depths appear to be controlled by reactivated NW-striking structures that follow the foliation planes of the MuSZ. The geothermal fluids are stored within Karoo sedimentary layers (e.g., sandstone) where it is mixed with cold water of shallow aquifers after reaching the surface (Fig. 14a). The maximum estimated basement depth of the Mwankenja and Mwesia basins are ~955 m.b.g.l and ~2400 m.b.g.l. along profile C - C', respectively (Fig. 9e and 14a). Finally, we suggest, based on the SPI method results that the estimated geothermal reservoir depths for the Mwankeja-Mwesia geothermal zone range from ~700 to ~1000 m.b.g.l. (Fig. 9e and 14a)

3.6.4.2 Chiweta geothermal zone

The Chiweta geothermal zone is within a hinge zone of the Karonga half-graben flanked by major faults (Fig. 1a) that have alternating polarities right in the area where the Chiweta hot springs emerge. The accommodation zone between the ~NW-striking Livingstone major fault dipping to the west and the ~N-striking Usisya major fault dipping to the east (Fig. 1b) is a favorable setting for geothermal fluids in this zone (Fig. 1a and 1b; Dávalos-Elizondo & Laó-Dávila, 2019).

The Chiweta geothermal zone lies within an NNE-striking basin formed during the Permo-Triassic Karoo rifting (Fig. 1a and 1b), which is filled by sediments of the Karoo group (K2 to K6; e.g., Kemp, 1975) and overlaid by Quaternary sediments close to the coastline (Fig. 10a). The Chiweta NE-striking basin is intersected by the NW-striking Cenozoic KFZ and reactivated NW-striking structures that follow the foliation planes of the Precambrian MuSZ. Therefore, we suggest that the Chiweta geothermal zone is in an area of high structural complexity related to the intersection of three major faults with NW, NE, and N strikes.

Additionally, the hottest Chiweta hot springs in the MRZ emerge from the intersections of these different oriented structures (e.g., Dávalos-Elizondo et al., 2021). Dávalos-Elizondo et al. (2021) estimated a geothermal reservoir temperature from Na-K geothermometry of ~190 °C in the Chiweta hot springs (Fig. 14b). Njinju et al. (2019) reported a heat flow of approximately 76 mW/m^2 for this zone.

We suggest that geothermal fluids are ascending from depth by NW-striking structures that follow the foliation planes of the MuSZ which may have been reactivated by the Cenozoic rifting. After ascending from depth, the geothermal fluid is stored within Karoo sedimentary layers, where it is mixed with cold water of shallow aquifers before reaching the surface (Fig. 14b). A NW-striking fault SW-dipping and with a minimum dip angle range from 40° to 55° (Fig. 10b and 10c) appears to control at shallow depths the emergence of the hot springs.

The maximum estimated magnetic basement depth of the Chiweta basin is ~2460 m.b.g.l. along profile D - D' (Fig. 11e). Based on the SPI method results, we interpret that the estimated geothermal reservoir depth for the Chiweta geothermal zone is about ~700 m.b.g.l. to ~1000 m.b.g.l. (Fig. 11e and 14b), which agrees with the geothermal reservoir depth of 700 m.b.g.l. reported for the Chiweta geothermal conceptual model by Gondwe et al. (2021).

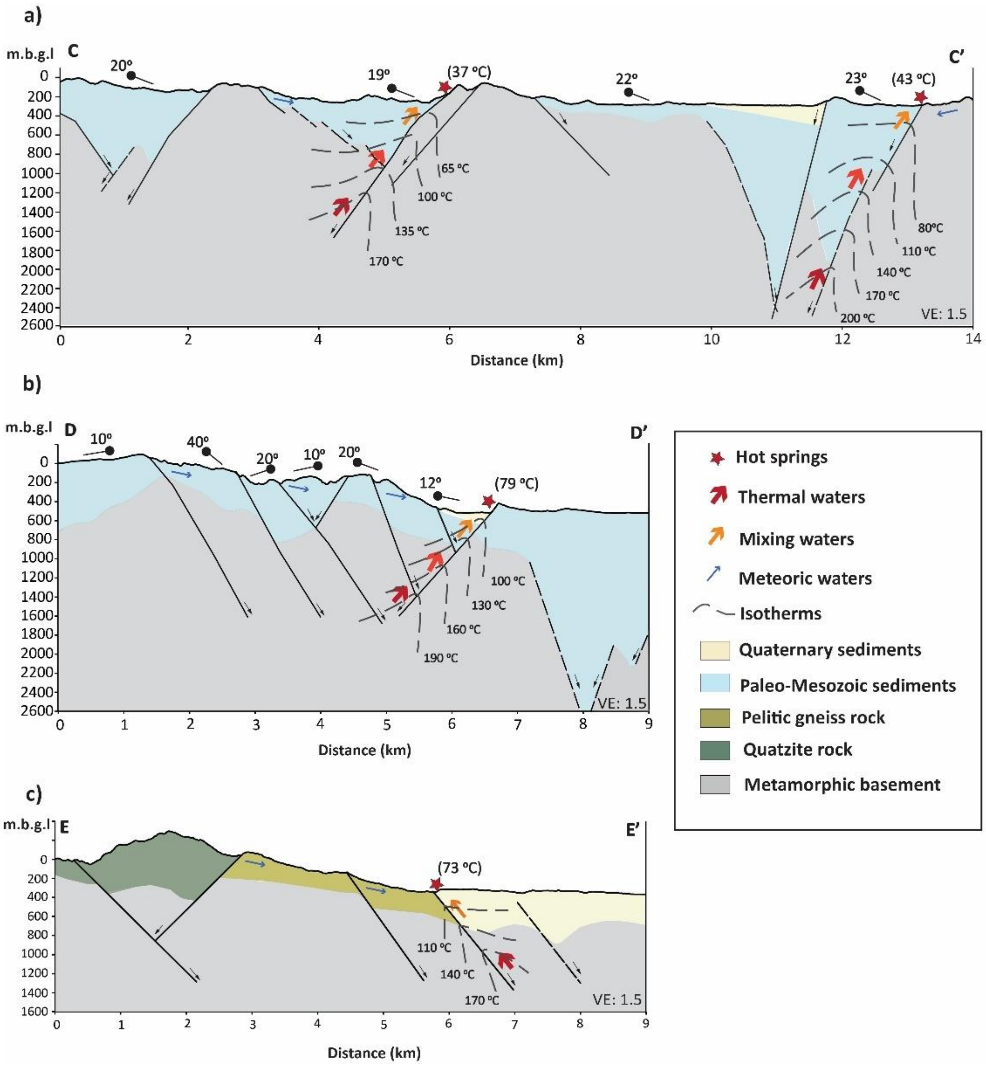

Figure 14. a) Mwankeja-Mwesia geothermal conceptual model. b) Chiweta geothermal conceptual model, and c) Mtondolo geothermal conceptual model. See a more detailed explanation in the text.

3.6.4.3 The Mtondolo geothermal zone

The Mtondolo geothermal zone is located between the Usisya basin and Bandwe basin near the southern tip of the N-striking Usisya major fault and close to the accommodation zone between the Usisya W-dipping half-graben and the Mbamba E-dipping half-graben (Fig. 1a). Additionally, the Mtondolo hot springs are located at the intersection between the Precambrian MwSZ with an ENE-striking and the Cenozoic N-striking border faults formed during the current rifting (Fig. 1a).

The reservoir temperatures estimated in the Mtondolo hot springs from cation geothermometry range between 120 – 140 °C (Dávalos-Elizondo et al., 2021). Njinju et al. (2019) reported a heat flow of approximately 79 mW/m^2 for this zone. The geology of the area is dominated by pelitic gneiss rocks, a quartzite intrusion, and quaternary alluvium and colluvium (Fig. 12a; Bloomfield, 1968).

We suggest that geothermal fluids are ascending from depth along ENE-striking structures that follow the foliation planes of the MwSZ which may have been reactivated by the Cenozoic rifting enhancing permeability at depth. After ascending, the geothermal fluid flows until reaching shallow structures (e.g., Quaternary faults) and is stored within Quaternary sedimentary rocks and/or fractured metamorphic rocks (Fig. 14c). The NNW-striking and E-dipping major fault with a minimum dip angle range from 35° to 40° (Fig. 12b and 12e) seem to be the primary control at the surface where the hot springs emerge.

Our results from the SPI method to determine the magnetic basement depth (Fig. 13b), which we interpreted in this study as the metamorphic basement rock, revealed a maximum estimated basement depth of ~600 m.b.g.l. for the Mtondolo basin in profile E - E' (Fig. 13e), which is located east of the hot springs. However, the area of the Mtondolo hot springs in profile E – E' shows a maximum magnetic basement depth of ~483 m.b.g.l., which is consistent with the geothermal reservoir depth of 500 m.b.g.l. reported in the Kasitu-Chiwe geothermal area by Gondwe et al. (2021) south of the Mtondolo hot spring.

3.7 Conclusions

We conducted a remote sensing and aeromagnetic data structural analysis of fracture networks to quantify and characterize their geometry and spatial distribution, topology, intensity, and connectivity frequency to understand the structural controls of the geothermal systems at the surface and depth in the northern part of the MRZ.

We found that the fracture networks in the Karonga and Nkhata region comprise a varying degree of complexity along strike. This structural complexity occurs in favorable zones such as (1) two fault segments coalescing to form hard-linked relays, (2) two different oriented fracture segments intersecting (splays or abuts) against each other, and 3) on the tips of major normal faults. We determined that most of the hot springs are in one or more of these favorable structural settings in the northern part of the rift.

Our results demonstrate that areas of high fracture intensity and connectivity tend to act as fluid flow conduits of the thermal waters in the northern part of the MRZ. Additionally, other parameters such as low-high magnetic basement depth transition zones, low-high tilt-derivative angle transition zones, and high slope angles could be used together with the intensity and connectivity proxies and other techniques as indicators to identify other permeable zones and possible hidden geothermal systems in the MRZ.

We concluded that N to NW-striking normal faults and buried normal faults related to the Cenozoic rifting and other inherited N to NNE-striking structures related to previous Paleo-Mesozoic rifting events are the primary structural controls at shallow depths for geothermal fluids in the northern part of the MRZ. While possible reactivated structures that follow the foliation planes of Precambrian shear zones, such as the Mugesse Shear Zone in the Karonga region and the Mwembeshi Shear Zone in the Nkhata region are controlling the thermal waters flow at greater depths in the northern part of the MRZ. However, a detailed structural geology analysis to estimate the local stress field and slip and dilation tendency should be conducted in selected geothermal zones to determine the reactivation potential of fracture networks and mainly of inherited structures.

Moreover, we conclude that geothermal fluids are hosted mainly in sedimentary basins while fractured Precambrian rocks also host some geothermal fluids. Likewise, high-temperature geothermal fluids are hosted in fractured upflows at depth and low-temperature fluids are mixed with cool-water aquifers mostly in sedimentary basin outflows. Thus, geothermal systems are non-magmatic and structurally controlled. However, the specific heat sources of geothermal systems in the MRZ are still uncertain and further studies are needed to determine their heat sources. Our aeromagnetic results show that some of the geothermal reservoirs in the northern part of the MRZ have estimated depths between ~500 and 1000 m.b.g.l.

Finally, the low-cost methodologies used in this study could reduce the risk of drilling non-productive wells in the early exploration phases, advance the exploration and production of hidden geothermal systems and Enhanced Geothermal Systems (EGS) in this region, and become an exploration strategy for the future development of similar geothermal systems in other countries of the Western Branch of the East African Rift System.

3.8 Acknowledgments

We are grateful to Luelseged Emishaw and Steven Johnson for all their help and shared knowledge on potential fields, and all the anonymous reviewers and editors whose thorough, critical, helpful, constructive comments and general help greatly contributed to improving this manuscript. Chase Watkins and Izabelle Buentello are acknowledged for their help in improving English in this paper. The authors are especially grateful to the Boone Pickens School of Geology and the Tectonics and Geophysics Investigation Fellows for all the support during this research. This is Boone Pickens School of Geology contribution 2021-.

3.9 References

Accardo, N.J., Gaherty, J.B., Shillington, D.J., Hopper, E., Nyblade, A.A., Ebinger, C.J., Scholz, C.A., Chindandali, P.R.N., Wambura-Ferdinand, R., Mbogoni, G., and Russell, J.B., 2020. Thermochemical modification of the upper mantle beneath the northern Malawi rift constrained from shear velocity imaging. *Geochemistry, Geophysics, Geosystems, 21*(6), p.e2019GC008843. https://doi.org/10.1029/2019GC008843.

Accardo, N.J., Shillington, D.J., Gaherty, J.B., Scholz, C.A., Nyblade, A.A., Chindandali, P.R.N., Kamihanda, G., McCartney, T., Wood, D. and Wambura Ferdinand, R., 2018. Constraints on rift basin structure and border fault growth in the northern Malawi rift from 3-D seismic refraction imaging. *Journal of Geophysical Research: Solid Earth, 123*(11), pp.10-003.

Addison, M.J., Rivett, M.O., Robinson, H., Fraser, A., Miller, A.M., Phiri, P., Mleta, P. and Kalin, R.M., 2020. Fluoride occurrence in the lower East African rift system, southern Malawi. *Science of the total environment, 712*, p.136260. https://doi.org/10.1016/j.scitotenv.2019.136260.

Allmendinger, RW., 2020. Stereonet 11.3. 0.

ASF DAAC 2015, ALOS PALSAR_Radiometric_Terrain_Corrected_high_res; Includes Material © JAXA/METI 2007. Accessed through ASF DAAC 11 November 2015. https://doi.org/10.5067/Z97HFCNKR6VA

Baranov, V., 1957. A new method for interpretation of aeromagnetic maps: pseudo-gravimetric anomalies. *Geophysics, 22*(2), pp.359-382. https://doi.org/10.1190/1.1438369.

Biggs, J., Nissen, E., Craig, T., Jackson, J. and Robinson, D.P., 2010. Breaking up the hanging wall of a rift-border fault: The 2009 Karonga earthquakes, Malawi. *Geophysical Research Letters, 37*(11).

Bjerkgard, T., Stein, H.J., Bingen, B., Henderson, I.H.C., Sandstad, J.S. and Moniz, A., 2009. The Niassa Gold Belt, northern Mozambique–A segment of a continental-scale Pan-African gold-bearing structure? *Journal of African Earth Sciences, 53*(1-2), pp.45-58.

Bloomfield, K., 1965. The Geology of the Zomba Area. *Government Printer, South Africa*.

Bloomfield, K., 1968. The Pre-Karoo geology of Malawi. *Government Printer, South Africa*.

Bloomfield, K., Garson, M.S., 1965. The Geology of the Kirk Range, Lisungwe Valley Area (No. 17). *Government Printer*.

Borrego, D., Nyblade, A.A., Accardo, N.J., Gaherty, J.B., Ebinger, C.J., Shillington, D.J., Chindandali, P.R., Mbogoni, G., Ferdinand, R.W., Mulibo, G. and O'Donnell, J.P., 2018. Crustal structure surrounding the northern Malawi rift and beneath the Rungwe Volcanic Province, East Africa. *Geophysical Journal International, 215*(2), pp.1410-1426.

Caine, J.S. and Forster, C.B., 1999. Fault zone architecture and fluid flow: Insights from field data and numerical modeling. *Geophysical Monograph-American Geophysical Union, 113*, pp.101-128.

Chapusa, F.W.P. and Harrison, D.R., 1975. The geology of the Nkhotakota-Benga area. *Bulletin 32*, pp.31–32.

Chorowicz, J., 2005. The east African rift system. *Journal of African Earth Sciences, 43*(1-3), pp.379-410. https://doi.org/10.1016/j.jafrearsci.2005.07.019.

Corti, G., van Wijk, J., Cloetingh, S. and Morley, C.K., 2007. Tectonic inheritance and continental rift architecture: Numerical and analogue models of the East African Rift system. *Tectonics, 26*(6).

Dávalos-Elizondo, E. and Laó-Dávila, D.A., 2019. Structural controls and slip tendency in the Chiweta geothermal zone: Northern part of the Malawi Rift, Africa: a progress report. *Geothermal Resources Council Transactions 43*, 178–199.

Dávalos-Elizondo, E., Atekwana, E.A., Atekwana, E.A., Tsokonombwe, G. and Laó-Dávila, D.A., 2021. Medium to low enthalpy geothermal reservoirs estimated from geothermometry and mixing models of hot springs along the Malawi Rift Zone. *Geothermics, 89*, p.101963. https://doi.org/10.1016/j.geothermics.2020.101963.

Dawson, S.M., Laó-Dávila, D.A., Atekwana, E.A. and Abdelsalam, M.G., 2018. The influence of the Precambrian Mughese Shear Zone structures on strain accommodation in the northern Malawi Rift. *Tectonophysics, 722*, pp.53-68.

De Waele, B., Kampunzu, A.B., Mapani, B.S.E. and Tembo, F., 2006. The Mesoproterozoic irumide belt of Zambia. *Journal of African Earth Sciences, 46*(1-2), pp.36-70.

Delvaux, D. and Hanon, M., 1991. Neotectonics of the Mbeya area, SW Tanzania. *Annual report of the Royal Museum of Central Africa, Department of Geology and Mineralogy, 1992*, pp.87-97.

Delvaux, D., 2001. Tectonic and palaeostress evolution of the Tanganyika-Rukwa-Malawi rift segment, East African Rift System. *Peri-Tethys Memoir, 6*, pp.545-567.

Dimmen, V., Rotevatn, A., Peacock, D.C., Nixon, C.W. and Nærland, K., 2017. Quantifying structural controls on fluid flow: Insights from carbonate-hosted fault damage zones on the Maltese Islands. *Journal of Structural Geology, 101*, pp.43-57. https://doi.org/10.1016/j.jsg.2017.05.012.

Dixey, F., 1927. The Tertiary and post-Tertiary lacustrine sediments of the Nyasan Rift-Valley. *Quarterly Journal of the Geological Society, 83*(1-5), pp.432-442.

Dockrill, B. and Shipton, Z.K., 2010. Structural controls on leakage from a natural CO2 geologic storage site: Central Utah, USA. *Journal of Structural Geology, 32*(11), pp.1768-1782.

Dulanya, Z., 2006. Geothermal resources of Malawi-an overview. In *Thirty-First Workshop on Geothermal Reservoir Engineering*, p. 5.

Dulanya, Z., Morales-Simfors, N. and Sivertun, Å., 2010. Comparative study of the silica and cation geothermometry of the Malawi hot springs: Potential alternative energy source. *Journal of African Earth Sciences, 57*(4), pp.321-327.

Ebinger, C.J., Rosendahl, B.R. and Reynolds, D.J., 1987. Tectonic model of the Malawi rift, Africa.*Tectonophysics*,*141*(1-3), pp.215-235.

Eichhubl, P., Greene, H.G., Naehr, T. and Maher, N., 2000. Structural control of fluid flow: offshore fluid seepage in the Santa Barbara Basin, California. *Journal of Geochemical Exploration, 69*, pp.545-549.

Eliyasi, C.N., 2016. Exploration for Geothermal resources using Geological structures with emphasis on faults-A case study of northern Malawi. In *Proceedings, 6th African Rift Geothermal Conference Addis Ababa, Ethiopia, 2nd–4th November*.

Faulds, J. and Hinz, N., 2015, April. Favorable tectonic and structural settings of geothermal systems in the Great Basin region, western USA: Proxies for discovering blind geothermal systems. In *Proceedings World Geothermal Congress, Melbourne, Australia, 19-25 April 2015* (No. DOE-UNR-06731-02). Nevada Bureau of Mines and Geology, University of Nevada, Reno.

Faulds, J.E., Coolbaugh, M.F., Vice, G.S. and Edwards, M.L., 2006. Characterizing structural controls of geothermal fields in the northwestern Great Basin: A progress report. *Geothermal Resources Council Transactions, 30*, pp.69-76.

Faulds, J.E., Hinz, N.H., Coolbaugh, M.F., Cashman, P.H., Kratt, C., Dering, G., Edwards, J., Mayhew, B. and McLachlan, H., 2011. Assessment of favorable structural settings of geothermal systems in the Great Basin, western USA. *Geothermal Resources Council Transactions, 35*, pp.777-783.

Faulds, J.E., Hinz, N.H., Dering, G.M. and Siler, D.L., 2013. The hybrid model–the most accommodating structural setting for geothermal power generation in the Great Basin, western USA. *Geothermal Resources Council Transactions, 37*, pp.3-10.

Fritz, H., Abdelsalam, M., Ali, K.A., Bingen, B., Collins, A.S., Fowler, A.R., Ghebreab, W., Hauzenberger, C.A., Johnson, P.R., Kusky, T.M. and Macey, P., 2013. Orogen styles in the East African Orogen: a review of the Neoproterozoic to Cambrian tectonic evolution. *Journal of African Earth Sciences, 86*, pp.65-106.

Gartrell, A., Zhang, Y., Lisk, M. and Dewhurst, D., 2004. Fault intersections as critical hydrocarbon leakage zones: integrated field study and numerical modelling of an example from the Timor Sea, Australia. *Marine and petroleum geology, 21*(9), pp.1165-1179. https://doi.org/10.1016/j.marpetgeo.2004.08.001.

Gay, S. P. Jr., 2009. Reactivation tectonics: The evidence and the consequences. *Salt Lake City, UT: American Stereo Map Co*.

Ghosh, K. and Mitra, S., 2009. Structural controls of fracture orientations, intensity, and connectivity, Teton anticline, Sawtooth Range, Montana. *AAPG bulletin, 93*(8), pp.995-1014.

Gondwe, K., Allen, A., Georgsson, L., Loga, U. and Tsokonombwe, G., 2012, November. Geothermal Development in Malawi–a Country Update. In *Proceedings 4th African Rift Geothermal Conference, Nairobi, Kenya* (pp. 21-23).

Gondwe, K., Mwagomba, T., Tsokonombwe, G., Eliasi, C. and Lungu, K. 2021, November. Geothermal Development in Malawi–a Country Update. In *Proceedings World Geothermal Congress, Melbourne, Australia, 19-25 April 2015*. Mzuzu University, Malawi.

Grijalva, A., Nyblade, A.A., Homman, K., Accardo, N.J., Gaherty, J.B., Ebinger, C.J., Shillington, D.J., Chindandali, P.R., Mbogoni, G., Ferdinand, R.W. and Mulibo, G., 2018. Seismic evidence for plume-and craton-influenced upper mantle structure beneath the northern Malawi Rift and the Rungwe Volcanic Province, East Africa. *Geochemistry, Geophysics, Geosystems, 19*(10), pp.3980-3994.

Hinz, N., Cumming, B. and Sussman, D., 2018. Exploration of fault-related deep-circulation geothermal resources in the western branch of the East African Rift System: examples from Uganda and Tanzania. In *The Proceedings, 7th African Rift Geothermal Conference Kigali, Rwanda 31st October–2nd November*.

Hopper, E., Gaherty, J.B., Shillington, D.J., Accardo, N.J., Nyblade, A.A., Holtzman, B.K., Havlin, C., Scholz, C.A., Chindandali, P.R., Ferdinand, R.W. and Mulibo, G.D., 2020. Preferential localized thinning of lithospheric mantle in the melt-poor Malawi Rift. *Nature Geoscience, 13*(8), pp.584-589.

Kalebe, Y.N., 2018. Chemical and Isotopic Composition of Thermal Waters in Northern Part of Malawi. In *UNU Geothermal Training Programme, Iceland*.

Kaonga, H., Tsokonombwe, G. and Kamanga, T., 2014, October. Status of geothermal exploration in Malawi. In *Proceedings of the 5th African Rift Geothermal Conference, Arusha, Tanzania* (pp. 29-31).

Kattenhorn, S.A., Aydin, A. and Pollard, D.D., 2000. Joints at high angles to normal fault strike: an explanation using 3-D numerical models of fault-perturbed stress fields. *Journal of structural Geology, 22*(1), pp.1-23. https://doi.org/10.1016/S0191-8141(99)00130-3.

Katumwehe, A.B., Abdelsalam, M.G. and Atekwana, E.A., 2015. The role of pre-existing Precambrian structures in rift evolution: The Albertine and Rhino grabens, Uganda. *Tectonophysics, 646,* pp.117-129.

Kemp, J., 1975. *The geology of the Uzumara area*. South Africa: Government Printer.

Kirkpatrick, I.M., 1969. The thermal springs of Malawi. In *Report XXIII International Geological Congress, 19*B, pp. 111–120.

Kolawole, F., Atekwana, E.A., Laó-Dávila, D.A., Abdelsalam, M.G., Chindandali, P.R., Salima, J. and Kalindekafe, L., 2018. Active deformation of Malawi rift's north basin Hinge zone modulated by reactivation of preexisting Precambrian Shear zone fabric. *Tectonics, 37*(3), pp.683-704.

Laó-Dávila, D.A., Al-Salmi, H.S., Abdelsalam, M.G. and Atekwana, E.A., 2015. Hierarchical segmentation of the Malawi Rift: the influence of inherited lithospheric heterogeneity and kinematics in the evolution of continental rifts. *Tectonics 34* (12), 2399–2417. https://doi.org/10.1002/2015tc003953.

Leseane, K., Atekwana, E.A., Mickus, K.L., Abdelsalam, M.G., Shemang, E.M. and Atekwana, E.A., 2015. Thermal perturbations beneath the incipient Okavango Rift Zone, northwest Botswana. *Journal of Geophysical Research: Solid Earth, 120*(2), pp.1210-1228.

Martel, S.J., 1990. Formation of compound strike-slip fault zones, Mount Abbot quadrangle, California. *Journal of Structural Geology, 12*(7), pp.869-882.

McCartney, T. and Scholz, C.A., 2016. A 1.3 million year record of synchronous faulting in the hangingwall and border fault of a half-graben in the Malawi (Nyasa) Rift. *Journal of Structural Geology, 91,* pp.114-129. https://doi.org/10.1016/j.jsg.2016.08.012.

McConnell, R.B., 1972. Geological development of the rift system of eastern Africa. *Geological Society of America Bulletin, 83*(9), pp.2549-2572.

Miller, H.G. and Singh, V., 1994. Potential field tilt—a new concept for location of potential field sources. *Journal of applied Geophysics, 32*(2-3), pp.213-217. https://doi.org/10.1016/0926-9851(94)90022-1.

Morales-Simfors, N., Dulanya, Z. and Sivertun, Å., 2015. Structural and Stratigraphic Controls of Malawi's Hotsprings: a Review. In *World Geothermal Congress 2015 Melbourne, Australia, 19-25 April 2015*. International Geothermal Association.

Msika, B.J., Saka, J.D.K. and Dulanya, Z., 2014. Spatial distribution, chemistry and subsurface temperatures of geothermal springs Nkhata bay, Malawi. *African Journal of Environmental Science and Technology, 8*(8), pp.464-475.

Njinju, E.A., 2016. *Crustal and sub-continental lithospheric mantle decoupling beneath the Malawi Rift* (Doctoral dissertation, Oklahoma State University).

Njinju, E.A., Kolawole, F., Atekwana, E.A., Stamps, D.S., Atekwana, E.A., Abdelsalam, M.G. and Mickus, K.L., 2019. Terrestrial heat flow in the Malawi Rifted Zone, East Africa: Implications for tectono-thermal inheritance in continental rift basins. *Journal of Volcanology and Geothermal Research, 387*, p.106656.

Nyberg, B., Nixon, C.W. and Sanderson, D.J., 2018. NetworkGT: A GIS tool for geometric and topological analysis of two-dimensional fracture networks. *Geosphere, 14*(4), pp.1618-1634.

Omenda, P., Ebinger, C., Nelson, W., Delvaux, D., Cumming, W., Marini, L., Halldórsson, S., Varet, J., Árnason, K., Ruempker, G. and Alexander, K., 2016, November. Characteristics and important factors that influence the development of geothermal systems in the western branch of East African Rift System". In *Proceedings, 6th African Rift Geothermal Conference, Addis Ababa, Ethiopia*.

Ray, G.E., 1975. The geology of the Chitipa-Karonga area. *Government printer, South Africa. Geological Survey, Malawi 42*, p.101.

Reynolds, D.J. and Rosendahl, B.R., 1984. Tectonic expressions of continental rifting. EOS, *Trans. Am. Geophys. Union, 65*, p.1055.

Ring, U. and Betzler, C., 1995. Geology of the Malawi Rift: kinematic and tectonosedimentary background to the Chiwondo Beds, northern Malawi. *Journal of Human Evolution, 28*(1), pp.7-21.

Ring, U., 1993. Aspects of the kinematic history and mechanisms of superposition of the Proterozoic mobile belts of eastern Central Africa (northern Malawi and southern Tanzania). *Precambrian Research, 62*(3), pp.207-226.

Ring, U., 1994. The influence of preexisting structure on the evolution of the Cenozoic Malawi rift (East African rift system). *Tectonics 13* (2), pp. 313–326.

Ring, U., 1995. Tectonic and lithological constraints on the evolution of the Karoo graben of northern Malawi (East Africa). *Geologische Rundschau, 84*(3), pp.607-625.

Ring, U., Betzler, C. and Delvaux, D., 1992. Normal vs. strike-slip faulting during rift development in East Africa: the Malawi rift. *Geology, 20*(11), pp.1015-1018.

Ring, U., Kröner, A., Buchwaldt, R., Toulkeridis, T. and Layer, P.W., 2002. Shear-zone patterns and eclogite-facies metamorphism in the Mozambique belt of northern

Malawi, east-central Africa: implications for the assembly of Gondwana. *Precambrian Research, 116*(1-2), pp.19-56.

Rosendahl, B.R., 1987. Architecture of continental rifts with special reference to East Africa. *Annual Review of Earth and Planetary Sciences, 15*(1), pp.445-503.

Rowland, J.V. and Simmons, S.F., 2012. Hydrologic, magmatic, and tectonic controls on hydrothermal flow, Taupo Volcanic Zone, New Zealand: Implications for the formation of epithermal vein deposits. *Economic Geology, 107*(3), pp.427-457.

Salako, K.A., 2014. Depth to basement determination using Source Parameter Imaging (SPI) of aeromagnetic data: An application to upper Benue Trough and Borno Basin, Northeast, Nigeria. *Academic Research International (AR Int) 5*(3), pp 74 – 80. http://journals.savap.org.pk/vol5n3.html.

Salem, A., Williams, S., Fairhead, J.D., Ravat, D. and Smith, R., 2007. Tilt-depth method: A simple depth estimation method using first-order magnetic derivatives. *The leading edge, 26*(12), pp.1502-1505. https://doi.org/10.1190/1.2821934.

Sanderson, D.J. and Nixon, C.W., 2015. The use of topology in fracture network characterization. *Journal of Structural Geology, 72*, pp.55-66. https://doi.org/10.1016/j.jsg.2015.01.005.

Saria, E., Calais, E., Stamps, D.S., Delvaux, D. and Hartnady, C.J.H., 2014. Present-day kinematics of the East African Rift. *Journal of Geophysical Research: Solid Earth, 119*(4), pp.3584-3600.

Scholz, C.A., Cohen, A.S., Johnson, T.C., King, J., Talbot, M.R. and Brown, E.T., 2011. Scientific drilling in the Great Rift Valley: the 2005 Lake Malawi Scientific Drilling Project—an overview of the past 145,000 years of climate variability in Southern Hemisphere East Africa. *Palaeogeography, Palaeoclimatology, Palaeoecology, 303*(1-4), pp.3-19. https://doi.org/10.1016/j.palaeo.2010.10.030.

Scholz, C.A., Shillington, D.J., Wright, L.J., Accardo, N., Gaherty, J.B. and Chindandali, P., 2020. Intrarift fault fabric, segmentation, and basin evolution of the Lake Malawi (Nyasa) Rift, East Africa. *Geosphere, 16*(5), pp.1293-1311. https://doi.org/10.1130/GES02228.1.

Shillington, D.J., Scholz, C.A., Chindandali, P.R., Gaherty, J.B., Accardo, N.J., Onyango, E., Ebinger, C.J. and Nyblade, A.A., 2020. Controls on Rift Faulting in the North Basin of the Malawi (Nyasa) Rift, East Africa. *Tectonics, 39*(3), p.e2019TC005633. https://doi.org/10.1029/2019TC005633.

Siler, D.L. and Kennedy, B.M., 2016. Regional crustal-scale structures as conduits for deep geothermal upflow. *Geothermics, 59*, pp.27-37.

Smith, R.S. and Salem, A., 2005. Imaging depth, structure, and susceptibility from magnetic data: The advanced source-parameter imaging method. *Geophysics, 70*(4), pp.L31-L38. https://doi.org/10.1190/1.1990219.

Tamagawa, T. and Pollard, D.D., 2008. Fracture permeability created by perturbed stress fields around active faults in a fractured basement reservoir. *AAPG bulletin, 92*(6), pp.743-764. https://doi.org/10.1306/02050807013.

Thurston, J.B. and Smith, R.S., 1997. Automatic conversion of magnetic data to depth, dip, and susceptibility contrast using the SPI (TM) method. *Geophysics, 62*(3), pp.807-813. https://doi.org/10.1190/1.1444190.

Tsokonombwe, G., 2017. Hydrogeochemistry Modelling of Chiweta Geothermal Prospect, Northern Malawi. Master's Thesis. University of Iceland, Reykjavik.

Van Wijk, J.W. and Blackman, D.K., 2005. Dynamics of continental rift propagation: the end-member modes. *Earth and Planetary Science Letters, 229*(3-4), pp.247-258.

Versfelt, J. and Rosendahl, B.R., 1989. Relationships between pre-rift structure and rift architecture in Lakes Tanganyika and Malawi, East Africa. *Nature, 337*(6205), pp.354-357.

Von Herzen, R.P. and Vacquier, V., 1967. Terrestrial heat flow in lake Malawi, Africa. *Journal of Geophysical Research, 72*(16), pp.4221-4226.

Wang, T., Feng, J., Liu, K.H. and Gao, S.S., 2019. Crustal structure beneath the Malawi and Luangwa Rift Zones and adjacent areas from ambient noise tomography. *Gondwana Research, 67*, pp.187-198.

Zheng, W., Oliva, S. J., Ebinger, C. and Pritchard, M. E., 2020. Aseismic Deformation During the 2014 M w 5.2 Karonga Earthquake, Malawi, From Satellite Interferometry and Earthquake Source Mechanisms. *Geophysical Research Letters, 47*(22), p. e2020GL090930. https://doi.org/10.1029/2020GL090930.

CHAPTER IV

PAPER 3: 3D STRUCTURAL MODEL AND SLIP-DILATION TENDENCY ANALYSIS OF THE CHIWETA ZONE: GEOTHERMAL SYSTEM IMPLICATIONS AND FAULT REACTIVATION POTENTIAL

4.1 Abstract

A 3D structural model and slip-dilation tendency analysis are used to assess the reactivation potential of shear and dilatational structures to investigate structurally controlled geothermal systems in the Chiweta Zone. The Chiweta Zone is in the northern part of the Malawi Rifted Zone, where an elevated heat flow anomaly and one of the hottest hot springs occur. Structurally controlled geothermal systems are poorly understood not only in Malawi but in the entire Western Branch of the East African Rift System. The objectives of this study were to (1) construct a three-dimensional structural geometry of the faults identified with remote sensing and aeromagnetic data, (2) perform a slip-dilation tendency analysis to assess the fault reactivation potential under a stress state condition at depths between ~700 – 1000 m.b.g.l. of the estimated reservoir, (3) identify, based on the results, which faults are critically stressed and serve as fluid conduits or barriers to the geothermal system, (4) combine geological, geochemical, and geophysical data with our results to improve the conceptual model of the Chiweta Geothermal System (CGS). Our findings indicate that ~NW- and ~NNE-striking faults southwest- and northwest dipping, respectively, show segments with the highest dilation values of T_d ~ 0.6 to T_d ~ 0.8 and probably behave as active fluid pathways. This is supported by the Chiweta Fault, an NW-striking and southwest dipping fault that controls the only thermal manifestations in the Chiweta Zone. NW- and NE-striking faults dipping to the northeast and southeast, respectively, show lower dilation values of T_d ~ 0.1 to T_d ~ 0.5 and probably act as fluid barriers. These results allowed us to define, for the first time, possible structural boundaries of the Chiweta geothermal reservoir and to improve its geothermal conceptual model. The results of this study together with preliminary information available on the study area can contribute to targeting the first exploratory wells in the Chiweta Geothermal System. Finally, the applied methodology is expected to be used around the Western Branch of the East African Rift System and help advance geothermal energy production in this region.

Keywords: Chiweta Geothermal System, 3D Structural Model, Stress State, Focal Mechanism Stress Inversion, Slip-Dilation Tendency Analysis

4.2 Introduction

Non-magmatic geothermal systems of extensional domains can be structurally controlled or controlled by structural leakage (Moeck, 2014). In structurally controlled geothermal systems, convection occurs when meteoric water infiltrates through deep structures, is heated by anomalous heat flow in the region, and rises from fracture networks and permeable zones towards the surface (Reed, 1982; Moeck, 2014). While, in structural-leakage geothermal systems, geothermal fluids rise from fracture networks into a permeable stratigraphically buried layer. The fluid then rises back through permeable structural zones to the surface (Moeck, 2014).

Fracture networks have strong controls over fluid flow and water-rock interactions in non-magmatic geothermal systems because they can act as conduits, barriers, or both for geothermal fluids (Caine et al., 1996). In general, fluid flow is concentrated in areas of complex fracture networks that show a wider range of orientations and high fracture intensity and connectivity (Caine & Forster, 1999; Eichhubl et al., 2000; Gosh & Mitra, 2009; Dimmen et al., 2017), such as termination of a major normal fault, step-over or relay ramp in a normal fault zone, accommodation zones, antithetic normal fault, fault intersections, pull-apart basins, strike-slip fault zones, displacement transfer zones, and others (e.g., Faulds et al., 2011; Fossen & Rotevatn, 2016; Dimmen et al., 2017). These favorable structures or complex fracture networks enhance permeability in specific areas and act as fluid pathways and storage.

However, favorable zones that promote fluid flow depend on other factors, such as fracture network geometry, reactivation potential, and local stress field. Therefore, understanding the reactivation potential of preexisting faults under a particular stress field is critical to identifying potential fluid pathways, delimitating the geothermal reservoir, and targeting productive wells (McFarland et al., 2012; Joli et al., 2015;

Barcelona et al., 2019). Some studies have shown that critically stressed faults increase dilation and slip tendency (Barton et al., 1995 1997; Ferrill and Morris, 2003; Joli et al., 2015). For this reason, other studies have successfully applied this structural analysis to the exploration and production of geothermal systems (e.g., Moeck et al., 2009; Siler & Faulds, 2013; Faulds et al., 2015; Jolie et al., 2015; Barcelona et al., 2019).

The Chiweta geothermal system (CGS) is in the northern part of the Malawi Rifted Zone (MRZ), which lies in the Western Branch, a magma-poor early-stage segment of the East African Rift System (EARS; Fig. 1). The Chiweta geothermal reservoir temperatures were estimated from geothermometry to range from 100 °C to 190 °C (e.g., Tsokonombwe, 2017; Kalebe, 2018; Dávalos-Elizondo *et al.,* 2021). The CGS is suggested to have the highest reservoir temperature in the entire MRZ (e.g., Kalebe, 2018; Dávalos-Elizondo *et al.,* 2021), to form as deep circulating water is heated by a high anomalous heat flow (e.g., Hinz *et al.,* 2018; Dávalos-Elizondo & Laó-Dávila, 2022), and to be non-magmatic and structurally controlled by a complex fracture network (Dávalos-Elizondo & Laó-Dávila, 2022). However, there is a lack of knowledge about the structural geometry, reactivation potential of preexisting structures that favor the fluid channels, geothermal reservoir boundaries, and as consequence, the geothermal conceptual model remains limited.

Dávalos-Elizondo & Laó-Dávila (2022) argued that the Chiweta Zone has a complex fracture network of reactivated Precambrian mobile belt (Mughese shear) structures ~NNW-SSE oriented, which are intersecting within ~NE-SW Permo-Triassic (Karoo basin) structures (Dávalos-Elizondo & Laó-Dávila, 2022). The hypothesis is that NNW-SSE and N-

S structures with dips ranging between ~ 45˚ - 70˚ are expected to encounter high reactivation potential within an ~ENE-WSW trending of σ_3 (e.g., Saria *et al.*, 2014; Stamps *et al.,* 2018; Williams *et al.,* 2019; Dávalos-Elizondo & Laó-Dávila, 2019). This study aims to provide the first three-dimensional structural characterizations and slip-dilation tendency analysis of the relationship between a local stress field and the reactivation potential of preexisting structures that promotes subsurface fluid flow pathways toward surface discharges in the CGS.

We built a three-dimensional structural-geothermal model for the Chiweta Zone that was validated by geological information, the surficial distribution and geochemistry of hot springs, and geophysical data. Finally, the reactivation potential of the structural framework was calculated by slip and dilation tendency analysis (Morris *et al*., 1996; Ferrill & Morris, 2003). Our results show favorably oriented structures that serve as conduits and barriers of the geothermal reservoir. The significant impact of this study can help to identify potential target areas for future geothermal wells and reduce the risk of drilling non-productive geothermal wells in the exploration and production stages. Additionally, this study may yield important knowledge of the structure and tectonic evolution of strain localization in the MRZ by understanding processes such as reactivation potential and fluid flow that affect pore fluid pressure and cohesion of rocks, which are factors that trigger earthquakes.

4.3 Background

4.3.1 Regional tectonic setting

The MRZ is part of the Western Branch of the EARS, a divergent plate boundary between the Nubian and Rovuma plates (Fig. 1A). The higher extensional rate of 2.2 mm/yr is estimated in the northern part of the MRZ from a GPS-derived model by Saria *et al.* (2014). The MRZ is characterized by an old, cold, and thick lithosphere associated with the extension of an early-stage segment of the EARS that localized strain along major faults (McCartney & Scholz, 2016). Recent studies about seismic velocities (S-wave) proposed that the thickness of the lithosphere is in the range of 36 to 38 km beneath most of the MRZ, and from 38 to 40 km depth in the southern part of the rift (Wang et al., 2019; Borrego et al., 2018). In addition, low anomalous seismic velocities (P-S and Rayleigh waves) at depths 150 – 200 km have been interpreted as the result of a mantle plume or partial melting of the lithospheric mantle underneath the north of the MRZ (Accardo et al., 2017; Grijalva et al., 2018). Furthermore, a high heat flow of 70 to 82 mW/m^2 and a high geothermal gradient between 29 to 32 °C/km were suggested by Njinju *et al.* (2019) within the Permo-Triassic basins in the northern part of the MRZ.

This anomalous geothermal gradient is responsible for the extension of the continental lithosphere (Ebinger et al., 1987; Njinju et al., 2019), as well as for the geothermal systems along the MRZ. It is suggested that low to medium enthalpy geothermal systems occur in the early-stage rifting of the MRZ and that they are primarily non-magmatic and structurally controlled (Gondwe et al., 2012; Dávalos-Elizondo et al., 2021). The Rungwe volcano, near the northern border between Malawi and Tanzania, is the only active volcano in the rift Tanzania (Fig. 1A). The MRZ extends ~750 km south to the Shire graben in southern Malawi (Ebinger, 1989; Ring & Betzler, 1995; Chorowicz, 2005; Laó-Dávila et al., 2015). The time of rifting initiation is still under debate, as well as the mechanism. Ebinger et al. (1984) suggested that the Quaternary Malawi Rift developed diachronously from north to south as evidenced by different thicknesses in depositional sequences and patterns in fault segments. K-Ar radiometric dating in the Rungwe volcanic complex indicates an age of ~18 Ma for the initiation in the northern part (Ebinger et al., 1989). However, fission-track ages for apatite extracted from Precambrian rocks in the north area of Malawi (Van der Beek *et al.* 1998) and the Rukwa Rift Basin in Tanzania indicate that the Western Branch of the EARS started to extend at around ~30 Ma (Roberts et al., 2012; Fagereng, 2013).

However, the MRZ has been affected by repeated rifting events previous to the Cenozoic Rifting (e.g., Delvaux, 2001). An early important rifting event during Late Carboniferous-Early Permian to Early Triassic times was responsible for forming the Karoo basins (Fig. 1A). It is suggested that the Karoo rifting event is related to an early stage of the Gondwana break-up in East-Central Africa (Ring & Betzler, 1995; Delvaux, 2001). The Karoo basins are narrow and asymmetrical rifts bounded by major normal faults, filled with sediments up to 3 km in thickness (Ring & Betzler, 1995). The most important Karoo basins were developed along NE- trends in the MRZ and comprise the Luangwa Rift (Fig. 1A), the Ruhuhu, Maniamba throughs, and the Shire Graben (Delvaux, 2001; Laó-Dávila et al., 2015).

The Cenozoic rift has a ~N-trend and consists of several asymmetric basins linked by accommodation and transfer zones (Ebinger et al., 1989; Flannery & Rosendahl, 1990; Ring & Betzler, 1995; Laó-Dávila *et al.,* 2015; Kolawole et al*.,* 2018). Four basins with alternate polarities comprise the northern region of the MRZ (Fig. 1A): the Karonga Basin (where the Chiweta zone is located), the Usisya Basin, Mbamba Basin, and Bandwe Basin (e.g., Ebinger et al., 1987; Rosendahl, 1987; Ring, 1994; Láo-Dávila et al., 2015).

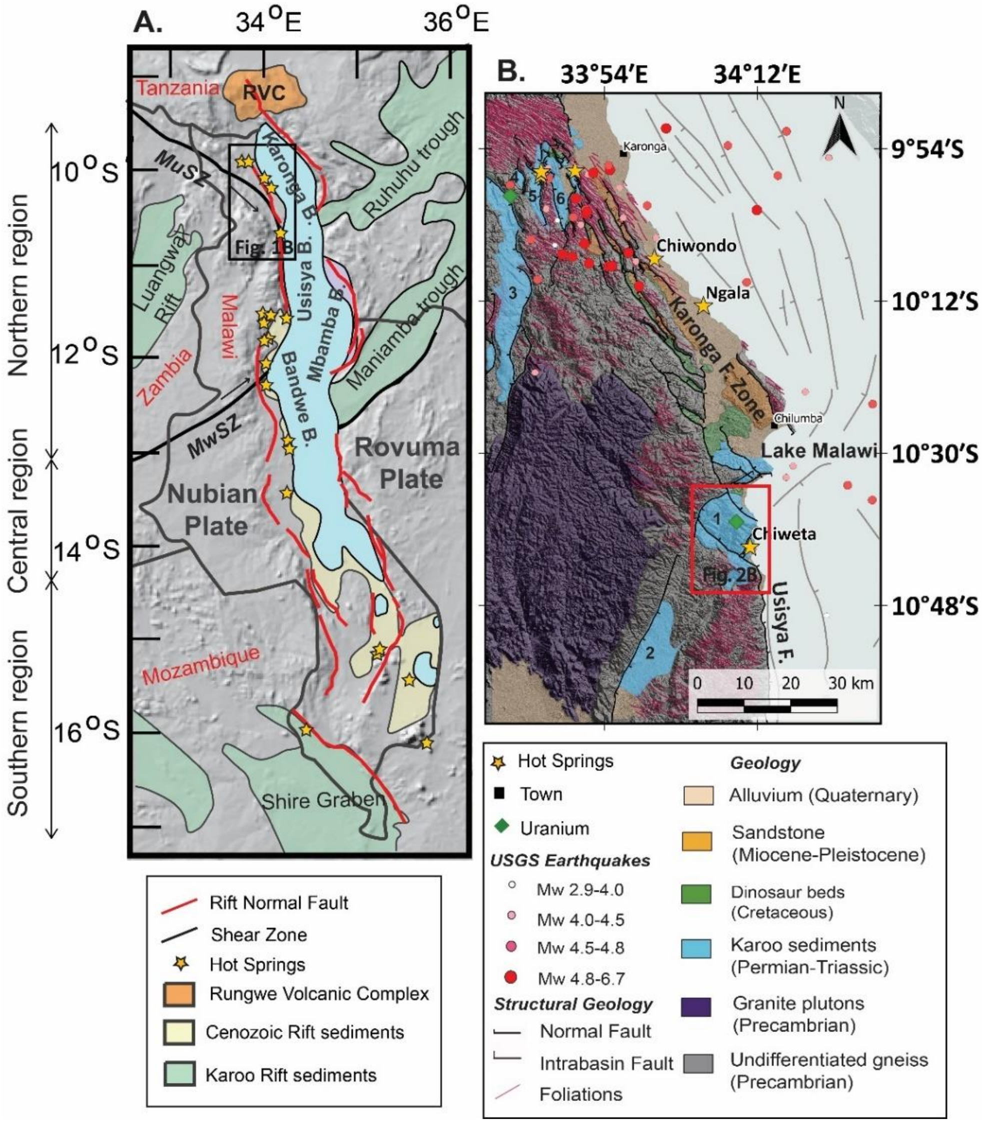

Figure. 1 A. Regional tectonic setting of the Malawi Rifted Zone (Modified from Dávalos-Elizondo et al., 2021) showing the main Permo-Triassic Karoo basins, the Cenozoic Malawi Rift border faults

(red lines), and the location of hot springs (yellow stars). RVC= Rungwe Volcanic Complex; MuSZ= Mughese Shear Zone; MwSZ= Mwembeshi Shear Zone. B. Geological and structural settings of the northern part of the Malawi Rift show the earthquakes that occurred in the region (Modified after Dávalos-Elizondo & Laó-Dávila, 2022). Karoo basins: 1. Livingstonia Basin; 2. Henga Basin; 3. North Rukuru Basin; 4. Mwapu Basin; 5. Mwankenja Basin; 6. Mwesia Basin.

4.3.2 Stress state at the Malawi Rifted Zone

Several dynamic and kinematic models of the EARS and only a few in the MRZ have been generated using a combination of focal mechanism inversion, fault displacement indicators, and GPS measurements (e.g., Saria et al., 2014; Stamps et al., 2018; Delvaux & Barth, 2010; Williams et al., 2019; Chorowicz & Sorlien, 1992; Ring et al., 1992). The results of these studies show a variety of different orientations of the horizontal minimum stress (S_{hmin}) from NE-SW, E-W, and NW-SE.

Focal mechanism stress inversion estimated by Delvaux and Barth (2010) in the Malawi rift showed a minimal compressive principal stress σ_3 subhorizontal (06/242) and a maximum compressive principal stress σ_1 subvertical (83/070). The S_{hmin}= 00/062 was also estimated by Delvaux and Barth (2010) and suggests causing NE-SW extension. Likewise, a focal mechanism stress inversion of a 2009 earthquake with Mb 5.9 in the northern part of Malawi suggests a subhorizontal σ_3 (10/073), subhorizontal σ_2 (00/356), and sub-vertical σ_1 (78/215). On the other hand, studies using slickenside measurements in the MRZ, such as Chorowicz and Sorlien (1992), suggested a NW-SE σ_3 NW-SE oriented. These stress inversions, using fault indicators, are consistent with NNE-trending faults that accommodate oblique extension NW-SE (Bloomfield & Garson, 1965; Chorowicz &

Sorlien, 1992; Ring et al., 1992; Wedmore et al., 2020). Similarly, seismic reflection surveys showing fault geometry within Lake Malawi are consistent with a NW-SE rift extension. (Mortimer et al., 2007; Scott et al., 1992).

However, geodetic strain models in EARS using GPS measurements indicate an extension of ENE-WSW with an azimuth of 086° related to the Nubia and Rovuma plate divergent movement (Saria et al., 2014; Stamps et al., 2018). The most updated stress inversion using 21 focal mechanisms for the MRZ is from Williams *et al*. (2019). Their results show a S_{hmin}= 00/073, which is similar to the extension direction from GPS stations in the MRZ (e.g., Saria et al., 2014; Stamps et al., 2018).

4.3.3 Geological setting of the Chiweta Zone

The Chiweta Zone is in the Livingstonia Karoo Basin (Late Carboniferous to Upper Permian) between the latitudes 34° 05'E and 34° 12'E and the longitudes 10° 35'S and 10° 47'S. The Livingstonia Basin is one of 12 Karoo basins located in the northern part of the MRZ (Fig. 1B): 1) Livingstonia, 2) Ngana, 3) Kibwe, 4) Lufira, 5) Mwankenja, 6) Mwapu, 7) North Rukuru, 8) Mwesia, 9) Mwenewenya, 10) Nthalire, 11) Henga, and 12) Hara.

The Livingstonia Basin is dominated by Karoo sedimentary rocks that were deposited during an early rifting stage related to the Gondwana break-up (Ring & Betzler, 1995; Delvaux, 2001). The NE-trending basin is suggested to be the southwestern extension of the Ruhuhu Basin (Fig. 1A; Maneya, 2012), which is in Tanzania and truncated by Lake Malawi (~65 km away).

The Livingstonia Karoo Basin overlies unconformably the Proterozoic Basement Complex (Fig. 2A), which is composed of amphibolite-facies metamorphic rocks within the NW-trending Ubendian Belt (Delvaux, 2001; Fritz et al., 2013; Kolawole et al., 2018). The southern end of the Neoproterozoic Mughese Shear Zone (MuSZ) extends into the Chiweta Zone (Fig. 1A, 1B). The MuSZ was formed during the contractional event between Ubendian and Irumide Belts (Ring et al., 2002; Fritz et al., 2013; Dawson et al., 2018). It has been suggested that the MuSZ structural fabric serve as inherited reactivation structure for the Cenozoic Karonga Fault Zone (Fig. 1B; Láo-Dávila et al., 2015; Dawson et al., 2018; Dávalos-Elizondo & Laó-Dávila, 2022).

The Livingstonia Basin is described as an intracratonic basin, densely faulted, situated southeastern of the Nyika Plateau, and particularly important because of its coal-bearing and uranium potential (Fig. 2B; Bennett, 1989). This basin is also important for its preserved lower and upper Karoo successions (Bennett, 1989). Its stratigraphic column is summarized in Fig. 2A by Ring (1995), which shows the lithostratigraphic nomenclature adopted for Karoo formations (K1-K7, Fig. 2A, 2B).

4.3.4 The Chiweta Geothermal System

The CGS is in the northern part of the MRZ and is associated with local meteoric water infiltrated at depth and heated by the anomalous geothermal gradient in the region (Dávalos-Elizondo et al., 2021). Njinju et al. (2019) estimated high heat flow values of ~76 mW/m^2 in the CGS and associated them with the Karoo rift basins. Likewise, Wanless et al. (2016) estimated the highest $^3He/^4He$ ratios in the northern part of the MRZ and suggested a mantle contribution of ~35%.

The CGS has the hottest reservoir temperatures of the entire MRZ, estimated from silica and cation geothermometers that range from ~130 to 200 ˚C (e.g., Tsokonombwe, 2017; Kalebe, 2018; Dávalos-Elizondo et al., 2021). The Chiweta hot springs emerge at temperatures of 80 ˚C from mudstones of the youngest Karoo sedimentary sequence (K7 and K6; Fig. 2A). The Dinosaur Beds sequence (K7/K6) outcrops only occur in a small down faulted block with a strike of azimuth (Az) 300˚ and a NE dip of 10˚ (Fig. 2A; Tsokonombwe, 2017). Tsokonombwe (2017) reported that the total flow rate estimated in the Chiweta hot spring is about 30 L/s and silica and sulfur hydrothermal minerals are deposited near the Chiweta hot spring with a sulfur smell noticed in the site.

The Chiweta hot spring is probably the only hot spring in the entire MRZ that has Na-Cl (SO4) waters in partial equilibrium (Dávalos-Elizondo et al., 2021). The CGS is suggested to be structurally controlled by deep circulation through fault zones (e.g., Dávalos-Elizondo & Laó-Dávila, 2019; Dávalos-Elizondo et al., 2021). Dávalos-Elizondo & Laó-Dávila, (2019) mentioned that the CGS lies into a favorable structural setting related to the accommodation zone between the Livingstone and Usisya faults (Dávalos-Elizondo & Laó-Dávila, 2019). In addition, Dávalos-Elizondo & Laó-Dávila (2022) suggested that the CGS is within an NNE-striking half-graben formed during Karoo rifting and intersected by NW-striking normal faults of the Cenozoic Karonga Fault Zone (Fig. 1B and 2B), reactivated from foliation planes of the MuSZ.

The CGS shows a complex arrangement of fracture networks with a wide range of orientations (NE, NW, N) and high values of fracture intensity and connectivity (Dávalos-Elizondo & Laó-Dávila, 2022) that control permeability and fluid flow. The aeromagnetic Source Parameter Imaging (SPI) results by Dávalos-Elizondo & Laó-Dávila (2022) showed a magnetic basement depth (interpreted as the metamorphic basement) in the CGS that ranged from ~0 to 3,000 m.b.g.l. and at a depth of ~700 m.b.g.l. below the Chiweta hot spring. Therefore, Dávalos-Elizondo & Laó-Dávila (2022) interpreted a geothermal reservoir depth for the CGS of about ~700 m.b.g.l. to ~1000 m.b.g.l., which is consistent with the reservoir estimation reported by Gondwe et al. (2021).

Preliminary conceptual models by Tsokonombwe (2017) and Dávalos-Elizondo & Laó-Dávila (2022) suggest that meteoric water (Ca-Mg-HCO_3) percolates from the northwest highlands. The water-rock interaction and high temperatures at depth change the initial water composition from Ca-Mg (HCO_3) to Na-Cl (SO_4). Tsokonombwe (2017) suggested impermeable mudstone and calcareous mudstones of Permo-Triassic Karoo sedimentary succession as bed caps of the Chiweta geothermal reservoir. The K3 arkose sandstone was also suggested as a possible reservoir rock at depth by Tsokonombwe (2017). A NW-striking fault with a dip angle of about ~55˚to the southwest appears to transport the thermal waters through the surface in the CGS due to the difference in density of the hot and cold water (Fig. 2B Tsokonombwe,2017; Dávalos-Elizondo & Laó-Dávila, 2022).

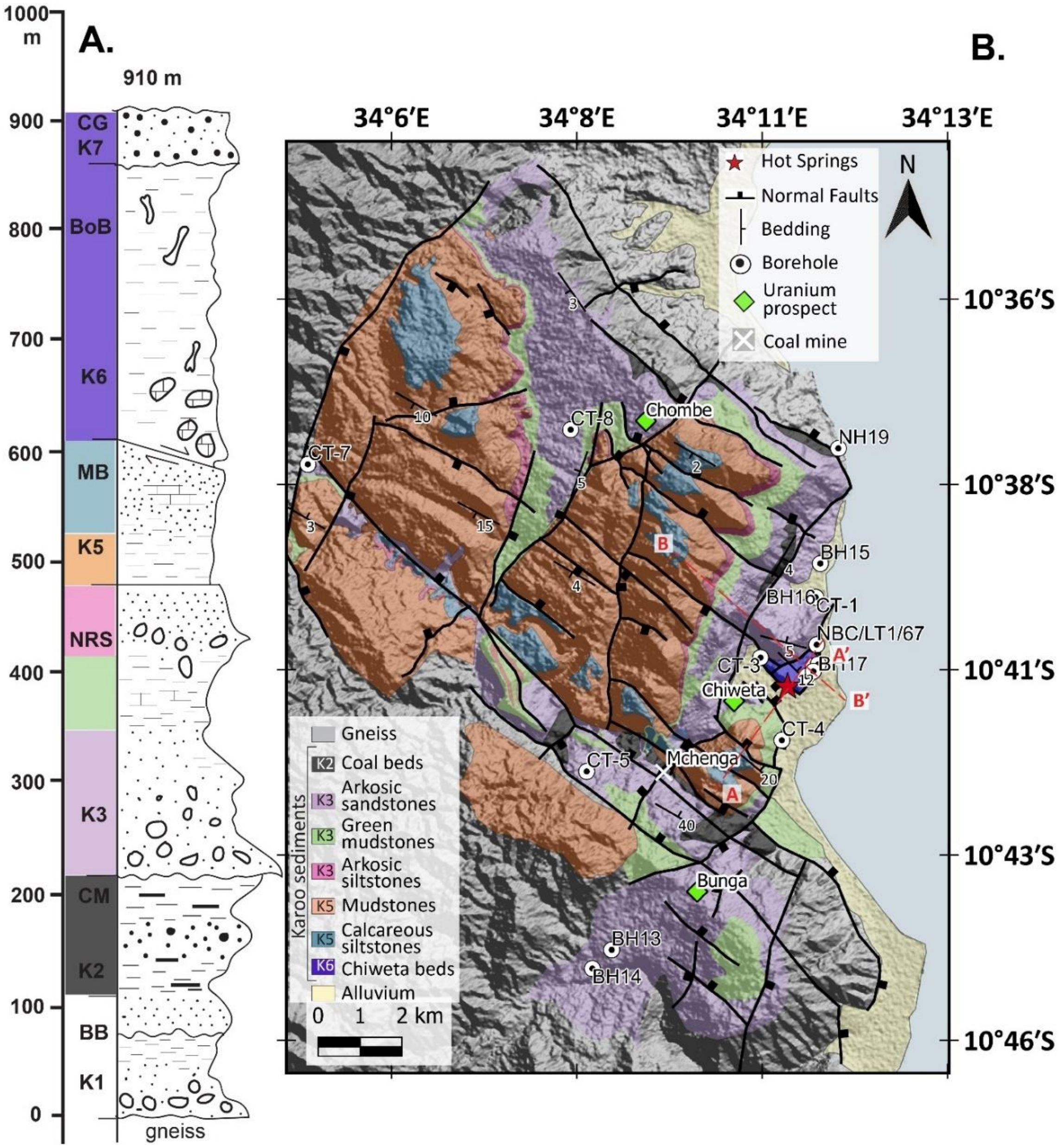

Figure. 2 A. Lithostratigraphic column of the Chiweta basin (Modified from Ring, 1995). BB= Basal Beds; CM= Coal Measures; NRS= North Rukuru Sandstone; MB= Mwesia Beds; BoB= Bone Beds; and CG= Chiweta Grit. B. Geological Map of the Chiweta Geothermal Zone (Modified after Kemp, 1975 and Dávalos-Elizondo & Laó-Dávila, 2022) showing the location of cross-sections A-A’ and B-B’ (as red dashed lines) in Fig. 3.

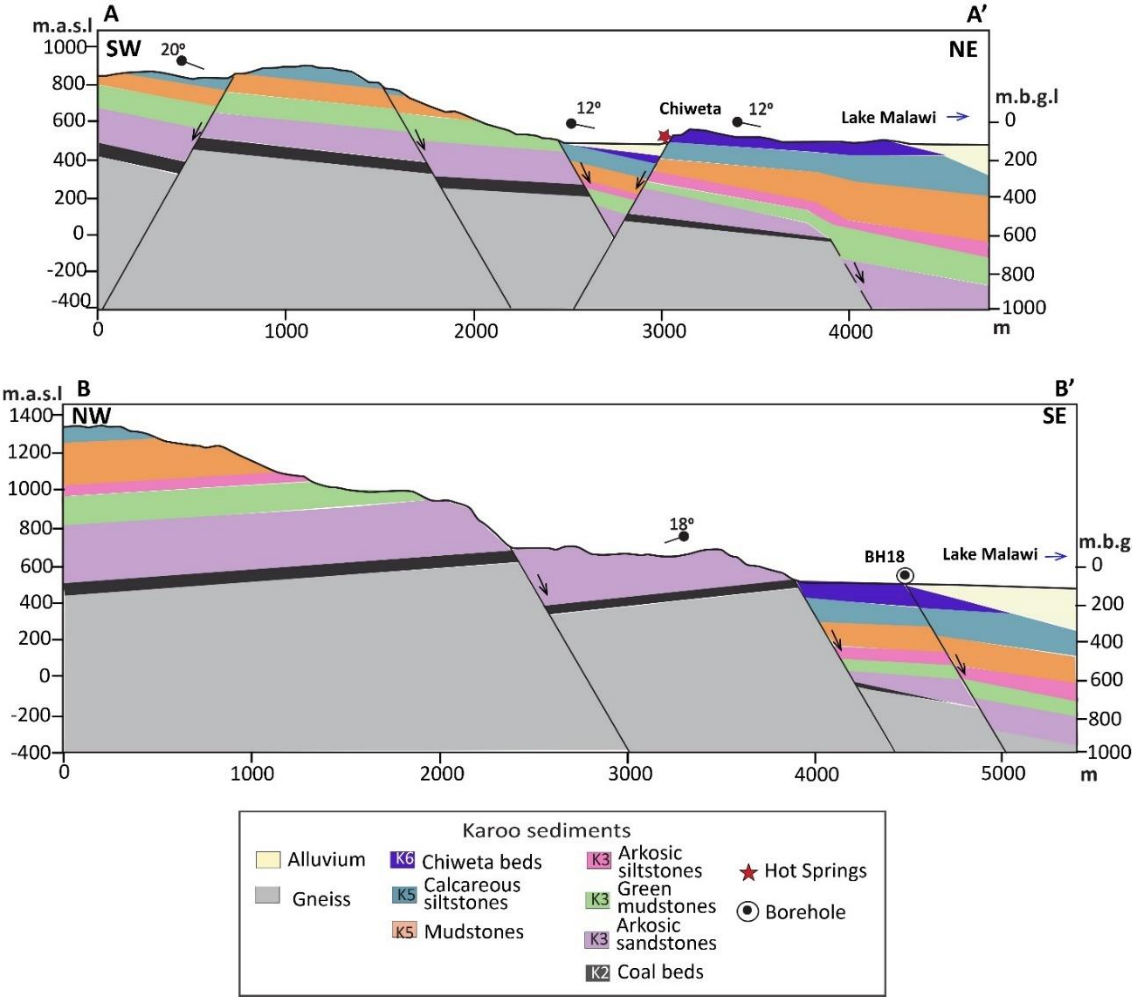

Figure. 3. Geological cross-sections show the main structures of the Chiweta Geothermal prospect.

4.4 Data and Methods

4.4.1 3D Structural model

The 3D structural framework of the Chiweta Zone was built using Petrel software. The dimensions covered for the geological model were approximately 15 km x 30 km x 1 km, reaching 1,000 m.b.g.l. depth (Fig. 2B). Geological, structural, and aeromagnetic data (e.g., Bloomfield, 1968; Kemp, 1975; Ring, 1995; Maneya, 2012; Tsokonombwe, 2017;

Dávalos-Elizondo & Laó-Dávila, 2022) were considered to construct a 3D structural geometry of the structures. Fault geometries were modeled based on a detailed mapping of fault scarp using remote sensing analysis of Digital Surface Model (DSM) data AW3D World of 2.5 m spatial resolution by the Japan Aerospace Exploration Agency (JAXA) and high-resolution aeromagnetic data previously analyzed by Dávalos-Elizondo & Laó-Dávila, 2022. Two sets of cross-sections were constructed based on the DSM, one perpendicular to the NW-SE Karonga fault system and one perpendicular to the NE-SW Karoo fault system. Additionally, two representative cross-sections of CGS were used for improving the geothermal conceptual model.

We used published strike and slip data (e.g., Tsokonombwe, 2017; Dávalos-Elizondo & Laó-Dávila, 2022), seismic data (e.g., Accardo *et al.*, 2020); Shillington *et al.*, 2020) and structural architecture extracted from DSM, such as slope (ranges from 40° to 75°; Dávalos-Elizondo & Laó-Dávila, 2022) to validate three-dimensional fault geometries. The architecture of buried structures was estimated from aeromagnetic data, such as the tilt derivative maps (Dávalos-Elizondo & Laó-Dávila, 2022).

We also reviewed published shallow well and lithology data (e.g., Bloomfield, 1968; Kemp, 1975; Ring, 1995; Maneya, 2012; Tsokonombwe, 2017). The Source Parameter Imaging (SPI^{TM}) method (Thurston & Smith, 1997; Smith & Salem, 2005) was used to constrain the depths between the sedimentary sequence and the metamorphic basement, as well as to estimate the depth of the geothermal reservoir (Dávalos-Elizondo & Laó-Dávila, 2022). Finally, a groundwater fluid flow direction map of the Chiweta Zone was estimated from shallow boreholes and cold springs data (see Table 1 and Fig. 2B) used by Tsokonombwe (2017) and compared with our DSM and the 3D structural geometry performed by this study.

Table 1. Borehole data showing coordinates UTM WGS84, altitude, depth, and water table level (Tsokonombwe, 2017).

Borehole	UTM X WGS84	UTM Y WGS84	Altitude	Depth m.b.g.l.	Water level m.a.s.l.
CT-2	630281	8819096	518.97	33	490.97
CT-10	630126	8818852	555.35	32	528.35
BH18	630285	8818969	461.82	33	433.82
BH17	630403	8819139	459.04	30	434.04
CT-3	629031	8819305	510.25	15	495.25
CT-4	629532	8817314	500.57	40	460.57
BH14	625000	8811840	861.12	46	820.12
BH13	625461	8812289	907.72	48	864.72
BH16	630351	8820748	455.58	36	424.58
BH15	630464	8821561	456.78	37	424.78
CT-8	624531	8824802	1047.93	48	1004.93
CT-7	618274	8823991	1025.65	42	988.65
CT-1	630352	8820747	500.12	40	465.12
CT-5	624883	8816581	978.86	37	946.86
NBC/LT1/67	630370	8819608	500.00	34	471.00
NH19	630904	8824329	463.07	40	423.07

m.a.s.l= meters above sea level; m.b.g.l.= meters below ground level

4.4.2 Stress field direction and magnitudes

In this study, we are using the stress analysis performed by Williams et al. (2019) in the MRZ, for some important reasons: (1) this inversion was performed using a total of

21 focal mechanisms of which 16 focal mechanisms were located in the northern part of the MRZ (see Table 2), (2) estimating stress states in rifts from fault slickensides are even more inconsistent because dip slip faults can host oblique slip and strike slip components due to converging patterns of coseismic slip (e.g., Roberts, 1996), (3) the S_{hmin} (00/073) estimated by Williams et al. (2019) agrees with the directions of extension from GPS stations in Malawi (Saria et al.,2014; Stamps et al., 2018), (4) the focal mechanisms used for this inversion (bodywave modeling) are considered more accurate than the Global Centroid Moment used by Delvaux and Barth (2010) inversion, and (5) the MRZ stress state estimated by Williams et al. (2019) from 21 focal mechanisms is consistent with a focal mechanism stress inversion for a 2009 Mw 5.9 earthquake in northern Malawi compiled by the World Stress Map Project, where σ_3 is subhorizontal (10°/073°), σ_2 is subhorizontal (07°/342°), and σ_1 is subvertical (78°/215°). Furthermore, Williams et al. (2019) demonstrated how the reactivation potential of three different striking active faults can be possible with a σ_3 oriented between ENE-WSW and E-W.

Thereby, the stress state estimated by Williams et al. (2019) provided the orientations of the principal stress axes: minimum compression σ_3 is subhorizontal (10°/072°), intermediate compression σ_2 is subhorizontal (02°/341°), and maximum compression σ_1 is subvertical (79°/239°), and the stress shape ratio of principal stress difference is $\Phi = (\sigma_2 - \sigma_{3\,/}\,\sigma_1 - \sigma_3) = 0.43$ (see Williams et al., 2019 for more information about this data).

We calculated the magnitudes of the principal stress to determine the reactivation potential of faults in the Chiweta geothermal zone. The magnitude of σ_1 was estimated by assuming an Andersonian normal fault stress state following the equation:

$$\sigma_1 = \sigma_v = \rho(z)gz \tag{1}$$

where σ_v is the vertical stress, $\rho(z)$ is the average density of the overlying crust for a given depth (z), and g is gravity (9.8 ms^{-2}).

The average density value of the upper crust models is suggested to be 2.65 g/cm^3 inferred for quartzofeldspathic rocks (e.g., Fagereng, 2013; Nyblade & Langston, 1995; Bjørlykke et al. 2015; Zhang, 2019). This average density value could be assumed in the study area because the lithology of sedimentary layers in the Livingstonia Basin is formed by siltstones, mudstones, and sandstones with a matrix composed mainly of quartzofeldespathic minerals (Fig. 2A). However, this average density value is not taking into consideration the porosity of the sedimentary rocks, which lowers the bulk density of sedimentary rocks (e.g., 2.1 – 2.5 g/cm^3; Fossen, 2016).

Unfortunately, no information is available about the average bulk density of the total sedimentary cover in the Livingstonia Basin. However, a study by Yasidu et al. (2017) in sandstones from the Mchenga coal mine (Fig. 2B), located near the CGS, shows a bulk density that varies according to the % of humidity between ~2.0 to 2.1 g/cm^3 for a fine-grained sandstone and between ~2.4 to 2.5 g/cm^3 for an arkose sandstone (K3, Fig. 2A). Likewise, another study about mechanisms of isostatic compensation in Kenya by Bechtel et al. (1987) mentioned a density model of a sedimentary cover layer with an average thickness of 500 m and a density of 2.3 g/cm^3. Based on this information an average density value of the sedimentary cover in the Chiweta Zone is assumed to be 2.3 g/cm^3 (see Appendix A for an analysis performed with a density value of 2.65 g/cm^3 and a μ_s value= 0.7, more representative of the basement rocks).

Table 2. 21 Focal Mechanisms of the Malawi Rifted Zone compiled from different sources by Williams *et al.* (2019).

No.	Longitude	Latitude	Date (yyyy/mm/dd)	Mw	Depth (km)	Strike	Dip	Rake
1	36.00	−16.50	1954/01/17	6.7	20	197	68	164
2	34.60	−15.70	1966/05/06	5.1	17	001	51	−56
3	34.45	−11.76	1978/01/08	4.9	15	158	45	−90
4	34.47	−13.68	1989/03/09	5.5	31	340	56	−99
5	34.49	−13.71	1989/03/10	6.1	32	336	56	−92
6	34.46	−11.80	1989/09/05	5.4	20	063	52	149
7	33.51	−9.42	1994/11/16	4.5	7	301	64	−11
8	34.84	−13.98	1995/07/22	4.9	33	158	42	−105
9	34.40	−13.82	1995/09/30	4.7	30	321	54	−75
10	34.10	−15.40	1996/08/30	4.5	10	154	71	−109
11	34.89	−13.77	1998/08/24	4.7	44	163	37	−95
12	34.20	−10.10	1999/09/01	4.7	10	022	81	−144
13	36.10	−16.10	2000/01/04	4.8	25	352	66	−70
14	34.23	−9.84	2002/08/31	5.0	20	355	53	−126
15	34.35	−10.08	2004/03/14	4.8	29	017	52	−117
16	34.44	−10.60	2004/08/21	4.7	12	084	75	−17
17	33.85	−10.13	2009/12/06	5.7	6	168	38	−91
18	33.88	−9.95	2009/12/09	5.8	6	167	41	−70
19	33.91	−9.94	2009/12/12	5.5	4	169	37	−95

20	33.82	−10.11	2009/12/19	5.9	5	149	46	−77
21	35.42	−16.76	2018/03/08	5.5	17	316	45	−94

The magnitude of σ_3 can be derived from the following equation related to the effective coefficient of friction (ϕi):

$$\sigma_1 = 2c\sqrt{\frac{1 + sin\phi i}{1 - sin\phi i}} + \sigma_3 \left(\frac{1 + sin\phi i}{1 - sin\phi i}\right) \tag{2}$$

where $\phi i = \tan^{-1} \mu_s$ and μ_s is the frictional strength of intact rock, and c is the cohesive strength. The c value for pre-existing structures (faults, fractures, foliation, etc.) can be considered zero. However, the high-grade metamorphic fabrics of the Malawi Rift are qualitatively cohesive (Williams et al., 2019). For that reason, we will use a Mohr-Coulomb failure criterion with two different stress envelopes: (1) c = 0, and (2) c= ~8 MPa, which is an average derived from sandstone tensile strength between 3.4 and 5.5 MPa estimated by Yasidu et al. (2017) from an indirect tensile strength analysis in the Mchenga mine (Fig. 2B). The μ_s value used in this study is 0.6 chosen by general calculations of solid rocks that vary from 0.47 to 0.7 (e.g., Fossen, 2016) and because μ_s values of the upper crust in Malawi are estimated to be $\mu_s = 0.6$ (e.g., Fagereng, 2013). Byerlee (1978) mentioned μ_s values in the range of 0.3 – 0.6 for rocks composed primarily of quartz and clay minerals. In addition, general μ_s values of sandstones, mudstones, and siltstone rocks in the literature show ranges of ~0.5 to 0.67 (e.g., Wines & Lilly, 2003; Zhang et al., 2019). A value of the frictional coefficient of 0.7 used by Williams et al. (2019) was also evaluated without significant variations in the obtained results (see Appendix A).

Finally, after calculating the magnitudes of the maximum and minimum compression stresses, the magnitude of σ_2 can be estimated from the stress shape ratio equation:

$$\Phi = \frac{\sigma 2 - \sigma 3}{\sigma 1 - \sigma 3} \quad (3)$$

4.4.3 Slip and dilation tendency analysis

We modeled the slip and dilation tendency of the interpreted fracture network geometry in the study area using 3DStress (Southwest Research Institute; Morris & Ferrill, 2009) and MohrPlotter v.3.0 by Richard W. Allmendinger© (2014 – 2019). This analysis will help to determine the reactivation potential of a 3D fault geometry with a high probability of acting as fluid flow pathways (Morris et al., 1996; Siler & Faulds, 2013). For this analysis, the following assumptions were considered:

(1) Two 3D structural models were performed using two different ranges of ~45° and ~60° fault dip angles. These dip angles are like those inferred at depth from geophysical data, structural data measured in the field, focal mechanisms, slope calculation of fault scarps from DSM in the Malawi Rift (Chorowicz & Sorlien, 1992; Delvaux & Bath, 2010; Biggs et al. 2010; Kolawole et al., 2018; Williams et al., 2019; Dávalos-Elizondo & Laó-Dávila, 2022).

(2) The slip-dilation tendency analysis was carried out at two different depths ~700 and 1000 m.b.g.l. These are the estimated depths of the geothermal reservoir in the Chiweta zone based on the results of the SPI method by Dávalos-Elizondo & Laó-Dávila (2022) and the information reported by Gondwe et al. (2021).

(3) The stress state orientation estimated by Williams et al. (2019) of 21 focal mechanisms with depths between 4 to 44 km is assumed to be similar at depths of ~700 to 1000 m in this study. Thus, local variations of the stress field are not considered because the derived principal stresses for a given depth are projected to all fault planes with constant magnitudes and orientations.

(4) pre-existing cohesionless faults were assumed for the 3D Stress software, while a cohesionless and cohesion value of 8 MPa were assumed for the envelopes for the MohrPlotter software (Yasidu et al., 2017).

Jaeger & Cook (1979) and Morris et al. (1996) defined the slip tendency (T_s) as the ratio of shear stress (τ) to normal stress (σ_n) acting on that surface:

$$T_s = \tau / (\sigma_n - P_f) \tag{1}$$

where the normal stress is proportional to the frictional resistance to sliding (e.g., Jaeger & Cook, 1979) and P_f is pore fluid pressure. Slip will occur on a surface when the shear stress exceeds the frictional resistance to sliding (Morris et al., 1996).

The dilation tendency (T_d) was defined by Hobbs et al. (1976) and Ferrill & Morris (2003), as the stress acting normal to a given surface:

$$T_d = (\sigma_1 - \sigma_n) / (\sigma_1 - \sigma_3) \tag{2}$$

where σ_1 is the maximum compressive principal stress and σ_3 is the minimum principal stress.

Then, slip and dilation tendency can be defined as the probability of a plane to slip and/or dilating in a current stress state (Hobbs et al., 1976; Morris et al., 1996). The slip tendency parameter varies from 0 to 0.7 and the dilation tendency varies between 0 and 1 and the higher the value, the higher the probability of failure. Therefore, fluid flow and fault reactivation potential are suggested to be controlled by favorably oriented fractures and their critical stresses for frictional failure (Barton et al., 1995; Sibson, 1996). The critically stressed fault postulation could reach the importance of faults in fluid flow at depth.

4.5 Results

4.5.1 Three-dimensional structural model

The structural model of the Chiweta Zone comprises a total of 52 faults (Fig. 4A and 5), all of them with a normal sense that is consistent with a typically extensional domain. The slip-dilation tendency analysis performed in the 3D Stress software shows that the slip direction of faults has a slightly lateral component. Two major normal fault systems and a third minor domain normal fault system are observed in the 3D structural framework of the study area. We observe the following:

1) A ~NW-SE normal fault system related to the Cenozoic Karonga Fault Zone (KFZ), with a total of 30 NW-striking normal faults with azimuth ranges between ~300° and 340° and both dip-polarities (SW and NE) were identified in the study area. Two graben structures formed by NW-trending normal faults are identified in the study area (see Fig. 4A). Additionally, a graben structure was identified in the southwestern part of the Chiweta Zone, called the Rumphi Graben in this study because the North Rumphi river is following the downward block and forming a river canyon (Fig. 4A). Likewise, a smaller

NW-trending graben is identified where the Chiweta hot spring emerges, referred to as the Chiweta Graben in this study. It is at the Chiweta Graben that the mouth of the North Rumphi River drains into Lake Malawi (Fig. 4A). The fault striking N129˚W and dipping to the SW is called the Chiweta Fault in this study (Fig. 4A).

2) ~NE-SW normal faults are intersected by NW-striking faults. Nineteen normal faults with azimuth ranges between ~20° and 70° and both dip-polarities (SE and NW) are identified in the study area. Three NE-trending half-grabens with SW-dips were identified (see Fig. 4A). This main fault is called the K3 fault in this study because sandstones of the Karoo sequence (K3) is primarily formed the fault scarp (Fig. 4A).

3) The ~N-S normal faults are sub-parallel to the Quaternary Usisya fault and are in the southeastern part of the Chiweta Zone. The azimuth of the N-striking normal faults varies from ~180° to 190° and the fault dips to the east (Fig. 4A).

Finally, we estimated the shallow groundwater movement using boreholes and cold springs data from Tsokonombwe 2017 (see Table 1). The result of the groundwater table using these data shows water levels between ~1277 to 448 m above sea level (m.a.s.l.) from northwest to southeast, respectively (Fig. 4B). The arrows in Fig. 4B display the groundwater flow direction of the study area. The main fluid flow direction moves from the northwest (highlands) to the southeast (lowlands) merging within the Chiweta graben (where hot springs emerge from ~495 m.a.s.l.) and then moving towards the east to Lake Malawi (Fig. 4B). Additionally, fluid flow from the northwest (highlands) appears to follow the NW-trending Rumphi graben (Fig. 4B).

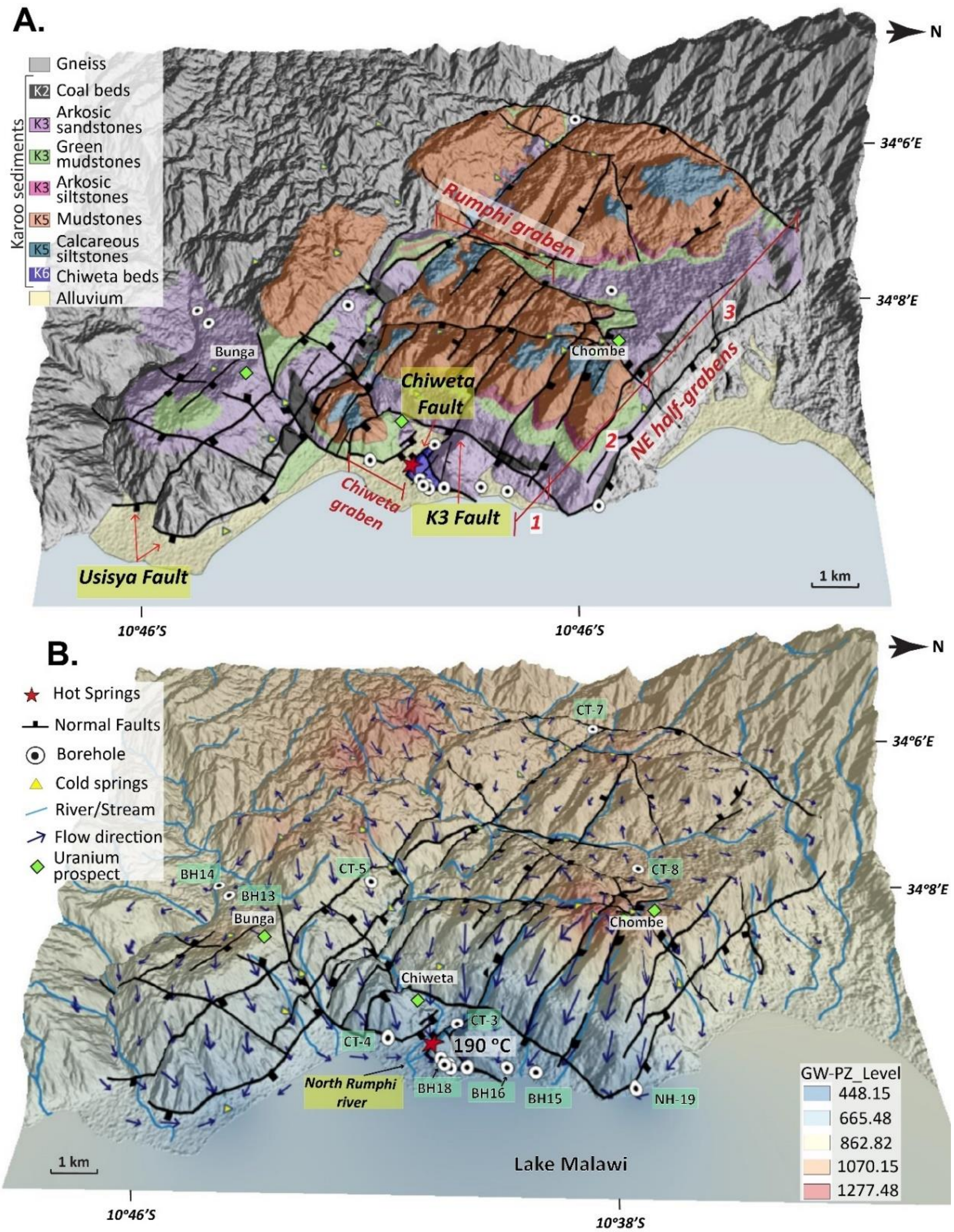

Figure. 4. A. Geological Map of the Chiweta Zone overlying a 3D view of the Digital Surface Model (DSM). B. Piezometric level map (blue-red colormap) and fluid flow direction map overlaying a 3D

view of the DSM estimated based on the borehole data in Table 1 and cold springs (yellow triangles) elevation data. Vertical Exaggeration = 3

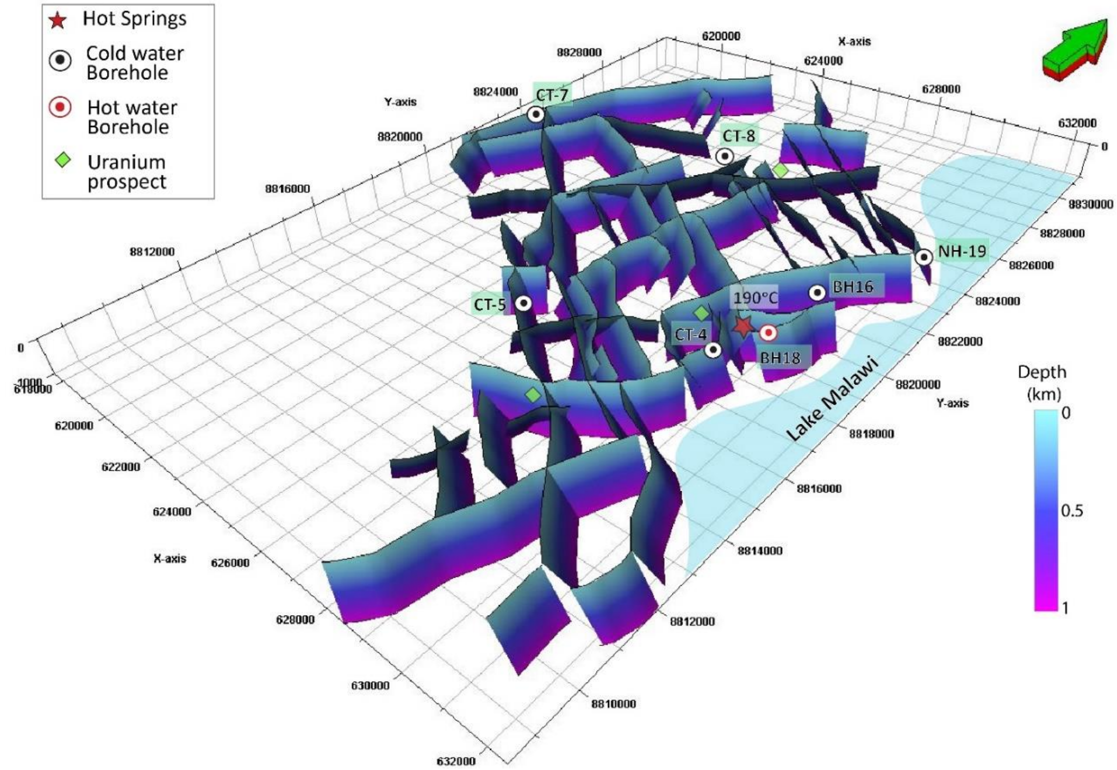

Figure. 5. 3D structural model for the Chiweta Zone showing 52 normal faults identified and projected from the surface to 1000 m depth below ground level. The green arrow shows North.

4.5.2 Magnitudes of principal stress and Mohr circle analysis

The results of the calculated magnitudes of the principal stresses at different depths ~700 and 1000 m.b.g.l. and under the prevailing stress state estimated by Williams et al. (2019) are summarized in Table 3.

The Mohr Circle analysis performed with the MohrPlotter software is summarized in Fig. 6. The slip tendency results show similar values for all the 52 faults when comparing the magnitudes estimated at ~700 and 1000 m.b.g.l. and considering the value of friction coefficient μ_s = 0.6. Our results show that with an envelope of c= 8 MPa all pre-existing faults have slip tendencies of 0 while cohesionless faults show higher values of slip tendencies depending on their orientation and dip angles (Fig. 6; see Appendix A, Fig. S1 shows a Mohr circle with Griffith envelope of c= 16 MPa and μ_s = 0.7). In general, faults performed at 60˚ dip show greater slip tendencies than those performed at 45˚, as argued by Anderson's normal fault theory (Anderson, 1951). In addition, the results show that preexisting fractures oriented from NNW-SSE to NNE-SSSW and dipping southwest and northwest, respectively, have the highest slip tendencies (red colors in Fig. 6 A-D), followed by NE-striking faults and dipping northwest (orange to yellow colors in Fig. 6 A-D). For instance, the NW-striking Chiweta Fault where the hot springs emerge shows high slip tendency values (red to orange colors). The lowest slip tendency values are attributed to faults-oriented NW-SE northeast-dipping, NE-SW southeast-dipping, and ENE-SSW with both dip-polarities (yellow to green colors in Fig. 6 A-D). Finally, the results show that a pore fluid pressure (P_f) value of 11 MPa is needed to cause failure to all cohesionless pre-existing fractures (see Fig. 6E).

Table 3. Magnitudes of the principal stress are estimated at depths ~700 and 1000 meters below the ground level.

			Magnitudes MPa	
Stress State	**Azimuth**	**Plunge angle**	**700 m**	**1000 m**
σ_1	239	79	16	23
σ_2	341	02	11	13
σ_3	072	10	4	6

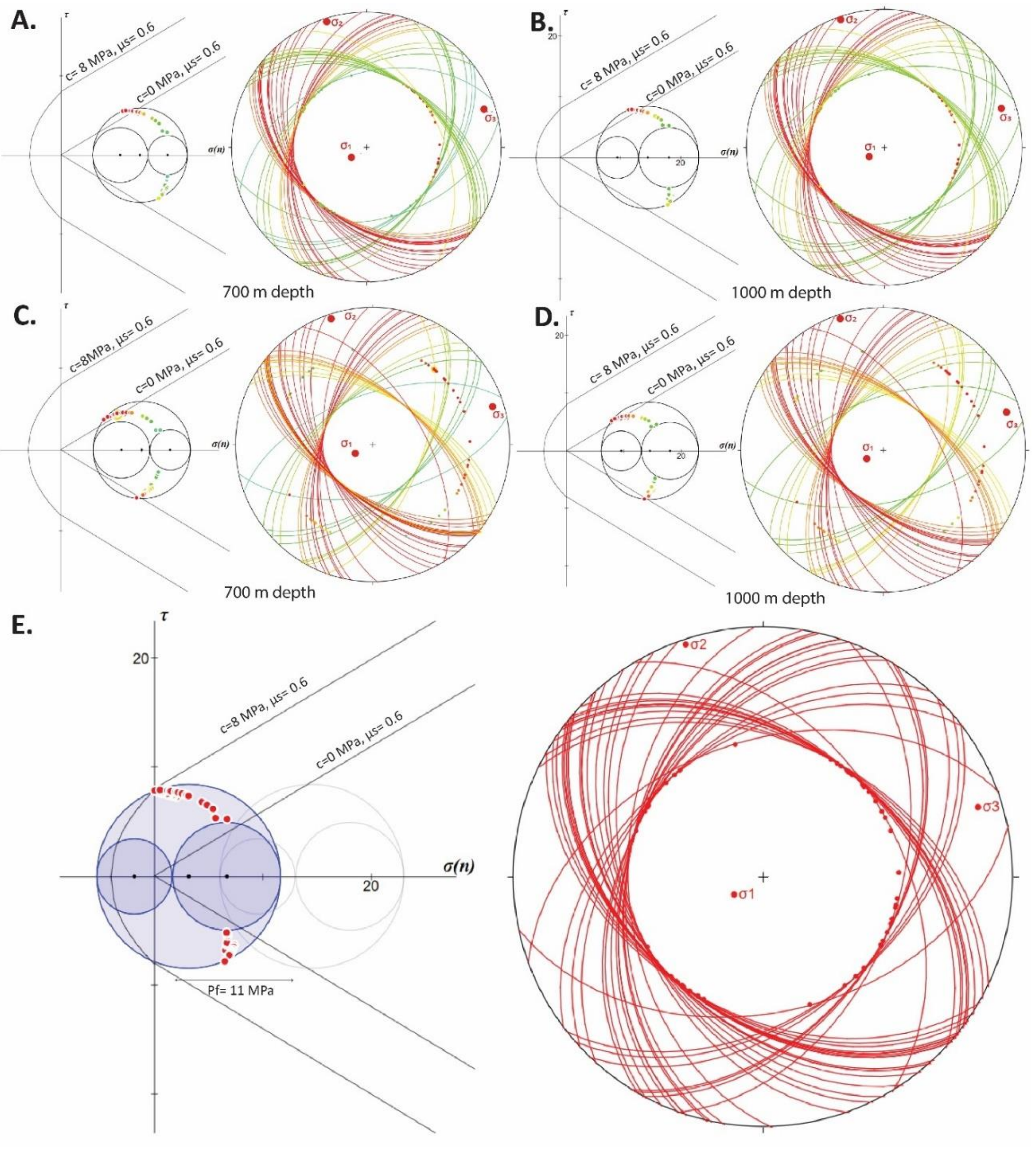

Figure. 6. 3D Mohr circle analysis for slip tendency of 52 normal faults (great circles) at 700 and 1000 m.b.g.l. with failure envelopes c= 0 MPa and c= 8 MPa and a μ_s= 0.6. A. and B. Mohr circle analysis and stereonet showing the slip tendency of an analysis performed at 700 and 1000 m.b.g.l., respectively with faults dipping 45°. C. and D. Mohr circle analysis and stereonet showing the slip tendency of an analysis performed at 700 and 1000 m.b.g.l., respectively with faults dipping 60°. E. Mohr circle analysis and stereonet calculating failure within increasing the pore

fluid pressure (11 MPa). The dots represent the poles of planes. Red and orange colors indicate a higher slip tendency than yellow and green colors.

4.5.3 Slip and dilation tendency analysis

A three-dimensional slip and dilation tendency analysis was estimated for the 52 faults identified in the Chiweta zone (Fig. 5) using the software 3D Stress. Our analysis shows similar slip and dilation tendency results for the estimated depths range of the reservoir (see section 4.2). For that reason, Fig. 7 and 8 show the results only of the analysis estimated at 700 m.b.g.l. but also representative of depth 1000 m.b.g.l (see Appendix B; Fig.S1 and S2).

The 3D model of ~45° dip faults shows low to intermediate dilation tendency values of T_d ~0.1 to T_d ~0.7. Moreover, NW- and NNE-trending faults (Az ~160° – 105° and ~215° – 185°) southwest- and northwest dipping, respectively, show the highest dilation tendency values between T_d ~0.4 to T_d ~0.7 (green and yellow colors in Fig. 7A). While NW-trending faults (Az ~340° – 285°) northeast-dipping and NE-trending faults (Az ~070° – 010°) southeast-dipping display the lowest dilation tendency from T_d ~0.1 to T_d ~0.3 (blue colors in Fig. 7A). The stereo plot in Fig. 7A synthesizes the results showing the variation of poles along-strike of all faults that are plotted in low and intermediate dilation tendency zones.

Slip tendency values of ~45° dip faults range from T_s ~0.2 to T_s ~0.7. The highest slip tendency results (T_s ~0.5 – T_s ~0.7) correspond to segments of NW-trending faults (Az ~160° – 130°) southwest-dipping (red to yellow colors in Fig. 7B), followed by NNE- and

N-trending faults (Az ~200˚ – 185˚) northwest- and west-dipping, respectively (red to yellow colors in Fig. 7B). While intermediate slip tendencies (T_s ~0.3 – T_s ~0.5) are mainly related to segments of NW-trending faults (Az ~325˚ – 290˚) northeast-dipping and NE-trending faults (Az ~070˚ – 010˚) southeast-dipping (green to yellow colors in Fig. 7B). The stereo plot in Fig. 7B synthesizes the results showing the variation of poles along-strike of all faults that are plotted in low and intermediate dilation tendency zones.

The 3D structural framework of ~60˚ dip faults shows a higher dilation tendency than ~45˚ dip faults. The dilation tendency shows intermediate to high values of T_d ~0.3 to T_d ~1.0. The highest dilation tendency values (T_d ~0.7 – T_d ~0.1) correspond to segments of NW-trending faults (Az ~165˚ – 115˚) southwest-dipping (red and yellow colors in Fig. 8A), followed by NNE-trending faults (Az ~200˚ – 185˚) northwest-dipping (red and yellow colors in Fig. 8A). The stereo plot in Fig. 8A synthesizes the results showing the variation of poles along-strike of all faults that are plotted in low and intermediate dilation tendency zones.

The slip tendency also shows higher values in ~60˚ dip faults. The intermediate and high values range from T_s ~0.3 to T_s ~0.7. The highest slip tendency values (T_s ~0.6 to T_s ~0.7; red colors in Fig. 8B) correspond to segments of faults NNW- (Az ~160˚ – 130˚ & ~340˚ – 300˚), NNE- and N- trending (Az ~210˚ – 190˚ and ~350˚ – 010˚). While the lower slip tendency values (T_s ~0.3 - T_s ~0.5) are related to segments of faults WNW- and ENE-trending. The stereo plot in Fig. 8B synthesizes the results showing the variation of poles along-strike of all faults that are plotted in low and intermediate dilation tendency zones.

Furthermore, it is important to mention that the Chiweta Fault with a dip of 45˚ or 60˚ shows high to intermediate values of both slip and dilation tendency (Ts ~0.5 – Ts ~0.7 and T_d ~0.5 – T_d ~0.1).

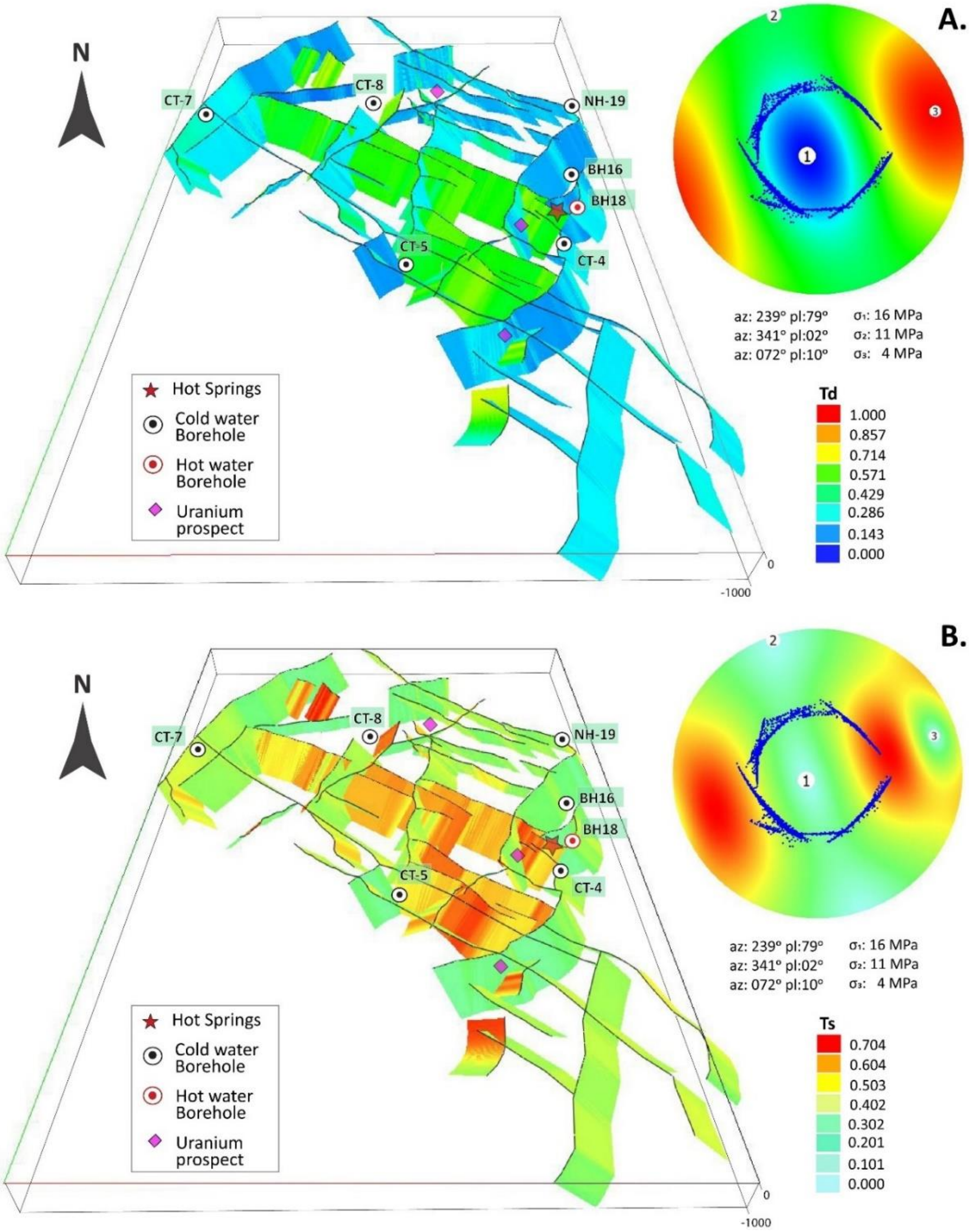

Figure. 7. 3D Structural Model of the Chiweta Geothermal Zone. A. Dilation tendency and B. Slip tendency, both showing the stereonet with poles along-strike variation of the 52 normal faults

with 45° dip. Analysis performed at 700 m.b.g.l. equal to the overburden pressure calculated with a rock density of 2.3 g/cm^3 and a frictional coefficient value of 0.6.

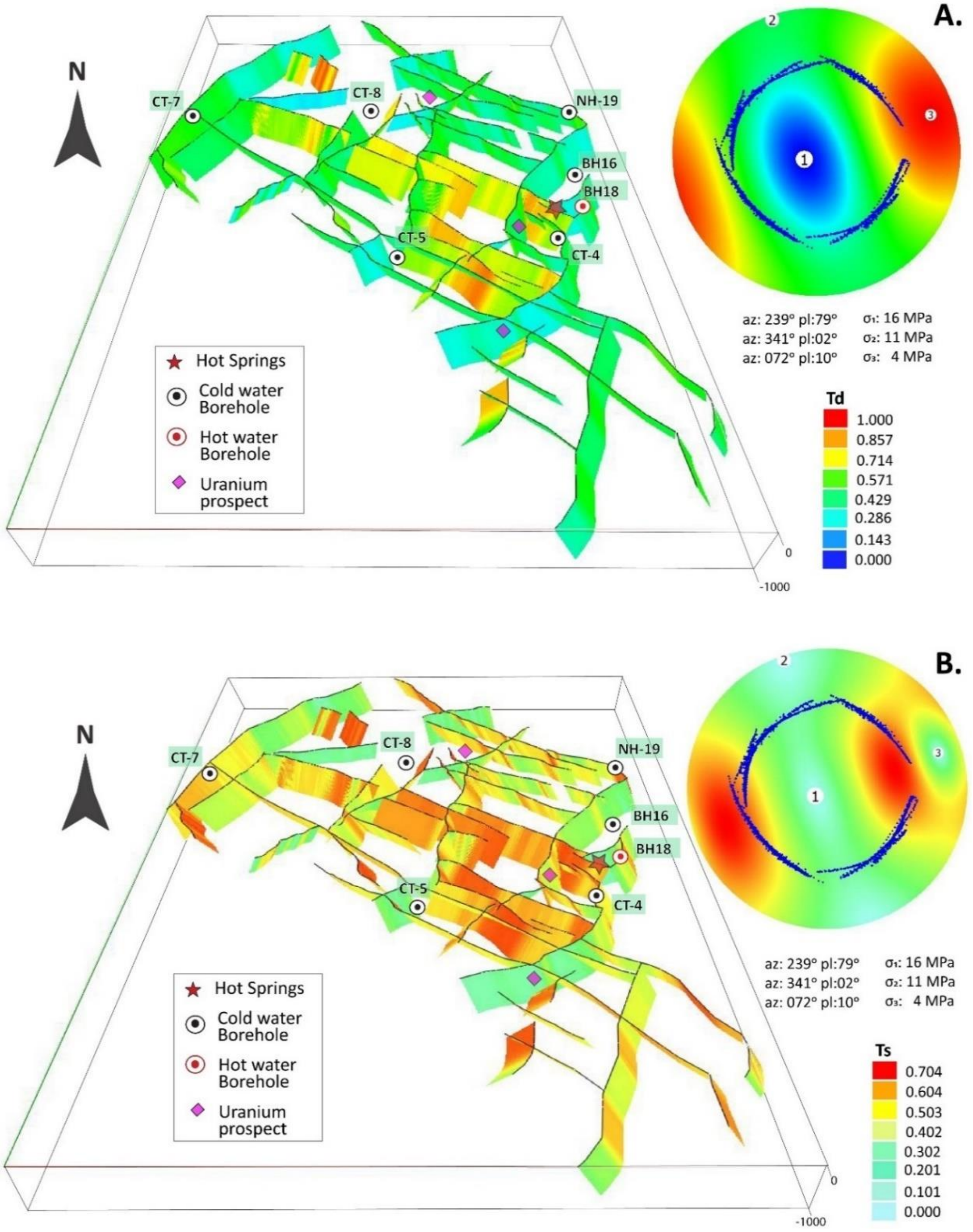

Figure. 8. 3D Structural Model of the Chiweta Geothermal Zone. A. Dilation tendency and B. Slip tendency, both showing the stereonet with poles along-strike variation of the 52 normal faults

with 60° dip. Analysis performed at 700 m.b.g.l. equal to the overburden pressure calculated with a rock density of 2.3 g/cm^3 and a frictional coefficient value of 0.6.

4.6 Discussions

4.6.1 The Chiweta Geothermal System

The 3D structural model supports that the CGS is a structurally controlled geothermal system that can also be classified as controlled by structural leakage (Moeck, 2014). Therefore, the CGS is not only controlled by structures but is also classified as a sedimentary and advective geothermal system, where changes in lateral permeability and hydraulic transmissivity are important aspects to consider.

Our reported data suggest that the CGS is probably part of a confined aquifer, compartmentalized primarily by NE-SW and NW-SE trending faults. We proposed a possible reservoir delimitation (Fig. 9A) based on the analysis of all the data collected by this study (e.g., geology, geochemistry of thermal water, hydrogeology, geophysical data) and the results of the slip-dilation tendency analysis in this research. However, possible reservoir dimensions and a more accurate reservoir geometry cannot be established until more advanced exploration and production stages of the field are reached.

The NE-striking normal fault (K3 Fault) southeast-dipping is suggested to have a total fault throw of 1000 m and be responsible for a hanging wall block formation, where the hot springs are located (Tsokonombwe, 2017). Our structural analysis shows that the K3 Fault has low to intermediate dilation and slip tendencies under the stress state estimated by Williams et al. (2019). For this reason, the K3 Fault appears to be a plausible structural boundary to the northwestern of the CGS (Fig. 9A). On the other hand, a NW-striking normal fault northeast-dipping (K5 Fault in Fig. 9A) with lower slip and dilation tendency values could also be a barrier of the CGS to the southwestern side (Fig. 9A), considering the distance of the surface manifestation and the fault reactivation potential.

The southeastern and northeastern limits are not yet well defined. Our results suggest that the northeastern boundary is the buried continuation of a NW-striking normal fault northeast dipping (CT1-Fault in Fig. 9A). This assumption is considering the low reactivation potential of this structure and the distance from the hot water borehole (BH18) located northeast of the surface thermal manifestations (Fig. 9A).

Likewise, Tsokonombwe (2017) mentioned the difficulty of identifying a possible boundary on the southeastern side of the CGS and recommended subsurface geophysical surveys to delineate hidden structures. Afterward, data reported by Dávalos-Elizondo & Laó-Dávila (2022) using aeromagnetic data, such as the Tilt derivative and SPI method, showed buried structures under Lake Malawi. Particularly in the CGS, N- and NE-striking faults can be delineated by following the SPI magnetic basement depths (light blue color line in Fig. 10A). Dávalos-Elizondo & Laó-Dávila (2022) suggested that the N-striking alignment may be related to the northern extension of the Usisya fault towards the CGS. While the NE-trend alignment is probably the northeast extension of a reactivated Karoo basin border major fault.

Therefore, we propose that the possible southeastern boundary is a combination of both hidden N- and NE- striking structures (Fig. 9A). Additionally, Tsokonombwe (2017) argued that a possible southeastern hidden structure acts as a barrier preventing water intrusion from Lake Malawi, which is located 2 km from the hot springs. In that regard, the geochemical data reported in the Chiweta hot springs show that there are no signs of recharge waters from Lake Malawi (e.g., Tsokonombwe, 2007; Dávalos-Elizondo et al., 2021).

The shallow groundwater movement estimated in this study using data from Tsokonombwe (2017) is consistent with previous results suggesting that the main recharge in the geothermal system comes from northwest and western highlands (Fig. 9A). Meteoric water is driven by a hydraulic gradient from an elevation above ~1277 m to elevations of ~448 m in the southeastern lowlands (Fig. 4A). Similarly, hot springs geochemical data reported by other studies (e.g., Tsokonombwe, 2007; Dávalos-Elizondo et al., 2021) support the argument that the hot springs are associated with local meteoric waters (Ca-Mg-HCO_3) deeply infiltrated. Fig. 9A shows the fluid flow of shallow groundwater coming from NW and W highlands, suggesting that meteoric waters seep deep underground through the NE-striking fault (K3 Fault) and NW-striking fault (K5 Fault) before rising heated by the anomalous gradient through the Chiweta Fault.

The geothermal conceptual model suggested by this study (Fig. 9B) shows that the infiltrated waters percolate at least 1000 m.b.g.l. before being heated by a high heat flow reported in the region (Njinju et al., 2019). Njinju et al. (2019) mentioned that radioactive decay of Uranium deposits could contribute to increasing the heat flow in the Karoo basin regions. Interestingly, a uranium prospect named Chiweta (Ministry of Energy and Mines, 2009) is located northwestern of the Chiweta hot spring (Fig. 9A). This is an important observation because the heat source of the geothermal system has been undetermined and poorly understood, and radioactive decay can serve as an additional heat source for the CGS, which is also considered a non-magmatic geothermal system. Herein, radioactive decay could be a good explanation of why Chiweta is one of the hottest geothermal systems (190 °C; Dávalos-Elizondo et al., 2021) in the entire MRZ. Further studies of these roll-front uranium deposits are needed to estimate the contribution of heat from radioactive decay. Additionally, other uranium prospects located in the Livingstonia basin (Chombe and Bunga; Fig. 2B) reported by the Ministry of Energy and Mines (2009) could be potential areas to explore for hidden geothermal systems.

Moreover, uranium deposits are reported to be economically concentrated within Karoo sandstones (K3; Ministry of Energy and Mines, 2009) directly above the coal measures sequence or of the basement rock (Fig. 9B). Both layers are suggested to be the reservoir of geothermal fluids in the CGS (Fig. 9B; Tsokonombwe, 2017) at depths between ~700 to 1000 m.b.g.l. (e.g., Gondwe et al., 2021; Dávalos-Elizondo & Laó-Dávila, 2022). Tsokonombwe (2017) suggested that beds of mudstones, calcareous mudstones, and siltstone (K3 – K5) cap the Chiweta geothermal reservoir (Fig. 9B).

The chemistry of the waters begins to change from Ca-Mg (HCO_3) to Na-HCO_3[SO_4] and Na-Cl [SO_4]) due to processes, such as heating the meteoric waters by the anomalous gradient and water-rock interactions in the reservoir. Then, thermal waters migrate upwards due to the density difference between hot and cold water (Fig. 9B). The latter constitutes an up-flow zone that in the case of the CGS is a NW-striking fault dipping to the southeast (Fig. 9B). This NW-striking fault (Chiweta Fault) forms a small graben within its antithetic NW-striking fault (Fig. 9B). The slip-dilation tendency analysis shows that the Chiweta Fault is favorably oriented under the stress state conditions and has high values of slip and dilation tendencies (Fig. 9B). Hence, it is controlling subsurface fluid flow that reaches the surface with a temperature of 80 °C in the CGS (Fig. 9B). We suggest based on our results that the Chiweta Fault and the arkose sandstones layer (K3; see Fig. 3A) are good targets for drilling an exploratory geothermal well. Additionally, it is suggested that the CGS is a liquid-dominant reservoir, for that reason a study by Mwagomba (2013) suggested a binary cycle geothermal power generation plant.

4.6.2 Reactivation potential

The dilation tendency analysis performed in the Chiweta Zone on the proposed structural framework and under the stress state proposed by Williams et al. (2019) suggests the existence of a preferential fluid path constrained by NNW-striking and southwest dipping normal faults (sub-parallel to the Livingstone Fault). On the other hand, the results indicate that southeast dipping NE- striking faults and northeast-dipping NW-striking faults probably act as hydrological barriers (Fig. 7A, 8A, and 10B). This is supported by the argument that dilation tendency is a more reliable proxy for assessing permeability and fluid flow across faults (Faulds et al., 2006; Jolie et al., 2015; Barcelona et al., 2019)

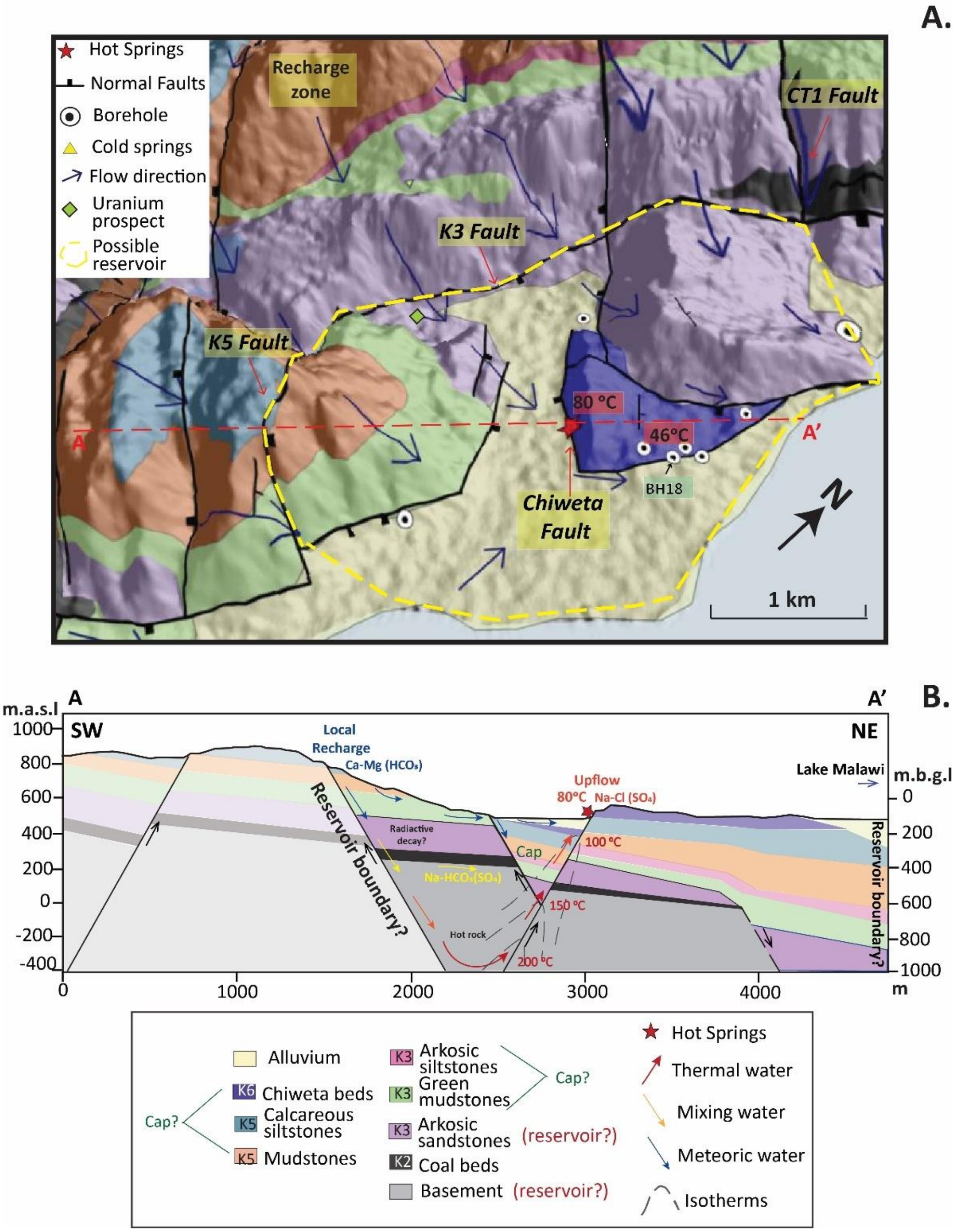

Figure. 9. A. Simplified Chiweta geothermal prospect map overlaying a 3D view of the Digital Surface Model. B. Geothermal conceptual model of the Chiweta geothermal system.

The fault reactivation potential together with the estimated water table could explain not only the alignment of hot springs on the Chiweta Fault (NW-striking southwest-dipping) but also the lack of hydrothermal manifestations in other areas of the Chiweta Zone. The geometry of the Chiweta Fault oriented N129°W and moderately (~45° – 60°) dipping southwest has dilation tendency values from $T_d \sim 0.6$ to $T_d \sim 0.8$ estimated at depths between ~700 and 1000 m.b.g.l. (Fig. 7A, 8A, and 10B), which are the proposed depths of the geothermal reservoir (e.g., Gondwe et al., 2021; Dávalos-Elizondo & Laó-Dávila, 2022). On the other hand, the faults considered barriers of the geothermal system (e.g., K3 and K5 Faults; Fig. 9) show lower values of dilation tendency from $T_d \sim 0.1$ to $T_d \sim 0.5$ (Fig. 7A, 8A, and 10B). Furthermore, according to the results of the stereo plots (see Fig.7 and 8), the highest dilation tendency would occur in favorably oriented structures with steeply (> 80°) dips. This is an important implication to consider in other geothermal zones of the MRZ, where reactivated foliation planes appear directly as favorable structural controls of the geothermal fluids (Dávalos-Elizondo & Laó-Dávila, 2022).

The slip tendency analysis using Mohr plotter and 3D stress software show similar results, even using a different overburden pressure calculated with a basement rock density of 2.65 g/cm^3 and a frictional coefficient value of 0.7 (see Appendix A). Nevertheless, the slip tendency results should be viewed with caution because fault slip is very susceptible to slight variations of subvertical maximum stress and magnitudes. The slip tendency under the same stress state conditions (Williams et al., 2019) shows the highest reactivation potential in NW-striking and SW-dipping faults and NNE-striking and NW-dipping faults (similar to the dilation tendency values) at ~700 – 1000 m.b.g.l. (Fig. 7B). But slip tendency values increase in some segments of favorably oriented faults with steeper (60°) dip-polarities (Fig. 8B and 10A). Following these results, the slip-tendency of the Chiweta Fault is also reaching the highest values from T_s ~ 0.6 to T_s ~ 0.7. However, unlike the dilation tendency values, some segments of the suggested barrier structures (K3 and K5 Faults; Fig. 9) with intermediate (~60°) dip, show high to intermediate slip tendencies values from T_s ~ 0.7 to T_s ~ 0.4.

The general concept of maximum slip- and dilation tendencies does not necessarily imply that faults are close to slipping or dilating. However, other important parameters need to be present, such as high pore fluid pressure values, to cause failure. Thus, segments with a higher slip-dilation tendency along favorably oriented faults would have higher probabilities of reactivation potential. In this regard, an increase of P_f =11 MPa would cause failures (see Fig. 6E) to all 52 faults (assuming a value of cohesionless for pre-existing fractures). In the case of the Chiweta Fault, the presence of hot springs suggests that the fault will have higher P_f values and thus a high reactivation potential.

Additionally, Fig. 10 shows a correlation between the deepest magnetic basement depths (Dávalos-Elizondo & Laó-Dávila, 2022) and the high reactivation potential values of faults estimated by this study. Likewise, the results of this study demonstrate the high reactivation potential not only for structures related to the Cenozoic rift (NNW- and N-striking) but also for specific segments of the Permo-Triassic Karoo rifting (NNE-striking) show high reactivation potential under the stress state condition.

Finally, all the structural results presented in this study are important from a geothermal point of view but also for geohazard assessment in the Geothermal Zone as a seismically active region and susceptible to landslide (e.g., Tsokononbwe, 2017). This seismic hazard is evidenced by the results of high reactivation potential for some favorable geometry of faults, but also by the results of pore fluid pressure that shows that structures transporting fluids can be more susceptible to failure.

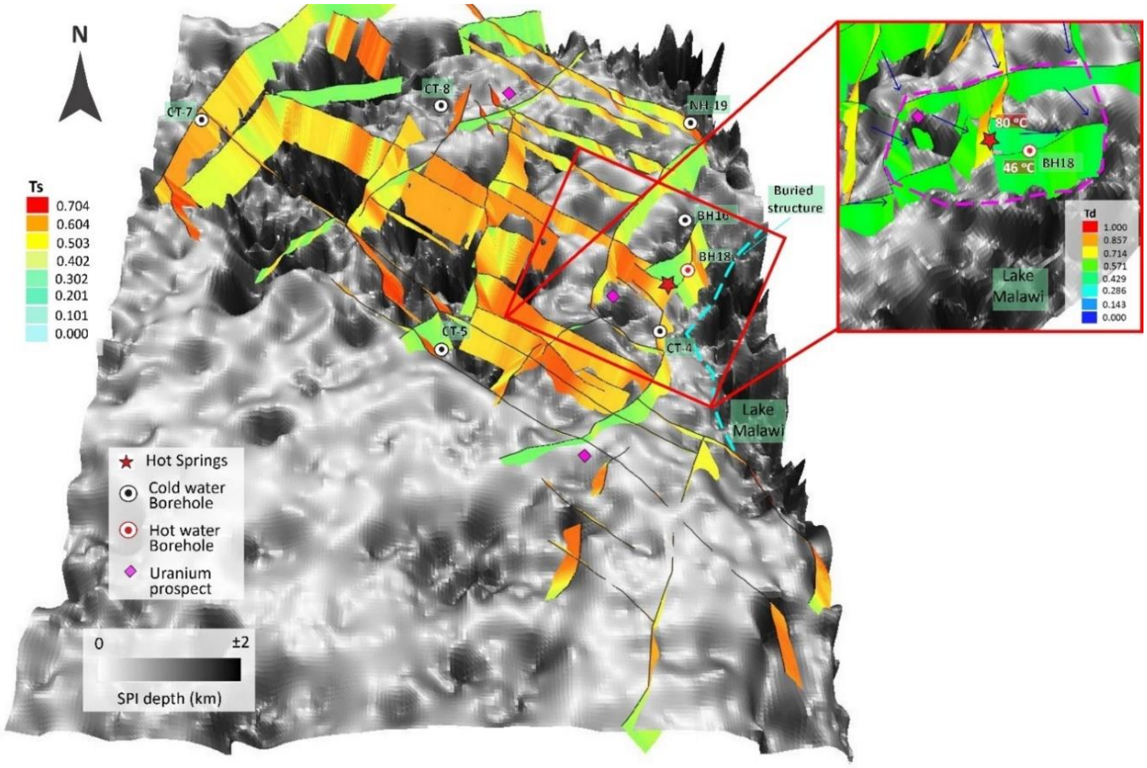

Figure. 10. A. 3D Slip tendency analysis of 52 normal faults in Fig. 8B overlying a 3D view of the SPI magnetic basement depth (Dávalos-Elizondo & Laó-Dávila, 2022). B. 3D Dilation tendency analysis of faults in Fig. 8A located in the Chiweta Geothermal prospect overlying a 3D view of the SPI magnetic basement depth (Dávalos-Elizondo & Laó-Dávila, 2022).

4.7 Conclusions

The purpose of this study was to investigate the architecture of structures and their reactivation potential in the Chiweta Zone. A combined approach of 3D structural modeling and slip-dilation tendency analysis, together with the assessment of already published geological, geochemistry, and geophysical data, allowed us to characterize the main geothermal system in the area and identify favorable structures that assist as geothermal fluids conduits and barriers.

The slip-dilation tendency analysis applied to 52 faults identified in the study area and carried out at depths of the estimated reservoir, shows that NW- to NNE-striking faults southwest- and northwest dipping are critically stressed for dilation. While NW- and NE-striking faults northeast and southeast dipping, respectively have low to intermediate dilation tendency. These results are consistent with the N129°W striking southwest dipping (~55° – 60°) normal faults that control the outcrop of geothermal fluids at the surface in the Chiweta geothermal prospect. Likewise, the identification of structures with low to intermediate reactivation potential at the Chiweta geothermal prospect served to define for the first time possible structural boundaries of the geothermal system. Additionally, the integration of all the information available and generated by this study allowed to improve the geothermal conceptual model (Fig. 9).

The results of this study were not limited to the CGS and may help identify hidden geothermal potential zones in the future. Furthermore, our observations about a uranium deposit near the thermal manifestations should be taken into consideration for future studies because it could play an important role as a source of radioactive decay heat. Additional studies are needed to improve and validate this model, including more subsurface geophysical data, such as magnetotelluric and seismic surveys, geomechanics of the sedimentary rocks, as well as data from deep exploration wells once the exploration stage progresses to this point.

Finally, the results of this study provide forecasting and visualization of favorable structures that control fluid pathways and storage of geothermal waters, as well as a holistic understanding of the geothermal system. All this information could be used to target the first exploratory wells in the Chiweta geothermal prospect. The applied methodology is expected to be used not only in Malawi but also around the Western Branch of the EARS, where structurally controlled systems are prevalent but not well understood.

4.8 References

Accardo, N. J., Gaherty, J. B., Shillington, D. J., Ebinger, C. J., Nyblade, A. A., Mbogoni, G. J., Chindandali, P. R. N., Ferdinand, R. W., Mulibo, G. D., Kamihanda, G., & Keir, D. (2017). Surface wave imaging of the weakly extended Malawi Rift from ambient-noise and teleseismic Rayleigh waves from onshore and lake-bottom seismometers. Geophysical Journal International, 209(3), 1892-1905.

Accardo, N. J., Gaherty, J. B., Shillington, D. J., Hopper, E., Nyblade, A. A., Ebinger, C. J., Scholz, C.A., Chindandali, P.R.N., Wambura-Ferdinand, R., Mbogoni, G. & Russell, J.B., (2020). Thermochemical modification of the upper mantle beneath the northern Malawi Rift is constrained from shear velocity imaging. Geochemistry, Geophysics, Geosystems, 21(6), e2019GC008843.

Barcelona, H., Yagupsky, D., Vigide, N., & Senger, M. (2019). Structural model and slip-dilation tendency analysis at the Copahue geothermal system: inferences on the reservoir geometry. Journal of Volcanology and Geothermal Research, 375, 18-31.

Barton, C. A., Hickman, S., Morin, R. H., Zoback, M. D., Finkbeiner, T., Sass, J., & Benoit, D. (1997). Fracture permeability and its relationship to in-situ stress in the Dixie Valley, Nevada, geothermal reservoir.

Barton, C. A., Zoback, M. D., & Moos, D. (1995). Fluid flow along potentially active faults in crystalline rock. Geology, 23(8), 683-686.

Bechtel, T. D., Forsyth, D. W., & Swain, C. J. (1987). Mechanisms of isostatic compensation in the vicinity of the East African Rift, Kenya. Geophysical Journal International, 90(2), 445-465.

Bennett, J. D. (1989). Review of Lower Karoo coal basins and coal resource development in parts of central and southern Africa with particular reference to northern Malawi. British Geological Survey.

Byerlee, J. (1978). Friction of rocks. In Rock friction and earthquake prediction (pp. 615-626). Birkhäuser, Basel.

Bloomfield, K. (1968). The pre-Karoo geology of Malawi. Government Printer, South Africa.

Bloomfield, K., & Garson, M. S. (1965). The Geology of the Kirk Range, Lisungwe Valley Area: Government Printer.

Bjørlykke, K., Høeg, K., & Mondol, N. H. (2015). Introduction to Geomechanics: stress and strain in sedimentary basins. In Petroleum geoscience (pp. 301-318). Springer, Berlin, Heidelberg.

Caine, J. S., Evans, J. P., & Forster, C. B. (1996). Fault zone architecture and permeability structure. Geology, 24(11), 1025-1028

Caine, J. S., & Forster, C. B. (1999). Fault zone architecture and fluid flow: Insights from field data and numerical modeling. Geophysical Monograph-American Geophysical Union, 113, 101-128.

Chorowicz, J. (2005). The East African rift system. Journal of African Earth Sciences, 43(1-3), 379-410. doi:10.1016/j.jafrearsci.2005.07.019

Chorowicz, J., & Sorlien, C. (1992). Oblique extensional tectonics in the Malawi Rift, Africa. Geological Society of America Bulletin, 104(8), 1015-1023.

Dávalos-Elizondo and Laó-Dávila, D.A. (2019). Structural controls and slip tendency in the Chiweta geothermal zone: Northern part of the Malawi Rift, Africa. A progress report: Geothermal Resources Council Transactions, v. 43.

Dávalos-Elizondo, E. and Laó-Dávila, D.A., (2022), Structural analysis of fracture networks controlling geothermal fluid flow in the northern part of the Malawi Rifted Zone from aeromagnetic and remote sensing data. Manuscript submitted for publication.

Dávalos-Elizondo, E., Atekwana, E. A., Atekwana, E. A., Tsokonombwe, G., & Laó-Dávila, D. A. (2021). Medium to low enthalpy geothermal reservoirs estimated from geothermometry and mixing models of hot springs along the Malawi Rift Zone. Geothermics, 89, 101963.

Dawson, S. M., Laó-Dávila, D. A., Atekwana, E. A., & Abdelsalam, M. G. (2018). The influence of the Precambrian Mughese Shear Zone structures on strain accommodation in the northern Malawi Rift. Tectonophysics, 722, 53-68.Delvaux, D. (2001). Tectonic and palaeostress evolution of the Tanganyika-Rukwa-Malawi rift segment, East African Rift System. Peri-Tethys Memoir, 6, 545-567.

Delvaux, D., & Barth, A. (2010). African stress pattern from formal inversion of focal mechanism data. Tectonophysics, 482(1-4), 105-128.

Dimmen, V., Rotevatn, A., Peacock, D. C., Nixon, C. W., & Nærland, K. (2017). Quantifying structural controls on fluid flow: Insights from carbonate-hosted fault damage zones on the Maltese Islands. Journal of Structural Geology, 101, 43-57.

Ebinger, C. J. (1989). Tectonic development of the western branch of the East African rift system. Geological Society of America Bulletin, 101(7), 885-903.

Ebinger, C. J., Deino, A. L., Drake, R. E., & Tesha, A. L. (1989). Chronology of volcanism and rift basin propagation: Rungwe volcanic province, East Africa. Journal of Geophysical Research: Solid Earth, 94(B11), 15785-15803.

Ebinger, C. J., Rosendahl, B., & Reynolds, D. (1987). Tectonic model of the Malaŵi rift, Africa. Tectonophysics, 141(1-3), 215-235.

Ebinger, C., Crow, M., Rosendahl, B., Livingstone, D., & LeFournier, J. (1984). Structural evolution of Lake Malawi, Africa. Nature, 308(5960), 627.

Eichhubl, P., Greene, H. G., Naehr, T., & Maher, N. (2000). Structural control of fluid flow: offshore fluid seepage in the Santa Barbara Basin, California. Journal of Geochemical Exploration, 69, 545-549.Fagereng, Å. (2013). Fault segmentation, deep rift earthquakes and crustal rheology: Insights from the 2009 Karonga sequence and seismicity in the Rukwa–Malawi rift zone. Tectonophysics, 601, 216-225. doi:10.1016/j.tecto.2013.05.012.

Faulds, J. E., Coolbaugh, M. F., Vice, G. S., & Edwards, M. L. (2006). Characterizing structural controls of geothermal fields in the northwestern Great Basin: A progress report. Geothermal Resources Council Transactions, 30, 69-76.

Faulds, J., & Hinz, N. (2015, April). Favorable tectonic and structural settings of geothermal systems in the Great Basin region, western USA: Proxies for discovering blind geothermal systems. In Proceedings World Geothermal

Congress, Melbourne, Australia, 19-25 April 2015 (No. DOE-UNR-06731-02). Nevada Bureau of Mines and Geology, University of Nevada, Reno.

Faulds, J. E., Hinz, N. H., Coolbaugh, M. F., Cashman, P. H., Kratt, C., Dering, G., Mayhew, B. & McLachlan, H. (2011). Assessment of favorable structural settings of geothermal systems in the Great Basin, western USA. Geothermal Resources Council Transactions, 35, 777-783.

Ferrill, D. A., & Morris, A. P. (2003). Dilational normal faults. Journal of Structural Geology, 25(2), 183-196.

Flannery, J., & Rosendahl, B. (1990). The seismic stratigraphy of Lake Malawi, Africa: implications for interpreting geological processes in lacustrine rifts. Journal of African Earth Sciences (and the Middle East), 10(3), 519-548.

Fossen, H. (2016). Structural geology. Cambridge university press.

Fossen, H., & Rotevatn, A. (2016). Fault linkage and relay structures in extensional settings—A review. Earth-Science Reviews, 154, 14-28.

Fritz, H., Abdelsalam, M., Ali, K.A., Bingen, B., Collins, A.S., Fowler, A.R., Ghebreab, W., Hauzenberger, C.A., Johnson, P.R., Kusky, T.M. and Macey, P., (2013). Orogen styles in the East African Orogen: a review of the Neoproterozoic to Cambrian tectonic evolution. Journal of African Earth Sciences, 86, 65-106.

Ghosh, K. and Mitra, S., (2009). Structural controls of fracture orientations, intensity, and connectivity, Teton anticline, Sawtooth Range, Montana. AAPG bulletin, 93(8), 995-1014.

Gondwe, K., Allen, A., Georgsson, L., Loga, U., & Tsokonombwe, G. (2012, November). Geothermal Development in Malawi–a Country Update. In Proceedings 4th African Rift Geothermal Conference, Nairobi, Kenya (pp. 21-23).

Grijalva, A., Nyblade, A. A., Homman, K., Accardo, N. J., Gaherty, J. B., Ebinger, C. J., & Ferdinand, R. W. (2018). Seismic Evidence for Plume-and Craton-Influenced Upper Mantle Structure Beneath the Northern Malawi Rift and the Rungwe Volcanic Province, East Africa. Geochemistry, Geophysics, Geosystems.

Hinz, N. H., Cumming, W. B., & Sussman, D. (2018). Exploration of fault-related deep-circulation geothermal resources in the western branch of the East African Rift System: examples from Uganda and Tanzania. In Proceedings, 7th African Rift Geothermal Conference, Kigali, Rwanda 31st October–2nd November.

Hobbs, B.E., Means, W.D., Williams, P.F. (1976). An Outline of Structural Geology. John Wiley, New York, N.Y (1976), 571.

Jaeger, J. C., Cook, N. G., & Zimmerman, R. (2009). Fundamentals of rock mechanics. John Wiley & Sons.

Jolie, E., Faulds, J., & Moeck, I. (2012). The development of a 3D structural–geological model as part of the geothermal exploration strategy—a case study from the

Brady's geothermal system, Nevada, USA. In Proceedings, thirty-seventh workshop on geothermal reservoir engineering, Stanford University (pp. 421-5).

Jolie, E., Moeck, I., & Faulds, J. E. (2015). Quantitative structural–geological exploration of fault-controlled geothermal systems—a case study from the Basin-and-Range Province, Nevada (USA). Geothermics, 54, 54-67.

Kalebe, Y. N. (2018). Chemical and isotopic composition of thermal waters in northern part of Malawi. United Nations University, UNU Geothermal Training Programme, Iceland. Report; 2017: 13.

Kemp, J. (1975). The geology of the Uzumara area. South Africa: Government Printer.

Kolawole, F., Atekwana, E. A., Laó-Dávila, D. A., Abdelsalam, M. G., Chindandali, P. R., Salima, J., & Kalindekafe, L. (2018). Active Deformation of Malawi Rift's North Basin Hinge Zone Modulated by Reactivation of Preexisting Precambrian Shear Zone Fabric. Tectonics, 37(3), 683-704.

Laó-Dávila, D. A., Al-Salmi, H. S., Abdelsalam, M. G., & Atekwana, E. A. (2015). Hierarchical segmentation of the Malawi Rift: The influence of inherited lithospheric heterogeneity and kinematics in the evolution of continental rifts. Tectonics, 34(12), 2399-2417. doi:10.1002/2015tc003953.

Maneya, G. J. (2012). An integrated study of coal geology and potential environmental impact assessment at Mchenga Coal Mine IN Livingstonia Coalfield in Malawi (Doctoral dissertation, University of Fort Hare).

McCartney, T., & Scholz, C. A. (2016). A 1.3-million-year record of synchronous faulting in the hangingwall and border fault of a half-graben in the Malawi (Nyasa) Rift. Journal of Structural Geology, 91, 114-129. doi:10.1016/j.jsg.2016.08.012.

McFarland, J. M., Morris, A. P., & Ferrill, D. A. (2012). Stress inversion using slip tendency. Computers & Geosciences, 41, 40-46

Ministry of Energy and Mines of Malawi (2009). Mineral potential of Malawi. Lilongwe, Malawi, November, 2009.

Moeck, I. S. (2014). Catalog of geothermal play types based on geologic controls. Renewable and Sustainable Energy Reviews, 37, 867-882.

Moeck, I., Kwiatek, G., & Zimmermann, G. (2009). Slip tendency analysis, fault reactivation potential and induced seismicity in a deep geothermal reservoir. Journal of Structural Geology, 31(10), 1174-1182.

Morris, A. P., & Ferrill, D. A. (2009). The importance of the effective intermediate principal stress (σ′ 2) to fault slip patterns. Journal of Structural Geology, 31(9), 950-959.

Morris, A., Ferrill, D. A., & Henderson, D. B. (1996). Slip-tendency analysis and fault reactivation. Geology, 24(3), 275-278.

Mortimer, E., Paton, D. A., Scholz, C. A., Strecker, M. R., & Blisniuk, P. (2007). Orthogonal to oblique rifting: effect of rift basin orientation in the evolution of the North basin, Malawi Rift, East Africa. Basin Research, 19(3), 393-407.

Njinju, E. A., Kolawole, F., Atekwana, E. A., Stamps, D. S., Atekwana, E. A., Abdelsalam, M. G., and Mickus, K. L., (2019). Terrestrial heat flow in the Malawi Rifted Zone, East Africa: Implications for tectono-thermal inheritance in continental rift basins: Journal of Volcanology and Geothermal Research.

Nyblade, A. A., & Langston, C. A. (1995). East African earthquakes below 20 km depth and their implications for crustal structure. Geophysical Journal International, 121(1), 49-62.

Reed, M. J. (1982). Assessment of low-temperature geothermal resources of the United States-1982 (No. USGS-CIRC-892). Geological Survey, Menlo Park, CA (USA).

Ring, U. (1994). The influence of preexisting structure on the evolution of the Cenozoic Malawi rift (East African rift system). Tectonics, 13(2), 313-326.

Ring, U., & Betzler, C. (1995). Geology of the Malawi Rift: kinematic and tectono sedimentary background to the Chiwondo Beds, northern Malawi. Journal of Human Evolution, 28(1), 7-21.

Ring, U., (1995). Tectonic and lithological constraints on the evolution of the Karoo graben of northern Malawi (East Africa). Geologische Rundschau, 84(3), 607-625.

Ring, U., Betzler, C., & Delvaux, D. (1992). Normal vs. strike-slip faulting during rift development in East Africa: the Malawi rift. Geology, 20(11), 1015-1018.

Ring, U., Kröner, A., Buchwaldt, R., Toulkeridis, T. and Layer, P.W., (2002). Shear-zone patterns and eclogite-facies metamorphism in the Mozambique belt of northern Malawi, east-central Africa: implications for the assembly of Gondwana. Precambrian Research, 116(1-2), 19-56.

Roberts, E. M., Stevens, N. J., O'Connor, P. M., Dirks, P. H. G. M., Gottfried, M. D., Clyde, W. C., & Hemming, S. (2012). Initiation of the western branch of the East African Rift coeval with the eastern branch. Nature Geoscience, 5(4), 289-294. doi:10.1038/ngeo1432.

Rosendahl, B.R., (1987). Architecture of continental rifts with special reference to East Africa. Annual Review of Earth and Planetary Sciences, 15(1), 445-503.

Saria, E., Calais, E., Stamps, D. S., Delvaux, D., & Hartnady, C. J. H. (2014). Present-day kinematics of the East African Rift. Journal of Geophysical Research: Solid Earth, 119(4), 3584-3600.

Scott, D. L., Etheridge, M. A., & Rosendahl, B. R. (1992). Oblique-slip deformation in extensional terrains: A case study of the lakes Tanganyika and Malawi Rift Zones. Tectonics, 11(5), 998-1009.

Siler, D. L., & Faulds, J. E. (2013). Three-dimensional geothermal fairway mapping: examples from the western Great Basin, USA (No. DOE-Pyramid-2842-dls-5). Geothermal Resources Council, Davis, CA (United States).

Smith, R.S. and Salem, A., (2005). Imaging depth, structure, and susceptibility from magnetic data: The advanced source-parameter imaging method. Geophysics, 70(4), 31-38. https://doi.org/10.1190/1.1990219.

Stamps, D. S., Saria, E., & Kreemer, C. (2018). A geodetic strain rate model for the East African Rift system. Scientific reports, 8(1), 1-8.

Thurston, J. B., & Smith, R. S. (1997). Automatic conversion of magnetic data to depth, dip, and susceptibility contrast using the SPI (TM) method. Geophysics, 62(3), 807-813.

Tsokonombwe, G. (2017). Hydrogeochemistry modeling of Chiweta geothermal prospect, Northern Malawi (Doctoral dissertation).

Van der Beek, P., Mbede, E., Andriessen, P., & Delvaux, D. (1998). Denudation history of the Malawi and Rukwa Rift flanks (East African Rift System) from apatite fission-track thermochronology. Journal of African Earth Sciences, 26, 363-386.

Wanless, V. D., Kurz, M. D., Elsenbeck, J., Curtice, J., Shaw, A. M., & Atekwana, E. A. (2016, December). Helium isotopes in hot spring gases as magmatic tracers during incipient rifting in Malawi and Zambia. In AGU Fall Meeting Abstracts (Vol. 2016, pp. T44C-05).

Wedmore, L. N., Williams, J. N., Biggs, J., Fagereng, Å., Mphepo, F., Dulanya, Z., Willoughby, J., Mdala, H. & Adams, B. A. (2020). Structural inheritance and border fault reactivation during active early-stage rifting along the Thyolo fault, Malawi. Journal of Structural Geology, 139, 104097.

Williams, J. N., Fagereng, Å., Wedmore, L. N., Biggs, J., Mphepo, F., Dulanya, Z., Mdala, H., & Blenkinsop, T. (2019). How do variably striking faults reactivate during rifting? Insights from southern Malawi. Geochemistry, Geophysics, Geosystems, 20(7), 3588-3607.

Wines, D. R., & Lilly, P. A. (2003). Estimates of rock joint shear strength in part of the Fimiston open pit operation in Western Australia. International Journal of Rock Mechanics and Mining Sciences, 40(6), 929-937.

Yasidu, U. M., Fujii, Y., Fukuda, D., Kodama, J. I., & Maneya, G. (2017, June). Effect of humidity on tensile strength of rocks in selected underground coal mines in Malawi. In 51st US Rock Mechanics/Geomechanics Symposium. OnePetro.

Zhang, J. J. (2019). Applied petroleum geomechanics. Gulf Professional Publishing.

Appendix A

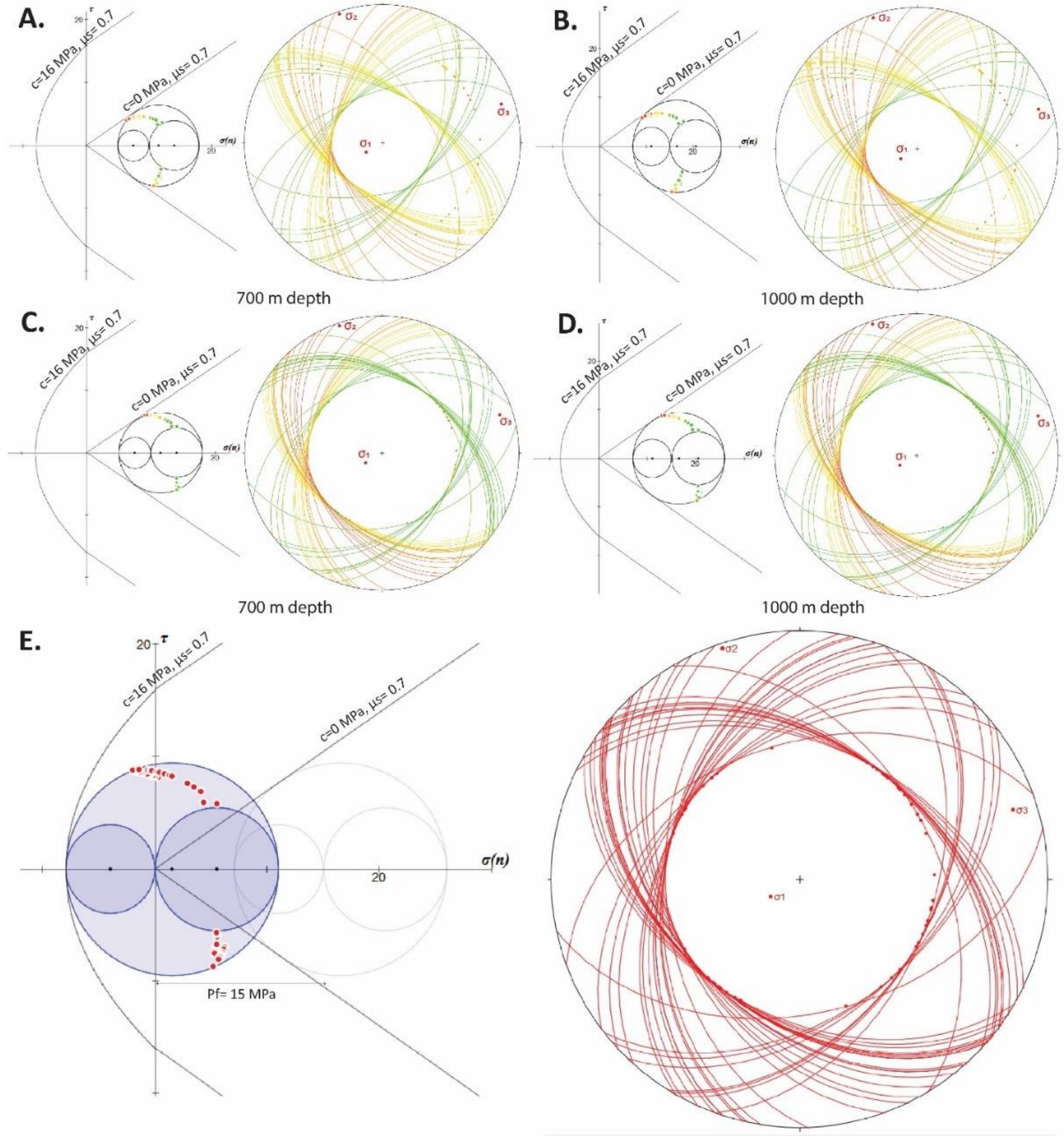

Figure. S1. 3D Mohr circle analysis for slip tendency of 52 normal faults (great circles) at 700 and 1000 m.b.g.l. with a Griffith failure envelopes c= 0 MPa and c= 16 MPa and a μs= 0.7. A. and B. Mohr circle analysis and stereonet showing the slip tendency of an analysis performed at 700 and 1000 m.b.g.l., respectively with faults dipping 60°. C. and D. Mohr circle analysis and stereonet showing the slip tendency of an analysis performed at 700 and 1000 m.b.g.l., respectively with faults dipping 45°. E. Mohr circle analysis and stereonet calculating failure within increasing the pore fluid pressure (15 MPa). The dots represent the poles of planes. Red and orange colors indicate a higher slip tendency than yellow and green colors.

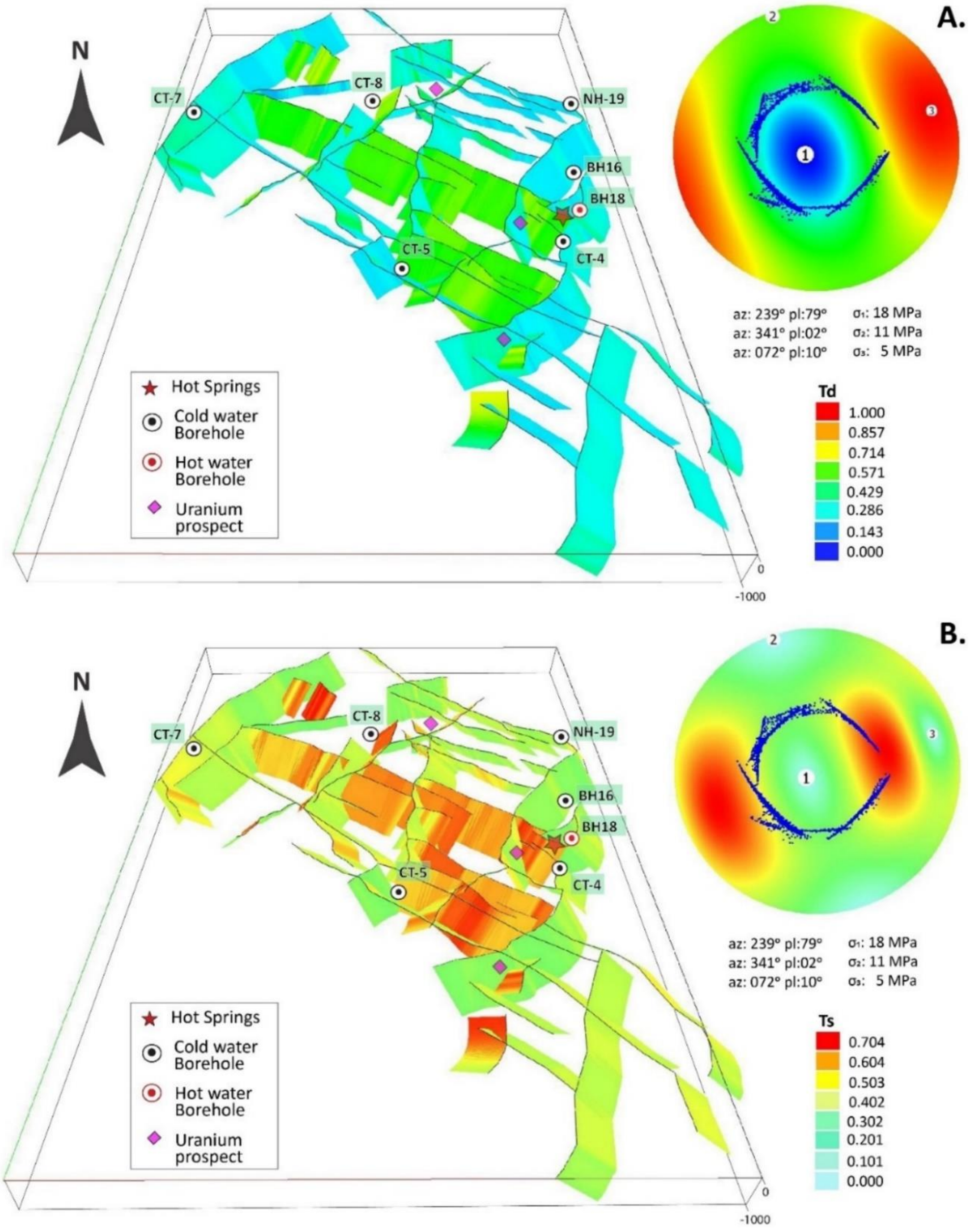

Figure. S2. 3D Structural Model of the Chiweta Geothermal Zone. A. Dilation tendency and B. Slip tendency, both showing the stereonet with poles along-strike variation of the 52 normal faults

with 45° dip. Analysis performed at 700 m.b.g.l. equal to the overburden pressure calculated with a rock density of 2.65 g/cm^3 and a frictional coefficient value of 0.7.

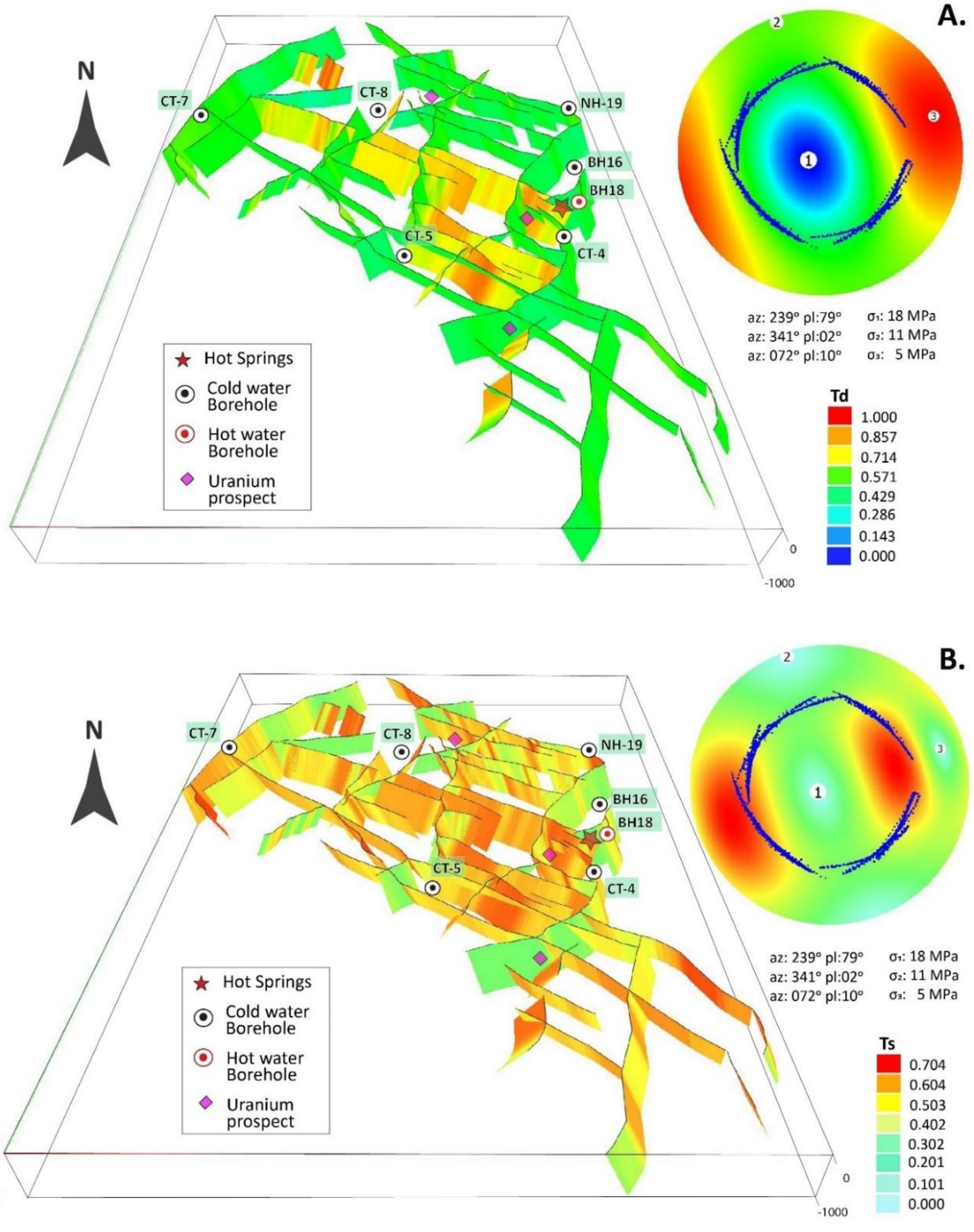

Figure. S3. 3D Structural Model of the Chiweta Geothermal Zone. A. Dilation tendency and B. Slip tendency, both showing the stereonet with poles along-strike variation of the 52 normal faults

with 60° dip. Analysis performed at 700 m.b.g.l. equal to the overburden pressure calculated with a rock density of 2.65 g/cm^3 and a frictional coefficient value of 0.7.

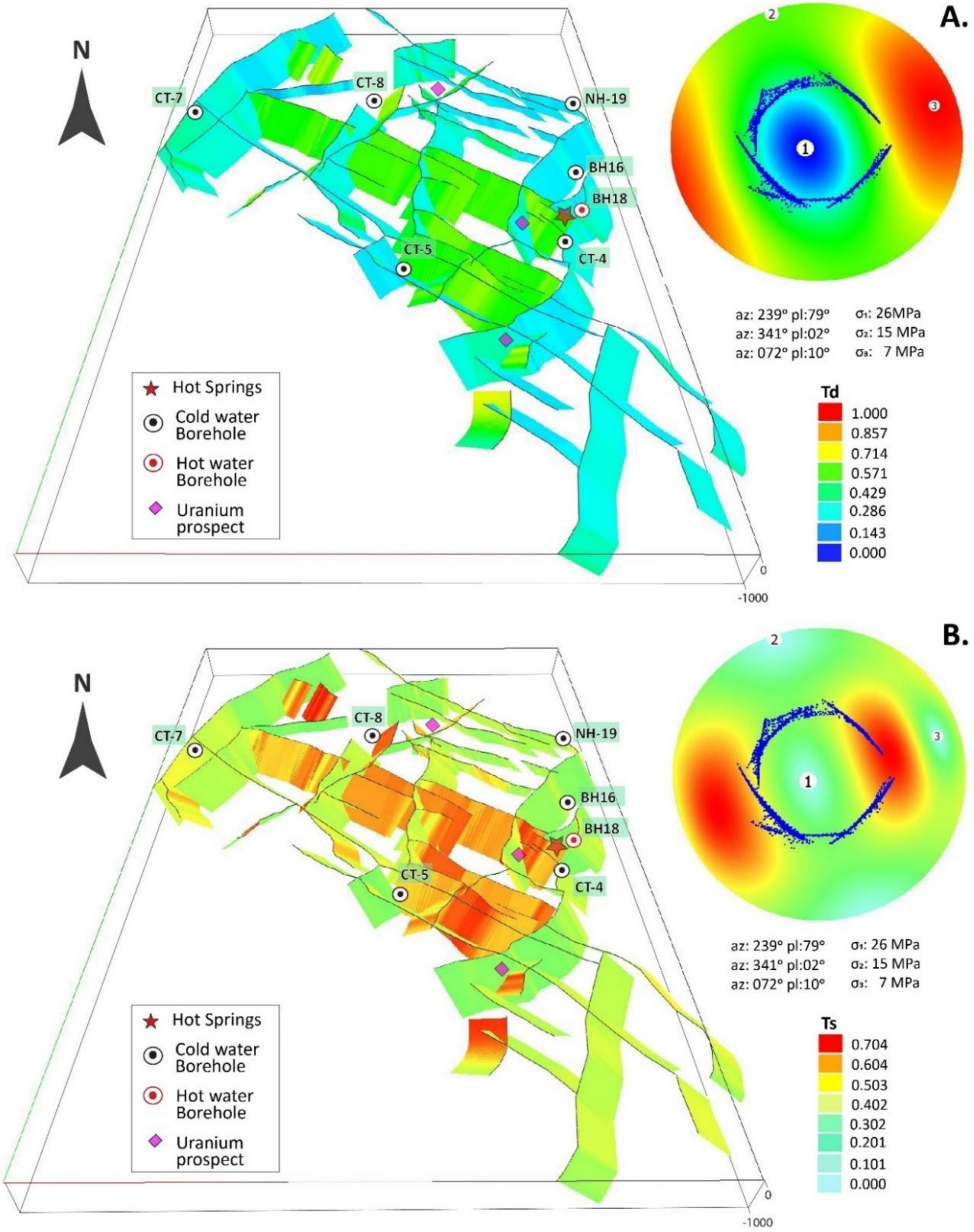

Figure. S4. 3D Structural Model of the Chiweta Geothermal Zone performed. A. Dilation tendency and B. Slip tendency, both showing the stereonet with poles along-strike variation of the 52 normal faults with 45° dip. Analysis performed at 1000 m.b.g.l. equal to the overburden pressure calculated with a rock density of 2.65 g/cm^3 and a frictional coefficient value of 0.7.

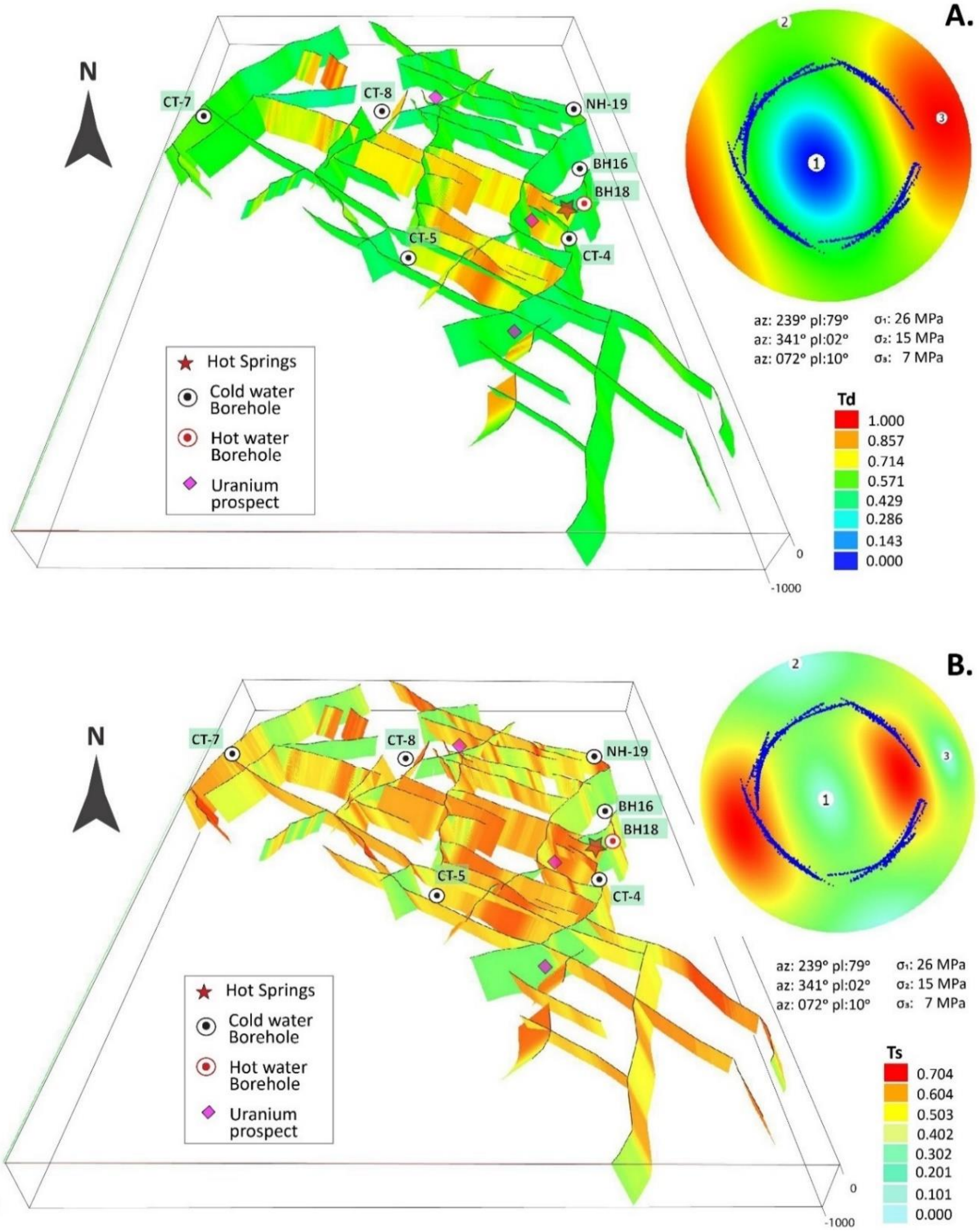

Figure. S5. 3D Structural Model of the Chiweta Geothermal Zone. A. Dilation tendency and B. Slip tendency, both showing the stereonet with poles along-strike variation of the 52 normal faults with 60° dip. Analysis performed at 1000 m.b.g.l. equal to the overburden pressure calculated with a rock density of 2.65 g/cm^3 and a frictional coefficient value of 0.7.

Appendix B

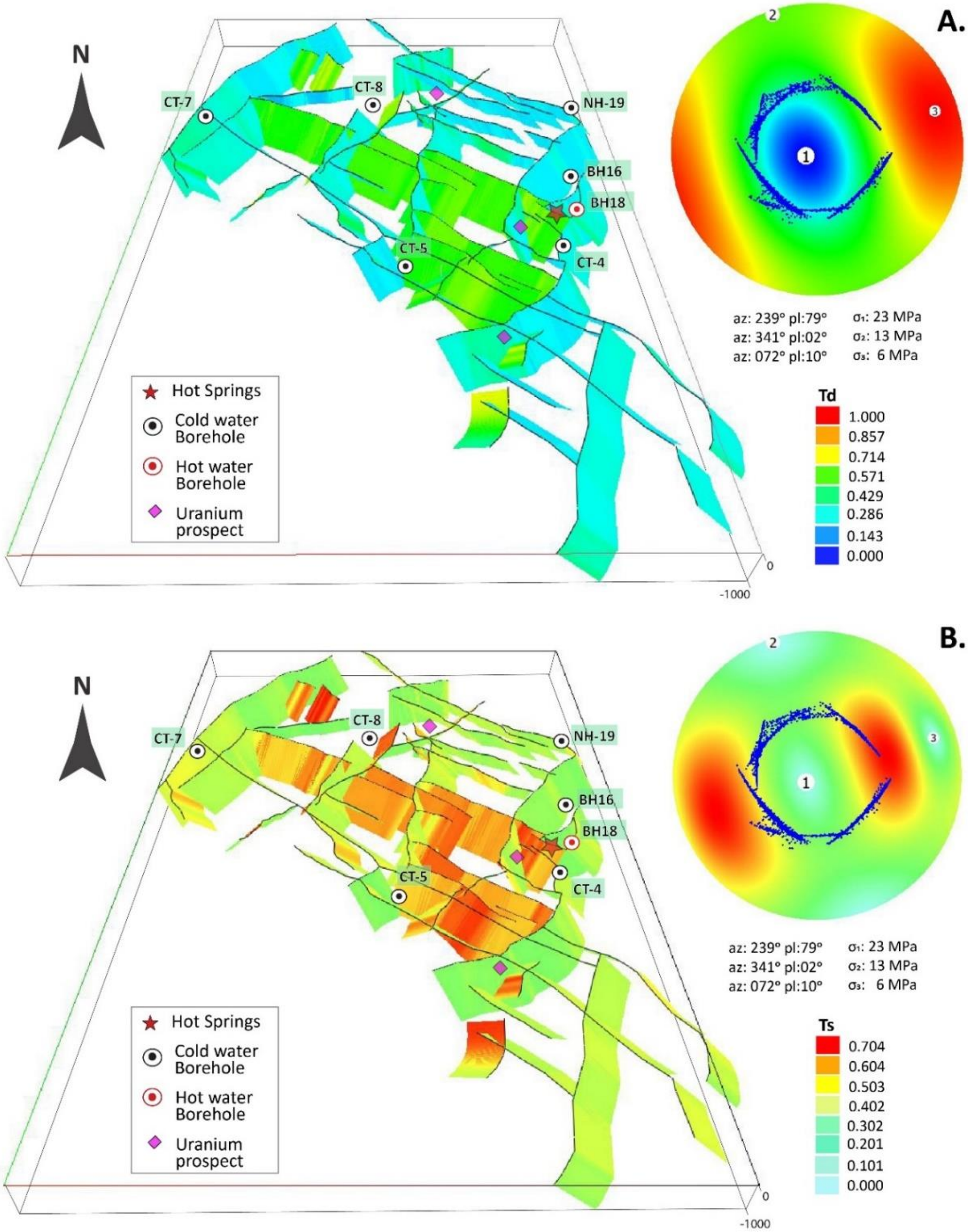

Figure. S1. 3D Structural Model of the Chiweta Geothermal Zone performed. A. Dilation tendency and B. Slip tendency, both showing the stereonet with poles along-strike variation of the 52 normal faults with 45° dip. Analysis performed at 1000 m.b.g.l. equal to the overburden pressure calculated with a rock density of 2.3 g/cm^3 and a frictional coefficient value of 0.6.

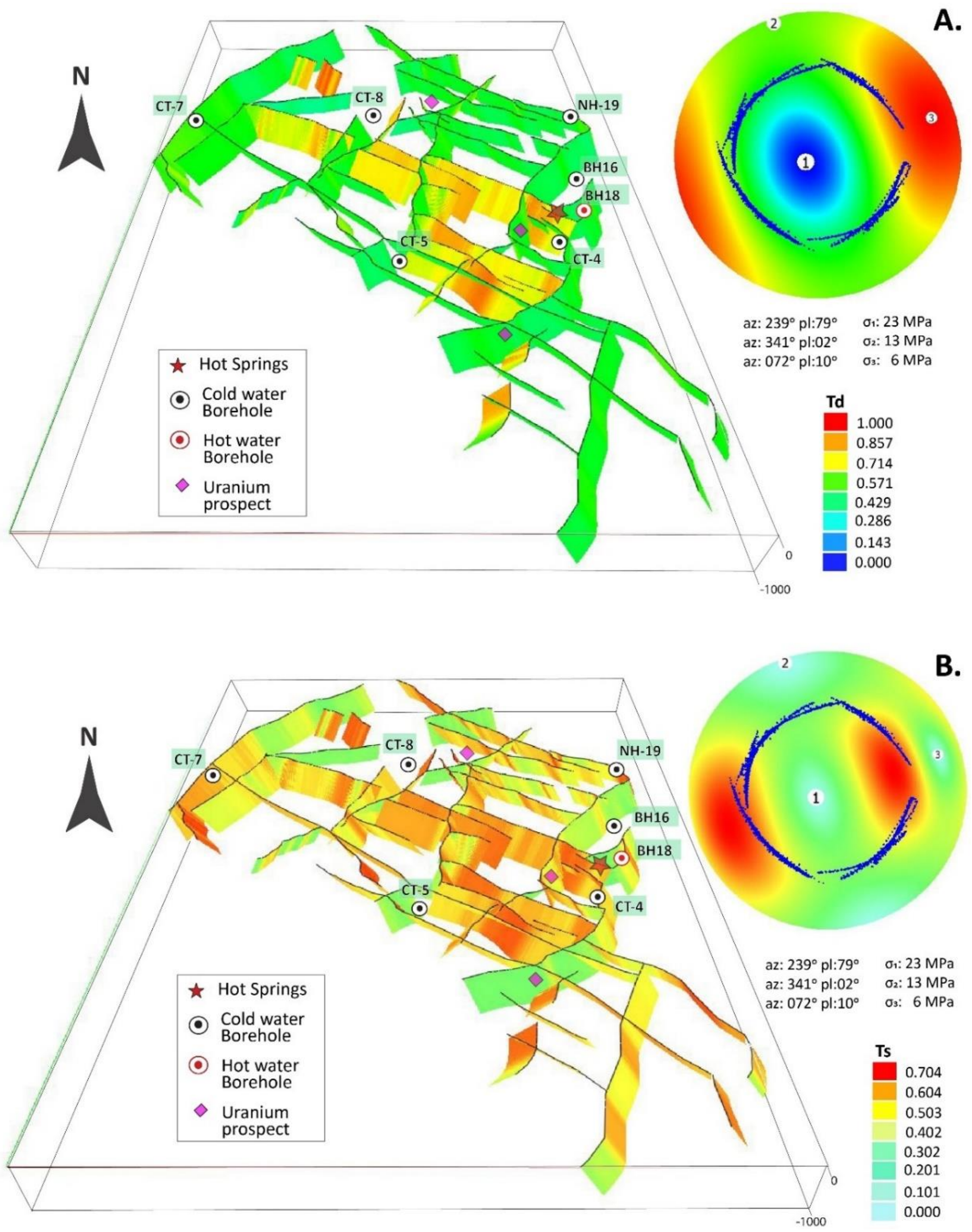

Figure. S2. 3D Structural Model of the Chiweta Geothermal Zone. A. Dilation tendency and B. Slip tendency, both showing the stereonet with poles along-strike variation of the 52 normal faults with 60° dip. Analysis performed at 1000 m.b.g.l. equal to the overburden pressure calculated with a rock density of 2.3 g/cm^3 and a frictional coefficient value of 0.6.

.

VITA

Estefanny Dávalos Elizondo

Candidate for the Degree of

Doctor of Philosophy

Dissertation: ASSESSING FRACTURE NETWORKS AND GEOCHEMISTRY OF GEOTHERMAL SYSTEMS IN MAGMA-POOR CONTINENTAL RIFTS: AN EXAMPLE FROM THE MALAWI RIFTED ZONE

Major Field: Geology

Biographical:

Education:
Completed the requirements for the Doctor of Philosophy in Geology at Oklahoma State University, Stillwater, Oklahoma in May, 2022.

Completed the requirements for the Bachelor of Geological Engineer at Autonomous University of Nuevo León, Nuevo León, Mexico in 2011.

Experience: Teaching Assistant, Boone Pickens School of Geology August 2017-December 2021. Research Scientist at the National Institute of Electricity and Clean Energies (INEEL), Cuernavaca, Mexico 2016 - 2017. Chief Exploration Geologist at Alternative Energies, Studies, and Projects (ENAL), Mexico City, Mexico 2012 - 2016.

Professional Memberships:
Geological Society of America (GSA), European Geoscience Union (EGU), Geological Society of America (GSA), Association for Women Geoscientists (AWG), Woman in Geothermal (WING), Geothermal Rising (GRC), Mexican Geothermal Association (AGM).